ROCKET MEASUREMENTS OF SOLAR AND LUNAR ULTRAVIOLET FLUX AND THE DETERMINATION OF ATMOSPHERIC MOLECULAR OXYGEN AND OZONE DENSITIES.

Mohammad Ilyas, B.Sc.(Jamia),
M.Sc.(Aligarh).

A Thesis
presented for the degree of
DOCTOR OF PHILOSOPHY
at the
University of Adelaide
Physics Department
October 1976

Frontispiece: Cockatoo rocket on launcher.
(Courtesy W.R.E.)

Dedicated to my Uncle, Mr. Mohammad Iqbal,

to whom I owe so much of my education.

CONTENTS

SUMMARY

The thesis describes a series of rocket experiments performed (i) to study the vertical distribution of molecular oxygen and nocturnal ozone in the upper atmosphere, and (ii) to measure absolute solar and lunar ultraviolet fluxes in several wavelength bands.

Absorption spectroscopy of solar ultraviolet radiation in two bands, the band being defined by the detectors spectral sensitivity, were used for the oxygen determinations. Band (a) is sensitive to λλ 105 (114) - 135 nm and utilises Lithium Fluoride (Magnesium Fluoride) window with nitric oxide gas filling. Band (b) is sensitive to λλ 155 - 169 nm and utilises Quartz window with Triethyl-amine gas filling. The wide variation of oxygen absorption coefficients between the two wavelength regions has allowed measurement of molecular oxygen concentrations over the highly variable region 70 - 95 km and the largely unmeasured region, i.e. between 105-135 km.

The construction of the detectors (ionchambers) is described including measures taken to improve the life-time and stability of the ionchambers used previously for similar experiments. The calibration of these detectors is described as well as the development and calibration of a solar aspect detector for use on unstabilized sounding rockets. Nine of eleven rocket flights conducted during the course of this work, were instrumented with, ultraviolet ionchambers and were used to study seasonal and diurnal variations of molecular oxygen at Woomera (Australia). For each of the two bands, used for oxygen determinations, a height dependent value of absorption cross-section is employed depending on the effect of radiation hardening.. In the wavelength band λλ 105 (114) - 135 nm, the solar spectrum is dominated by the Hydrogen Ly-α line (about .1 nm wide with a line centre at 121.57 nm). The detector signal is almost exclusively due to this line and absorption coefficients at this

line alone need to be considered in the region 70 - 95 km. However, the temperatures at the above mesospheric altitudes are generally lower than room temperature, at which laboratory measurements of absorption coefficient are generally made. Only recently, high resolution Ly-α absorption data at lower temperatures have been obtained in our laboratory. The new absorption data appropriate to the mesospheric low temperature condition have been used for evaluating the hight-dependent effective absorption cross-section for deriving oxygen densities from present Ly-α absorption measurements. Similar effective cross-section corrections have been made to the other published Ly-α absorption measurements of mesospheric oxygen. The data so corrected is used to obtain subsidiary information relating to the latitudinal and

seasonal variations of mesospheric oxygen and derived kinetic temperatures. This analysis shows clear seasonal and latitudinal variations in oxygen and kinetic temperatures at mesospheric altitudes. The new observational mean profile of mesospheric oxygen is found to be in better agreement with the standard Reference Model.

Useful results from one of the two rocket measurements of night-time ozone density utilizing absorption spectroscopy of lunar radiation in middle ultraviolet (200-300 nm) were obtained. These results are presented. Laboratory measurements of quantum efficiency of sodium-salicylate in the 110 - 270 nm region and its variation with the age of the coating over a period of more than a year are presented. These results are discussed in the context of absolute calibration of Ultraviolet (UV) detectors and have been used to obtain solar and Lunar UV fluxes in the wavelength bands of the detectors used.

This thesis contains no material which has been accepted for the award of any other degree or diploma in any University. To the best of the author's knowledge and belief it contains no material previously published or written by another person, except where due reference has been made in the text.

(Mohammad Ilyas)

ACKNOWLEDGEMENTS

The rocket experiments described in this thesis were carried out in co-operation with the Flight Projects and the Upper Atmosphere Research Groups of the Weapons Research Establishment at Salisbury, South Australia. The author would like to thank all persons involved with the preparation and launching of the rocket vehicles, in particular Dr. G.G. O'Connor for assisting throughout this work.

Thanks are due to Mr S. Dowden formerly of the Physics Department for his valuable technical assistance and to Messrs R. Hurn and R. Walker of the Physics Department for designing and constructing the rocket electronic circuitry.

The author gratefully acknowledges the considerable assistance given by Dr. R.C. Schaeffer during the course of this work. The author would also like to thank Mr T.G.K. Murty for many useful discussions and assistance in proof-reading the typed copy.

Special thanks are due to the author's wife, Noor, for the unique help and support she has given by assuming full responsibilities of the family and for her great patience as well as to Abidah for being very patient during this period.

Finally, the author would like to thank his supervisors, Professor J.H. Carver and Dr. B.H. Horton, for their guidance and encouragement during the course of this work, and the writing of this thesis.

Part of the rocket program was financed through grants to the University of Adelaide from Australian Research Grants Committee.

The author gratefully acknowledges the support provided by an Adelaide University Research Grants Postgraduate Scholarship and a full-time demonstrating position with the University of Adelaide.

Thanks are due to Mrs. B. Young for typing the thesis.

CHAPTER 1

INTRODUCTION

1.1 SCOPE OF THE PRESENT WORK

Although considerable effort has been expanded in measuring the properties of the total neutral atmosphere, relatively few measurements have been made of the properties of the individual atmospheric constituents. This is especially true with regard to molecular oxygen above about 90 km, where both its dissociation into atomic oxygen and diffusion begin to become important. Therefore, the region between 95 km and 120 km is of particular importance (Johnson, 1973). Ironically, this region (95-120 km) is perhaps the least studied part of the 70-150 km region and the nature of seasonal, latitudinal and temporal variations is largely unknown.

This is reflected in the fact that statistical studies of thermospheric oxygen data have been restricted to altitudes above 120 km (Danilov 1972, Offerman, 1974). At lower altitudes, where molecular oxygen is a well-mixed species, more information is available from measurements of the total neutral atmosphere. However, even here more information is needed on the molecular oxygen distribution and its variations with season, latitude and time of day. Additional measurements in the upper mesosphere (70-90 km) and lower thermosphere will be helpful in understanding atomic oxygen and ozone photochemistry as well as vertical and horizontal transport mechanisms in a region where several of these problems are probably important. These measurements will also be helpful in improving existing "standard or reference atmospheres", that attempt to give a dynamic interpretation of the behaviour of the real atmosphere. As pointed out by Schilling (1968), even minor variations in the properties of a reference atmosphere in the upper mesosphere - lower thermosphere region can lead to very large variations in its properties at higher altitudes. Therefore, a proper interpretation of the variations of the

upper atmosphere, as detected by earth-orbiting satellites, depends upon a thorough knowledge of the variations in these lower regions.

There have been very few determinations of molecular oxygen density in the southern hemisphere. At mesospheric altitudes, the number of observations prior to this work was about half a dozen. The addition of another six mesospheric oxygen profiles as obtained in this work, has allowed the detection of a possible hemispherical asymmetry in mesospheric molecular oxygen. There are only four rocket determinations of lower thermospheric oxygen (100-120 km) at southern latitudes.

Ozone is one of the most important minor constituents in the upper atmosphere playing a vital role in the atmospheric photochemistry. Although ozone distribution and its variations in the atmosphere have been studied in greater detail, relatively few accurate measurements are available at altitudes above about 60 km and experimentally little is known about ozone variations at higher altitudes.

UV absorption spectroscopy provides a useful method for determining the concentrations of oxygen and ozone in the upper atmosphere. In fact, absorption spectroscopy has provided almost all the oxygen data below about 95 km. Besides, the same absorption detectors can be used to determine absolute fluxes of the source.

Different parts of the solar UV spectrum (100-120 km) are absorbed in different but limited height intervals due to a wide variation in absorption cross-section of molecular oxygen (Sections 2.2 and 2.6). Therefore, detectors can be so chosen to allow absorption measurements in specific height intervals. Absorption spectroscopy of solar Ly-α radiation, allows the determination of molecular oxygen concentrations in the altitude region 65-95 km. The radiation in the wavelength band around 160 nm is absorbed in the altitude region of about 100-140 km whereas the radiation around 145 nm is absorbed at altitudes 10-15 km higher up. Since a Cockatoo vehicle, as used in the present work, is capable of carrying rocket payloads to altitudes less than 140 km, a

combination of two detectors, one operative around Ly-α (121.7 nm) and the other operative around 160 nm, is ideal to cover the entire range 70-140 km, enveloping in the important 100-120 km region. Therefore, a combination of Ly-α and quartz-triethylamine (155-169 nm) ionchambers as detectors, was used for oxygen determinations. The detectors were also used to obtain solar fluxes. The absolute flux determinations in the latter case are of specific importance in establishing the solar minimum brightness temperature (Section 1.2). These results are presented in Chapter 5.

A statistical analysis of mesospheric data was made to study different variations in mesospheric oxygen and derived temperatures and the results are presented in Chapter 6.

Absorption spectroscopy of lunar radiation in several bands between 200 nm and 300 nm was used to determine night-time ozone concentrations. Since the lunar radiation is due to reflection, absolute lunar fluxes provide a measure of lunar reflectivity. These results are presented in Chapter 7. Solar UV radiation, the absorption of which forms the major part of this work, is briefly described in the following sections of this chapter.

1.2 THE SOLAR UV SPECTRUM AND ITS ORIGIN

The primary source of energy for most atmospheric phenomena is the sun. It is, therefore, most important to know the energy spectrum of solar radiation and how this radiation reacts with the atmosphere. Until 1946, knowledge of the solar spectrum was limited to wavelengths longer than about 290 nm. Shorter wavelengths are prevented from reaching terrestrial or balloon-borne equipment by the strong absorption processes that take place in the upper atmosphere (Section 2.1). The first measurements of the solar spectrum beyond the atmospheric cut-off were made with a normal incidence grating spectrograph carried by a V-2 rocket to an altitude of 88 km and the results showed a continuation of the visible

continuum down to 210 nm. Although considerable improvements in the resolution of spectrographs were achieved in the following years, the spectrum could not be extended to wavelengths below 210 nm for some years. This was mainly because of the rapid decrease in the continuum intensity below this wavelength. In these years, a biaxial pointing control system was developed which has been used since 1952 for investigations of the solar ultraviolet spectrum employing dispersive instruments. Non-dispersive detectors (phosphors, Geiger counters and ionchambers) have also been used simultaneously for measurements of solar UV intensities below 210 nm since 1948. Significant success has been achieved in measuring the solar spectrum over a very wide range. Recently, Smith and Gottlieb (1974) have reviewed the measurements of solar flux and its variations at all wavelengths.

The VUV part of the spectrum (100-300 nm) is of particular relevance for the absorption measurements described in the following chapters. Tousey (1963), Goldberg (1967) and more recently Noyes (1971) have presented detailed reviews of the solar ultraviolet measurements. Most recently, Donnelly and Pope (1973) have developed a very useful model of solar ultraviolet flux at fine wavelength intervals (1 nm). The moderate resolution spectrum is shown in Figure (1.3) in which line intensities have been integrated. More detailed measured spectrum in the region 100 nm to 320 nm is shown in Figures (1.1 and 1.2).

Observations of the solar spectrum have led to a description of the solar atmosphere in terms of three emitting zones:

(i) The Photosphere: This is the innermost zone of about 350 km thickness extending from the limb of the visible solar disk down to the deepest observable layers. The temperature decreases from about 9000 K at the bottom to about 4500 K at the top.

(ii) The Chromosphere: This zone lies immediately above the photosphere. It is about 20,000 km thick. Its temperature increases from 4500 K where it meets the photosphere to about 40,000 K where it meets the corona.

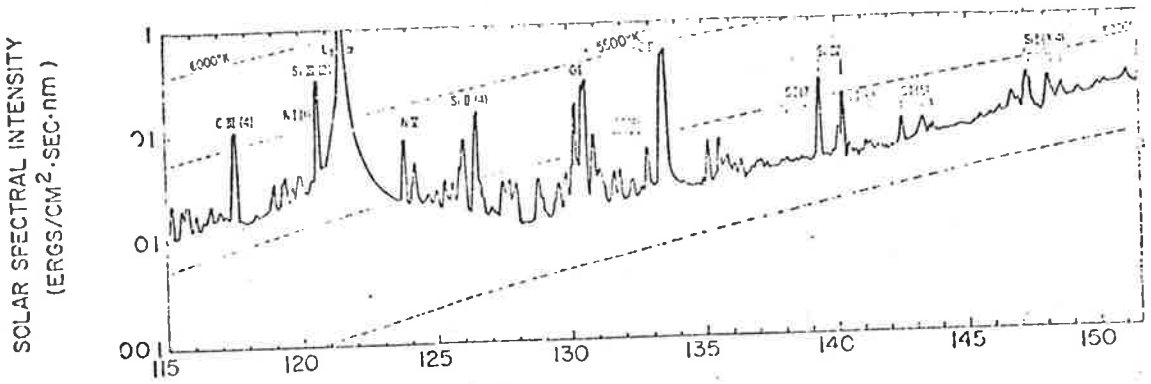

Figure 1.1a The intensity distribution of the solar spectrum between 115nm and 152 nm determined by the density tracing of photographic exposures (Tousey, 1964).

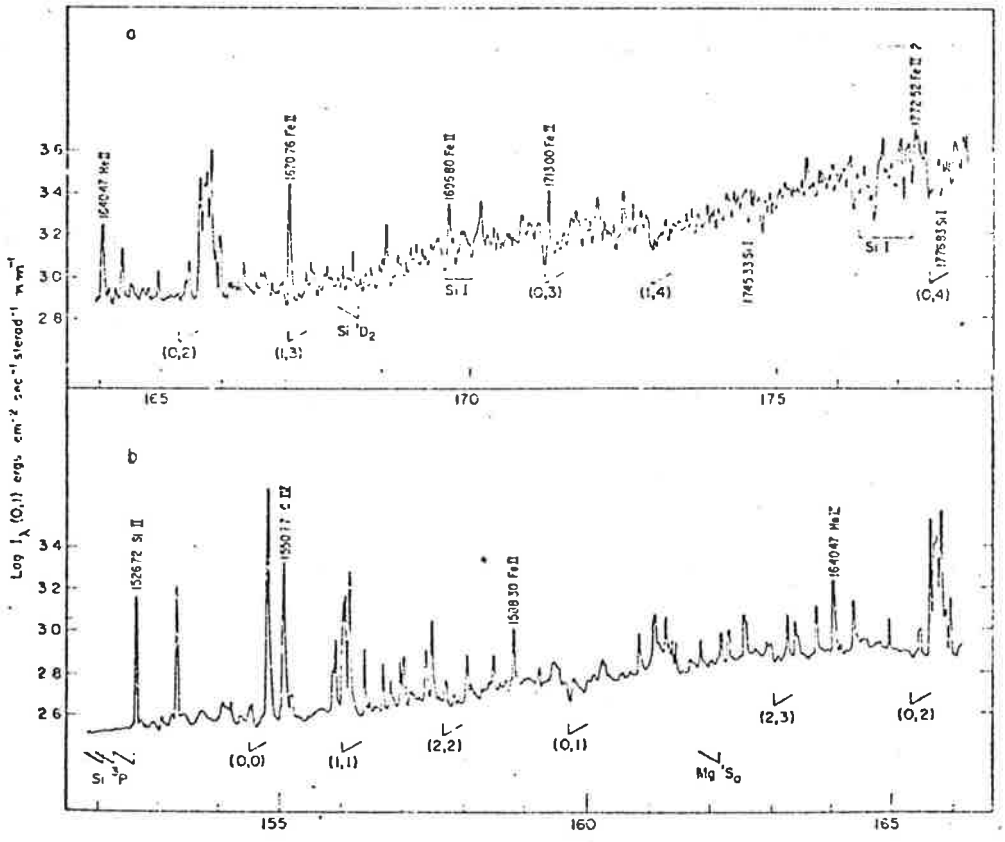

Figure 1.1b The intensity distribution of the solar spectrum between 152 nm and 178 nm. The spectra were obtained by the density tracing of photographic exposures. No attempt should be made to read line intensities, as the spectra were traced in rapid scan and some of the lines may therefore not have been properly recorded (Widing et al., 1970).

(iii) The Corona: This is the outermost zone. During total solar eclipse, it has been seen to extend to a distance of at least 40 solar radii. Between the chromosphere and the corona there is a very narrow transition region where the temperature rises from 40,000 K to about 1 million degrees. The general coronal temperatures are between 1 and 2 million degrees.

The visible solar radiation comes almost entirely from the photosphere and consists of a continuum, with a radiation temperature* of about 6300 K, crossed by numerous Fraunhofer absorption lines. The continuous opacity of the solar gases is a minimum in the visible spectral range where it is predominantly due to the free - free and bound free transitions of the negative hydrogen ion. At wavelengths both longward and shortward of the visible spectrum, the continuous opacity increases, with the result that the emergent solar continuum originates in progressively higher layers. Therefore, it is expected that in both the extreme ultraviolet and far infra-red, the radiation temperature of the continuum will pass through a minimum at some wavelength for which the radiation is emitted from the temperature minimum region between the photosphere and chromosphere.

Beginning in the near ultraviolet, the continuous opacity increases towards shorter wavelengths as the ionization limits of the abundant neutral metals are crossed. As a result the radiation temperature of the continuum drops from 6300 K to about 5500 K at 210 nm. Near 208.7 nm the character of the solar spectrum undergoes a rapid change with the continuum intensity falling by a factor of five in a short space of about 1.5 nm (Boland et al. 1971). At 200 nm, the radiation temperature has dropped to 5000 K while the cores of the absorption lines follow a 4900 K black body curve both above and below the continuum discontinuity.

---

* The radiation temperature of the sun at a particular wavelength is the temperature of a black body which would emit the same intensity of radiation at that wavelength as the sun.

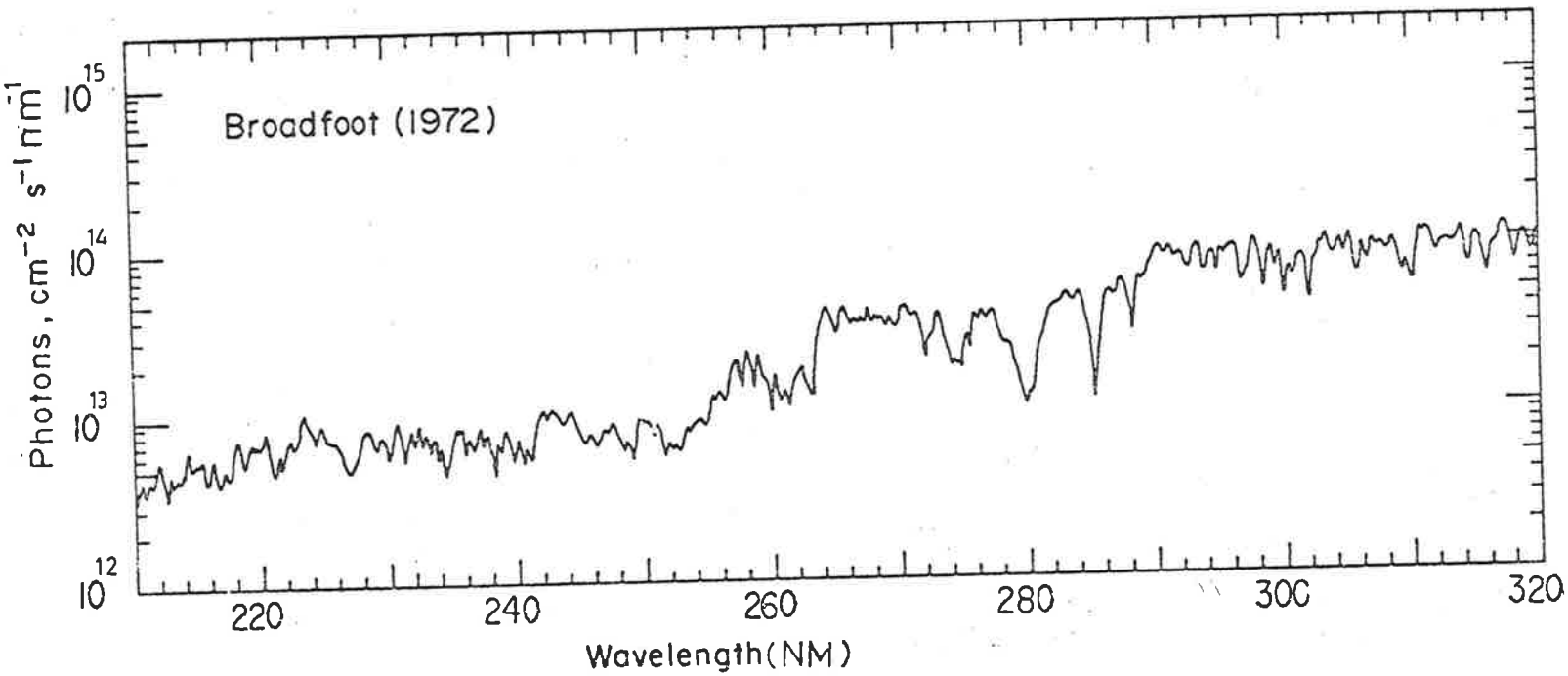

Figure 1-2 *The solar ultraviolet spectrum in the wavelength range 210 -320nm, Based on fig. 3 of Broadfoot, 1972.*

(Donnelly & Pope, 1973)

It is concluded that the continuum radiation below about 208 nm arises only a short distance below the region of the temperature minimum, while the absorption lines are formed slightly closer to the temperature minimum where the temperature is a little lower.

More recent measurements of the continuum intensity below 200 nm are those of Widing et al. (1970), Parkinson and Reeves (1969), Brueckner and Moe (1972), Nishi (1973, 1975), Ackerman and Simon (1973) and Carver et al. (1972). These are briefly described and discussed in Section (6.4). These measurements are in general agreement except for the large discrepencies in the intensity level. Qualitatively, below 200 nm continuum follows a descending black body curve down to about 170 nm. Between 170 nm and 140 nm there is a broad radiation temperature minimum. Below 140 nm (Figure 1.1a), the temperature begins to slowly rise with a more rapid increase occurring as the wing of the very intense Ly-α line begins to dominate. On the short wavelength side of the Ly-α line, the radiation temperature falls to another minimum on the long wavelength side. Below 118 nm, the radiation temperature of the continuum rises again to a maximum at 97 nm.

In the 200 nm to 100 nm range, the type of line seen against the continuum changes from absorption to emission. The first emission lines appear just below 200 nm and towards shorter wavelengths the absorption lines progressively disappear as the emission lines become more numerous. Below 168.2 nm (which corresponds to the ^1D absorption edge of SiI) there are no atomic absorption lines and the only absorption features are the band heads of CO. All of the emission lines show limb brightening in keeping with their origin in the chromosphere where the temperature is increasing outwards.

The spectral range 168.2 nm to 152.5 nm is of particular interest because the emergent continuum radiation can be shown from observations to arise from the region of the temperature minimum. Above 168.2 nm the continuum is still photospheric in origin. This is shown by the continued

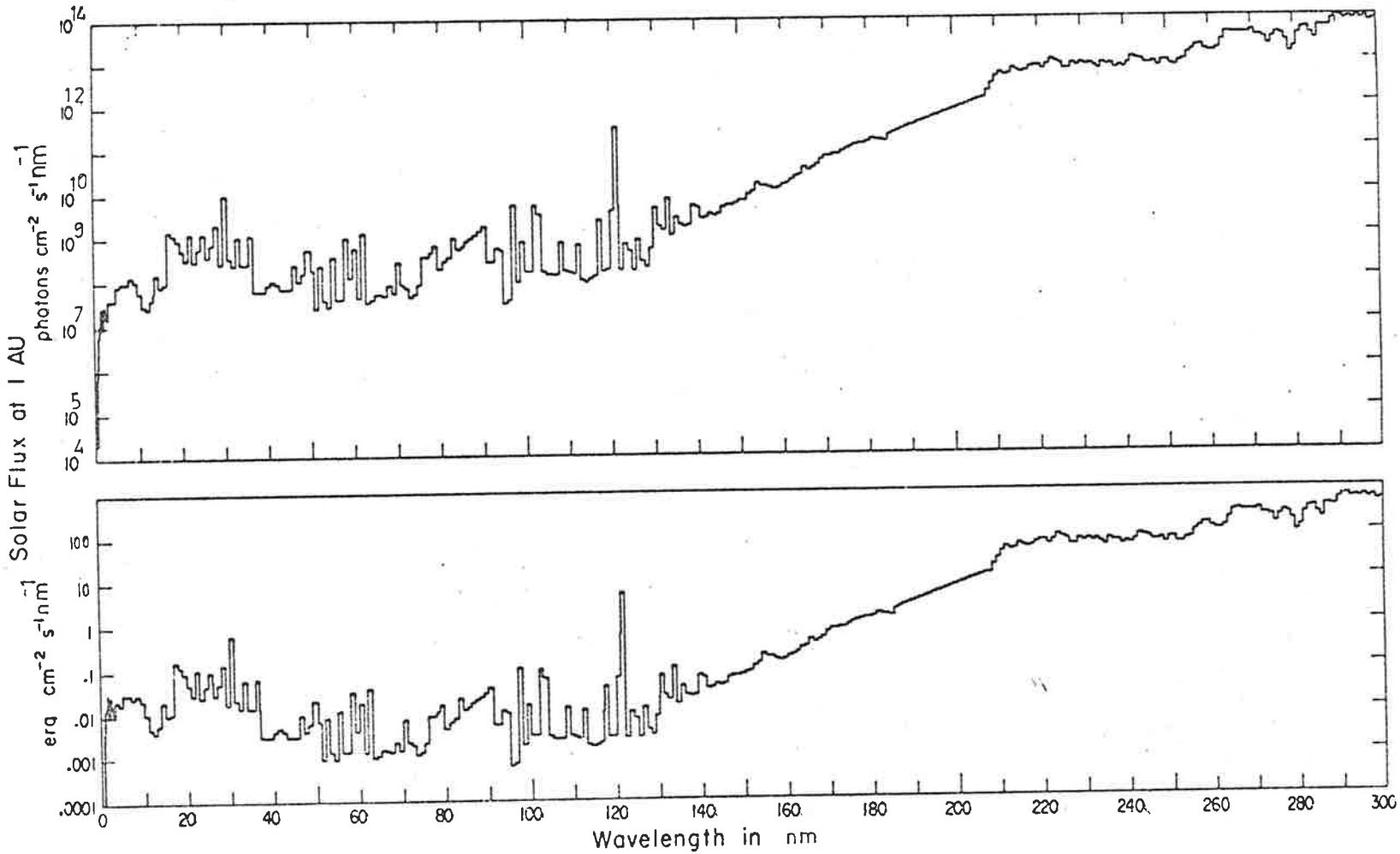

Figure 1.3 . The 1-300 nm solar flux for a moderate level of solar activity. The line emission is combined with the flux in the wavelength intervals that are 1 at wavelengths above 4 nm.
(Donnelly & Pope, 1973)

presence of shallow absorption lines (Figure 1.2b). This, as mentioned above, indicates that the emergent continuum arises from just below the temperature minimum region where the temperature is still decreasing outwards. Additional confirmation of this is given by the fact that above 168.2 nm, the continuum is still limb darkened. There is a small but rapid change in the continuum intensity at 152.5 nm which coincides with the 3p absorption edge of SiI. The intensity is highest to the short wavelength side of the edge and this, coupled with the strong limb brightening observed below 152.5 nm, implies that the continuum radiation below 15.25 nm is chromospheric in origin. Between 168.2 nm and 152.5 nm, there are no atomic absorption lines and the centre to limb variations are small (Brueckner and Moe, 1972). Both of these characteristics are expected for radiation arising from the region across the temperature minimum.

Recent theoretical models (Cuny, 1971, Gingerich et al, 1971) are in agreement with the observations in suggesting that the region between 152.5 nm and 168.2 nm is particularly significant for investigations of the temperature minimum. The quartz-triethylamine ionchamber (158-164 nm, FWHM) used in the present work is therefore particularly suitable for intensity measurements near the solar temperature minimum. These results are compared with other measurements in this region in Section (6.4).

1.3 THE SOLAR LY-α LINE

The solar H-Ly-α line at 121.57 nm is an extremely strong emission line. The flux from just this line usually exceeds the combined flux from all shorter wavelengths. However, the energy per Ly-α photon is too low to ionize the major constituents of the upper atmosphere. The line happens to be in a close proximity with a window in the O_2 absorption cross-section which allows its atmospheric penetration to much lower altitudes compared to the continuum. Because of this, absorption spectroscopy of this line alone has provided almost all the mesospheric oxygen measurements (Section 2.2.4). Many attempts have been made to study the

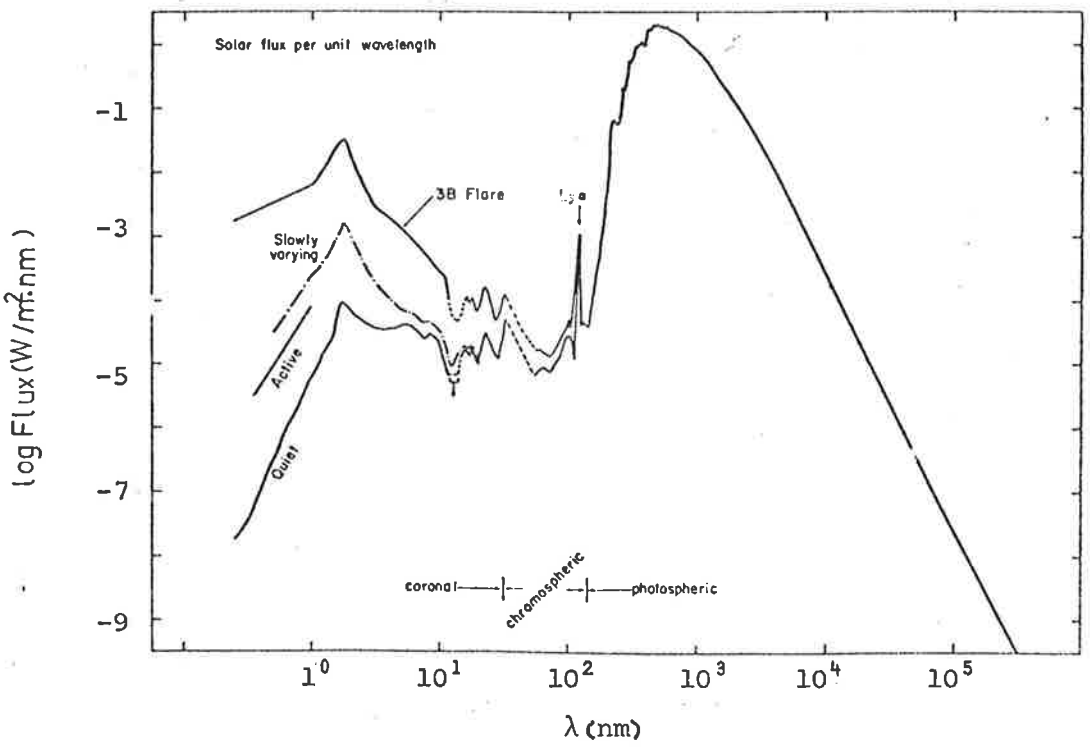

Figure 1.4 Summary of solar irradiance at all wavelengths. (Smith and Gottlieb, 1974).

shape of this line. Some of the earlier high resolution studies were made by Tousey and coworkers in 1959, 1960 and 1962 respectively (Purcell and Tousey, 1960; 1961; Tousey, 1963). Profiles were also taken in 1966 by Bruner and Parker (1969) and Quessette (1970) and in 1967 by Bruner and Rense (1969). All of these measurements have shown that the line profile is characterized by a half maximum width of about 0.1 nm, a wide shallow self-reversal formed by absorption due to atomic hydrogen between the rocket and the sun. Vidal-Majdar (1975) monitored variations in the shape of the line with changes in the level of solar activity. As the value of the absorption cross-section of molecular oxygen changes rapidly near the Ly-α wavelength, the shape of the Ly-α line is of importance when determining the effective absorption cross-section of molecular oxygen for the whole Ly-α line (Section 2.2.3). The shape of the line as measured in 1959 by Purcell and Tousey (1960) is shown in Figure (2.10).

CHAPTER 2

THE ATMOSPHERIC ABSORPTION OF SOLAR UV RADIATION

The development of a generally effective radiation absorption equation applicable to the atmospheric condition, is followed by the description of a procedure for evaluation of effective absorption cross-sections for two specific detectors used in the present work to determine molecular oxygen densities. The effects of other parameters such as temperature and water vapour contamination of the detector gas on the evaluation of the effective cross sections and derived oxygen (O_2) densities are also discussed in detail.

2.1 INTRODUCTION

Solar radiation is the major energy source for terrestrial processes. A small part of this radiation i.e., the visible is able to reach the earth's surface directly while the rest, of which ultraviolet radiation forms a significant and important part interacts with the atmosphere. Outside the visible region and the radio bands the solar radiant flux incident on the top of the earth's atmosphere is depleted on its downward path; mainly due to absorption by constituent gases of the atmosphere. Although the atmosphere is a mixture of many gases, there are wavelength regions in which the absorption is known to be due almost entirely to one constituent. In such cases the specificity of absorption in certain wavelength intervals or at certain wavelengths (such as Ly-α) permits the determination of the densities of individual absorbing species. Two such regions in which the above argument is applicable are the middle ultraviolet and the adjoining vacuum ultraviolet parts of the spectrum. In the middle ultraviolet (200 - 300 nm) absorption by ozone is dominant, while in the vacuum ultraviolet (100 - 200 nm) the only major constituent which absorbs strongly is molecular oxygen. Therefore absorbtion spectroscopy of radiation in these wavelength intervals has been used to infer the vertical distributions of

these two species. Experiments designed for this purpose are described in the following Chapters (3 and 7). Radiation below 100 nm is predominantly absorbed by nitrogen(N_2) and atomic oxygen (O) while radiation below about 10 nm is absorbed by total air ($n(O_2)+n(O)+n(N_2)$) and is useful for determining air densities by absorption technique. Figure(2.1) shows the heights at which the incident vertical flux is attenuated by the factor 'e' (penetration heights) as a function of wavelength. The dominant absorbers are also indicated in the figure. Ground level observations are restricted to wavelengths above about 295 nm at the short wavelength side. Detectors for the measurement of radiant intensity at wavelengths shorter than this should be taken above the altitudes shown in the Figure (2.1) corresponding to the wavelength region being studied if significant intensity measurements are to be made.

2.2 VERTICAL DENSITY DISTRIBUTION FROM UV ABSORPTION MEASUREMENTS

2.2.1 Atmospheric Absorption - General

According to the Beer-Lambert law, attenuation of a parallel monochromatic beam of radiation of wavelength, λ, on passing from the top of the atmosphere to a height h above the earth's surface is

$$\phi(\lambda,h) = \phi_\infty(\lambda) \exp[-\sigma(\lambda)N(h)] \qquad (2.1)$$

where $\phi(\lambda,h)$ = is the photon flux at height h in photons cm^{-2} sec^{-1}

$\phi_\infty(\lambda)$ = absorption cross section of the absorbing species in cm^2 (O_2 and O_3 in the present case)

and $N(h)$ = is the integrated vertical column density above a height, h, i.e. the number of oxygen molecules in a column of area 1 cm^2 along the path of the radiation.

If more than one species, say n different species, are contributing to the absorption of the monochromatic radiation of wavelength λ, then

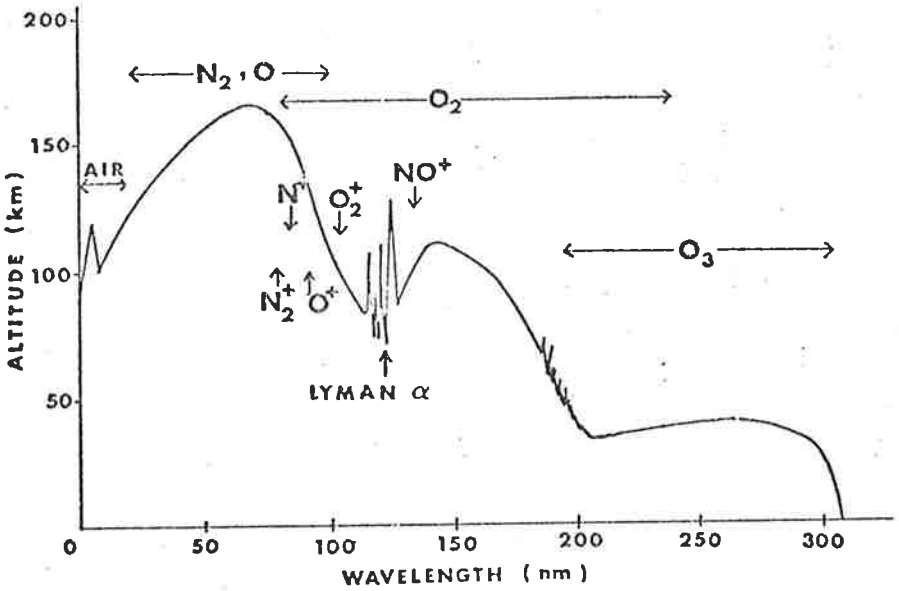

FIGURE 2.1 ATMOSPHERIC ABSORPTION HEIGHTS

(after Herzberg, 1965)

The curve shows the altitude at which vertically incident radiation is attenuated to $I/I_0 = 1/e$, i.e. unity vertical optical depth. Also included are the dominant absorbers and their ionization limits.

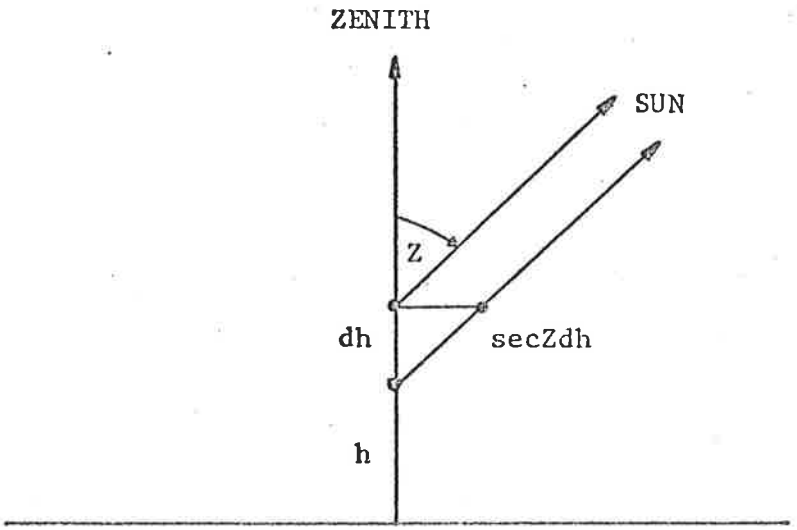

Figure 2.2 Geometry for the flat-earth approximation.

equation (2.1) can be written in its modified form to take this into account:

$$\phi(\lambda,h) = \phi_{\infty}(\lambda) \exp\left[-\sum_{i=1,n}(\sigma_i(\lambda)N_i(h))\right] \qquad (2.2)$$

σ_i and N_i are defined for i^{th} constituent as above.

This would be the situation if we were to use absorption spectroscopy in the extreme ultraviolet region (below 90 nm) where more than two species contribute towards the absorption. However, in the VUV range of 100 nm to 170 nm and in MUV range of 230 nm to 290 nm, the absorption is almost entirely due to one constituent i.e. O_2 and O_3 respectively. Therefore absorption measurements in these spectral ranges (as was the case in the present work) can be described simply by equation (2.1) and further treatment is restricted to a one component situation. A detailed treatment of a multi-component system has been given by Hinteregger (1962). Nevertheless, small absorption effects due to other constituents need to be taken into account in the final density evaluation in appropriate cases as discussed in Section (2.3).

In practice, any radiation detector will have a finite bandwidth, $\Delta\lambda$, within which it will respond. From equation (2.1), the flux in photons cm^{-2} sec^{-1}, within the instrumental bandwidths, from λ to $\lambda+\Delta\lambda$ can be written as

$$\phi(\lambda,\Delta\lambda,h)=\int_{\lambda}^{\lambda+\Delta\lambda} \phi_{\infty}(\lambda) \exp\left[-\sigma(\lambda)N(h)\right]d\lambda \qquad (2.3)$$

If $\varepsilon(\lambda)$ represents the spectral response function of the detector (Section 3.8) then the detector's signal at a height, h, is given by

$$I(h) = \int_{\lambda}^{\lambda+\Delta\lambda} \varepsilon(\lambda)\phi_{\infty}(\lambda) \exp[-\sigma(\lambda)N(h)]d\lambda \qquad (2.4)$$

or

$$I(h) = \int_{\lambda}^{\lambda+\Delta\lambda} \varepsilon(\lambda)\phi(\lambda,h)d\lambda \qquad (2.5)$$

where $\phi(h,\lambda)$ is given by equation (2.1).

Therefore the differentiation of equation(2.5)can be written as

$$\frac{dI(h)}{dh} = \int_{\lambda}^{\lambda+\Delta\lambda} \frac{\partial\phi(\lambda,h)}{\partial h} \varepsilon(\lambda)d\lambda \qquad (2.6)$$

The differentiation of equation (2.1) can be written as

$$\frac{\partial\phi(\lambda,h)}{\partial h} = -\phi_{\infty}(\lambda)\ \sigma(\lambda)\ \frac{dN}{dh}\ \exp[-\sigma(\lambda)N(h)] \tag{2.7}$$

or

$$\frac{\partial\phi(\lambda,h)}{\partial h} = -\sigma(\lambda)\ \frac{dN}{dh}\ \phi(\lambda,h) \tag{2.8}$$

Substituting for $\frac{\partial\phi}{\partial h}$ from equation (2.8) in equation (2.6) we arrive at the relation

$$\frac{dI}{dh} = \int_{\lambda}^{\lambda+\Delta\lambda} -\sigma(\lambda)\phi(\lambda,h)\ \frac{dN}{dh}\ \varepsilon(\lambda)d\lambda \tag{2.9}$$

using equation (2.5) we can write

$$\frac{1}{I}\ \frac{dI}{dh} = \frac{-\frac{dN}{dh}\int_{\lambda}^{\lambda+\Delta\lambda}\phi(\lambda,h)\sigma(\lambda)\varepsilon(\lambda)d\lambda}{\int_{\lambda}^{\lambda+\Delta\lambda}\phi(\lambda,h)\varepsilon(\lambda)d\lambda} \tag{2.10}$$

or

$$\frac{1}{I}\ \frac{dI}{dh} = -\frac{dN}{dh}\ \sigma_{eff(h,Z)} \tag{2.11}$$

where $\sigma_{eff(h,Z)}$ is defined by

$$\sigma_{eff(h,Z)} = \frac{\int_{\lambda}^{\lambda+\Delta\lambda}\phi(\lambda,h)\sigma(\lambda)\varepsilon(\lambda)d\lambda}{\int_{\lambda}^{\lambda+\Delta\lambda}\phi(\lambda,h)\varepsilon(\lambda)d\lambda} \tag{2.12}$$

and Columnar density N can be written as

$$N(h,Z) = \int n(h)\ F\ (h,Z)\ dh \tag{2.13}$$

where F(h,Z) is optical depth factor at height h and for solar zenith angle Z*. F(h,Z) can be replaced by SecZ for zenith angles $\leqslant 75^{\circ}$ under the flat earth approximation (Figure 2.2). For zenith angles greater than 75°, evaluation of F can be carried out as described by Swider (1964) (also Weeks and Smith (1968)).

The value of $\sigma_{eff(h,Z)}$ can only decrease or remain constant as the radiation penetrates down through the atmosphere. It will decrease when $\sigma(\lambda)$ varies across the bandwidth of a detector because the radiation of

---

* The solar zenith angle Z is defined as the angle between the direction of the sun and the local zenith.

wavelengths where $\sigma(\lambda)$ is larger will be absorbed more strongly, leaving a higher proportion of the radiation of wavelengths at which σ is smaller. This changing distribution of the radiation within a detector's bandwidth is known as "radiation hardening".

By combining equations (2.11) and (2.13) we can write the following relationship between the measured detector signal I(h) and the related number density at this height n(h):

$$n(h) = \frac{1}{I(\lambda)} \frac{dI}{dh} \frac{1}{F} \frac{1}{\sigma_{eff(h,Z)}} \qquad (2.14)$$

Equation (2.14) is the fundamental equation to be used for deriving the number density for a particular species for which a signal profile (I(h)) is known. The effective absorption cross-section $\sigma_{eff(h,Z)}$ is given by the equation (2.12) in its most fundamental form which can be used to evaluate $\sigma_{eff(h,Z)}$ for a specific observed profile. Equations (2.12) and (2.14) are particularly suitable for deriving both oxygen (O_2) and ozone (O_3) number densities from a measured flux profile.

It can be seen that, if the operational bandwidth of the detector, $d\lambda$, is such that the absorption cross-section $\sigma(\lambda)$ of the species being studied remains constant within $d\lambda$, the equation (2.12) is reduced to its most simple form:

$$\sigma_{eff(h,Z)} = \sigma(\text{constant}) \qquad (2.15)$$

Therefore detectors can sometimes be selected in such a way that the absorption cross-section of the species being studied does not vary within the operative bandwidth of the detector.

Further treatment in this chapter will be restricted to the measurement of oxygen (O_2) densities and the evaluation of $\sigma_{eff(h,Z)}$ and vertical distribution for ozone detectors will be discussed in Chapter 7 .

2.2.2 Atmospheric Absorption of Radiation Between 100 nm and 170 nm and Oxygen Densities

In the wavelength range from 100 nm to 170 nm, the absorption is mainly due to molecular oxygen and absorption effects of other constituents can generally be neglected (Section 2.3). Therefore equations (2.12) and

(2.14) can be written for the vertical distribution of oxygen as

$$n_{O2}(h) = \frac{1}{I(h)} \quad \frac{dI(h)}{dh} \quad \frac{1}{\sigma_{eff(h,Z)}} \frac{1}{F(h,Z)} \tag{2.16}$$

and the effective absorption cross-section is given by

$$\sigma_{eff(h,Z)} = \frac{\int_{\lambda}^{\lambda+\Delta\lambda} \phi(\lambda,h)\varepsilon(\lambda)\sigma_{O2}(\lambda)\,d\lambda}{\int_{\lambda}^{\lambda+\Delta\lambda} \phi(\lambda,h)\varepsilon(\lambda)\,d\lambda} \tag{2.17}$$

where $\phi(\lambda,h)$ is the flux at height h given by

$$\phi(\lambda,h,Z) = \phi_{\infty}(\lambda) \exp\left[-\sigma_{O2}(\lambda)N_{O2}(h,Z)\right] \tag{2.18}$$

and

$$N_{O2}(h,Z) = \int_{h}^{\infty} n_{O2}(h)F(h,Z)\,dh \tag{2.19}$$

The quantity I(h) and hence dI(dh) is the detector signal observed during the rocket flight and can be directly used from the flight data (when corrected for detector angular response). F is the optical factor and can be easily evaluated for a given zenith angle from Swider (1964). In fact for zenith angles $\leqslant 75^{\circ}$ F can be approximated by sec Z for an inaccuracy of less than 1% (Weeks and Smith, 1968).

The only other quantity to be evaluated before equation (2.16) can be used to derive the vertical distribution of n_{O2} is the effective absorption cross-section $\sigma_{eff(h,Z)}$ as given by equation (2.17). As pointed out earlier, if $\sigma(\lambda)$ can be replaced by a constant cross-section, σ, then equation (2.17) can be simplified to the form

$$\sigma_{eff} = \sigma \text{ (constant)}$$

An example is provided by an ionchamber, such as the one with a saphire window and xylene filling gas. The bandwidth of this detector is 142 nm to 148 nm and the variation of the molecular oxygen absorption cross-section across this wavelength range can be neglected to an accuracy of ± 5% (Weeks, 1975b).

For both the detectors used in the present work it was found necessary to evaluate σ_{eff} by using the equation (2.17). Therefore this aspect will be discussed in detail in the following sub section.

2.2.3 Evaluation of the effective absorption cross-section

(a) The Absorption Cross-section of Molecular Oxygen

The photo absorption cross-section of molecular oxygen in the vacuum ultraviolet region has been investigated by a number of workers. Detailed measurements of Watanabe et al (1953a), Metzer and Cook (1964) and Blake et al (1966) are substantially in agreement with one another. All of these measurements utilised photoelectric techniques and the general nature of the absorption spectrum can be seen from Figure (2.3). The Schumann-Runge dissociation continuum extends from about 130 nm to about 175 nm with the maximum cross-section of 1.48×10^{-17} cm^2 at 142.5 nm. It is associated with the dissociation

$$O_2(3\Sigma_g^-) \rightarrow O(3_p) + O(1_D)$$

The Schumann-Runge bands are at wavelengths longer than 175 nm. It can be seen from the Figure (2.3) that the cross-sections of these bands decrease with increasing wavelength until they merge into the weak Hertzberg continuum. One of the two detectors used in the present work has an operative band in Schumann-Runge continuum of 155 nm to 169 nm. Absorption cross-section values for the evaluation of the effective absorption cross-section (Section 2.2.3c) for this detector were taken from Blake et al (1966).

At wavelengths shorter than 130 nm, the oxygen spectrum shows a number of strong absorption bands separated by "windows" where the cross-section is much lower. The most important of these windows is the one that almost exactly coincides with the very strong solar hydrogen Ly-α line. The shape of the window and the shape of the Ly-α line are shown in Figure (2.10). Although the window is very narrow, there is a close proximity of the Ly-α line to the centre of the window. It means that only this line is able to penetrate down to altitudes 65 - 70 km in

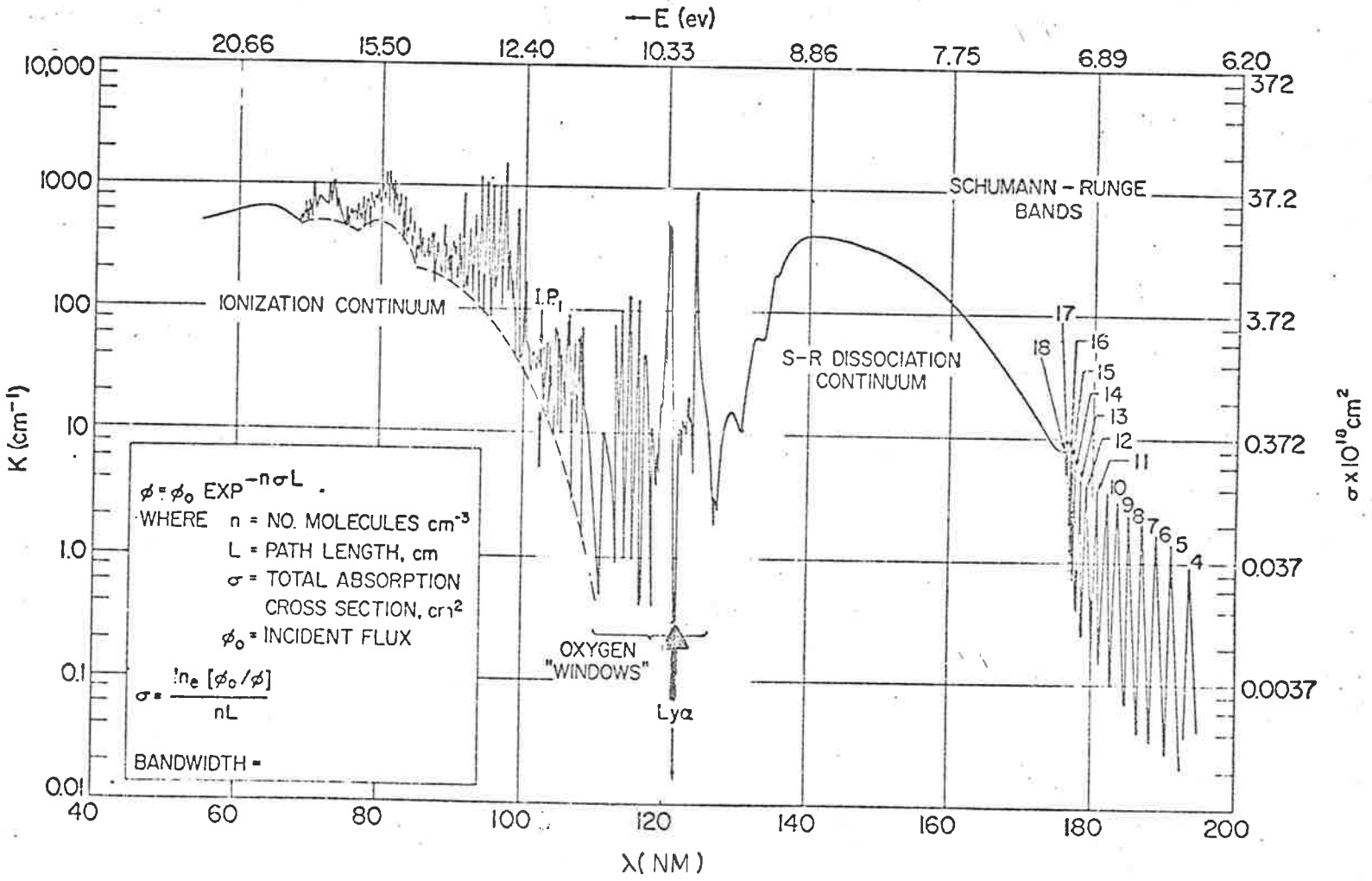

Figure 23 The absorption spectrum of molecular oxygen (from Cook and Ching (1965)).

the solar spectrum between 100 nm and 135 nm. This has the obvious advantage that even if a wide band detector is employed to observe the radiation in this region of the spectrum, only Ly-α radiation will be recorded by the detector up to altitudes of about 95 km which in turn simplifies greatly the reduction of the data at these altitudes. The importance of this window can be realized from the fact that absorption photometry of this line alone has provided the measurements of molecular oxygen concentration at lower mesospheric altitudes. The Ly-α detector used in the present work has an operative bandwidth of 105 - 135 nm. However up to altitudes of about 95 km (this height increases with increasing zenith angle - see Section 2.6) the ionchamber signal is purely due to the Ly-α line and therefore the absorption cross-section of molecular oxygen only at Ly-α is needed for such data reduction.

In view of the importance of this line considerable effort has been put in measuring the absorption cross-section of molecular oxygen at Ly-α, employing both photoelectric and photographic techniques. The earliest measurement is that of Preston (1940) who employed a photoelectric technique. His value of 1.04×10^{-20} cm^2 at the line centre is substantially in agreement with the later measurements of Watanabe et al (1953a), Metzger and Cook (1964), Shardanand (1967), Ogawa (1968), Gaily (1969) and a very recent measurement of Carver et al (1976). All of these measurements employed a photoelectric method. The measurements of Ditchburn et al (1954) and Lee (1955) are significantly lower than the above group of measurements. Both of these measurements employed a photoelectric technique and the cross-section values are in good agreement with each other. In most of the photoelectrical measurements, a pressure dependence of absorption cross-section was observed in contrast to the photographic method in which there was no apparent pressure dependence. Thus there is some discrepency

between the results obtained by the photoelectric and photographic methods.

The measurements of Ogawa (1968) and Carver et al (1976) have been made at higher resolution and lower pressure than the rest of the photoelectrical measurements. The values of the absorption cross-section at the Ly-α line as measured by various workers at room temperature are summarized in Table (2.1). Carver et al (1976) have also measured absorption cross-sections over the line width at lower temperatures.

Table 2.1

Investigator(s)		Cross-section(σ) 10^{-20} cm^2	Pressure range used in torr	Reported values extrapolated to
Preston	(1940)	1.04	30 - 290	zero pressure
Watanabe et al	(1953a)	1.00	70 - 490	zero pressure
Ditchburn et al	(1954)	0.84	- 20	No pressure dependence observed
Lee	(1955)	0.85	- 23	No pressure dependence observed
Metzger and Cook	(1964	1.04	- 9.3	-
Shardanand	(1967)	1.08	25 - 400	Zero pressure
Ogawa	(1968)	1.03 - 121.572 nm	1.2 - 6.5	-
Gaily	(1969)	2.37	760	
Carver et al	(1976)	1.06 - 121.56 nm	15 - 20	Zero pressure
		0.93 _ 121.58 nm		

In the present work, calculations of the effective absorption cross-section for the Ly-α ionchamber were made by using the data of Ogawa (1968) as well as the recent results of Carver et al (1976) for the shape of the window .

These are shown in Figure (2.10) along with the shape of the solar Ly-α line as measured by Purcell and Tousey (1960). However the final value to be used for the effective absorption cross-section at Ly-α should be considered in relation to any temperature effects on the cross-section in the mesospheric low temperature conditions. A discussion of this follows in Section (2.2.4).

(b) Effective Cross-section for the Q-T Ionchamber (155 to 169 nm) data

Effective absorption cross-section for a detector responding to radiation of wavelength λ to $\lambda+\Delta\lambda$ with a spectral response function $\varepsilon(\lambda)$ is given by equation (2.12) i.e.

$$\sigma_{eff(h,Z)} = \frac{\int_{\lambda}^{\lambda+\Delta\lambda} \phi(\lambda,h)\sigma(\lambda)\ \varepsilon(\lambda)d\lambda}{\int_{\lambda}^{\lambda+\Delta\lambda} \phi(\lambda,h)\varepsilon(\lambda)d\lambda} \qquad (2.20)$$

where $\phi(\lambda, h,Z)$ is the flux at wavelength λ and height h, observed by the detector and can be related to the flux outside the atmosphere by the equation (2.1) i.e.

$$\phi\ (\lambda,h,Z) = \phi_{\infty}(\lambda)\ \exp\ [-\sigma(\lambda)N(h,Z)] \qquad (2.21)$$

By combining equations (2.20) and (2.21) we can write a complete equation for the effective absorption cross-section at height h in terms of $\phi_{\infty}(\lambda),\varepsilon(\lambda),N(h)$ and $\sigma(\lambda)$

$$\sigma_{eff(h,Z)} = \frac{\int_{\lambda}^{\lambda+\Delta\lambda} \phi_{\infty}(\lambda)\ \exp[-N(h)\sigma(\lambda)]\ \sigma(\lambda)\ \varepsilon(\lambda)\ d\lambda}{\int_{\lambda}^{\lambda\ \Delta\lambda} \phi_{\infty}(\lambda)\ \exp[-N(h)\sigma(\lambda)]\ \varepsilon(\lambda)\ d\lambda} \qquad (2.22)$$

and

$$N(h,Z) = \int_{h}^{\infty} n(h)\ F\ (h,Z)\ dh \qquad (2.23)$$

The variation of σ_{eff} with height was investigated for the quartz-triethylamine ionchamber using the following assumptions.

(i) The vertical distribution of molecular oxygen was assumed to be that given by (a) 1965 mean CIRA atmosphere up to 300 km (b) CIRA (1965) model 5 (mean solar activity) 0800

hrs local time from 300 km to 800 km.

(ii) The variation of the molecular oxygen absorption cross-section between 155 and 170 nm was assumed to be that given by Blake et al (1966)

(iii) The typical spectral response used was that shown in Figure (3.9).

(iv) The wavelength distribution of the solar flux in this spectral region was taken to be that of a black body at a radiation temperature T.

The values of σ_{eff} are not strongly dependent on the assumed flux. It can be seen from Table (2.2) that the relative variation in σ_{eff} for a variation in temperature (Te Sun) by ± 50° K is insignigicant. Therefore a value of 4600° K was used for this purpose (Section 6.4). For illustration the spectral distribution of σ, ϕ_∞ and ε is shown in Figure (2.4).

Table 2.2

h(Km)	σ_{eff} (Q - T) x 10^{18}		
	T = 4500° K	4600° K	4650° K
95	1.736	1.737	1.738
100	2.628	2.633	2.636
105	2.844	2.849	2.852
110	3.157	3.164	3.167
115	3.313	3.320	3.324
120	3.387	3.395	3.398
125	3.426	3.433	3.437
130	3.448	3.455	3.459
135	3.461	3.468	3.472
140	3.470	3.477	3.481

Calculations of σ_{eff} were carried out for zenith angles, $Z(\leqslant 75^\circ)$ so that F(h,Z) in equation (2.23) could be replaced

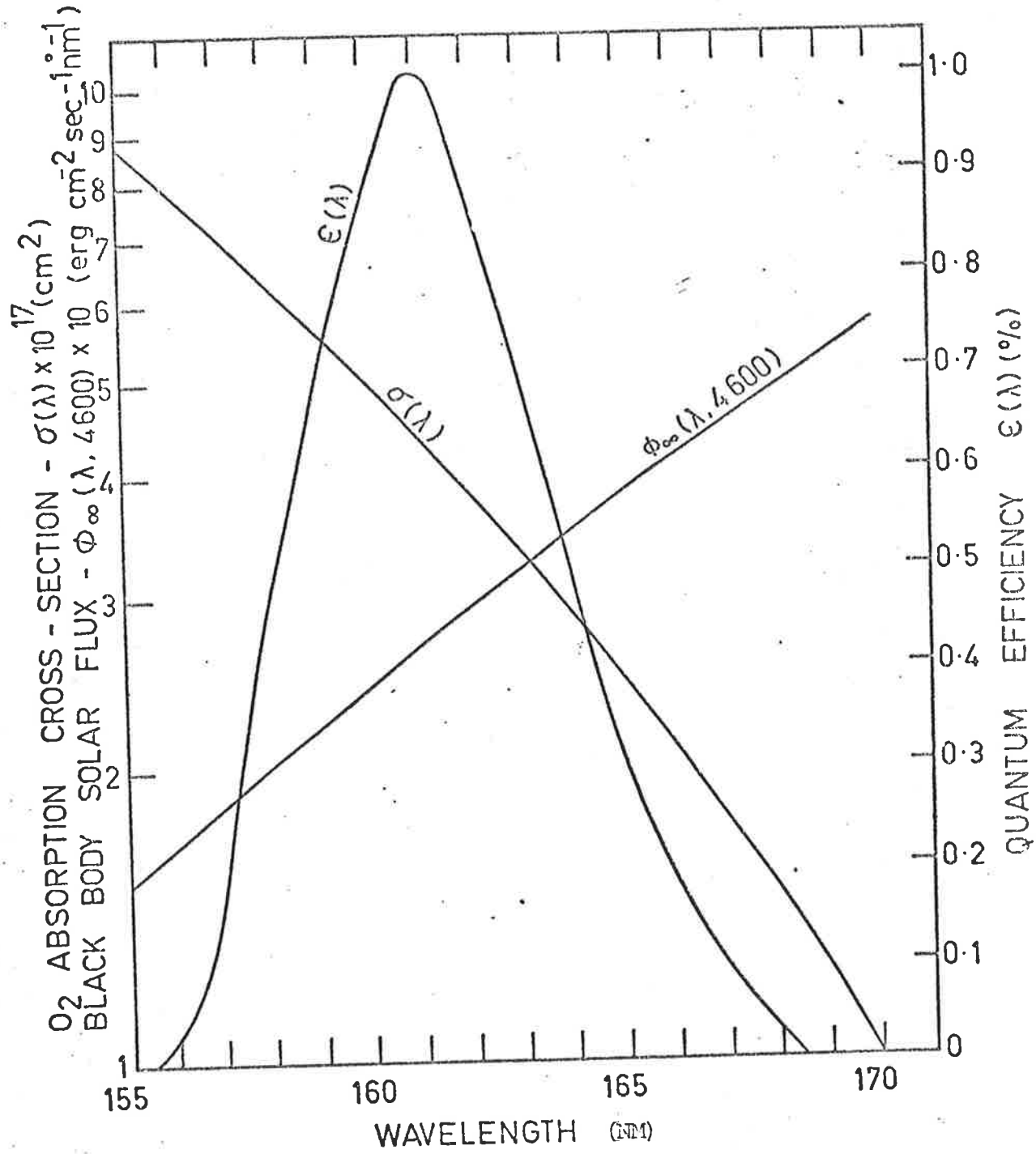

FIGURE 2.4 SOLAR FLUX OUTSIDE THE ATMOSPHERE. MOLECULAR OXYGEN ABSORPTION CROSS - SECTION AND NORMALIZED QUANTUM EFFICIENCY OF Q - T CHAMBER AS A FUNCTION OF WAVELENGTH.

by secZ. It can be noticed that the denominator in equation (2.22) right hand side is nothing else but the detector signal I(h). Therefore calculations $\sigma_{eff(h,Z)}$ for small Z, and I(h,Z) or $I(h,Z)/I_\infty$ can be simultaneously made for a given zenith angle. These calculations can be used to plot a graph of $\sigma_{eff(h,Z)}$ Vs $\frac{I(h,Z)}{I_o}$. This graph is then the relationship of $\sigma_{eff}(I/I_o)$ Vs I/I_o and can be used to obtain $\sigma_{eff(h,Z)}$ for experimentally observed value of $\frac{I(h,Z)}{I_o}$. As expected, it was found that σ_{eff} (I/I_o) is independent of zenith angles Z and therefore the curve of Figure (2.5) is valid for all zenith angles (Z).

The values of σ_{eff} shown in Figure (2.5) are virtually independent of the assumed density distribution. This can be seen from Figure (2.6), where N(h) is plotted against $\sigma_{eff}(h)$ for Z = 0, that σ_{eff} varies rather slowly with a variation in N(h) (variation in N by a factor of 10 results in a variation in σ_{eff} of less than 20%).

The estimation of I_∞ can be carried out as described in Section (5.8), if direct measurement of it is not available. However equation (2.2) can directly be used to calculate $\sigma_{eff(h,Z)}$ and a computer program was used to calculate these values for the measurements in the present work as further discussed in Chapter 5.

(c) Effective Cross-section for the Ly-α Ionchamber (105 (114) - 135 nm) data

The spectral response curves for these detectors are shown in Figure (3.8) responding to the radiation in the wavelength interval of 105 - 135 nm and 114 - 135 nm respectively. This includes the hydrogen Ly-α line (121.6 nm). As pointed out previously (Section 2.2.3a) the solar hydrogen Ly-α line, is a very strong line in the 105 - 135 nm or 114 - 135 nm region of the solar spectrum and contributes more than 80% of the

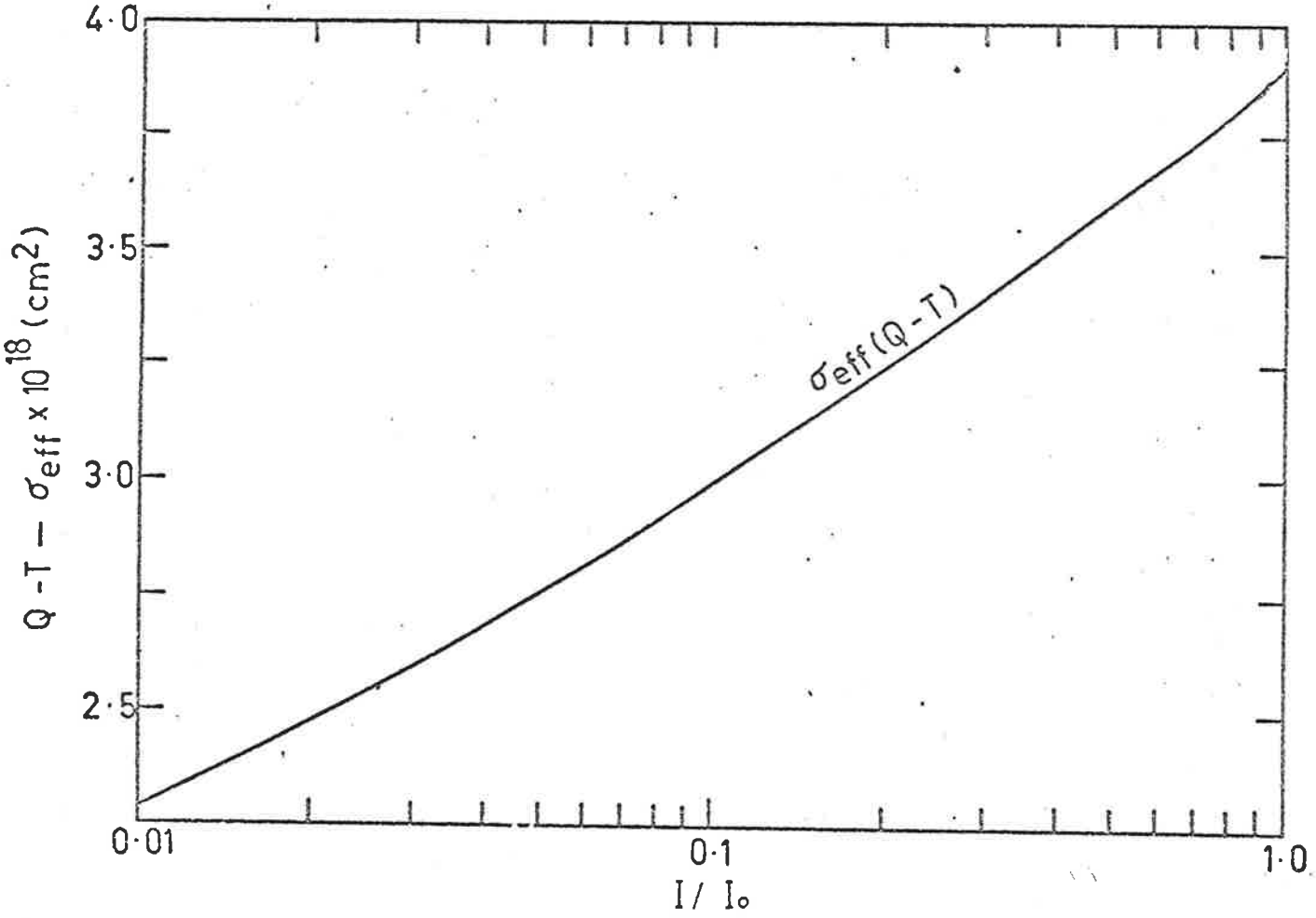

FIGURE 2·5 THE EFFECTIVE ABSORPTION CROSS - SECTION AS A FUNCTION OF EXTINCTION

unattenuated detector signal at altitudes above the oxygen atmosphere.

Moreover, the deep window in the oxygen absorption cross-section almost at Ly-α allows this line to penetrate and be observed at altitudes down to 65 - 70 km. The other radiation in the detector pass band is absorbed at altitudes above about 95 km. Therefore up to altitudes where the detector signal is almost entirely due to Ly-α (~ 95 km), we need to consider only Ly-α radiation for evaluation of the effective absorption cross-section for this detector. The precise value of the height will depend on such things as solar zenith angle, Z, intensity of the line relative to the other radiation (which varies slowly with solar activity) and the water vapour contamination of the detector which reduces the relative efficiency of the detector at Ly-α. In view of the importance of these factors, a detailed description of these problems is given separately in Section (2.4).

Equations (2.22) and (2.23) can be used to calculate the effective cross-section as in the case of the other detector. Under the conditions described above, the integration in equation (2.22) is over the width of the Ly-α line. Although the width of this line is very small (~ 0.1 nm), the absorption cross-section variation over this line width is significantly large (Figure 2.10).

The effective cross-section for this detector was investigated using the following assumptions which are similar to those of Section (2.2.3b).

(i) The vertical distribution of molecular oxygen was assumed to be that given by CIRA (1965) up to 800 km (Section 2.2.3b(i)).

(ii) The spectral intensity distribution of solar Ly-α line was taken to be that given by Purcell and Tousey (1960) Figure (2.10).

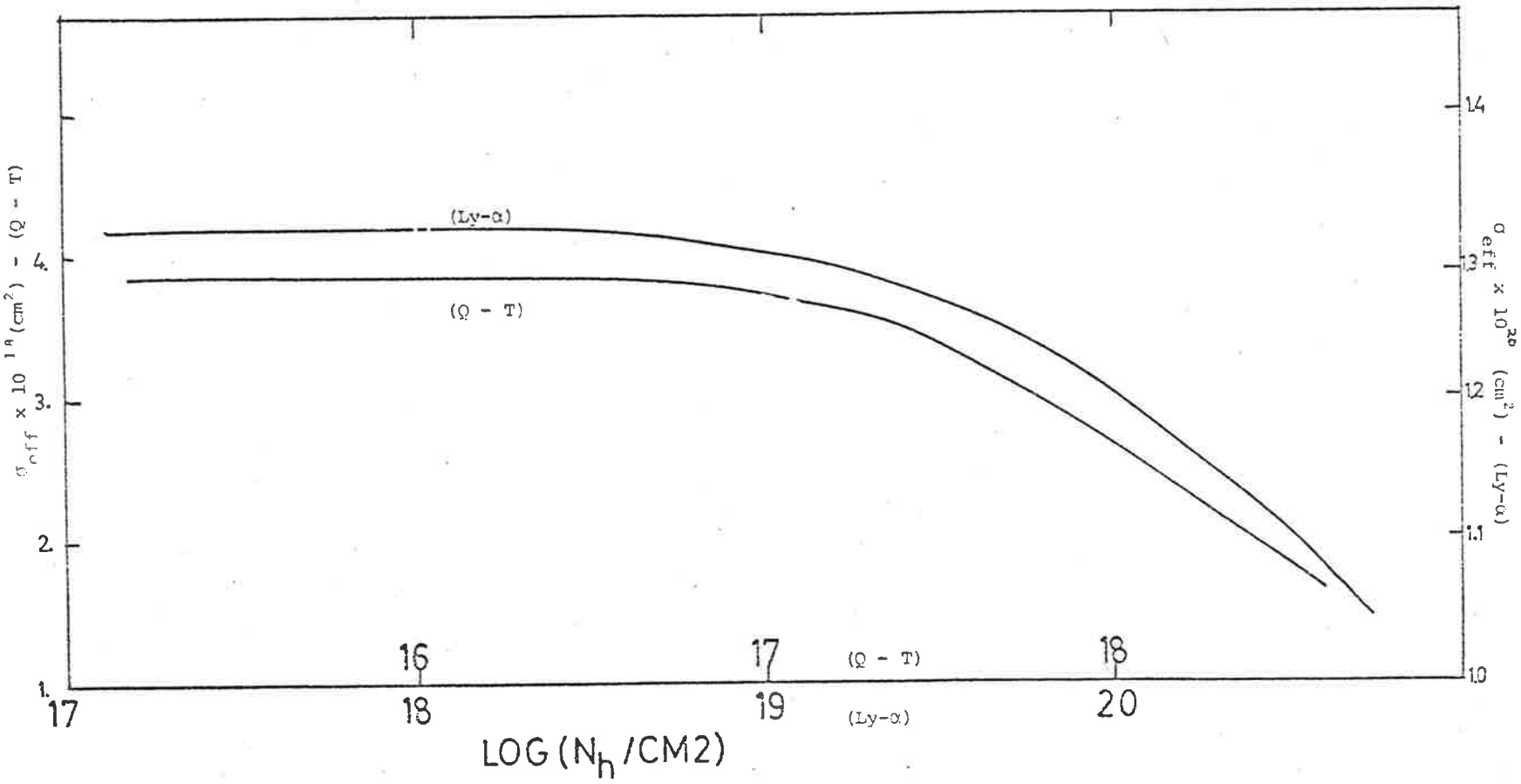

Figure 2.6 Variation of effective cross section as a function of column density for two detectors.

(iii) The spectral response, $\epsilon(\lambda)$ can be taken as a constant over the width of the line.

(iv) High resolution molecular oxygen absorption cross-section measurements across the width of the solar Ly-α line have been made by Ogawa (1968) at room temperature (300° K) and by Carver et al (1976) at room temperature as well as below room temperature (82° K, 195° K). All of these profiles (Figure 2.10) were employed. An additional theoretically estimated profile for mesospheric conditions (Section 2.2.4) was also used.

(v) Hall (1972) estimated the effect of other absorbers to be about 5 percent and included a term 5×10^{-22} cm^2 in $\sigma(\lambda)$ for his calculations of σ_{eff} for this ionchamber. Since this contribution is largely uncertain (Section 2.3) we have assumed this factor to be zero in the following calculations. However, this effect, can be easily taken into account by simply adding the appropriate term 'f' to the evaluated effective cross-sections for various cases if and when required.

Calculations of σ_{eff} for small zenith angles identical to those described in the previous section were carried out in order to evaluate σ_{eff} $(I/I_o) \alpha I/I_o$ as well as $\sigma_{eff(h,Z)}$ as a function of height. These calculations are shown in Figure (2.7) where a similar estimation of σ_{eff} by Hall (1972) is also shown. Hall used Ogawa's cross-section. As expected the agreement between Hall's estimate and our calculations for Ogawa's cross-section is very good (there is a constant difference of about 5×10^{-22} cm^2 since we have neglected the correction term $f = 5 \times 10^{-22}$ cm^2). There is a large discrepency between the room temperature cross-section profiles of Ogawa (1968) and Carver et al (1976) at the blue wing of the line profile (Figure 2.10).

This results in a disagreement in σ_{eff} which increases with height

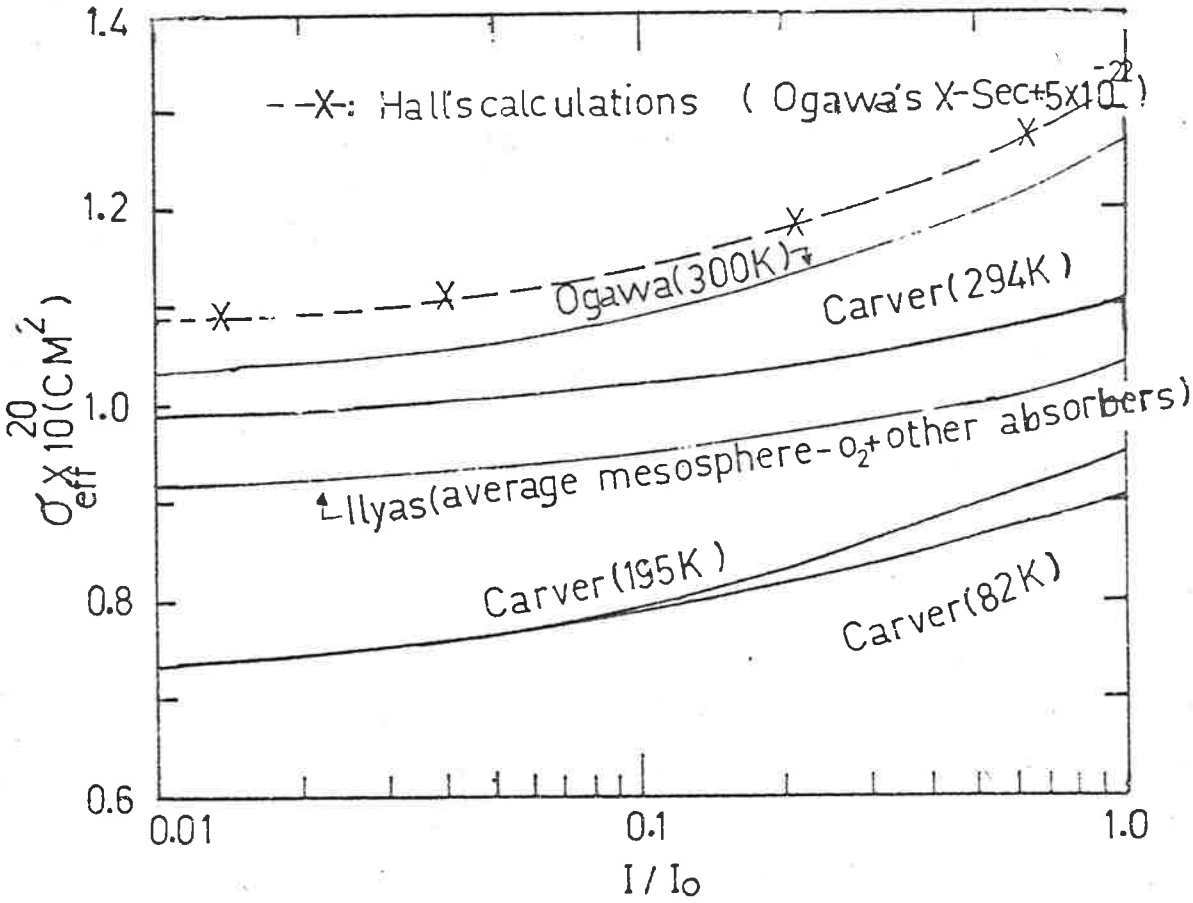

Figure 2.7 Effective O_2 cross sections for solar Ly-α data as a function of extinction using absorption cross section profiles shown in Figure 2.10.

to about 16% as I/I_o gets closer to unity. The weak dependence of effective cross-section values on the assumed model is illustrated in Figure (2.6) for this ionchamber.

The estimation of I_o can be carried out as described in Section (5.8) since direct measurement of I_o (Ly-α) will be rather difficult due to uncertainty in the total contribution of other than Ly-α radiation to the detector signal when the sun is viewed from above the absorbing atmosphere (Section 2.4). The appropriate curve from Figure (2.7) can thus be used to evaluate effective cross-sections from the observed values of $I(h)/I_c$. Equation (2.22) can also be used directly to evaluate $\sigma_{eff(h,Z)}$ for a given zenith angle. It should be pointed out that until quite recently it was a common practice to use a constant value for the effective cross-section. The value of the cross-section was taken at the centre of the line and the variation across the width was assumed not to be important. The most common value used was of 1.00×10^{-20} cm^2 after Watanabe et al (1953). Recently it was shown that the effect of the cross-section variation across the width of the line is significant and failure to take it into account will result in erroneous derived number densities (Hall, 1972; Ilyas and Horton, 1974; Weeks, 1975a, see Figure 2.7). However, Smith and Miller (1974) have since questioned the validity of the effective cross-section based on Ogawa's (1968) cross-section under the low temperature conditions of the mesosphere. They have argued that significant temperature effect may be encountered in the absorption cross-section at mesospheric temperatures of less than 200° K. The results of Carver et al (1976) clearly indicate a significant temperature effect. The results of Carver et al (1976) are substantiated by an indirect estimation of an absorption cross-section profile at Ly-α appropriate for the mesospheric temperature conditions. Details of these computations are given in the following Subsection (2.2.4) where this problem of temperature effect is considered in detail.

2.2.4 Temperature Effect on the Effective Cross-section

(a) Introduction

Generally laboratory measurements of absorption cross-section (σ)

are carried out at room temperature (~ 300° K). However in the altitude ranges where absorption measurements are carried out, atmospheric temperature conditions can be significantly different. Therefore we need information on the variation of cross-section (σ) with temperature so that an appropriate value of σ, relevant to the atmospheric temperature condition in which a measurement is made can be used in equation (2.17) to evaluate effective cross-section. At mesospheric altitudes, temperatures are significantly lower than room temperature whereas above about 120 km temperature rises sharply and becomes higher than room temperature. The absorption of radiation around 160 nm takes place above 100 km and the temperature is expected to be still below room temperature for another 10 - 15 km above which it increases sharply and becomes higher than 300° K. However according to the study of Hudson et al (1966) temperatures significantly higher than the room temperature do not affect the absorption cross-section value for molecular oxygen around 160 nm by any appreciable amount. Therefore any temperature effect on the effective cross-section for a Q - T ionchamber at thermospheric altitudes can be neglected assuming one can extrapolate the high-temperature results to low temperatures. Further discussion is hence restricted to the temperature effect on the absorption cross-section of molecular oxygen at Ly-α (121.57 nm).

As mentioned earlier temperature conditions at mesospheric altitudes can be drastically different from the laboratory temperatures. Until very recently no attempt was made to study the effect of such low temperatures on the oxygen absorption cross-section at Ly-α. Jursa et al (1965) did consider the possible temperature effect under mesospheric conditions in order to find some explanation for their rather low O_2 density results but concluded that the effect was insignificant. Recently Smith and Miller (1974) reported a series of molecular oxygen measurements

using Ly-α ionchambers and compared them with neutral density data taken at about the same time. They observed the ratio (O_2/ρ) to be about 20% lower from the model ratio with good internal consistency between the various density profiles. The O_2 densities were derived for a constant cross-section of 1.00×10^{-20} cm^2 rather than a much larger variable cross-section based on Ogawa's (1968) cross-section. They have argued that this low density data could be interpreted as the result of the value of $1.00 \times 10^{-20} cm^2$ for effective cross-section being too high and suggested a value of about $0.8 \times 10^{-20} cm^2$ for the cross-section applicable under the cooler conditions of the atmosphere at mesospheric altitudes; for instance temperature at 80 km is about 100° K less than the laboratory temperature at which the cross-section measurements are generally made. Since the number density is inversely proportional to the cross-section; the lower value of 0.8×10^{-20} cm^2 against $1.00 \times 10^{-20} cm^2$ would be translated into a 25% shift upward in O_2 densities needed to bring their inferred ratios close to the model (CIRA, 1972)

(b) Temperature Effect in O_2 Absorption Cross-Section at Ly-α

In view of the sensitivity of the value of cross-section in Ly-α absorption measurements, we have attempted to study this problem of cross-section theoretically by re-analysing the reported O_2 measurements. Each individual profile listed in Table (6.1) was used to recompute O_2 density profile for a variable cross-section corresponding to four absorption cross-section data given below. A mean profile was then obtained from these recomputed profiles for each case and was compared with the model. Generally effective cross-section calculations involve a Ly-α line profile, a model atmosphere and absorption cross-section data across the width of the line. Throughout this study of temperature effect, the solar Ly-α Line profile of Purcell and Tousey (1960) and CIRA model (1965)

were used and only the absorption cross-section was used as a variable. The method of evaluation of effective cross-section $\sigma_{eff(h,Z)}$ for a zenith angle (in the present case corresponding to each flight) has already been described in Section (2.2.3). A given O_2 profile may be corrected for a different effective cross-section through the relationship:

$$n_{O2}(\text{corrected}) = n_{O2} \cdot (\sigma/\sigma_{eff(h,Z)}) \qquad (2.24)$$

where σ is the cross-section used to derive n_{O2} - the listed O_2 density at height h. Hall (1972) has estimated an absorption cross-section for absorption of Ly-α by constituents other than oxygen to be about 5.0×10^{-22} cm^2. This term is generally added to the O_2 absorption cross-section for evaluating effective absorption cross-section (Section 2.2.3). Since this estimate is based on absorption cross-sections of other constituents at room temperature and the uncertainty in the estimated factor is large (see Section 2.3); this factor has been neglected in these calculations.

Firstly, absorption cross-section data of Ogawa (1968) was used to obtain a height-dependent variable cross-section and secondly, a constant absorption cross-section across the solar Ly-α line with a value of 1.00×10^{-20} cm^2 was used which resulted in a more widely used constant effective cross-section of 1.00×10^{-20} cm^2 to be used in equation (2.24). All the earlier measurements that used a different effective cross-section (only a few) were corrected to this value and some recent measurements that used a variable cross-section were also recomputed for this value.

Mean O_2 profiles for each of the above two cases were computed which showed significant departures from the CIRA, 1972 model (Figure 2.11). The departure in one of the two cases may be either real or as a result of inadequate value of

cross-section used in both cases. Assuming that the latter is the case a fictitious cross-section curve was obtained as described below, which when used in the first case mentioned above, results in a variable cross-section resulting finally in a mean O_2 profile in good correlation with the model atmosphere.

A computer program was used in which varying shaped O_2 cross-section profiles were used (Figure 2.8) to obtain effective cross-section values for each flight. These were then used to correct the density profile through equation (2.24). The so corrected profiles were used to obtain a mean profile which was compared with the model for each cross-section value. The mean profiles were normalized such that a ratio of 1.00 with the model was obtained at 70 km. From the so normalized mean O_2 profiles, plotted as ratio to the model (Figure 2.9), the mean profile showing best correlation with the model over the entire height range of 70 - 90 km was taken to be as the result of the approximately correct shape of the absorption cross-section profile across the width of the Ly-α line. It was found that the normalization of a particular cross-section profile results in a new variable cross-section related through a constant to the original cross-section, i.e.

$$\sigma_{eff}' = \sigma_{eff/K} \text{ and } n_{02}' = n_{02} \cdot K$$

where σ_{eff} is a variable cross-section resulting from a specific absorption cross-section profile and σ_{eff}' is a variable cross-section resulting from the same cross-section normalized by a constant factor very close to K itself. This means that an O_2 profile may be shifted upwards or downwards by a constant factor by simply normalizing the cross-section profile by a suitable factor. The absorption cross-section profile selected as mentioned above was then normalized such that the mean O_2 profile had a ratio of about 1.00 with the model and the resultant cross-section

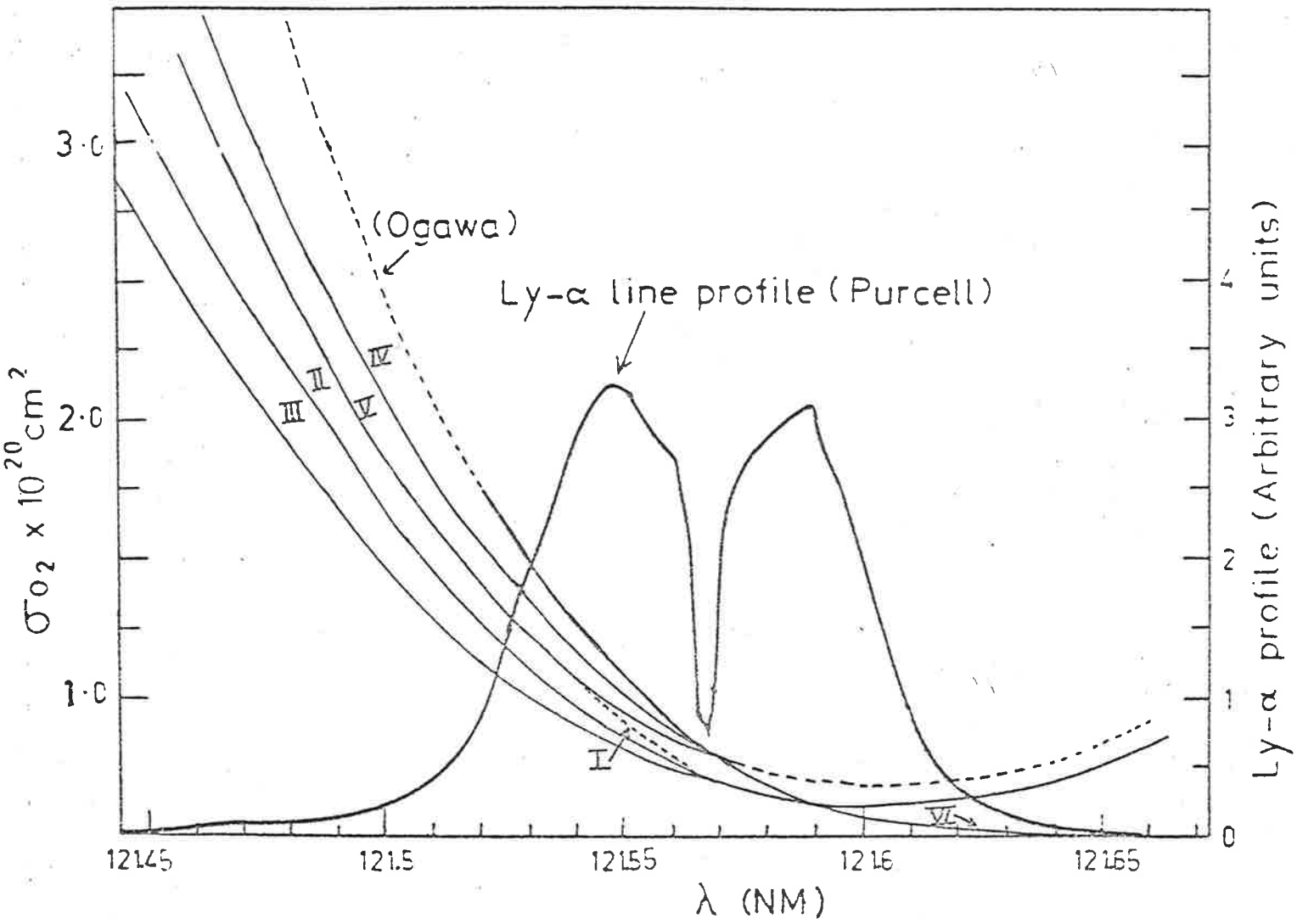

Figure 2.8 Shape of the Ly-α line profile (after Purcell and Tousey; 1960) and various assumed O_2 absorption cross section profiles used to study temperature effect.

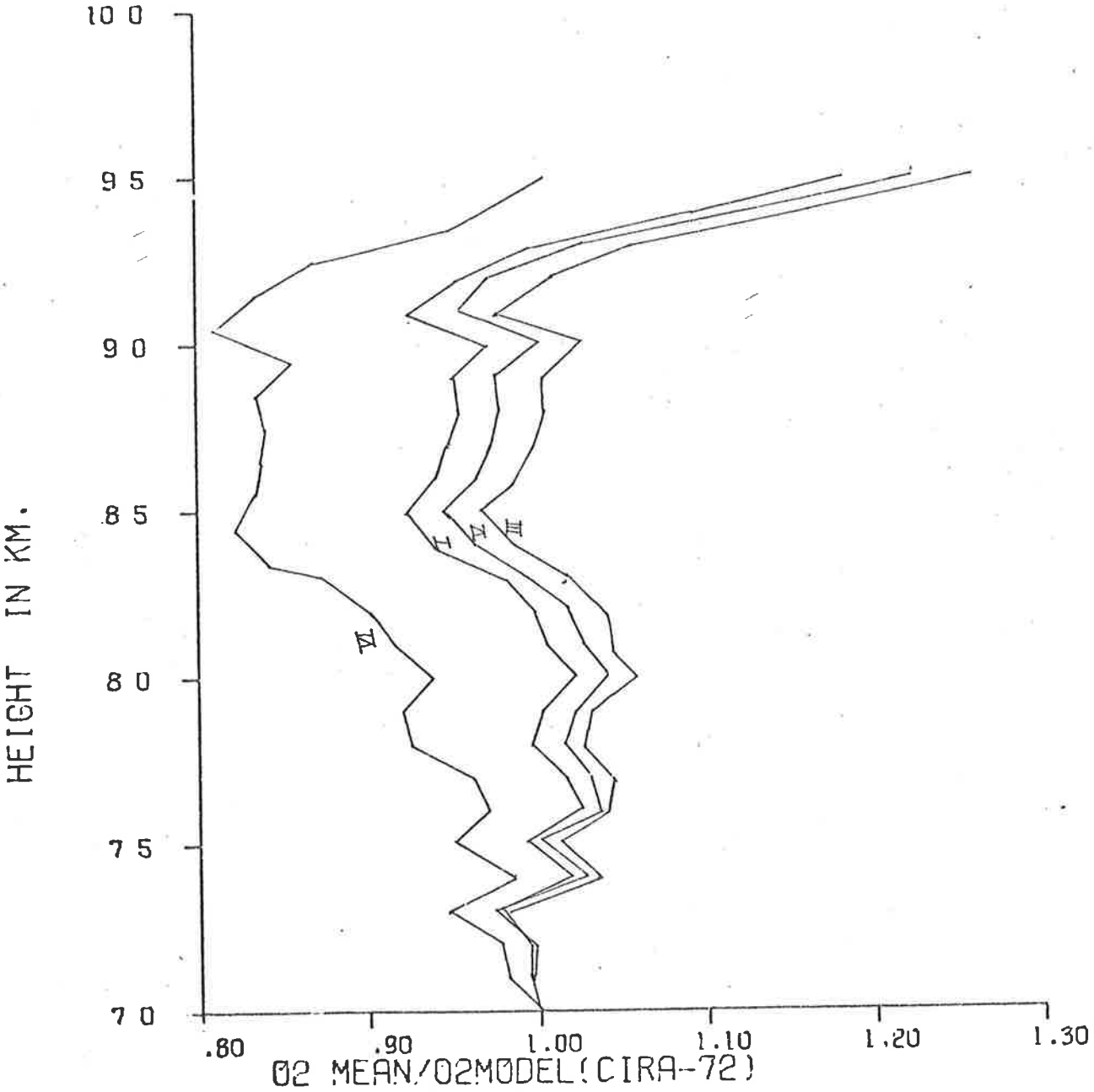

Figure 2.9 Mean O_2 ratios for several assumed absorption cross section profiles shown in Figure 2.8.

profile (Figure 2.10) is taken to be appropriate for the mesospheric temperature conditions. The corresponding mean O_2 profile is shown in Figure (2.11).

Finally, the recently measured absorption cross-section profile of Carver et al (1976) at 195° K was used to calculate effective cross-sections for each profile of Table (6.1) and the profiles were then corrected using equation (2.24). The resultant mean profile is shown in Figure (2.11) as ratio to the mean model.

A negative departure at lower altitudes for a constant cross-section suggests the application of a height dependent absorption cross-section (variable cross-section) that becomes smaller at lower altitudes. A relatively large negative departure (ratio less than 1.00) over most of the region of interest for Ogawa's cross-section suggests the possibility of smaller O_2 cross-sections applicable to the oxygen data than Ogawa's room temperature cross-section. This has been now experimentally confirmed by the results of Carver et al (1976). The experimental profile at 195° K in fact results in a positive departure from the model of about 15% in the mean oxygen profile. No account has been made of absorption due to other constituents in deriving the mean profile for this case. However, the theoretical profile shown in Figure (2.10) represents an average total absorption profile for oxygen as well as other constituents for average mesosphere. Therefore perhaps part of the positive departure is because of neglecting the effect of other absorbers in the computations of effective cross-section (Section 6.3). It is interesting to note that the effective cross-sections for Ly-α at 82° K are not significantly different from those at 195° K (Figure 2.7).

As more laboratory measurements of temperature effect become available, the situation will become more definitely clear. Still measurements by independent techniques, possibly mass-spectrometry

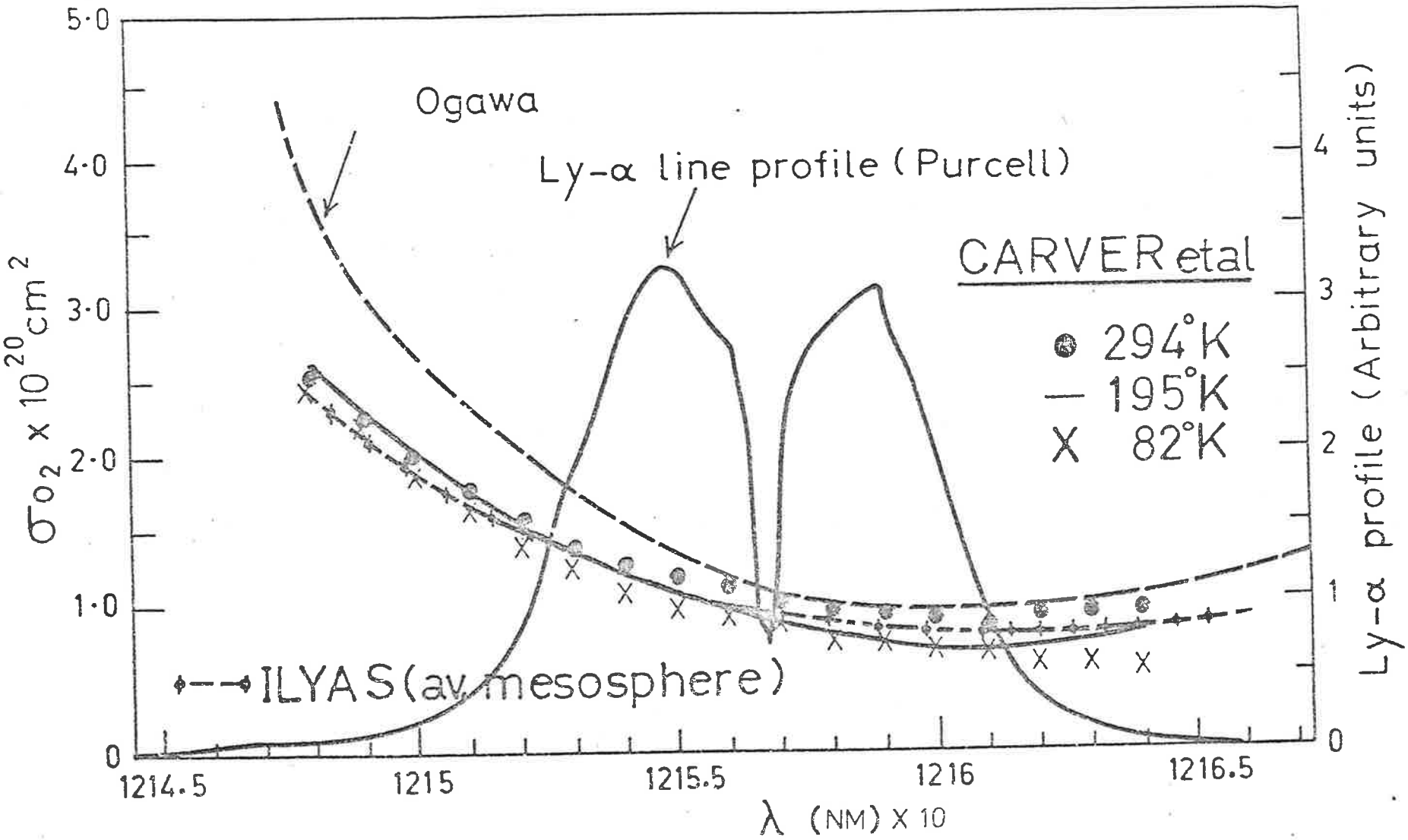

Figure 2.10 Shape of the Ly-α profile (after Purcell and Tousey; 1960) and various O_2 absorption cross section as a function of wavelength.

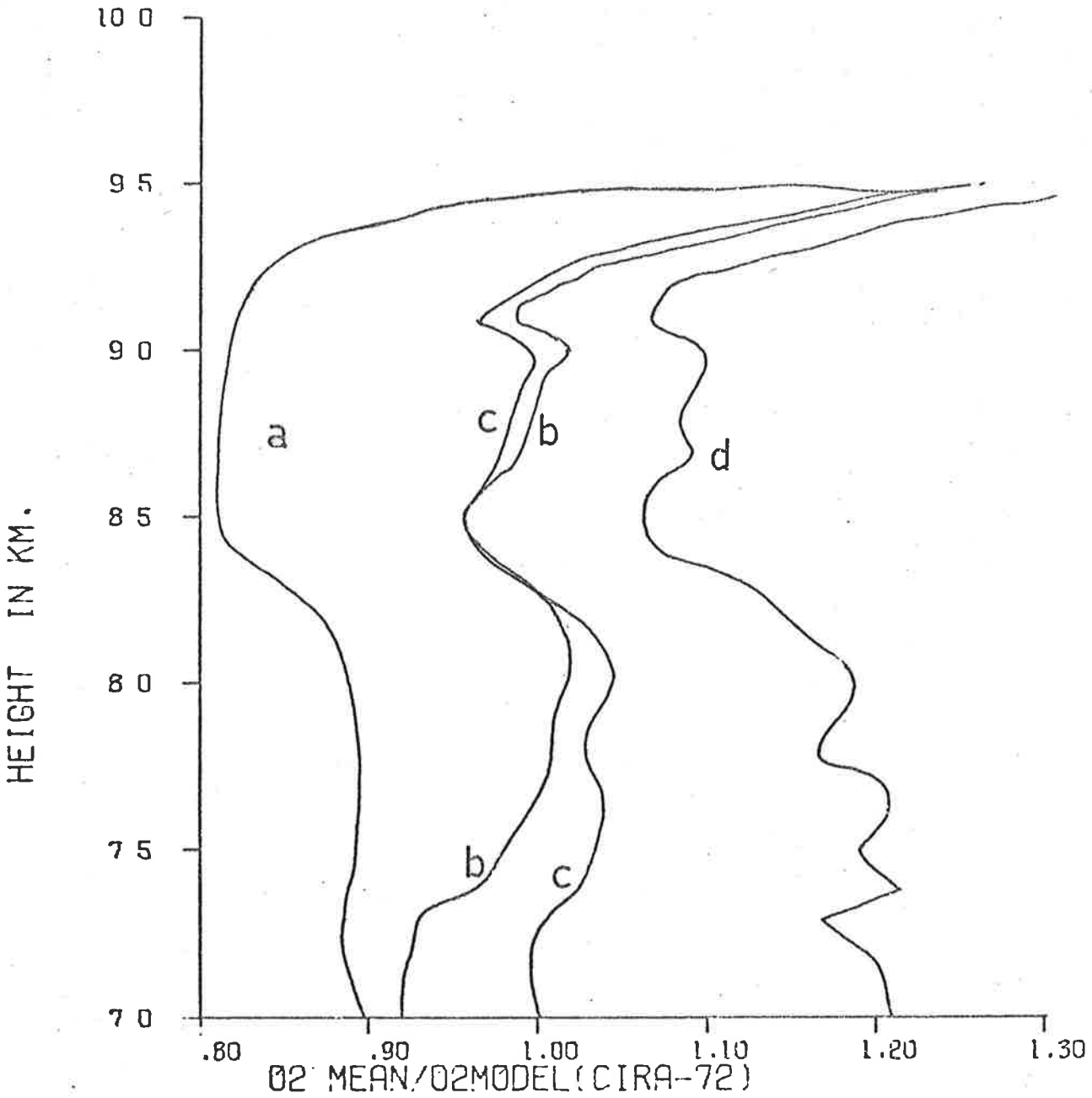

Figure 2.11 Mean O_2 ratios using different cross sections.
(a) Ogawa's cross section
(b) Constant cross section (1.0×10^{-20} cm^2).
(c) Theoretical profile appropriate for average mesosphere.
(d) Carver et al. (1976) cross section at 195 K.

would be of prime importance for direct comparisons of the O_2 data (Section 6.1).

(c) Conclusions:

The temperature effect on the effective absorption cross-section for a Q - T ionchamber can be neglected. However, the oxygen absorption cross-section at Ly-α decreases significantly as the temperatures are decreased below room temperature. The effective cross-sections at about 200° K are lower by about 15-20% from those at room temperature. This difference is found to further increase if Ogawa's room temperature data is employed. In the first few kilometres (70-76 km) mean temperatures are still higher than 200° K and for the data in this region, a cross-section profile at comparable temperatures (this will probably result in somewhat larger effective cross-sections) is needed. The change in effective cross-sections at 200° K are substantially in agreement with the suggestion made by Smith and Miller (1974).

2.3 ABSORPTION OF RADIATION BETWEEN 100 AND 200 nm BY CONSTITUENTS OTHER THAN MOLECULAR OXYGEN

Throughout the wavelength range 100 nm - 170 nm and in the height range near where dI/dh is a maximum, atmospheric absorption is due almost entirely to molecular oxygen.

i.e. $$\sigma_{O2}(\lambda) n_{O2}(h) >> \sigma_2(\lambda) n_2(h) + \sigma_3(\lambda) n_3(h) + \ldots$$

where the cross-sections σ_2, σ_3 etc and the number densities n_2, n_3 etc, refer to the constituents other than molecular oxygen. However, Ly-α radiation almost exactly coincides with a window in the molecular oxygen absorption spectrum where the cross-section is particularly low (Figure 2.3). Also, several minor constituents have absorption cross-sections higher than that of oxygen at this wavelength (Table 2.3). Therefore, even small concentrations of these constituents may make some contribution to the absorption of Ly-α radiation. For illustration of absorption contribution due to constituents other than molecular oxygen, at 121.6 nm and 161 nm,

TABLE 2.3

Constituent	σ/σ_{O_2} (Ly-α)	n/n_{O_2}		$n\sigma/n_{O_2}\sigma_{O_2}$	
		75 km	90 km	75 km	90 km
O2(M)	1.00	1.00(1)	1.00(2)	1.00	1.00
N2(M)	$<6.\times10^{-3}$	3.724	2.094	$<2.234\times10^{-2}$	1.256×10^{-2}
CO2(H)	7.4	1.4×10^{-3}	1.40×10^{-3}	1.036×10^{-2}	1.036×10^{-2}
H2O(H)	1.4×10^{3}	1.09×10^{-5}	2.80×10^{-6}	1.526×10^{-2}	3.92×10^{-3}
O3(H/M)	2.3×10^{3}	4.355×10^{-7}	1.87×10^{-6}	1.002×10^{-3}	4.30×10^{-3}
NO(H)	2.7×10^{2}	1.73×10^{-6}	8.85×10^{-6}	4.671×10^{-4}	2.39×10^{-4}
CH4(H)	1.8×10^{3}	3.46×10^{-8}	7.03×10^{-9}	6.23×10^{-5}	1.265×10^{-5}

$\sigma_{O_2} = 1.0\times10^{-20}\,cm^2$ 1. $n_{O_2}(75)=1.8239\times10^{20}/M^3$

2. $n_{O_2}(90)=1.422\times10^{19}/M^3$

	σ	σ/σ_{O_2} (161 nm)	n/n_{O_2}		$n\sigma/n_{O_2}\sigma_{O_2}$	
			110 km	135 km	110 km	135 km
O2(M)	4.16×10^{-18}	1.00	1.00(3)	1.00(4)	1.00	1.00
N2(M)	$<2.\times10^{-22}$	4.81×10^{-5}	6.34×10^{0}	8.24×10^{0}	3.05×10^{-4}	3.96×10^{-4}
CO2(H)	$\sim2\times10^{-20}$	4.81×10^{-3}	2.004×10^{-2}	1.30×10^{-3}	9.8×10^{-5}	6.25×10^{-6}
H2O(H)	$3.\times10^{-18}$	7.21×10^{-1}	2.004×10^{-6}	1.03×10^{-6}	1.45×10^{-6}	7.43×10^{-7}
O3(M/H)	$9.\times10^{-20}$	2.16×10^{-2}	5.42×10^{-8}		1.16×10^{-9}	
NO(H)	2.0×10^{-19}	4.81×10^{-2}	2.52×10^{-4}	2.06×10^{-3}	1.21×10^{-5}	1.0×10^{-4}
CH4(H)	1.0×10^{-21}	4.81×10^{-2}	7.11×10^{-9}		1.71×10^{-12}	

σ_{O_2} (161 nm) $= 4.16\times10^{-18}$

3. $n_{O_2}(110)=2.5\times10^{17}/M^3$

4. $n_{O_2}(135)=9.7\times10^{15}/M^3$

H : Hunt (1973) model for densities

M : Model (CIRA, 1972) for densities

the absorption by each atmospheric constituent, σ_n, will be expressed as a fraction of the absorption due to molecular oxygen, $\sigma_{O_2} n_{O_2}$, at each wavelength. The results of these calculations are shown in Table (2.3). A brief discussion is given below in respect of absorption of Ly-α by some important absorbers listed in Table (2.3).

(a) Molecular-nitrogen

Above 100 nm the absorption spectrum of molecular nitrogen consists only of the very weak band systems corresponding to several forbidden transitions. Upper limits that have been determined for the cross-section at Ly-α are $2 \times 10^{-22} cm^2$ (Preston, 1940), $3 \times 10^{-22} cm^2$ (Watanabe et al, 1953b) and $6 \times 10^{-23} cm^2$ (Ditchburn et al, 1954). Using the lowest upper limit of the cross-section, the absorption due to molecular nitrogen, at heights below 90 km, is less than 2% of that due to molecular oxygen (Table 2.3). At greater heights, this percentage will be slightly greater due to the more rapid fall off in molecular oxygen density due to dissociation (see $n(n_2)/n(O_2)$ at 110 km in Table 2.3). Recently, Weeks (1975a) has argued, on the basis of more recent results of Tanaka et al (1964, 1974) which show N_2 structural bands near Ly-α with weak absorption that the molecular nitrogen absorption is insignificant.

(b) Carbondioxide

The absorption cross-section of carbondioxide at Ly-α has been measured as $7.00 \times 10^{-20} cm^2$ (Nakata et al, 1965), $7.33 \times 10^{-20} cm^2$ (Inn et al, 1953) and $7.47 \times 10^{-20} cm^2$ (Preston, 1940). There is no experimental evidence concerning the distribution of carbon-dioxide in the region above 70 km. However, Bates and Witherspoon (1952) have concluded that the rate of dissociation of carbondioxide is appreciable only above 100 km and so it seems likely that the fraction of carbondioxide in the atmosphere is constant up to 100 km. A recent photochemical calculation of Hunt (1973) also gives weight to this assumption. The absorption due to carbondioxide relative to that due to molecular oxygen is estimated to be about 1% below

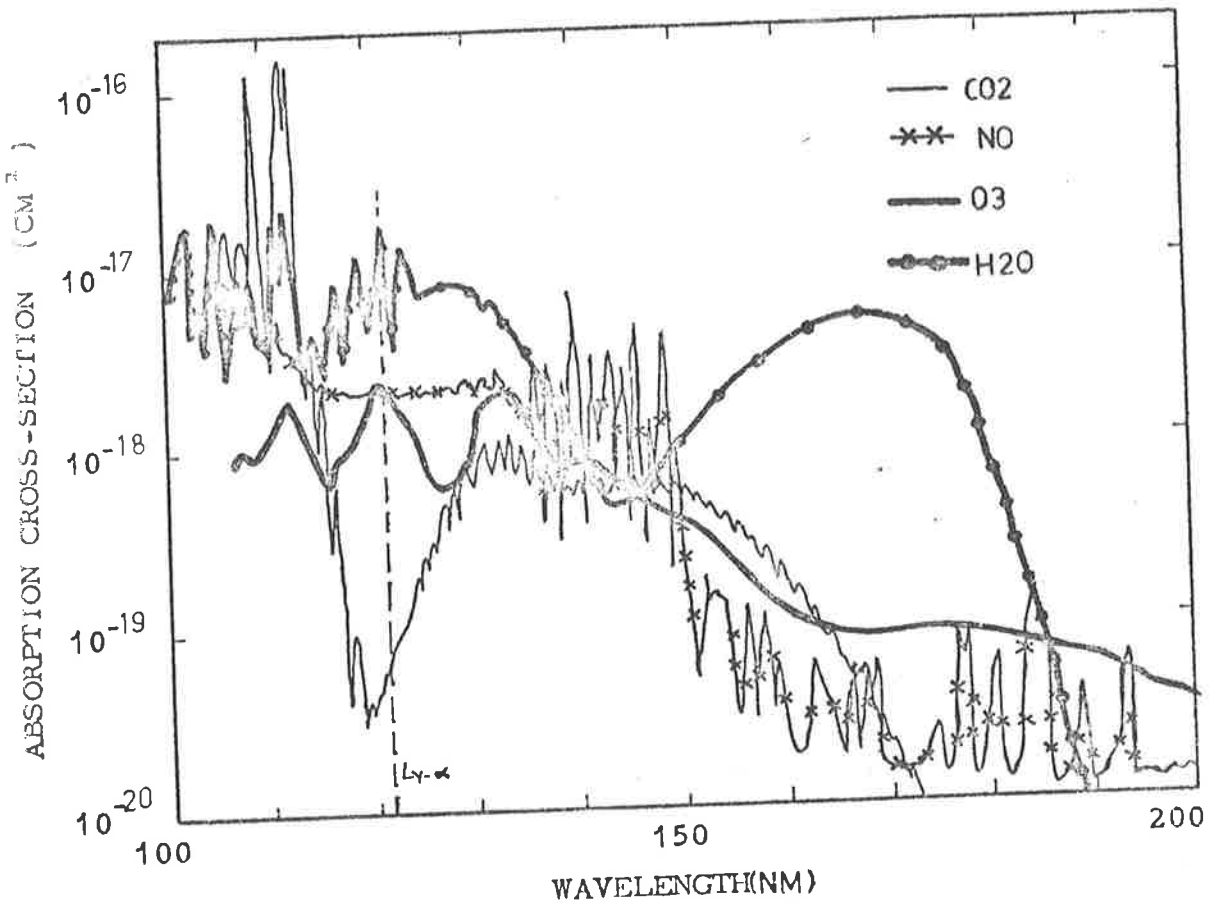

Figure 2.12 The absorption spectrum of nitric oxide (Marmo, 1953), carbondioxide (Inn et al., 1953), Ozone (Tanaka et al. 1953) and water vapour (Watanabe and Zelikoff, 1953).

100 km and even less at greater heights.

(c) Ozone

Tanaka et al (1953) have obtained a value of $2.3 \times 10^{-17} cm^2$ for the absorption cross-section of ozone at Ly-α. Only a few measurements of ozone concentrations above about 70 km have been made and these have a large uncertainty (Rawcliffe et al, 1963; Hays and Roble, 1973 and Miller and Ryder, 1973). Therefore the absorption due to ozone relative to that due to molecular oxygen is estimated from the ozone distribution given by Hunt (1973) and the results are shown in Table (2.3).

(d) Water Vapour

The absorption spectrum of water vapour is shown in Figure (2.12) from which it can be seen that Ly-α occurs near a maximum in the absorption spectrum. The values of the cross-section obtained at Ly-α by various workers are $1.45 \times 10^{-17} cm^2$ (Preston, 1940), $1.45 \times 10^{-17} cm^2$ (Ditchburn et al, 1954). As these values are more than a thousand times the value for molecular oxygen, even very small concentrations of water vapour above 70 km could contribute significantly to the absorption of Ly-α radiation. The very strong band structure in the water vapour absorption spectrum occurs within the 105 (114) nm to 135 nm bandwidth of the ionchamber used in the present work to detect Ly-α radiation. Due to the very high cross-section values at the peaks of these bands, even very small traces of water vapour in the nitric oxide filling gas of this detector can seriously affect its operation (Section 2.4).

There have been no experimental determinations of water vapour concentrations above 70 km but a recent theoretical profile is given by Hunt (1973) in a photochemical model. The formation of noctilucent clouds near an altitude of 80 km, in summer and at latitudes above 45°, has been studied by Chapman and Kendall (1965). They have concluded that these clouds are formed when water vapour is carried (by convection at night) up to 80 km, where it condenses

on dust particles. As these clouds appear infrequently, it must be assumed that the transport of water vapour to these heights is a rare phenomenon. It should not therefore affect the overall concentration of water vapour at these heights.

There is obviously still a great uncertainty in the concentration of water vapour above 70 km but for the present work it was assumed that the water vapour concentration is as calculated by Hunt (1973). Under this assumption the absorption due to water vapour, relative to that due to molecular oxygen is estimated to be about 1.5 percent at 75 km and 0.4 percent at 90 km and less at greater heights.

(e) Nitric Oxide

A value of $2.5 \times 10^{-18} cm^2$ has been obtained for the absorption cross-section of nitric oxide at Ly-α (Marmo, 1953). There is a wide scatter in the NO data of Barth (1966), Meira (1971), Pearce (1969) and Tisone (1973) and the possible effect is therefore quite variable due to this uncertainty of perhaps more than a factor of 10 in the NO distribution. The photochemical profile of Hunt (1973) has been used for present estimation of No effect and the results shown in Table (2.3) indicate a negligible effect.

(f) Conclusion

Atomic oxygen and atomic nitrogen exhibit continuous absorption only below their first ionization limits which are at 91 nm and 85.2 nm respectively. They can therefore be neglected when considering absorption processes above 100 nm. Similarly the inert gases which have ionization limits at 88.6 nm (Kr), 78.4 nm (A) and 57.5 nm (Ne) need not be considered.

The estimates of absorption of Ly-α radiation by constituents other than molecular oxygen as discussed above and presented in Table (2.3) are based on absorption cross-sections of various constituents measured at room temperatures. As discussed in the earlier section the average mesospheric temperatures are

significantly lower than room temperature. Also it is shown in the same section that both theoretical studies and experimental observations indicate a decrease in absorption cross-sections at Ly-α that decreases with temperature. A similar effect on absorption cross-section of other constituents is yet largely unknown and would require similar measurements. In addition, the concentrations of two important constituents - NO and H_2O - are in great uncertainty. Therefore no definite correction for absorption due to other constituents are possible and no such corrections have been applied to the Ly-α data in the present work.

In the wavelength band 155 nm to 169 nm (the bandwidth of the other ionchamber used in this study), the effective absorption cross-section of molecular oxygen is about 300 times the value at Ly-α. As a result, the contribution to the absorption of radiation in this wavelength band, due to atmospheric constituents other than molecular oxygen, is negligible.

2.4 WATER VAPOUR CONTAMINATION OF THE Ly-α IONCHAMBER AND SOME OBSERVED DENSITY ANOMALIES

Ionchambers with LiF or MgF_2 windows and NO filling gas have a spectral response band of 105 - 135 nm and 114 - 135 nm respectively. It has already been pointed out in Section (2.2.3(c)) that although the detectors respond to the radiation in the above band passes, during a rocket (or satellite) flight, the solar radiation observed by the detector is almost entirely due to Ly-α radiation up to a certain height for the reasons that (i) Ly-α radiation is very strong relative to the other radiation in the detector pass band and (ii) absorption cross-section of molecular oxygen has a window at Ly-α. This simplifies the data reduction up to such heights h_L (to be evaluated) so that all the radiation observed by the detector at heights below h_L is essentially due to Ly-α. The contribution due to radiation other than Ly-α in the pass band of the

detector (to be termed as "other radiation") increases above h_L and becomes significant in the total observed signal. If the analysis of observed profile is extended beyond h_L with the assumption of pure Ly-α radiation; the density data would be in error and may show some anonalous behaviour. Furthermore, in order to monitor Ly-α flux, one requires knowledge of the total contribution of "other radiation" in the unattenuated detector signal.

The contribution of radiation other than Ly-α at a given height depends primarily on zenith angle and the spectral response curve of the detector. It has been seldom realized that the spectral response curve of the Ly-α ionchamber (particularly the widely used LiF - NO ionchamber) is strongly dependent upon water vapour contamination of the filling gas. Therefore knowledge of the level of contamination in terms of the measured spectral response may be of use in estimation of (i) the upper limit of the height range (h_L) below which assumption of signal being purely due to Ly-α radiation would be valid and (ii) the total contribution of other radiation in the unattenuated signal.

Although some estimates of the height, (h_L) and total contribution of "other radiation" have been reported, no systematic attempt has ever been made to study the effect of contamination of the detector gas by water vapour. This is perhaps one of the main reasons for the scattering of the reported estimates in Table (2.4).

The purpose of this study was to investigate the contamination effect on these parameters. Four representative ionchambers were selected which consisted of a pair of LiF - NO(LNO) and another pair of MgF_2-NO(MNO). These pairs were selected from two respective batches of these detectors after measuring the spectral response curves for each of them. Each selected pair consisted of one contaminated (to be denoted by a script C) and one relatively uncontaminated or good (to be denoted by a script G) ionchambers. Spectral responses of these chambers were measured as

described in Section (3.8). The attenuation of solar flux as seen by one of these detectors if flown aboard a rocket was estimated using equation (2.4) i.e.,

$$I(h,Z) = \int_{\lambda}^{\lambda+\Delta\lambda} \phi_{\infty}(\lambda) \exp[-\sigma(\lambda) N(h,Z)] \varepsilon(\lambda)\, d\lambda \qquad (2.25)$$

where

$$N(h,Z) = \int_{h}^{\infty} n(h) F(h,Z)\, dh$$

First, signal due to Ly-α alone - I(h,Z) was computed from equation (2.25) by integrating over the width of the solar Ly-α (~ 0.1 nm wide).

TABLE 2.4

The upper limit (h_L)

Ionchamber Type	Zenith Angles	h_L (km)	Reference
LiF - NO	50°	125	Grobecker (1967)
MgF_2 - NO	75° - 80°	100	Martini and Shyutte (1973)
LiF - NO	32°	105	Quessette (1970)
LiF - NO	60°	94	Weeks and Smith (1968)
MgF_2 - NO	⩽ 40°	92	Weeks (1974)
MgF_2 - NO	60°	90	Smith and Miller (1974)

The shape of the line (hence flux distribution over this width) was used from Purcell and Tousey (1960) with a total photon flux of 2.38×10^{11} $cm^{-2}sec^{-1}$. The absorption cross-section was used from Carver et al (1976) at 195° K (Section 2.2.4). Over the width of the line the detector response function ε(λ) remains almost constant and can be used as 1. Model atmosphere (Section 2.2.3(b)) was used for $NO_2(h)$.

Then signal due to "other radiation" only - I'(h,Z) was computed in a similar fashion by integrating the equation (2.25) over the entire bandwidth of the detector (105 - 135 nm or 114 - 135 nm). The distribution of solar flux was taken from Donnelly and Pope (1973). The intense lines - excluding Ly-α - within the bandwidth of the detectors were integrated in

the continuum flux. The absorption cross-section of O_2 was used from Watanabe (1958). Spectral responses shown in Figure (3.8) were normalized to 1.00 at Ly-α before being used in equation (2.25) so that a direct comparison could be made for signals I(h,Z) and I'(h,Z) for all of the four detectors. These quantities were then used to calculate the contribution of "other radiation" relative to "Ly-α radiation" at a given height, for a number of zenith angles i.e. I'(h,Z(/(I(h,Z) which is shown in Figure (2.13). Also calculated was the total signal from the detector which is represented relative to Ly-α flux above the atmosphere i.e. (I(h,Z)+I'(h,Z)/I(∞,Z)). This representation in Figure (2.14) has the obvious advantage of giving observed profiles relative to purely Ly-α profile normalized to 1 above the atmosphere. The degree of deviation from the assumption of signal being due to Ly-α alone at a given height can be readily seen from this Figure. The results of this analysis can be described as follows:

(a) Upper limit of the height interval (h_L)

From Figures (2.13 and 2.14) we can see that for a given zenith angle the contribution of "other radiation" from LNOC is much more than from LNOG. Further more, the signal due to "other radiation" becomes significant in the total detector signal at somewhat lower altitudes for LNOC compared to LNOG as expected. The unattenuated signal due to "other radiation" amounts to about 13% and 8% of the signal due to Ly-α radiation alone for the two detectors respectively. The photon flux of the Ly-α radiation has been taken as 2.38×10^{11} photons/cm^2/sec representing a mean solar activity situation. It should be remarked here, that the Ly-α flux undergoes a significant variation (Vidal-Majdar, 1975). Printz (1974) has suggested that the flux can be as low as 2.16×10^{11}p/cm^2/sec whereas considerably lower values have been reported by a number of workers (see Weeks, 1967). The flux for continuum in the band 105 - 135 nm or 114 - 135 nm is not expected to show any substantial variations associated with the

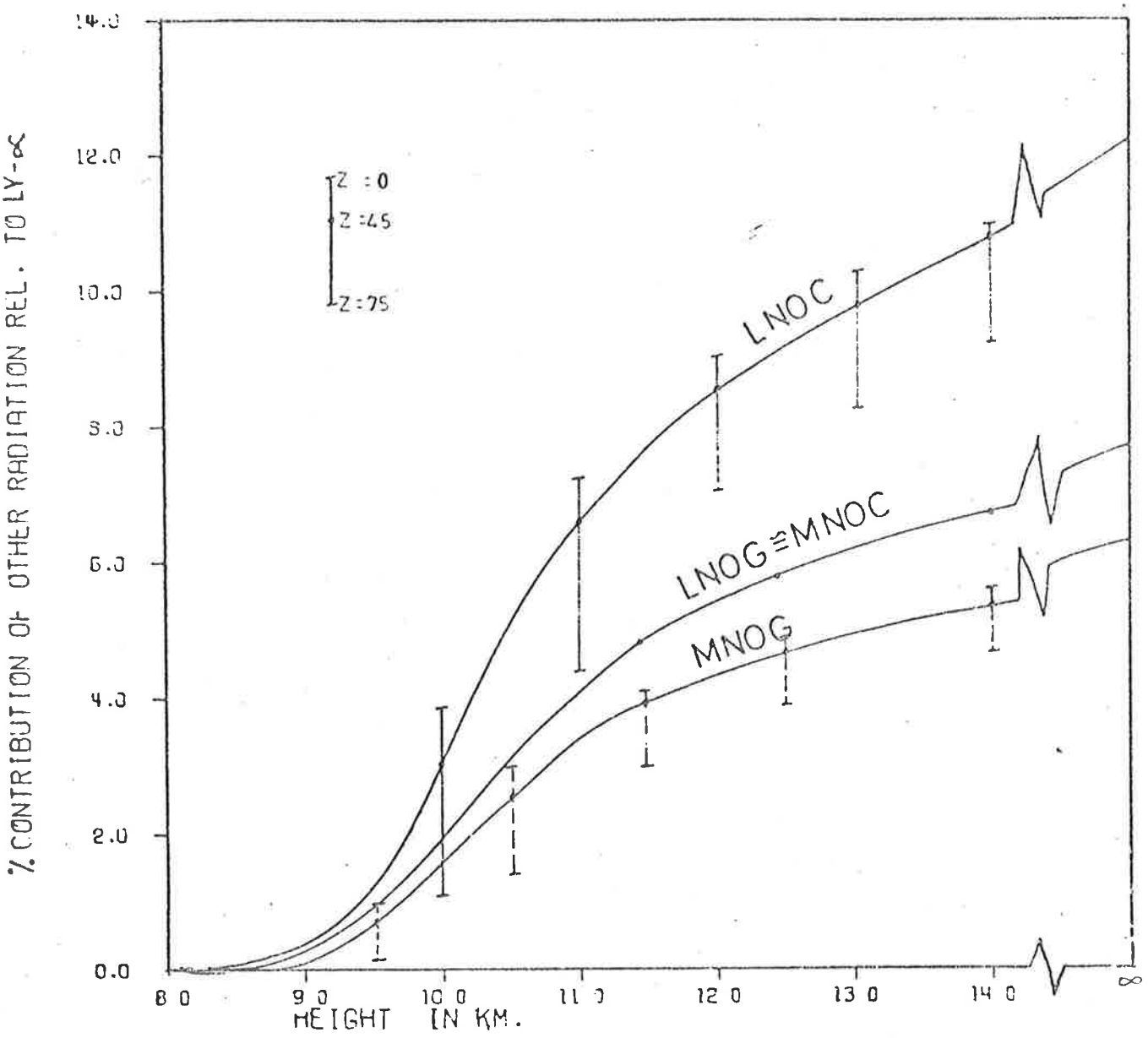

Figure 2.13 Variation of contribution due to other radiation in the signal of Ly-α ionchamber for four ionchambers. The vertical bars show the effect of variation in zenith angle for two ionchambers.

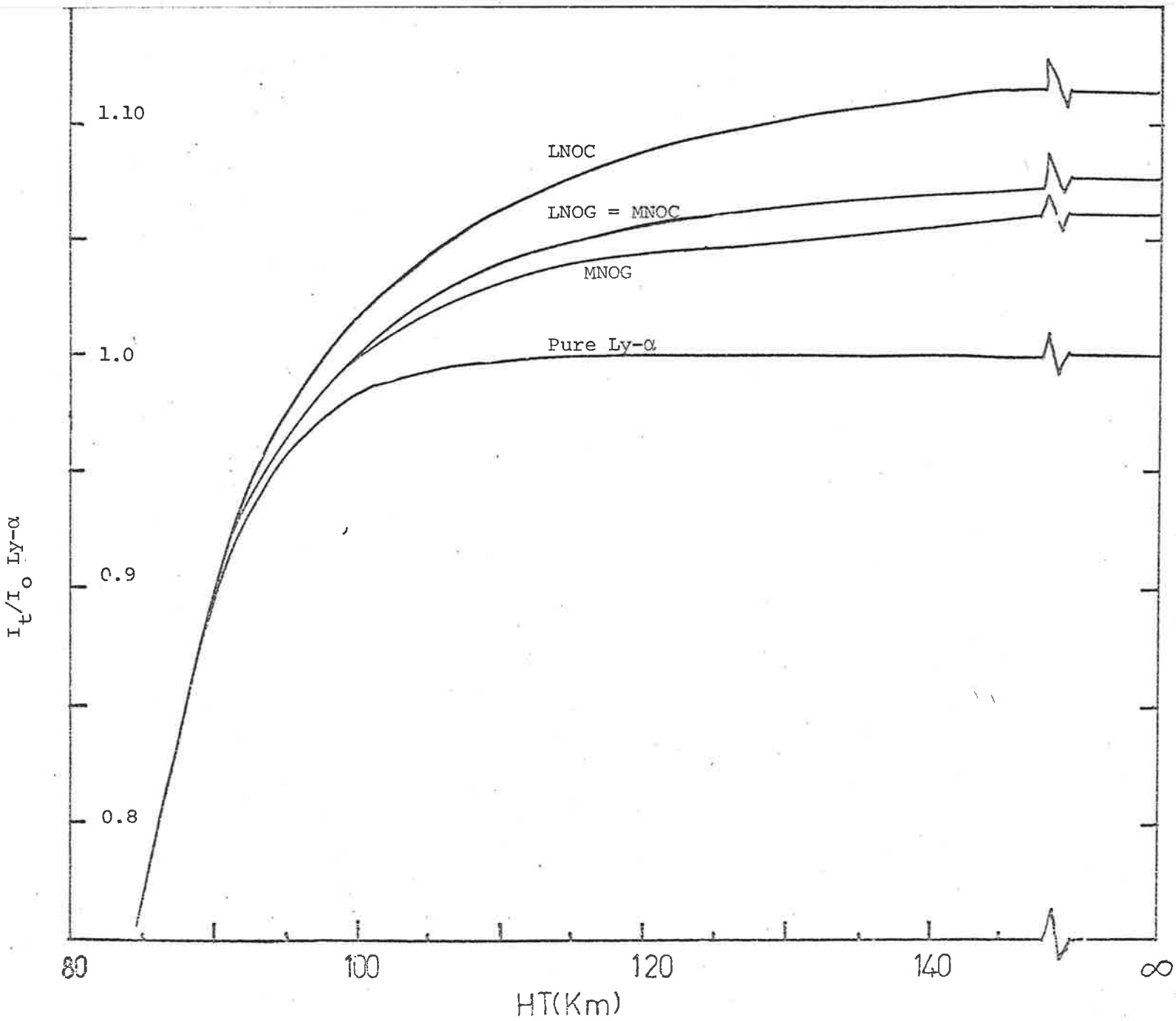

Figure 2.14 Effect of other radiation in Ly-α ionchamber signal.

solar activity. Therefore the relative contribution of other radiation may be even larger at a given height if intensity of Ly-α radiation happens to be significantly less than the flux value used in these computations. Of course, if intensity of Ly-α radiation at the time of a particular observation happens to be significantly larger than the value used in these computations (values have been reported as large as 3.9×10^{11} p/cm^2/sec, see Weeks, 1967; Vidal-Majdar, 1975) the contribution due to "other radiation" will decrease consequently at a given height. These diagrams also show similar calculations for MgF_2-NO (MNO) ion-chambers. Although some MNO chambers may be more contaminated than shown by the spectral response of MNOC (Figure 3.8), the risk of contamination is much less for chambers of this type due to the lower H_2O affinity of MgF_2.

It may be seen that the total contribution of "other radiation" for LNOG is approximately equal to that exhibited by MNOC and this contribution is further reduced although not drastically for MNOG.

Therefore it may be concluded that the upper limit of the height range will decrease significantly with the amount of contamination of the LNO chamber. Interestingly, the effect of contamination on MNO chambers is found to be much less severe for reducing the upper limit of the height range which makes an MNO chamber preferable to an LNO chamber.

(b) Anomalous Behaviour of O_2 Profile above h_L:

Analysis of data from LNO chambers is generally restricted to below 100 km for zenith angles $\leqslant 50^\circ$. In some of the reported cases, data analysis has been carried to much higher altitudes with the assumption that the detector signal is due to Ly-α radiation only (Table 2.3). Quessette (1970) assumed that for a zenith angle of 30°, at least up to 105 km, signal is due to Ly-α radiation only and derived an O_2 density profile up to this

altitude. The O_2 profile shows an anomalous behaviour above 92 km which has been used at least partially by Tchen (1971) for the development and confirmation of a turbulent theory. In an attempt to clarify the situation we used our computed flux profiles to observe any anomaly in the derived O_2 density. To maximize the effect of other radiation, the derived total signal profile for LNOC corresponding to a solar zenith angle of 45° was used (Figure 2.14). An effective cross-section with a value of $1.00 \times 10^{-20} cm^2$ for the region above 90 km was used. This is good enough to illustrate the relative effect of other radiation. The resultant O_2 profiles are shown in Figure (2.15). The density profile (b) exhibits anomalous higher concentrations above about 92 km. The profile very much resembles the one reported by Quessette* (1970). It is also interesting to note that the profile (b) indicates a region of almost constant densities simply due to the other radiation effect. The results of Grobecker (1971) which show this constant density anomaly are perhaps due to this effect. In a preliminary analysis of satellite-born Ly-α ion-chamber data, Lockey et al (1969) also observed this constant density anomaly at somewhat higher altitudes. This is probably due to other radiation effect shifted to higher altitudes due to large zenith angle situation. Therefore, the turbulent explanation of Tchen (1971) for the anomalous results of Quessette (1970) and Lockey et al (1969) is perhaps not valid; the observed behaviour being mainly due to other radiation effect.

(c) Contribution of "Other Radiation" to the Total Unattenuated Flux.

We have shown above that the contribution of other radiation is dependent on the amount of contamination particularly for the LNO chamber. Hinteregger (1965) reported this contribution to

---

* The actual instrumentation used by Quessette was somewhat different. He made use of a grating (100 - 140 nm) in front of an LNO chamber operated at a gas gain of 300.

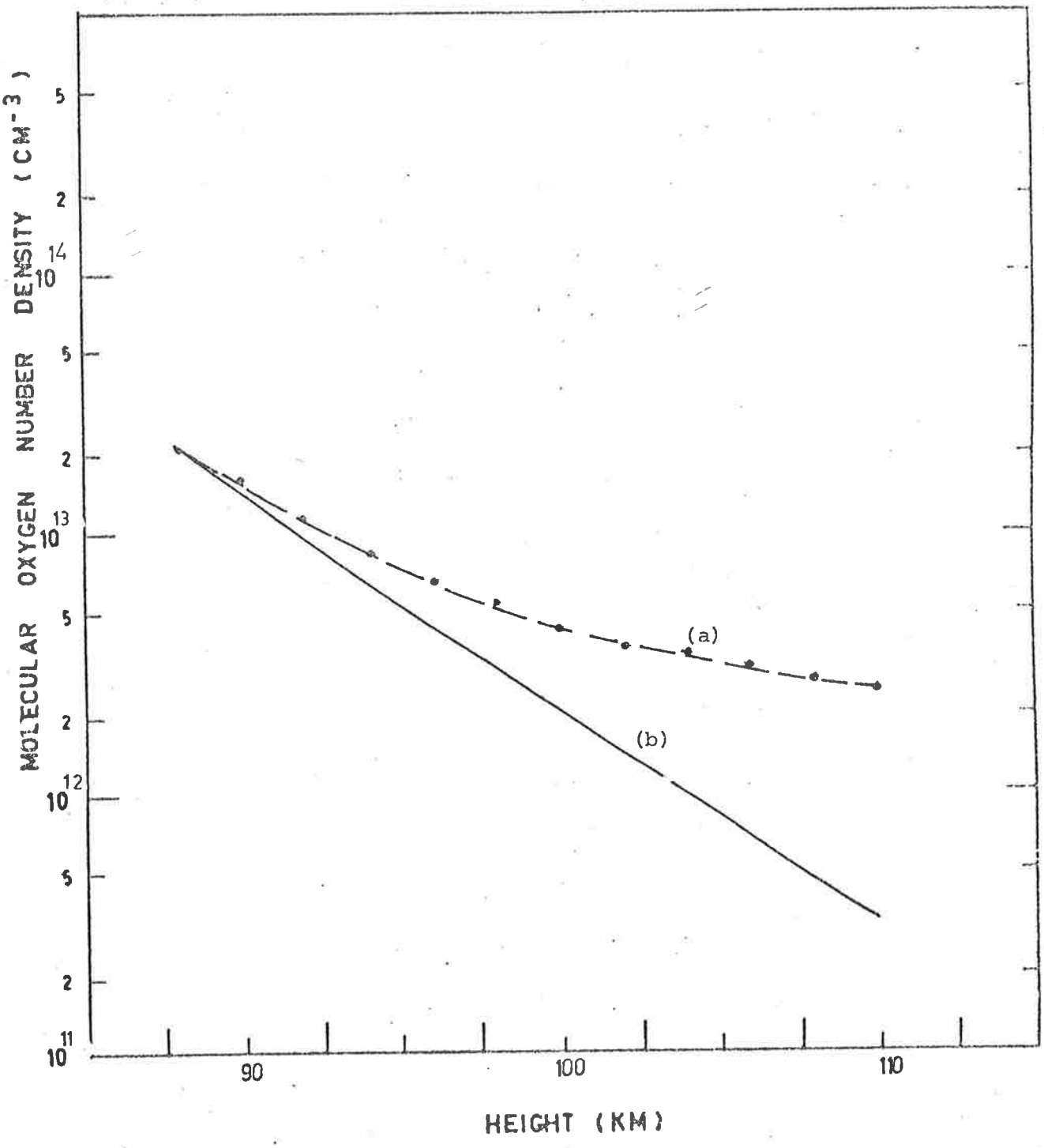

Figure 2.15 Effect of other radiation on derived molecular oxygen density above 90 km (a) Density profiles due to Ly-α radiation only, (b) Due to Ly-α and other radiation for LNOC.

vary from 10% to 30% of the Ly-α signal. Higashino et al (1966) have reported this contribution to be as large as 45%. We find that this radiation should not be more than 15% of the Ly-α signal (our calculations showed 7.5%) if an LNO chamber is reasonably uncontaminated by water vapour. Therefore a significantly higher contribution due to other radiation may be an indication of the high degree of contamination of the detector. Nevertheless as mentioned earlier, it should be realized that solar Ly-α radiation undergoes significant intensity variations and the relative contribution should be seen in that context as well.

It may be concluded from the above discussion that the water vapour contamination has but marginal effect on the MNO chamber for the "other radiation" signal although an LNO chamber is affected significantly. There is a greater problem of contamination of an LNO chamber compared to an MNO chamber as discussed in Section (3.5). Moisture effect on transmission of a Magnesium Fluoride window is found to be almost negligible (Masuoka and Oshio 1974). Therefore Magnesium Fluoride windowed ionchambers would be superior for use as flux monitors. The upper limit h_L appears to be below 95 km for zenith angles less than 75° for a moderate solar activity.

2.5 THE DETERMINATION OF TEMPERATURE PROFILES FROM OXYGEN DENSITY PROFILES

The basic equations governing the structure of the atmosphere are:

(a) $p_i = n_i kT$ (The gas law)

where p_i is the partial pressure and n_i the number density of the constituent i, k is Boltzmann's constant, and T is the absolute temperature.

We may also write

$p = nkT$ $\qquad p = \varepsilon n_i$

where p and n are the total pressure and the total number density.

(b) $\rho i = mi\ ni; \rho = \Sigma\ mi\ ni$

where ρi is the density and mi the molecular mass of constituent i, and ρ is the total density.

(c) $dp = -\rho g\ dh$ (The Hydrostatic Law)

The determination of the number density of one constituent ni(h) as a function of height will not in general allow a temperature profile to be calculated. However, there are two special situations in which the calculations can be made. These are:

(a) Diffusive Equilibrium

This is the situation where each constituent is distributed in height just as if it were the only constituent i.e., each constituent behaves independently of the others. Then

$$pi\ (ho) = \int_{ho}^{\infty} \rho i(h)\ g\ dh$$

$$= mi \int_{ho}^{\infty} ni(h)\ g\ dh \qquad (2.26)$$

and

$$T\ (ho) = \frac{mi \int_{ho}^{\infty} ni(h)\ g\ dh}{ni(ho)\ K} \qquad (2.27)$$

(b) Mixing

In this case each constituent occupies a constant fraction by volume (i.e. number density) of the air. If the fraction occupied by the constituent i is ri = ni/n and we define a mean molecular mass $\bar{m} = \sum mi\ ni/n = \rho/ni$; then

$$\rho = n\bar{m} = \bar{m}\ ni/ri. \qquad \text{Therefore}$$

$$pi(ho) = ri\ p(ho)$$

$$= ri \int_{ho}^{\infty} \rho(h)\ g\ dh$$

$$= ri \int_{ho}^{\infty} \bar{m}\ ni(h)\ g\ dh/ri$$

$$= \bar{m} \int_{ho}^{\infty} ni(h)\ g\ dh \qquad (2.28)$$

and

$$T(ho) = \frac{\bar{m} \int_{ho}^{\infty} ni(h)\, g\, dh}{ni(ho)k}$$

Molecular oxygen is probably in diffusive equilibrium above about 120 km during the day (Killman-Bijl and Sibley, 1963), and below 90 km there is mixing, the mean molecular mass being 28.96 (CIRA 1972). Between 90 and 120 km, where the photodissociation of oxygen takes place, neither of the above two situations is exclusively applicable.

Since the number density measurements do not extend to an infinite height, rather only to some maximum height hm, the integrals in equations (2.26) and (2.27) cannot be evaluated from the measurements alone. There are two ways of overcoming this difficulty. The first is to make a direct estimate of $\int_{hm}^{\infty} ni(h)\, g\, dh$ from an extrapolation of the ni(h) curve. The second, more usual method is to assume a temperature Tm at hm and calculate $\int_{hm}^{\infty} ni(h)\, g\, dh$ from

$$Tm = \frac{mi \int_{hm}^{\infty} ni(h)\, g\, dh}{ni(hm)k} \qquad \text{for case (a)} \tag{2.30}$$

and

$$Tm = \frac{\bar{m} \int_{hm}^{\infty} ni(h)\, g\, dh}{ni(hm)k} \qquad \text{for case (b)} \tag{2.31}$$

The actual choice for evaluation of the integral i.e., either using ni(h) curve or using Tm and evaluating the integral through relations (2.30) (or 2.31) has little effect on the temperature since the integral above hm soon becomes a very small part of the total integral as the integration is extended down from hm. This is so because ni(h) increases approximately exponentially as h decreases.

The mesospheric oxygen measurements therefore can be used to infer kinetic temperatures with the help of equations (2.29 and 2.31) i.e.

$$T(ho) = \frac{\bar{m}}{ni(ho)k} \left[\int_{ho}^{hm} ni(h)\, g\, dh + \frac{ni(hm)k\ Tm}{\bar{m}} \right] \tag{2.32}$$

where the second term corresponds to the integral $\int_{hm}^{\infty} ni(h)\, g\, dh$.

The value of g will usually be sufficiently constant over the height range used in the integration for an average value $\bar{g}$ to be used. However in the present calculations the variation of g with height was calculated from the exact expression:

$$g(Z) = 979.3244 - 3.0866 \times 10^{-4}Z + 7.259 \times 10^{-11}Z^2 \ (\text{cm sec}^{-2})$$

where Z is height in metres above the earth's surface (CIRA 1965).

It may be noted that in the case where the initial absorption measurement is made with monochromatic radiation, the integral $\int_{ho}^{hm} ni(h)\ dh$ may be obtained from the flux measurements using the relation

$$\int_{ho}^{hm} ni(h)\ dh = \frac{1}{\sigma \sec Z}\ \ell n\ \frac{\phi(ho)}{\phi(hm)} \qquad (2.33)$$

Equation (2.32) was used to obtain temperature profiles from observed oxygen profiles and the values of Tm were taken from the mean reference atmosphere (CIRA 1972). These results are presented in Chapter 6.

2.6 HEIGHT RANGE FOR DETERMINING MOLECULAR OXYGEN DENSITIES

There is a practical limit to the height range over which molecular oxygen densities can be determined by absorption techniques using a detector with a particular absorption cross-section. To illustrate this, let us consider the following simplified situation. Assume that,

(a) the absorption is due only to molecular oxygen,

(b) the effective molecular oxygen cross-section for a finite width detector ($\Delta\lambda$) may be taken as constant, and

(c) the number density of molecular oxygen varies exponentially with height, i.e. $n(h) = no \exp[-h/H]$, where H is the scale height for molecular oxygen. This is a good approximation over a limited height-range.

Equation (2.11) may be rewritten as:

$$I(h) = I_o \exp[-\tau(h)] \qquad (2.34)$$

where the optical depth for the wavelength band λ to $\lambda+\Delta\lambda$ is given by

$$\tau(h) = \sigma N(h) \qquad (2.35)$$

Therefore, at the penetration height, h* (see footenote)

$$\tau(h^*) = \sigma N(h^*) = 1 \qquad (2.36)$$

using $n(h) = no \exp [-h/H]$ and $F(h,Z) = \sec Z$

for small zenith angles Z, we get

$$N(h) = -\int_h^\infty no \exp [-h/H] \sec Z \, dh$$

$$= no H \exp [-h/H] \sec Z$$

So, from equation (2.35),

$$\tau(h) = \sigma no H \exp (-h/H) \sec Z \qquad (2.37)$$

Using equations (2.34) and (2.37), the variation of I with height can be determined as shown in Table(2.5).

It can be seen from Table(2.5)that the absorption takes place over a height range equal to about 4H and represents the practical limit to the range over which densities can be determined by the measurement of absorption at one value of σ. This range is limited in the region of high attenuation by the difficulty in measuring very small values of I while the limitation in the region of low attenuation is introduced by the difficulty in measuring the very small changes in I with height. The most accurate densities will in general be obtained near the penetration height, where the rate of change of signal with height is a maximum and therefore the errors due to data reduction a minimum

From equation (2.36),

$$\sigma no H \sec Z \exp (-h^*/H) = 1 \qquad (2.38)$$

Therefore, the value of h* will be increased as Z is increased without altering the values in Table(2.5). As a result, the absorption takes place higher up but over the same height range. From equation (2.38), it can be seen that as the zenith angle changes from 0 to Z, the value of h* is increased by an amount Δh^*, such that $\sec Z = \exp [\Delta h^*/H]$. Values of $(\Delta h^*/H)$ are given in Table (2.6) for various values of Z. It can be seen

---

* The atmospheric penetration height is the height above the earth's surface at which the solar flux has been attenuated to 1/e of its value above the atmosphere.

from this Table that even for large changes in the zenith angle, the height range over which oxygen densities can be determined is not shifted by a large amount. This statement is strictly true only when the flat-earth approximation is valid. In fact, due to the curvature of the earth, the range is not raised more than several scale heights for zenith angles up to 90°. Nevertheless, observations at large zenith angles provide a useful way of extending, significantly, the range of heights over which densities can be measured at one value of σ. For zenith angles less than 70°, the normal height range for determining molecular oxygen densities is 70 km to 95 km with Ly-α ionchambers and 100 km to 135 km with Quartz-triethylamine (Q - T) ionchambers; both of which were used in the present measurements.

TABLE 2.5

h	τ	I/I_∞
h* - H	2.7	0.07
h*	1.0	0.37
h* + H	0.37	0.67
h* + 2H	0.14	0.87
h* + 3H	0.05	0.95

TABLE 2.6

Z	$\Delta h^*/H$
0	0.00
20	0.06
40	0.27
60	0.69
70	1.07

Weeks and Smith (1968) raised the observational range of their ionchamber measurements considerably by using large zenith angles near sunrise and sunset. Similarly this range is shifted upwards when measurements with satellite born photometers are made in satellite-sunrise-and-sunset geometry.

CHAPTER 3

THE CONSTRUCTION AND TESTING OF VUV IONCHAMBERS

In this chapter, the construction and testing of the ionchambers is described in detail. The procedure for calibrating these detectors is described and discussed. Effects of water vapour contamination and temperature on spectral response are also discussed along with the steps taken to improve the life time of these detectors.

3.1 DETECTION OF VUV RADIATION (100 nm - 200 nm)

In principle, it is possible to fly a narrow band dispersive instrument to measure the transmission of solar radiation through the terrestrial atmosphere (Hall et al, 1965; 1967). However, especially when using unstabilized rocket vehicles, a simpler and more practicable method is to use non-dispersive but spectrally selective detectors.

The broad-band non-dispersive detectors used for the detection of UV radiation in the range 100 nm to 200 nm can be put into two following categories:

(i) Photomultipliers or photodiodes having high work function photocathodes that restrict their sensitivities to regions below approximately 200 nm.

(ii) Detectors utilizing the photoionization of gases and having relatively narrow band-passes in the range 100 nm to 180 nm.

The short wavelength limits of both types of detectors are determined by the use of various window materials that can only transmit radiation of wavelengths longer than some definite value.

Detectors of the first type work on the principle of photoelectric emission from surfaces. These have been described by Dunkelman et al (1962) who have detailed a variety of high work function photocathodes - both opaque and semitransparent - that have been developed to produce detectors spectrally selective to the vacuum ultraviolet. Typical examples of such materials are Cu-I, Cs-I, and K-Br. However, the nature of the

photoemissive process is such that the decrease in sensitivity towards longer wavelengths is only gradual. As the intensity of solar radiation increases rapidly towards longer wavelengths, these detectors have poor spectral selectivity when used in experiments where the sun is the source of radiation. Besides they require large volumes.

Detectors of the second type operate on the gas ionization principle. The molecular structure of some gases causes them to have a sharply defined ionization threshold, where the ionization efficiency of radiation drops rapidly over a narrow wavelength range which is characteristic of the gas. The use of such gases in these detectors will therefore result in a sharp long wavelength cut-off in direct contrast to the first case. This long wavelength limit is set by the energy needed to ionize any molecule of the filling gas. Apart from a small low energy tail, mainly due to the thermally excited vibrational and rotational states of the neutral molecules (Watanabe, 1957), this energy corresponds to the adiabatic ionization potential (IP) of the gas. Watanabe et al (1962) have given the IP values of about 300 molecules in the range 7 to 15 eV.

The earliest detectors employing the photoionization of a gas were the Geiger counters described by Chubb and Freidman (1955). The counters proved unreliable and were replaced by ionchambers (Freidman et al, 1958). Ionchambers with machined copper bodies have been used at the U.S. Naval Research Laboratory (Freidman et al, 1964) and at University College London (Willmore, 1961). An internally plated ceramic form has been used at NASA's Godard Space Flight Centre (Stober et al, 1963; Dunkelman et al, 1963), the Meteorological Office, Bracknell (Wildman et al, 1969) and Heinrich-Hertz Institute, Berlin (Felske et al, 1972). Ionchambers with bodies of extruded copper and stainless steel tubing have been used at the University of Adelaide (Carver and Mitchell, 1964; Carver et al, 1969) and the University of Tokyo (Mausoka and Oshio, 1972) respectively. Chambers of copper tubing as used in the present work are described in Section (3.3).

These detectors, with their wide field of view, excellent spectral selectivity, ruggedness and small size have been flown in small unstabilized rocket vehicles.

3.2 PRINCIPLES OF IONIZATION CHAMBER OPERATION

An ionchamber consists essentially of a volume of ionizable gas, a container for the gas with an area of a suitable window material, and a system of electrodes to collect the ions and electrons for measurement.

The three aspects of the generation of a signal current by the incident photon flux are as follows:

3.2.1 Absorption

A beam of radiation of a particular wavelength will be attenuated while passing through the chamber window. Materials which are suitable as windows for vacuum ultraviolet radiation detectors have a sharp transmission cut-off, with negligible transmission of wavelengths shorter than the limit. For each application, the window material is chosen to give the desired short-wavelength limit to the chamber response.

The radiation which passes through the gas volume is absorbed at a rate determined by the gas pressure and absorption coefficient at that wavelength (in the same manner as described in equation 2.1). The absorption coefficient of the gas may vary over the range of wavelengths admitted to the chamber. Strongly absorbed wavelengths produce ions in the space immediately behind the window, and efficient ion collection from this volume is then important if the detector response is not to be excessively sensitive to gas pressure.

3.2.2 Ionization

Photons of energy exceeding the ionization threshold of the gas can ionize gas molecules on absorption. The ionization efficiency varies with wavelength and drops suddenly in the vicinity of the threshold. The efficiency near the threshold is dependent on temperature (Carver and Mitchell, 1967), so the long wavelength limit of the chamber response

shifts slightly with temperature. In the middle of the response range, the ionization efficiency is not markedly temperature dependent. The photons able to enter the chamber through the window do not have enough energy to ionize more than one molecule, so the ionization efficiency is less than unity and is known from laboratory measurements as mentioned in Section (3.1).

Radiation which is not strongly absorbed in the gas can reach the walls of the chamber and the collecting electrodes where it may release photoelectrons from the surfaces. The resultant photoelectric current cannot be distinguished from the true ionization current. The most serious photoelectric effects are produced by radiation at wavelengths longer than the gas cut-off (Section 3.7.4), as radiation shorter than the window transmission limit can produce photoelectrons only outside of the chamber.

3.2.3 Charge Collection

The ions and electrons are swept from the gas volume by the electric field between the conductors in contact with the gas. Chambers used in this work had, as the collecting electrode, a rod fixed along the axis of the chamber; the other electrode being the side wall of the chamber.

The signal current from a chamber with constant radiation input depends on the bias voltage applied to it. As the applied voltage is increased, the output current increases in the bias direction. At some voltage (typically 35 volts for the chamber used), the current becomes almost independent of the voltage. The field strength above this voltage is sufficient to collect almost all of the ionization charge before recombination can occur. Below approximately 80 volts, no significant gas multiplication occurs, and one electron is collected in the signal circuit for each ionization event in the gas. A chamber run in this plateau region of the bias signal curve is said to be operating at unity gain (Figure 3.8). The sensitivity of the chamber at unity gain depends only on the transmission of the window and the absorption coefficient and ionization efficiency of the gas at each wavelength.

At higher applied voltages the signal current again becomes voltage

dependent as multiplication occurs within the gas. The degree of current amplification depends upon the composition and pressure of the gas, and on the field strength; a chamber operating under these conditions is said to be in gas gain mode. Ionchambers in the gas gain mode have been used by O'Connor (Carver et al, 1974). All the chambers used in this work were operated in the unity gas gain mode.

3.3 CONSTRUCTION OF THE COPPER BODIED IONCHAMBERS:

The chambers were of the type described by Friedman et al (1958) and of a design following Carver and Mitchell (1964) with some modifications. Cross-sectional diagrams of both detectors - one after Carver and Mitchell (1964) and one used in the earlier part of this work - can be seen in Figure (3.1). It can be clearly noticed from the diagram that the detector in (b) as used in this work is similar in design but has the advantage of being simpler to construct and much easier to clean. The body consisted of a 2.22 cm length of copper tubing with an outside diameter of 2.07 cm and a wall thickness of 2.39 mm. The support for the centre electrode was a Kovar-glass seal which incorporated a guard ring. After cleaning in an ultrasonic bath, the leakage resistance between the guard ring and the centre electrode was always greater than 5×10^{13} Ω. The seal was soft soldered on to the back of the copper tube and at the same time a filling tube was soft soldered into the metal flange of the seal (more recently into the copper wall near the window). The catbode was a length of solid, ground tungsten rod of 1 mm diameter which was hard soldered on the tip and then soft soldered into the back seal. The assembled chambers were cleaned in nitric acid and then boiled in detergent. They were then scrubbed with steel wool, washed in distilled water and finally washed in acetone.

Both, ionchamber body and window were heated in an oven to a temperature of approximately 90° C and the window was then attached to the body with the epoxy resin Araldite AV100. Lithium fluoride (LiF)

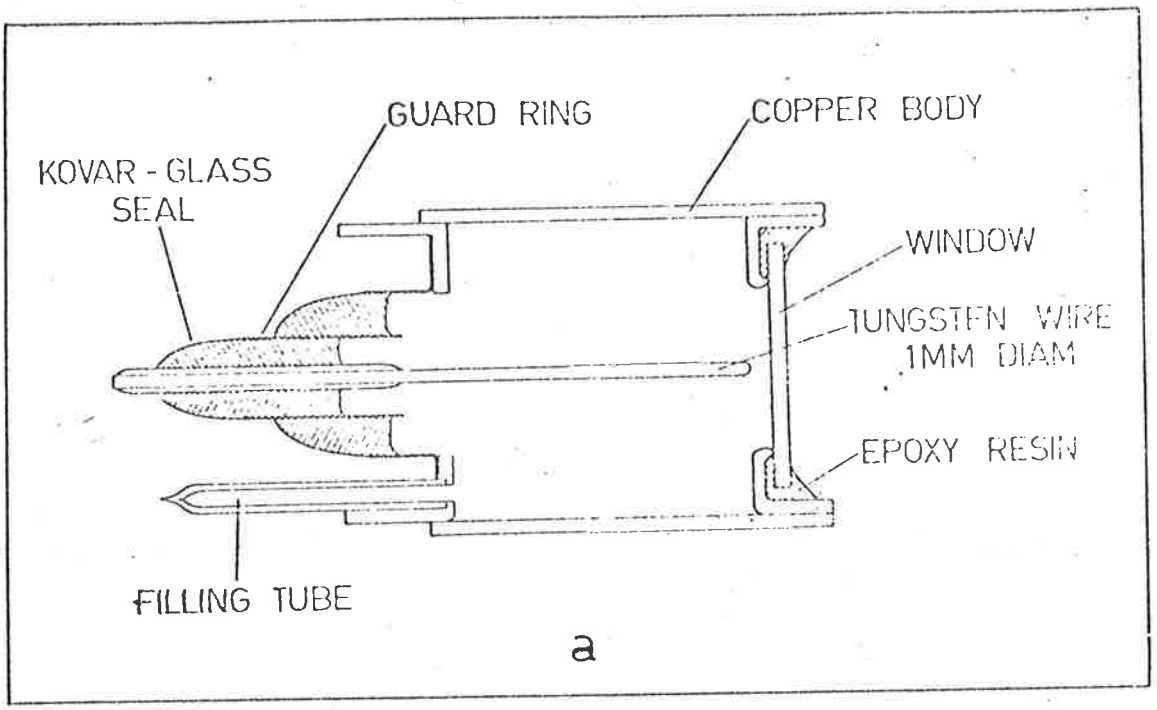

Figure 3.1 A cross-sectional diagram of a copper-bodied ion chamber of the type first used by Carver and Mitchell (1964).

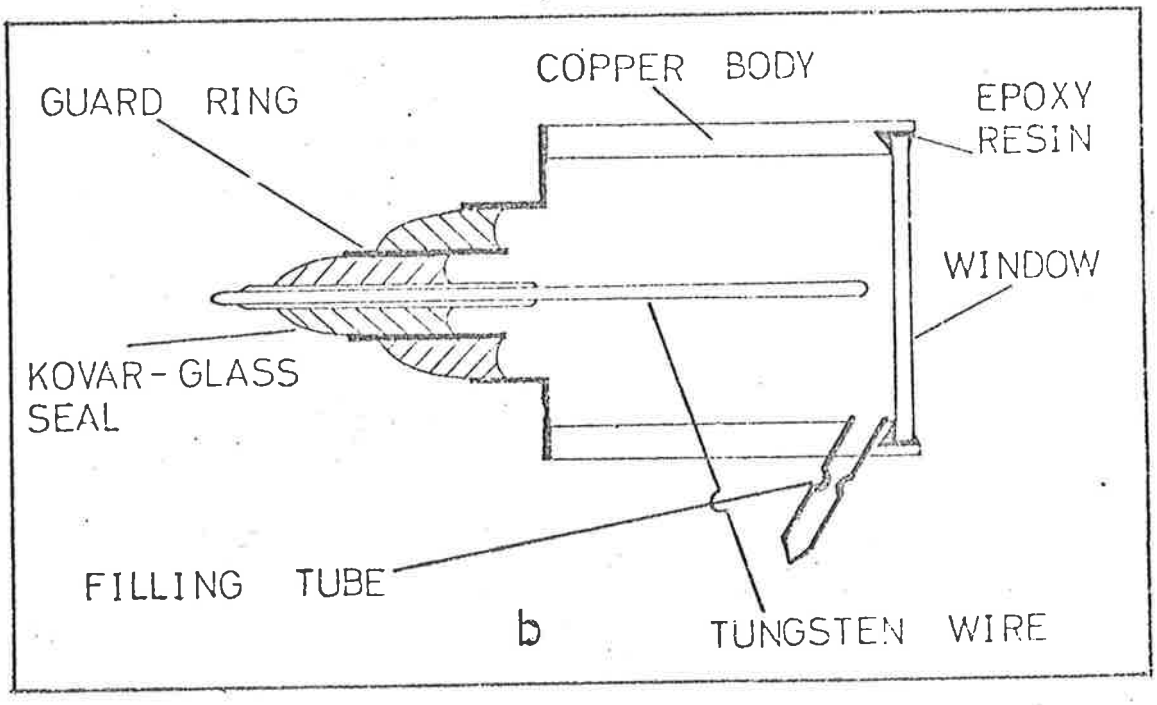

Figure 3.1 A cross-sectional diagram of a more recently designed copper bodied ion chamber.

windows were heated to temperatures in the vicinity of 250° C before being attached to the copper body. At the same time, a glass extension was joined on to the copper filling tube with the epoxy resin, so that the ionchamber could be connected to the glass manifold of the filling system. These chambers ready for filling were then kept in an electric oven for several days before being attached to the filling system.

3.4 WINDOW MATERIALS

The preperties of window materials used in this work are listed in Table (3.1)

TABLE 3.1

WINDOW PROPERTIES

Material	Dimensions	Transmission	Supplier
Lithium Fluoride	1.9 cm diameter (1-1.5 mm thick)	104.5 nm	Harshaw & Co.
Magnesium Fluoride	1.9 cm diameter (1 mm thick)	114.5 nm	Harshaw & Co.
Quartz (Spectrosil A)	1.9 cm diameter (1.0 mm thick)	154.5 nm	Thurmul Syndicate.

The transmission limit as given in Table (3.1), represents the shortest wavelength transmitted by the window. The lithium fluoride windows were unpolished, cleaned crystals while the megnesium fluoride and quartz windows were polished plates. A highly refined variety of quartz known as Spectrosil A was used to obtain a transmission limit at much shorter wavelengths than the nominal 180 nm of naturally occuring quartz.

3.5 SPECIAL PRECAUTIONS FOR THE LiF and MgF_2 WINDOWS

Contamination by water vapour of a LiF-NO and MgF_2-NO chamber could be easily detected by the appearance of absorption dips in its spectral response (Section 3.7.3). For LiF windows special care needs to be

Figure 3.2 Two types of ionchambers shown after assembly and filling.

taken. The contamination was found to be removed by baking the window to a high temperature for a period of several hours attaching it to the chamber. Figure (3.3) shows the transmission, as a function of wavelength, of a 1.5 mm thick cleaved lithium fluoride window, before and after baking in an electric oven for two hours at a temperature of 300° C.

It can be seen that the transmission is improved at all wavelengths as a result of heating. This improvement can be permanent if the window is kept in a dry atmosphere but deteriation will take place if it is left in the laboratory atmosphere. This is due to the formation of a surface layer of water which comes off if the window is baked thus improving the transmission. If the window is not baked before its attachment to a chamber, the water layer to the inner surface of the window subsequently outgases into the nitric oxide thereby reducing the quantum efficiency of the ionchamber at Ly-α (Section 3.7.3). This as such will not affect the accuracy of the derived oxygen densities in the height range where only Ly-α radiation is able to penetrate but would introduce errors in the determination of the contribution due to radiation other than Ly-α (Section 2.4). If this film of water from either side of the window, vapourises during a rocket or satellite flight, there will be a change in the sensitivity of the detector during one complete observation. This could be caused by rapid heating of ionchamber window as the rocket ascends. This will result in the discrepency between upleg and downleg and generally in such situations downleg data would be more reliable (Section 5.9).

Therefore, LiF windows were baked and then attached to the body. The assembly was kept in a heated atmosphere before being filled (Section 3.6.2). The chambers after gas filling, were stored in a desicator to prevent any water film formation on the outside surface of the window or its contamination.

Magnesium Fluoride (MgF_2) windows make a superior replacement of LiF windows when the detector is used to study radiation above about 116 nm.

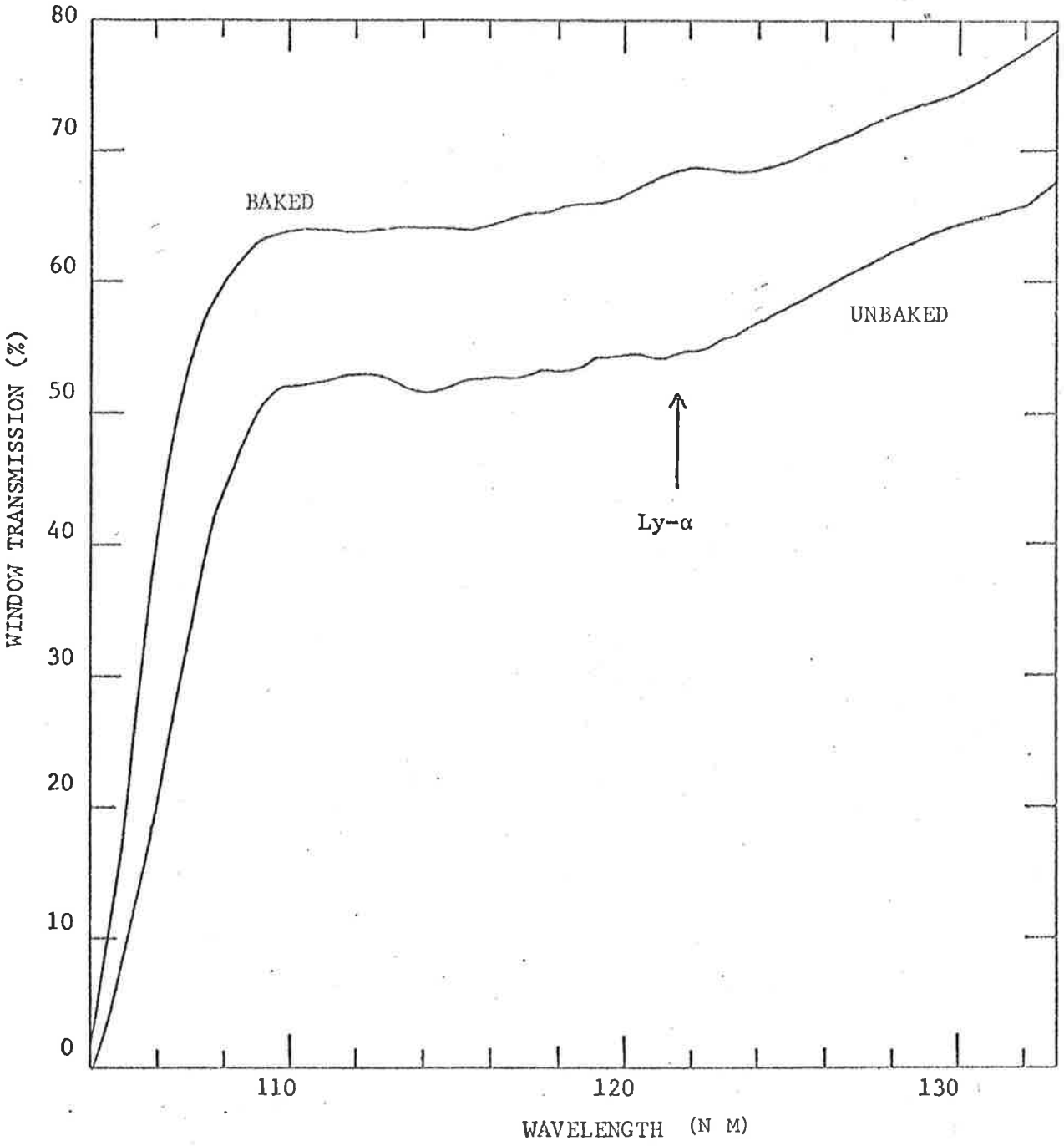

Figure 3.3 The transmission of a lithium fluoride window as a function of wavelength, both before and after baking. (Lockey, 1972).

The water contamination effect on the transmission of a MgF_2 window is relatively insignificant. This is thought to be due to relatively very low solubility of MgF_2 in water (Mausoka and Oshio, 1974). In the later flights, MgF_2-NO chambers were also included in the payloads. As a precaution, these chambers were stored along with the LiF-NO chambers in a desicator.

3.6 IONCHAMBER FILLING

3.6.1 General

A number of gases and vapours suitable for use as ionchamber filling are listed in Carver and Mitchell (1964).

In this work only nitric oxide (NO) and Triethylamine ($C_6H_{15}N$) were used. The filling pressure was selected to give the chamber maximum detection efficiency in the operative spectral range. The pressure of the filling gas is somewhat critical for the following two reasons:

(a) The absorption of radiation of any wavelength follows the form of equation (2.1). Therefore the pressure should be high enough to absorb the radiation particularly in regions of low cross-section.

(b) The ion production rate in the gas for a particular wavelength decreases exponentially over a pathlength determined by the gas pressure and its absorption coefficient for that wavelength.

Hence if the pressure is too high, the radiation for which σ is high will be absorbed too close to the window. Due to the weaker strength of the collecting field in the vicinity of the window, recombination of the ions will be a likely process.

Therefore the gas pressure should not be higher than necessary to fulfill the requirement in (a).

3.6.2 Gas Purification

Triethylamine was obtained as AR grade reagents and no purification was required. It was introduced to the filling system from a small phial

of the liquid form, warmed slightly to fill the system with the vapours.

The nitric oxide was obtained from a cylinder of commercial gas. It was then purified by passing in succession through traps filled with silica gel and with crushed glass, cooled to near -80° C by immersion in a carbon tetrachloride-chloroform slush mixture (Figure 3.4). The gas was collected in glass bulbs, with breaker seals and 'cold-finger' tubes, attached. The entire purification system was made out of glass with no metal components which might react with the gas. The glassware including the receiving bulb was baked out under vacuum before the collection of the purified gas. The receiving bulb was isolated when filled to about 90% of atmospheric pressure. Finally it was removed by a flame seal.

This purification system was designed particularly to remove two contaminants i.e. water vapour (H_2O) and nitrous oxide (N_2O_4). Both of these have strong absorption bands between 105 to 135 nm.

Nitrous oxide (N_2O_4) has a boiling point of 21° C and a vapour pressure near 1.00×10^{-1} mm Hg at -80° C. The vapour pressure of water at -80° C is near 5×10^{-4} mm Hg.

3.6.3 Chamber Filling Procedure

The chambers ready for filling after assembly were kept in an electric oven for a few days and then were attached to glass stems of the filling system simply by joining the glass tube attached to the copper filling tubes (Section 3.6.1). The entire filling system including the attached chambers was evacuated by an oil diffusion pump which has a back-up of a rotary oil pump, for several days. During this time the chambers and filling system were baked for periods at near 100° C to remove absorbed gases from the tube walls.

The filling system is shown schematically in Figure (3.5). The flask of purified nitric oxide gas (as described in Section 3.6.2) was attached so that gas could be admitted to the filling systems. As the vapour (triethylamine) was liquid at room temperature, it was introduced into the filling system from a small glass phial containing approximately

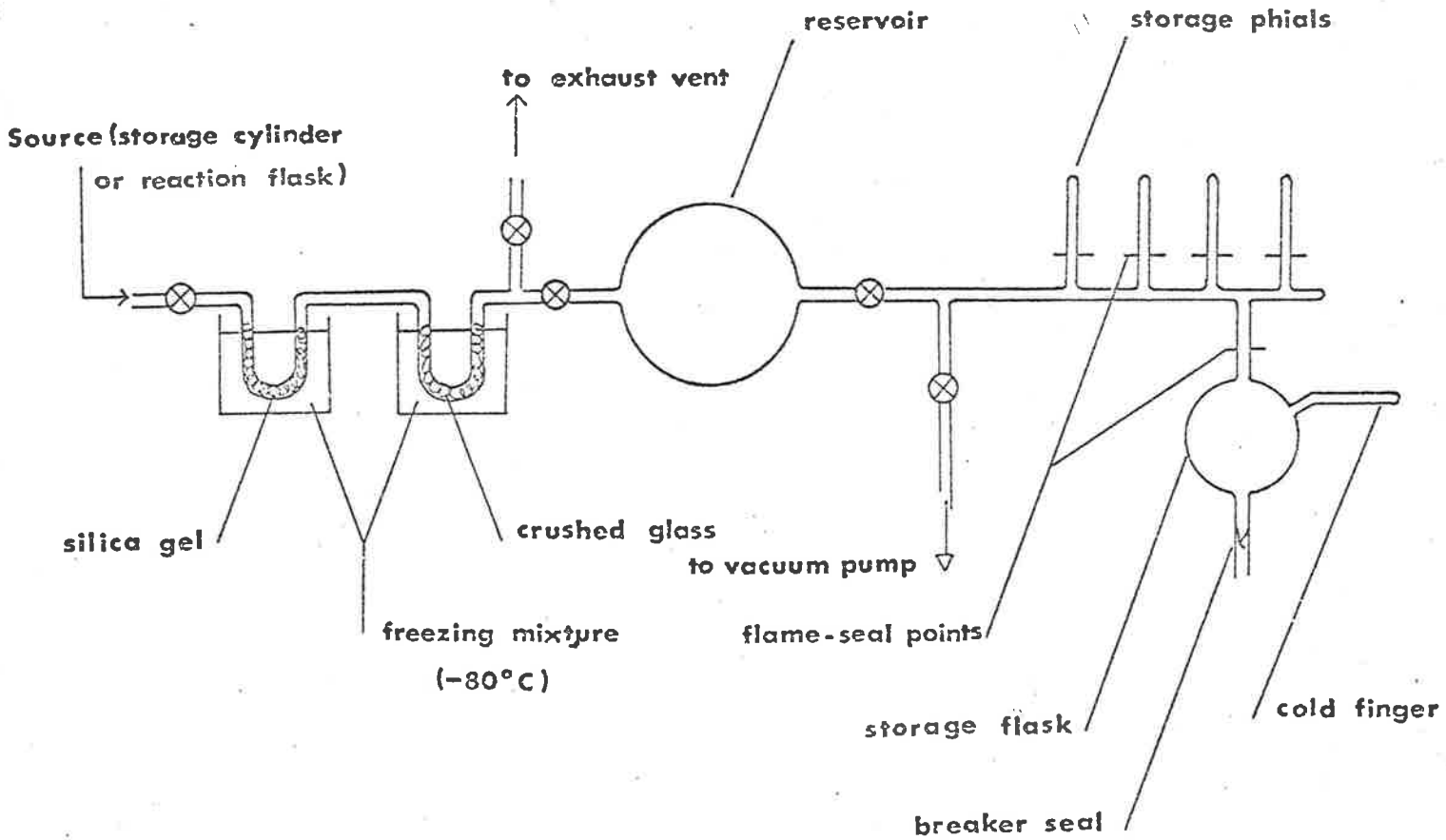

FIGURE 3.4 GAS PURIFICATION SYSTEM (NITRIC OXIDE)

5 ml of liquid. The air in the phial was pumped away by the rotary pump. Under near vacuum conditions in the filling system, triethylamine liquid would be boiling, filling the parts of the system with its vapours. These vapours were pumped out of the system with the phial disconnected by a valve from the main system. This was repeated about 3 times before finally filling up the chambers with this gas. A similar method was used for the NO gas before the final introduction into the chambers to remove any contaminants from the system and to allow for surface absorption.

The sensitivity of each chamber was monitored during gas admission, with a d.c. discharge between tungsten electrodes in hydrogen at a pressure of 4 Torr as the source. D.C. excitation was used as it produced no interference in the measuring circuitary. The window of the lamp was placed in firm contact with the chamber window to minimise atmospheric absorption. Each chamber was operated at 50 volts and the output current was monitored as the gas was introduced. The pressure was chosen to give maximum output current and hence sensitivity. The most common pressures are listed in Table (3.2). If the sensitivity was satisfactory, the chamber was sealed off by a flame at the attached glass tube. The copper filling tube was then compressed in two places approximately 1 cm apart. A seal was then made between these compressions by cutting the filling tube with a pair of pincers. This formed a vacuum-tight cold weld provided the copper tubing had been well annealed. The seal was coated with epoxy resin to give it mechanical strength. Separate filling systems including the entire glass-ware were used for each gas to eliminate the risk of contamination by gas residues.

Some of the chambers were found to have rather short life and low detection efficiency. To detect the problem, a batch of chambers was manufactured using windows of premeasured transmission. The detection efficiencies were found to vary and in one case the efficiency was very small. This indicated that the problem was with the filling of gas.

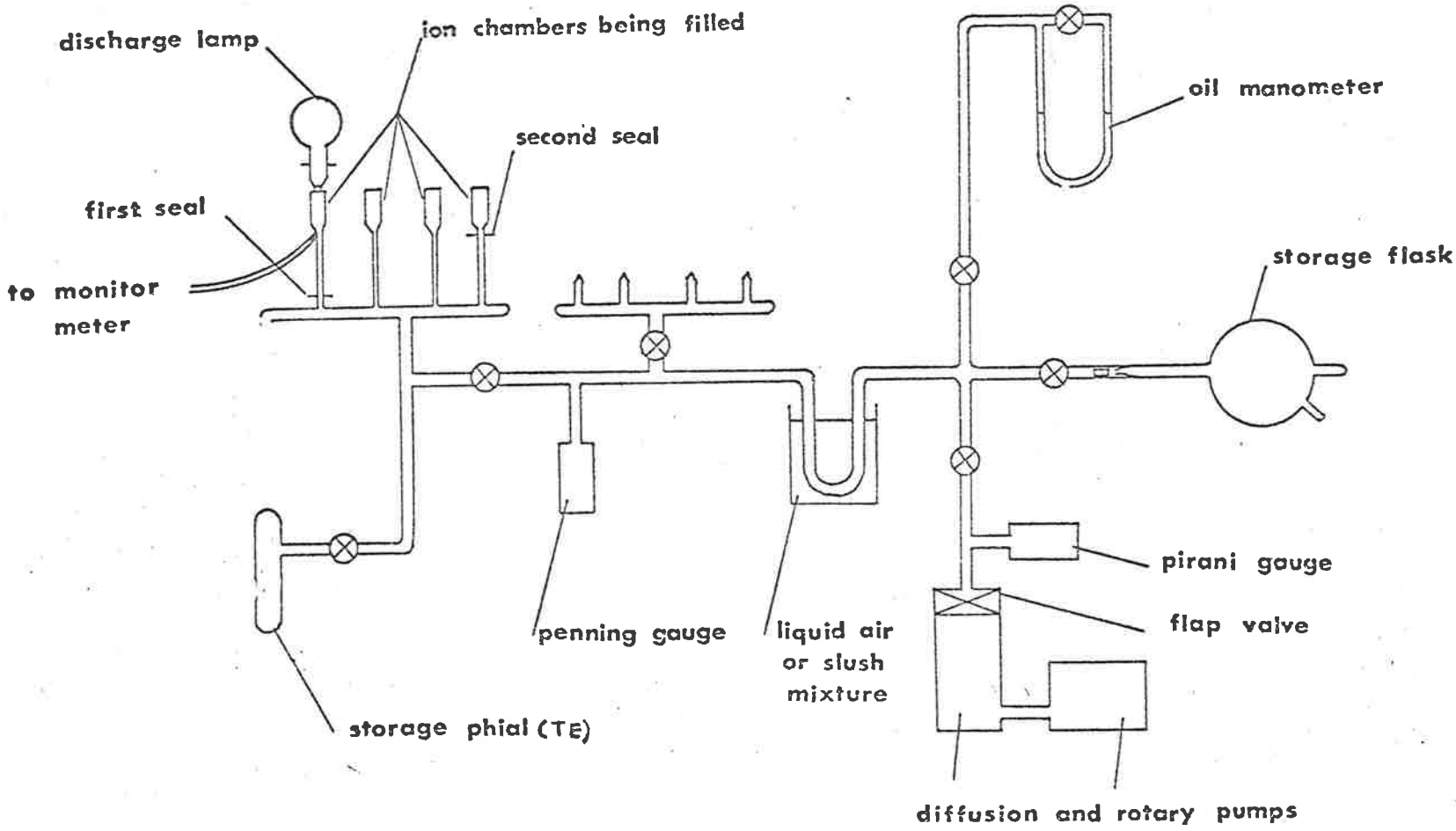

FIGURE 3.5 CHAMBER FILLING SYSTEM

TABLE 3.2

ION CHAMBERS

Window	Gas	Filling Pressure	Spectral Response	Abbreviation
Lithium fluoride	Nitric oxide (NO)	15-20mm of Hg	105-135 nm	LiF - NO (LNO)
Magnesium fluoride	Nitric oxide	15-20mm of Hg	114-135 nm	MgF_2 - NO (MNO)
Quartz	Triethylamine ($C_6H_{15}N$)	9.5 mm of Hg	155-169 nm	Q - T

Following this experiment a batch of ionchamber with filling tubes of larger diameter were manufactured. The efficiencies were found to be comparable and close to the values expected from the window transmission. These chambers (Figure 3.2) flown in later flights, have been found to be very stable in each case over a period of several months.

3.7 TESTING OF ION CHAMBERS

From the manufacture phase right through to the installation in the rocket payload, many tests and checks need to be made on the ion-chambers. These tests are required to ensure the optimum performance of the detectors under the experimental conditions of the atmosphere. Therefore tests were made of the overall performance of the detectors, their electrical characteristics and interference and their response to heating during the flight. These tests are described in the following subsections.

3.7.1 Electrical Properties

The construction had to be such as to allow the collection of small signal currents (down to $\sim 10^{-12}$ Amps for the quartz triethylamine chamber). All chambers had guard rings between the anode and the cathode. In the laboratory, it was observed that an e.m.f. could be generated between the anode and the guard ring if there was even a minute trace of contaminant on the glass surface. This problem was found to be particu-

larly serious in the case of Q - T chambers since the signals to be recorded are smaller by about an order of magntiude compared to a LiF-No. Ionchamber E.M.F.'s of up to 1/2 volt with a source impedance usually near 10^{11} ohms were observed. The polarity of this e.m.f. could be parallel to the applied voltage or against it depending on the contaminant. Even substantially smaller e.m.f. can introduce serious offsets into the amplifiers. Therefore care was taken to ensure that there was no significant e.m.f. developed between the guard ring and the anode of a chamber by ensuring cleanliness particularly in the vicinity of the anode. Measurements of leakage currents were made with Keithly Model 610 C electrometer with typical leakage currents of the order of 5×10^{-14} Amps. Shielding of the ionchamber signal leads was used to avoid electrical interference.

3.7.2 Water Vapour Contamination

Water vapour is the most troublesome contaminant in the chamber gases. Its effect is most critical in the nitric oxide chamber intended for measurements of Ly-α. Water vapour has a series of strong absorption bands in the wavelength range of these chambers as indicated in Figure (3.8). It can be seen from the same figure that the wavelength of Ly-α lies close to the centre of a strong water vapour absorption band (see Figure 2.12). Water penetrates the surface of metals (and glass), and is very difficult to remove completely. Outgassing from the chamber walls is accelerated by heating which may result in a rapid change in the quantum efficiency at Ly-α during a single observation as in case of a moisture film evaporating from the window. Since absorption of Ly-α photons by water vapour produces no ionization so an increase in the $[H_2O]:[NO]$ ratio reduces the quantum efficiency at Ly-α and renders the chamber virtually useless. As mentioned in Section (3.5), the necessary precautions to avoid water vapour contamination were taken during the filling and the storage procedures.

The presence of water vapour in the NO gas is easily identified from the spectral response curve of the chamber, an example of which can be seen in Figure (3.6). A measurement of the ratio of efficiencies at

121.6 nm and 123 nm can be used as a quick check of the amount of water vapour absorption.

3.7.3 Temperature effects

The ionchambers used in rocket vehicles are subjected to a wide range of temperatures. Carver and Mitchell (1967) investigated the effects of temperature variations from 15° C to 100° C on the sensitivities of a number of ionchambers including the LiF-NO and Q - T ionchambers. An increase in temperature was found to result in a shift of cut-offs at both ends of the spectral response to longer wavelengths. The shift in the short wavelength limit due to variations in the window transmission has been found to be linear with temperature with typical values for rate of variations as 0.22 nm/° C and 0.016 nm/° C for LiF and Quartz windows respectively (Carver and Mitchell, 1967). These results show the rates of variation of long wavelength sensitivity to be relatively small.

Therefore, the overall sensitivity changes of the presently used ionchambers would be small. Furthermore, since the central part of the spectral response of a wide band ionchamber such as LiF-NO remains practically unchanged, the temperature effect on Ly-α measurements would be negligible in this respect.

3.7.4 Photo-electric response to Longer Wavelength Radiation

The cathode of an ionchamber should give negligible photo-electric emission during its operation. This will ensure that the spectral response of the chamber has a sharp long wavelength cut-off. This is usually so as the filling gas absorbs strongly at wavelengths greater than its photo-ionization threshold wavelength. Therefore, as the photo-electric yield of metal surfaces decreases rapidly with increasing wavelength, the radiation most efficient at producing photo-electrons is absorbed before it can reach the exposed surfaces. In addition to the immediate longer wavelengths, ionchambers should also be able to operate in large fluxes of middle ultra-violet (200-300 nm) radiation without producing a significant corresponding out-put current. All the chambers used in the present work were operated

with the chamber walls as the anode. Therefore, the centre electrode and back seal were the only possible emitters of photo-electrons. No significant photo-electric response was recorded during any of the rocket flights.

3.7.5 Intense UV Irradiation Effect

One of the problems in the use of ionchambers for detection of solar UV radiation arises from the fact that these detectors are also exposed to the other UV radiation. Because of this, Carver and Mitchell (1967) investigated the effects of intense UV irradiation for a number of ionchambers. LiF-NO ionchamber was found to be unaffected after exposing it for 10 minutes while a Q - T chamber did show gradual deterioration in sensitivity amounting to about 8 percent after 10 minutes exposure. During the rocket flights in the present work, these chambers were never exposed for more than 2 minutes ensuring that any sensitivity change due to this effect would be negligible. As a precaution unnecessary and excessive irradiation was avoided during routine sensitivity tests prior to flight. It could be pointed out that the hydrogen discharge lamp used for the routine sensitivity checks is much less intense than the sun above 150 nm.

3.7.6 Vibration

Leads between detectors and the electronics were reduced to smallest possible length and provided with a secure support in the instrumentation structure. Since these detectors are operative well after the motor burnt out during the rocket flight, vibration effects were found to be negligible.

3.8 ABSOLUTE CALIBRATION OF THE IONCHAMBERS

3.8.1 Introduction

Ionchambers were calibrated by measuring their quantum efficiency as a function of wavelength. As mentioned earlier, all chambers used in this work were run at unity gas gain. The quantum efficiency of an ionchamber, at a given wavelength, is defined as the number of ions collected at the cathode, divided by the number of photons of that wavelength incident on the wondow. Figure (3.6) shows typical gas gain curves for both, positive

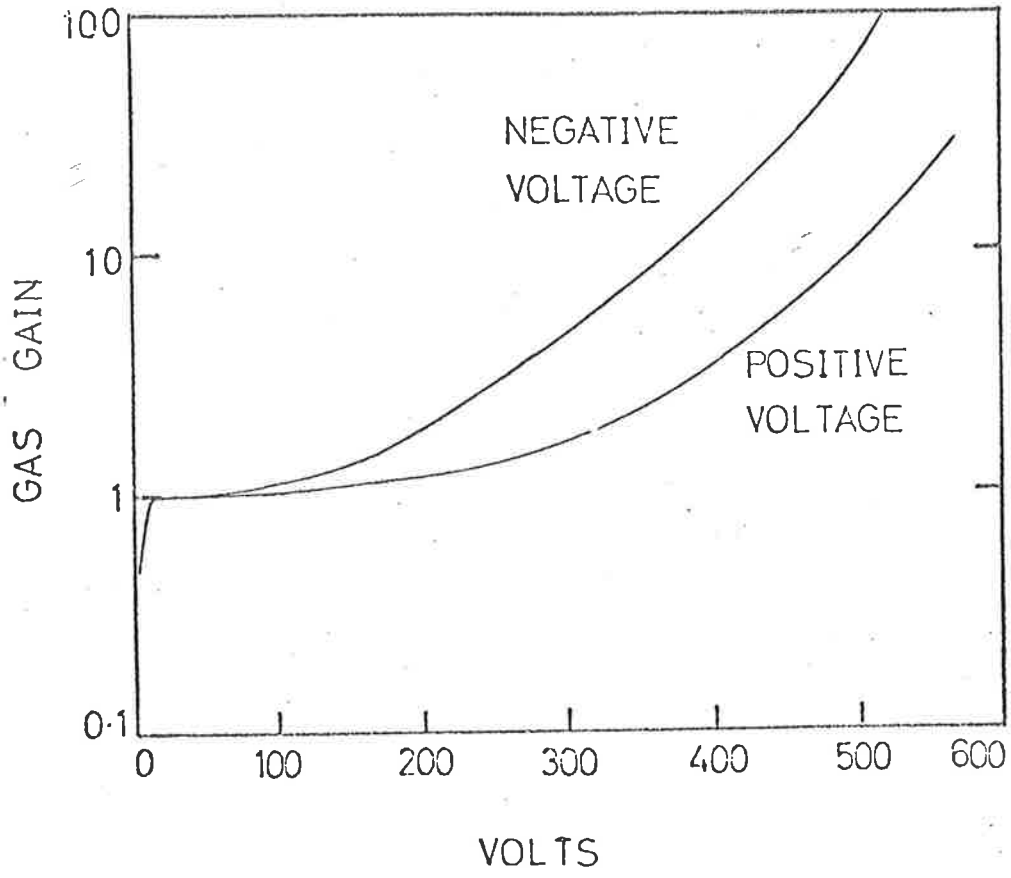

Figure 3.6 Typical ion chamber gas-gain curves for negative and positive voltage applied to the chamber body.

and negative voltages applied to the chamber body. A positive voltage in the plateau region of about 45 volt was applied to the case.

The dispersed ultraviolet radiation used for the calibrations was obtained from a half-metre McPherson vacuum monochromator (Model 235) with a discharge through a continuous flowing stream of hydrogen as the source. The lamp radiation was pumped through the entrance slit of the monochromator. A grating with 1200 lines mm^{-1} gave a dispersion of 600 μ nm^{-1} at the exit slit. The exit slit was set to give a required resolution (Section 3.8.2). The intensity of the monochromator beam was monitored by means of a photomultiplier that viewed the fluorescent radiation from a sodium-salicylate-coated wire grid placed in the beam (Ditchburn 1962). The photomultiplier current was taken to be proportional to the beam intensity within the bandwidth of either type of ionchamber (i.e. LiF-NO ionchamber and Q - T ionchamber).

3.8.2 Spectral Response

Experimental arrangement for determining the shape of the spectral response of an ionchamber is shown in Figure (3.7). Radiation from the exit slit of the monochromator passed through the salicylate-coated grid and entered the ionchamber which was electrically insulated from the monochromator. A voltage of + 45 V was applied to the ionchamber body so that the chamber operated at unity gain. The fluorescent radiation from the sodium salicylate was transmitted to a photomultiplier (EMI 95145) by a polished perspex light pipe. Relatively fresh coatings, obtained as described in Section (8.3.3), were used.

The currents from the ionchamber and photomultiplier were monitored on Keithley micro-micrometers (Model 610) and the ratios of these currents, as a function of wavelength, gave the shape of the spectral response curve independent of the lamp spectrum. An absolute efficiency scale was then derived for this curve as described in Section (3.8.3). The width of the exit slit was set to give a resolution of 0.5 nm for Ly-α ionchambers (LiF-NO and MgF_2-NO) and 0.2 nm for Q-T ionchambers. The

Figure 3.7 The ½M monochromator and aparatus used for calibrations of ionchambers.

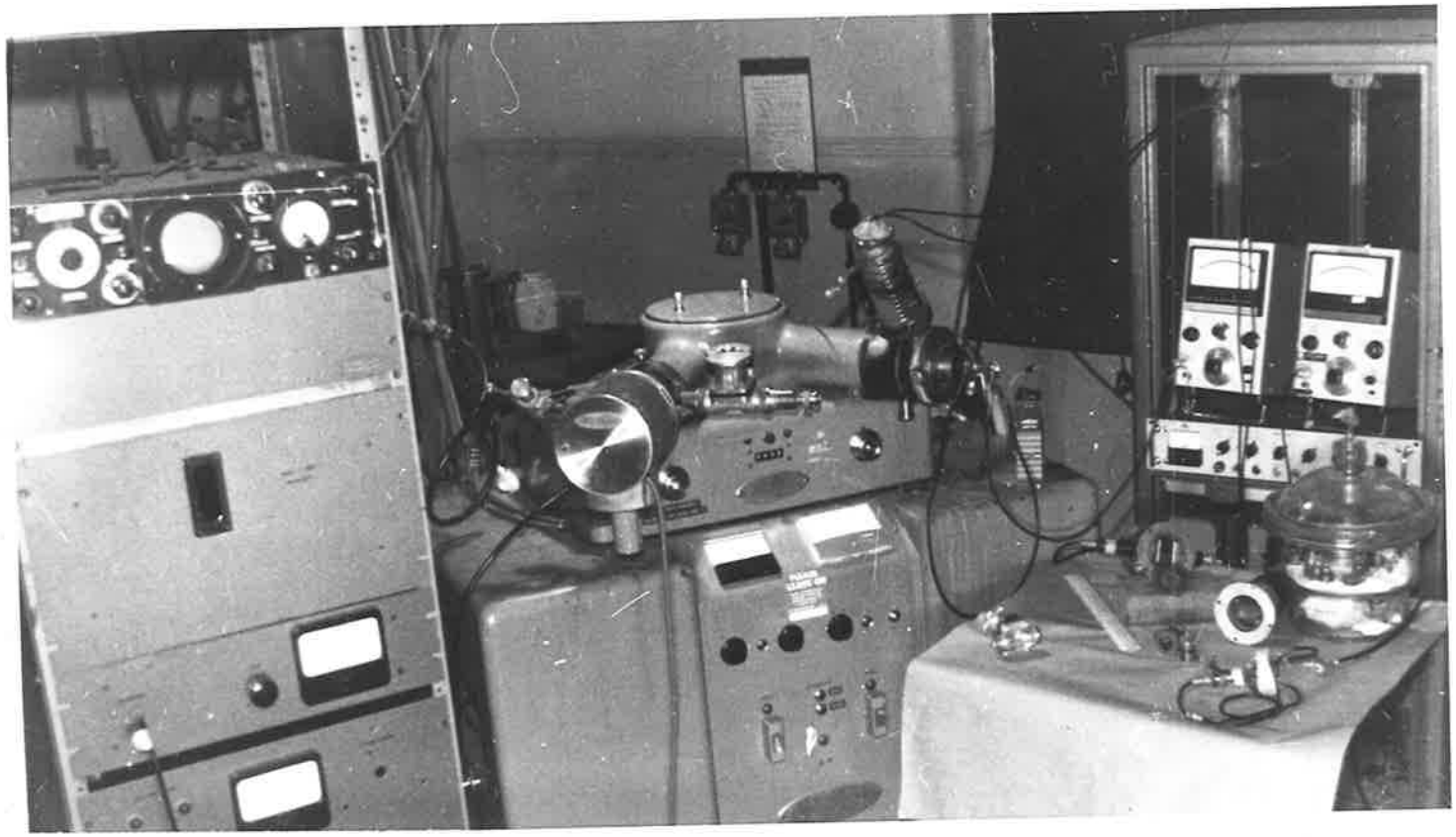

quantum efficiency of sodium salicylate was assumed to remain constant over the wavelength range 100 nm to 170 nm (Section 8.5).

In Figure (3.8) are shown typical spectral response curves for Ly-α ionchambers. All the four curves have been normalized by different normalixing factors to bring them on a similar scale. The curve (a) is for a LiF-NO ionchamber with a prebaked window as described in Section (3.4). Curve (b) is the spectral response of a LiF-NO ionchamber contaminated by water vapour. The remaining two curves are the spectral responses of MgF_2-NO ionchambers, one of which is relatively contaminated. Water vapour contamination is thought to be due to outgassing of water vapour from the walls and unbaked LiF windows in case (b) (Section 3.5). The effect of water vapour contamination in derived oxygen densities and Ly-α fluxes has already been discussed in Section (2.4).

A typical spectral response curve for a Q-T ionchamber is shown in Figure (3.9).

3.8.3 Absolute Quantum Efficiency

(a) The Standard Parallel Plate Ionchamber

The quantum efficiency of a Ly-α ionchamber (LiF-NO or MgF_2-NO) was calculated by comparing its ioncurrent with that from a standard ionchamber subjected to the same beam of radiation from the monochromator. The quantum efficiency of any other ionchamber was obtained by comparison with the calibrated one.

The standard parallel-plate ionchamber (Figure 3.10) was of the single parallel plate type with a sodium salicylate-photomultiplier combination as the detector of transmitted radiation. A LiF window was attached to the exit slit of the monochromator so that NO used in the standard ionchamber may be contained within the standard ionchamber. A brass plate was attached to the entrance end of the standard ionchamber but insulated from the ionchamber casing. This plate was electrically connected

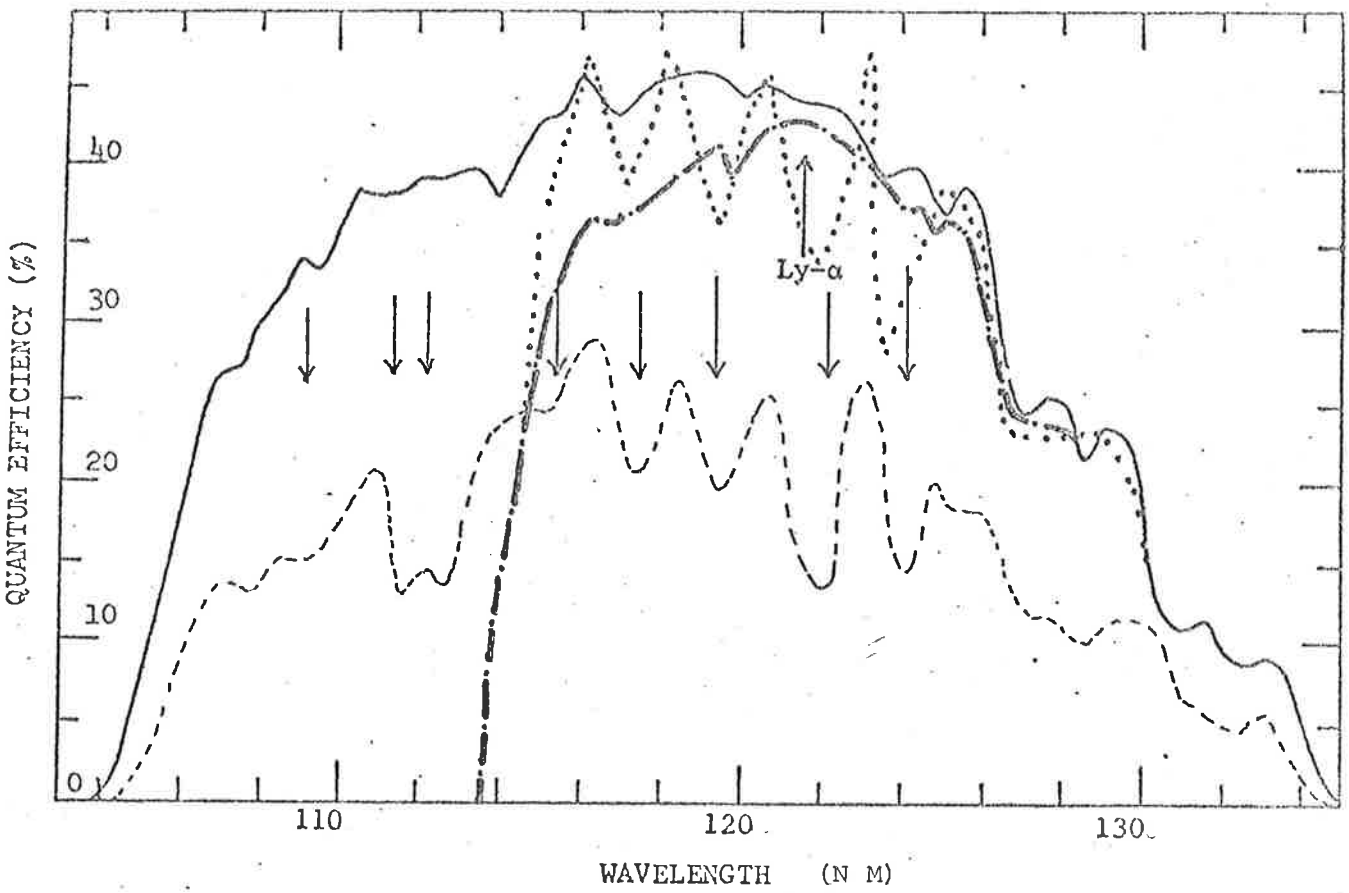

Figure 3.8 Spectral response curves of contaminated as well as uncontaminated Ly-α ionchambers. The peaks of the strongest bands in the water vapour absorption spectrum are indicated by small arrows.

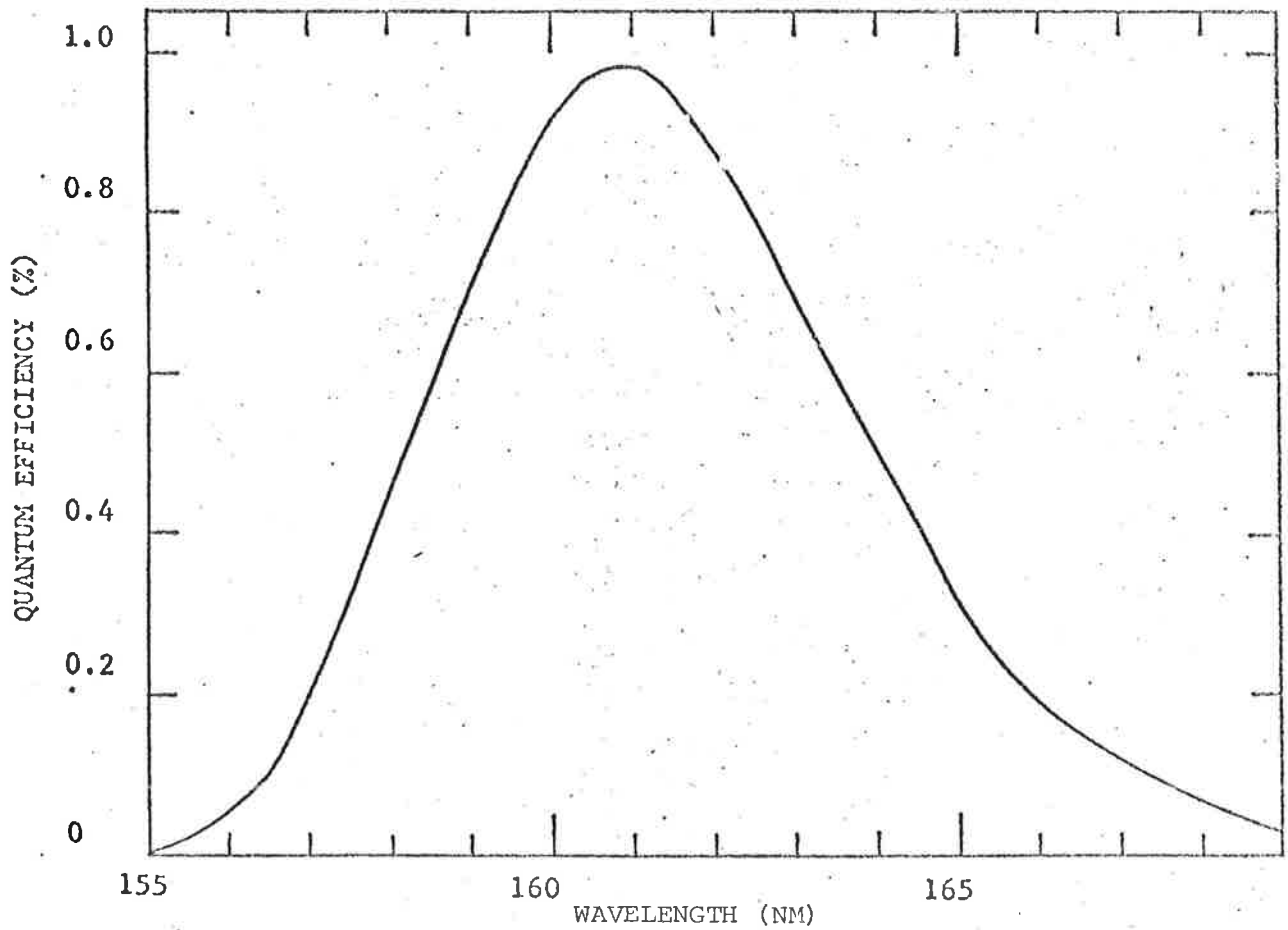

Figure 3.9 Spectral response curve for Q - T ionchamber.

to the positive plate (-45 V) of the standard ionchamber in order to provide an adequate collecting field for ions formed close to the window. The standard ionchamber was evacuated for more than 24 hours by a rotary-diffusion pump combination during which it was heated by a heat gun to ensure complete outgassing from the inside walls. Then NO gas was introduced through one of the inlets. Measurements were made of the ionization current and the transmitted light signal over a range of gas pressures. When these were plotted against one another, the extrapolation to the axis, corresponding to total absorption in the gas, gave the ioncurrent due to complete absorption without recombination (Figure 3.11). The calibrations were done at Ly-α and the ionization efficiency of Ly-α for NO was assumed to be 81% (Watanabe et al, 1967). Suppose I_S and I_{SPM} are the readings for extrapolated standard ionchamber current and side photomultiplier monitoring the beam intensity. Then the standard ionchamber is replaced by a Ly-α ionchamber. Suppose the signal at Ly-α from this chamber is i_L and the side photomultiplier reading is I'_{SPM} (usually $I'_{SPM} \simeq I_{SPM}$ if lamp intensity is stable). The quantum efficiency of the Ly-α ionchamber, Q_L, is then given by:

$$Q_L = \frac{(i_L / I'_{SPM})}{(I_S / I_{SPM})} \cdot 81\ \%$$

Other Ly-α ionchambers can be absolutely calibrated by comparison with this chamber.

The Q-T ionchambers were then calibrated using a calibrated Ly-α ionchamber. Suppose signals from a Q-T ionchamber and the side photomultiplier for a wavelength, λ (within the sensitive range of the detector - usually around 160 nm) are i_λ and I_λ respectively. If the signals from a Ly-α ionchamber and the side photomultiplier at Ly-α are i_L and I_L then the quantum efficiency of the Q-T ionchamber at wavelength λ is given by:

$$Q_\lambda = Q_L \cdot \left(\frac{i_\lambda}{I_\lambda}\right) \cdot \left(\frac{I_L}{i_L}\right) \cdot C_{\lambda_L}$$

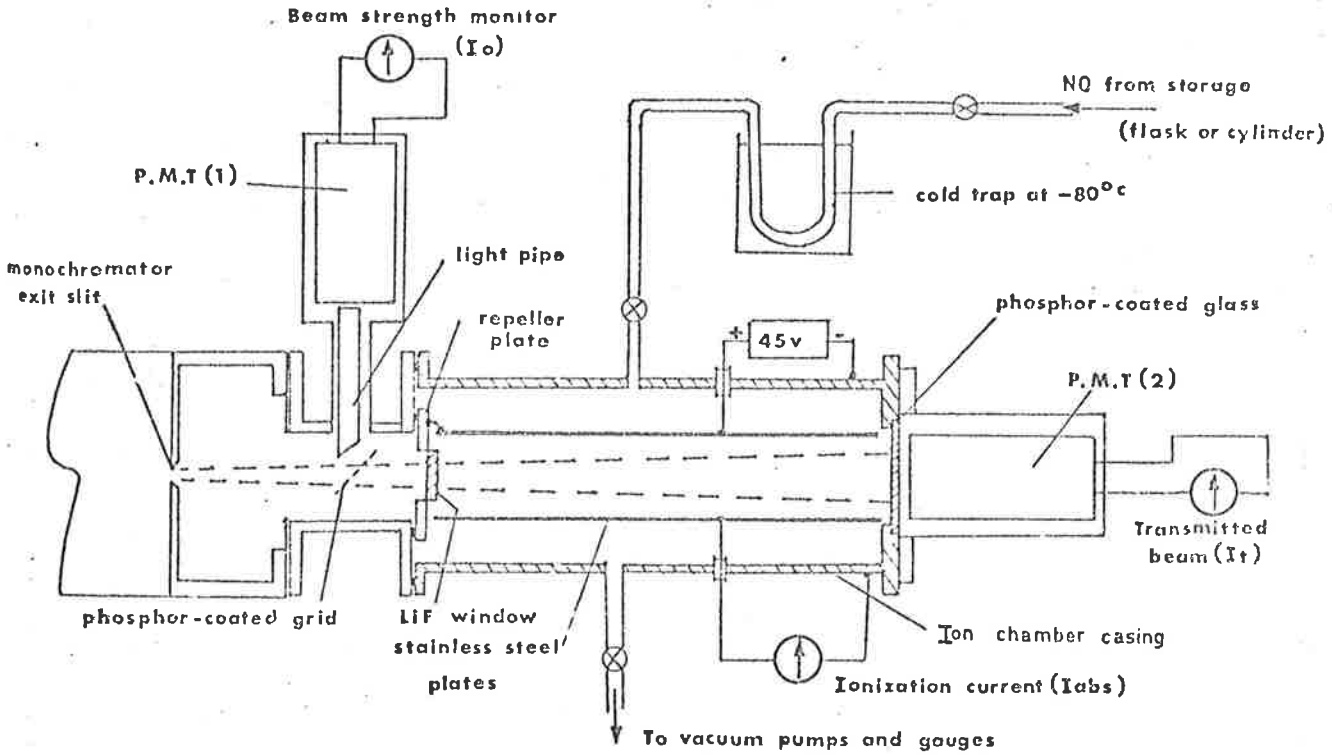

FIGURE 3.10 THE STANDARD ION CHAMBER CALIBRATION SYSTEM

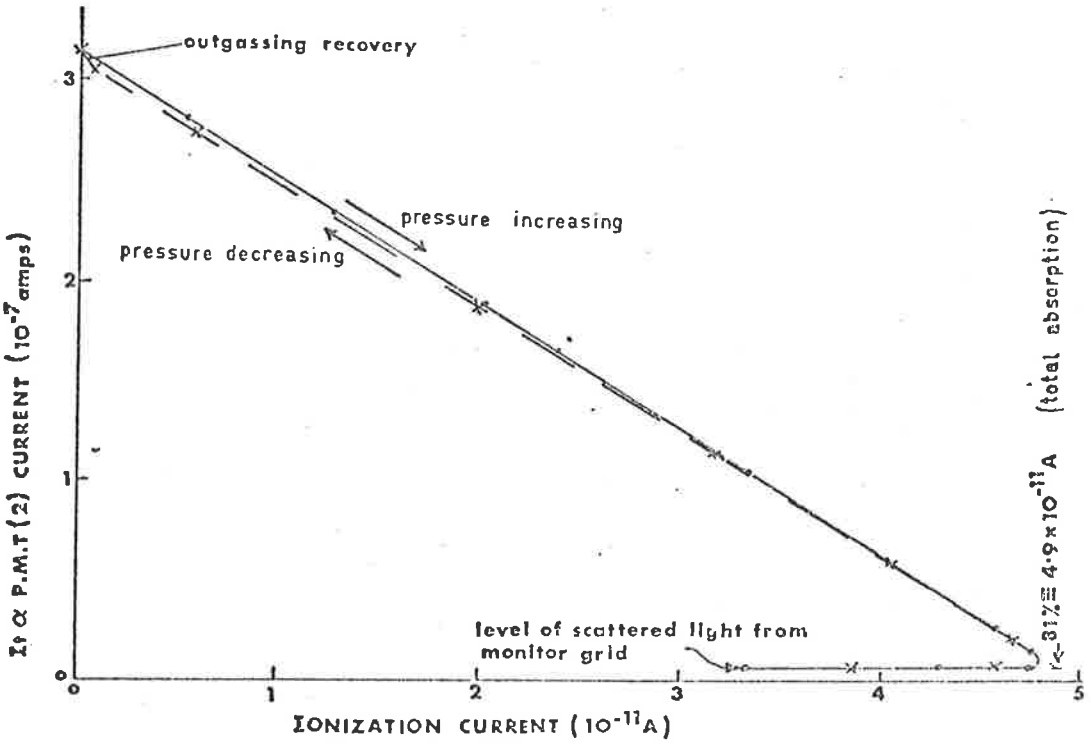

FIGURE 3.11 A CALIBRATION CURVE FOR THE STANDARD ION CHAMBER

where Q_L is the quantum efficiency of the Ly-α chamber at Ly-α and $C_{\lambda L}$ is quantum efficiency of sodium salicylate at wavelength λ relative to its quantum efficiency at Ly-α. This factor can be taken as unity for wavelengths below about 170 nm (Section 8.5) which greatly simplified the calibrations.

(b) Standard Reference Photodiode

Towards the end of this work a calibrated Far UV photodiode was obtained (Section 8.3.2). The chambers could be calibrated easily by direct comparison. The absolute efficiency curve for this detector is shown in Figure (8.2). The calibration of this detector at Ly-α was checked using the Standard Parallel Plate ionchamber and was found to be in agreement. It was used for calibrations of ionchambers in the last pair of flights.

3.8.4 Angular Response

When ionchambers are used in sounding rockets to measure the intensity of solar radiation, some corrections are needed for the output signal of the chamber due to aspect angle variations (Section 4.1). Therefore a laboratory calibration of angular response was obtained. The ionchamber was mounted in a chamber on the end of a rotatable shaft that passed through an O-ring seal in the top of the chamber. The lamp was a portable hydrogen discharge lamp with a lithium fluoride window. A glass tube, about 100 cm long, mounted into the side of the chamber was used to provide a vacuum-tight connection between the chamber and the lamp. A series of baffles inside the tube helped in preventing reflections from the walls of the tube and ensured that the beam reaching the ionchamber was parallel. The chamber and the connecting glass tube were evacuated and the signal from the ionchamber was monitored as the ionchamber was rotated in the beam. In several rocket flights, it was possible to obtain an inflight calibration of one or more ionchambers when the ionchamber aspect was zero. The laboratory curve as well as the in-flight curves were found to be well represented by the function $\cos^2\theta$ for angles, θ, less than about 35°.

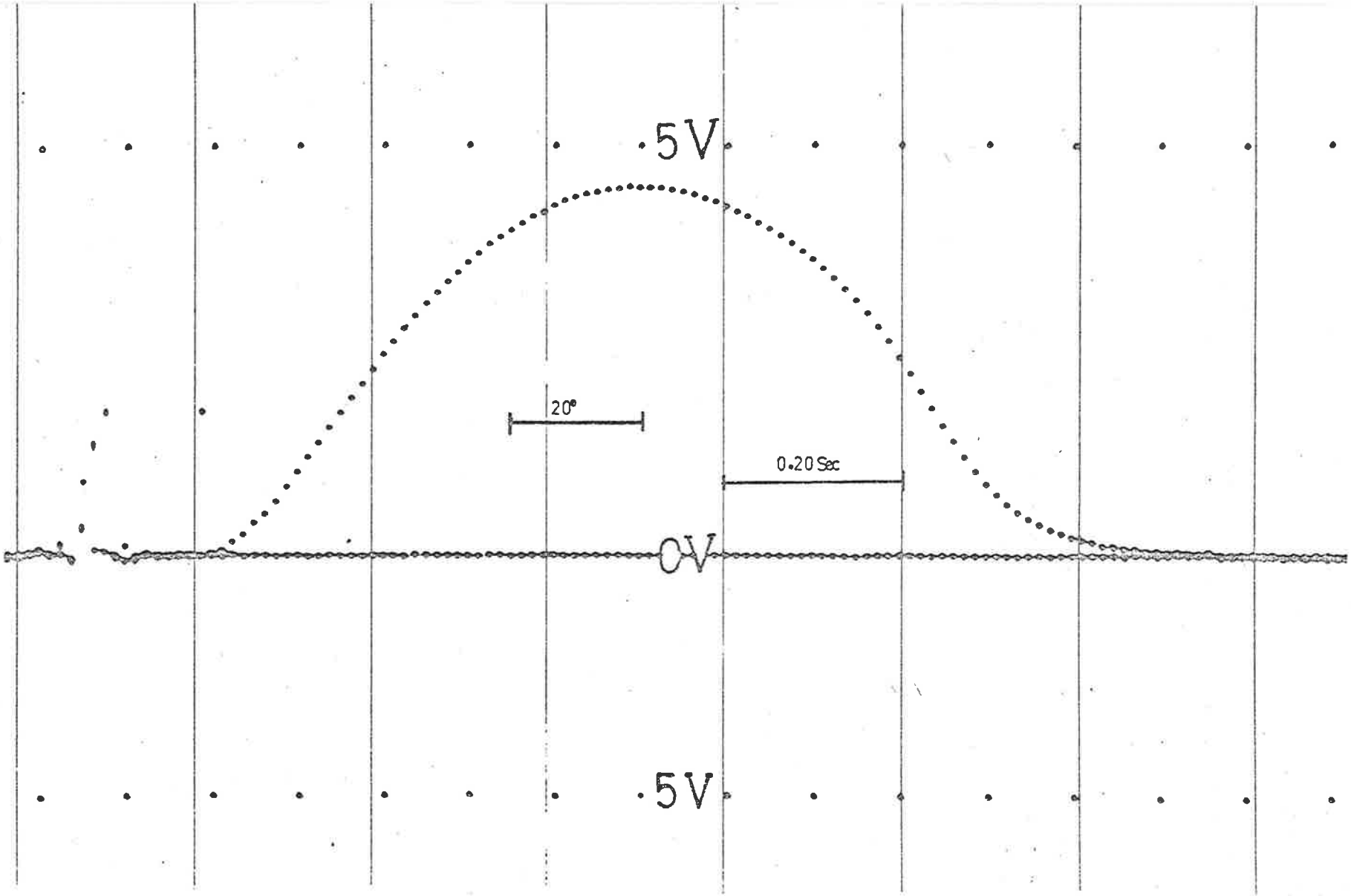

Figure 3.12(a) The signal variation of an ionchamber during a flight due to rocket spin as shown by the film records. As the rocket aspect angle was zero for this particular spin, the response represents an in-flight angular response. The vertical lines indicate a flight-time advancement by 0.2 sec which would be easily converted to angular rotation. Similar in-flight angular responses in several flights were obtained and were found to be consistent.

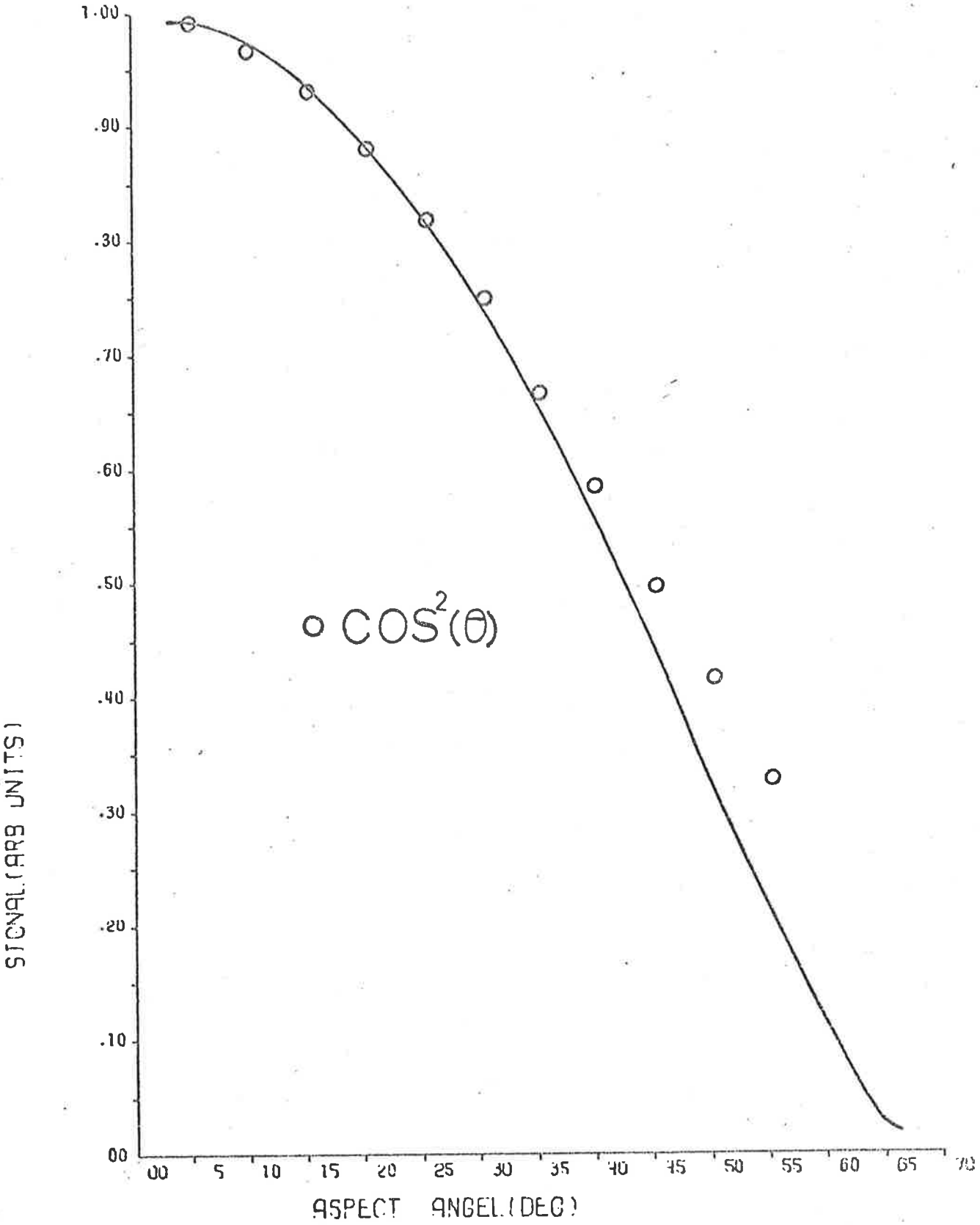

Figure 3.12(b) A typical angular response curve for an ionchamber.

3.9 SUMMARY

Several types of ionization chambers have been constructed for use in sounding rockets. The important advantages these detectors have are, their manufacturing simplicity, compactness and high efficiency. The chambers have been markedly improved for their stability and life time.

CHAPTER 4

ROCKET ASPECT SENSORS

The problem of rocket aspect sensing is discussed. Description is given of simple techniques of aspect sensing and several types of detectors used for aspect sensing are described. Two new aspect sensors developed and used in the present work are described in detail.

4.1 INTRODUCTION

A number of rocket experiments require additional information about the orientation coordinates of the rocket as a function of flight time. For a relatively large rocket this information can be obtained by such techniques as (i) photography of the rocket throughout flight by tracking telescopes (ii) use of gyroscopes in the rocket payload (iii) use of photographic camera in recoverable payloads to provide inflight photographs of a bright object say the Sun and earth's horizon. A description of these techniques is given in Van Allen (1952), Newell (1953) and others. Simpler and more reliable system compared to these types would be an optical aspect system described by Kupperian and Kreplin (1957). It makes use of a pair of photoelectric detectors with narrow and wide field of views and high and low sensitivity respectively. A set of orthogonally oriented magnetometers have also been used to determine the rocket orientation with respect to the magnetic field which can be related to the payload orientation relative to some other object such as the sun or the moon. Inclusion of an optical aspect sensor has been found very helpful in data reduction (Thomas and Davison, 1972; O'Connor, 1973).

However, a number of scientific experiments are of such a nature that the complete information about the rocket orientation is not required. In these experiments - such as absorption spectroscopy of solar or lunar radiation - one needs only the half angle of the cone about the detector-source axis on whose surface lies the axis of interest. Commonly detectors

are mounted perpendicular to the rocket axis, and it is the angle between the detector-source direction and the maximum sensitivity axis of the detector or detector normal axis in which we are interested. We shall call this angle, the aspect angle and the sensors used for this purpose aspect sensors.

The ionchamber or photometer response varies with the aspect angle and knowledge of this relationship (the angular response) can be obtained either in the laboratory or, under favourable circumstances, deduced from flight data. Along with the inflight aspect angles this information provides the necessary corrections to be applied to the flight data before it can be used to deduce the vertical distribution of a particular species.

Usually, the roll rate is greater than the rate at which the roll axis changes its orientation in space. Therefore, an ionchamber or photometer will show one peak in its output for each roll of the rocket. The peak value occurs when the source (sun or moon) aspect angle is a minimum for each roll. It is just this angle, termed the detector aspect angle, α, which must be measured if the data reduction is to be done only at flight times of peaks in the photometer signal. By restricting analysis to peak signals, data reduction is greatly simplified without any significant data loss if the roll rate is not too slow.

Although very sophisticated systems (both in instrumentation as well as in accuracy) are commercially available, the costs involved are large (in comparison to other instrumental costs), at least for the geophysical sounding rockets such as Cockatoo. Besides, the accuracy provided by the more sophisticated aspect systems is quite often not required. Therefore, it is of prime importance to provide an aspect sensor system which is relatively inexpensive but adequately reliable and tolerably accurate for the data reduction. Several types of aspect sensors were employed during the course of this work to suit the anticipated rocket behaviour and other instrumentation requirements. The two basic techniques of aspect sensing, the basis of the sensors, are briefly described in the following section. Specific details of each aspect sensor employed are given afterwards.

4.2 TWO BASIC TECHNIQUES OF ASPECT SENSING

The two basic techniques of aspect sensing are (a) time modulation and (b) amplitude modulation. A brief description of each follows.

4.2.1 Aspect Sensing Using Time Modulation

In this technique an optical detector is employed in such a way that it responds only when the optical source (in most cases the sun or moon) crosses one of several planes fixed relative to the rocket body as the rocket spins. The aspect information is derived from the spacing in time of the pulses so produced. These sensors rely on a suitable roll rate to produce the pulses and are of little use if the motion of the rocket is slow or irregular.

On the other hand a roll rate which is too fast will be unsuitable when using a telemetry system such as the one used in the Cockatoo rockets where each channel is sampled 160 times per sec. The advantage of this type of sensor over those using amplitude modulation (Section 4.2.2) is, that variations either in the intensity of the light to which it is responding or in the sensitivity of the sensor by the same amount do not affect the accuracy. Obviously the background radiation or earthshine has no effect on the accuracy.

These sensors are commonly known as "slits" (sunslits or moon-slits as the case may be) since the radiation sensor is situated behind a set of slits cut or produced by some other technique in a flat or non-flat surface. An earlier use of this type of sensors was made on a Skylark rocket and has been described by Gross and Heddle (1964). This employed two slits cut in a flat surface behind which a detector viewed the source as it scanned across the slits. Several versions of this system have been used (O'Brian, 1973; McKinnon and Smith, 1964). A modified version of this as used in Cockatoo vehicles is described in Section (4.3).

4.2.2 Aspect Sensing Using Amplitude Modulation

A sensor of this type relies on the principle that the output from the detector varies with the angle of the radiation falling on the detector to which it responds. The variation in signal is due to variation of the effective area of the detector with varying angles of radiation incident. A typical detector of this type consists of a photocell sensitive to visible light mounted behind a filter glass window.

The main problem with an aspect sensor of this type is that the light to which it is responding may be attenuated in passing down through the atmosphere owing to Rayleigh scattering (increasing as the wavelength decreases) and absorption by ozone and water vapour. However, the scattering and absorption will take place mainly in the lower, more dense atmosphere, so that in the region perhaps above about 40 km but certainly above 65 km where O_2 measurements are made the intensity of the visible and near infrared radiation will be constant. Thus if the aspect angle can be determined at one particular time while the rocket is above the absorbing region, this information enables the level of the laboratory calibration curve to be adjusted so that the aspect angles can be determined at other times. The extra information may be obtained, for example from the sunslit sensor if the roll rate is adequate (flights C1029 and C4006). However, the information required to adjust the level of the calibration curve may not be available, particularly if the motion of the rocket is irregular or the spin rate is too high. To overcome this difficulty Mitchell (1966) designed a double amplitude-modulation sensor employing a pair of two sensors which had the same spectral responses but different angular responses. The angular responses can be so chosen that the ratio of the two responses is a unique function of the aspect angle. Since both sensors respond to the same radiation the ratio will also be independent of the intensity. A modified version of this system was used in the earlier part of this work and is described in the next section (Section 4.3).

4.3 ASPECT SENSORS USED IN THE SLOW SPINNING NON-STABILIZED ROCKET FLIGHTS

In the earlier part of this work rockets used were non-stabilized slow spinning (a typical spin of 0.5 rev/sec) vehicles. Two types of optical sensors were used to obtain aspect information. Also a set of fluxgate magnetometers were included in the payloads but little use of them was made in analysing the aspect information. The two optical sensors are described below.

4.3.1 Sunslits

As mentioned in Section (4.2) this type of detector responds only when the source crosses one of the several planes fixed relative to the rocket body and the aspect angle is deduced from the time interval between the pulses produced in this way. We shall refer to the detectors as "sunslits". The sunslits used in the Cockatoo rockets were a modification of the lunar slits described by Gross and Heddle (1964). In the present case the planes of response were defined by three slits, 0.3 mm wide, cut in an aluminium hemisphere (inset Fig 4.1). One plane contained the rocket roll axis while the other two made an angle of 45° with the roll axis (Figure 4.1). The three planes intersected along a line that was perpendicular to the rocket roll axis and passed through the centre of the detector. The light detector was a small silicon photovoltaic cell (Mullard type BPY 10) which was mounted behind a pinhole fixed at the centre of curvature of the aluminium hemisphere.

In Figure (4.1), which illustrates the operation of the sunslits, β represents the angle between the planes of the sunslits ($\beta = 45°$ in this case) and α in the rocket aspect angle. It is assumed that the ionchambers or at least one ionchamber is pointing in the same direction as the sunslits. If the rocket rolls through an angle γ, in the time interval between two pulses from the sunslits, then the angle α is given by

$$\tan \alpha = \sin \gamma \cot \beta = \sin \gamma$$

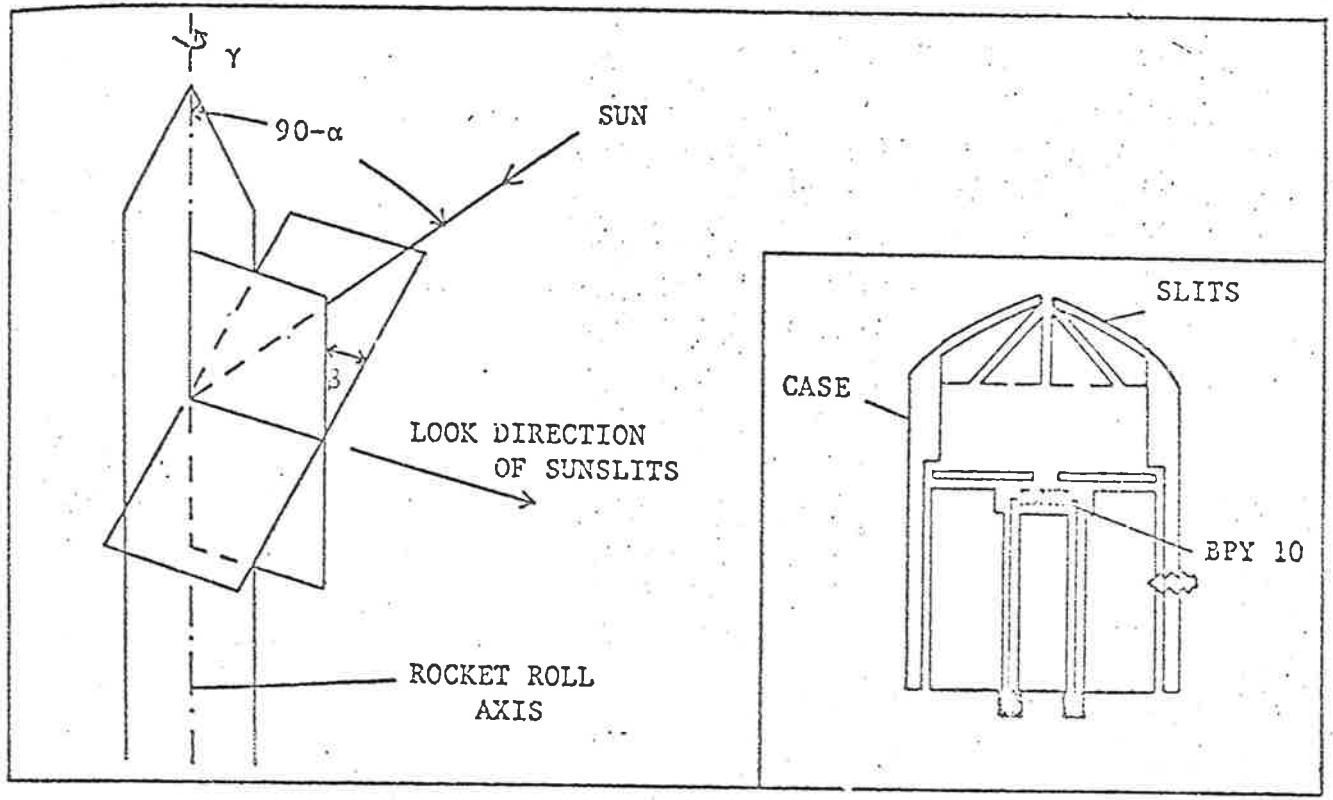

Fig. 4.1 Diagram illustrating the operation of the sunslits. The inset shows a cross-sectional diagram of a typical sensor.

Therefore, by measuring the roll rate and the time between successive pulses from the sulslits, γ and hence α can be determined. A number of sunslits were calibrated by rotating them in front of a mercury-iodide lamp placed behind an aperture. The distance between the aperture and the sunslits was adjusted so that the aperture subtended an angle at the sensor equal to the angular diameter of the sun. The above relationship was found to hold for aspect angles up to about 40°. At greater angles no signal was obtained through the 45° slits.

The above relationship is valid only if the roll axis of the rocket coincides with its longitudinal axis and the roll axis does not change its position in space significantly during the time interval between the pulses from the outer slits. The main advantage of using three slits over two (as originally used by Gross and Heddle, 1964) is that if the rocket behaves otherwise, it becomes obvious from the uneven spacings of the three pulses. Naturally this is a disadvantage with these detectors in that, under such non-uniform rocket behaviour, sunslits can become useless.

Also, if the rocket spin rate is too high, sunslits may become useless as indeed was the case for the later fast spinning rockets used in the present work. For example, if the telemetry sampling rate is about 160 samples/sec then for a roll rate of 4 cps, the error in determining the angular separation of the two 45° slits is $\simeq \pm 4.5^{\circ}$ (cf roll rate of C4007 ~ 7 cps). Except Cockatoo C1020, in all the other flights, two telemetry channels were allocated to each sunslits, thus doubling the effective smapling rate. Sunslits provided useful aspect data in several Cockatoo flights. Details of these are given in Chapter 5.

4.3.2 Amplitude Ratio Aspect Sensors

The other type of detector used was the double amplitude modulation sensor discussed in Section (4.2.2). Each of the two detectors employed a small vacuum phototube (RCA type IP42) surrounded by a teflon insert inside an aluminium holder (Figure 4.2). In principal teflon inserts of different

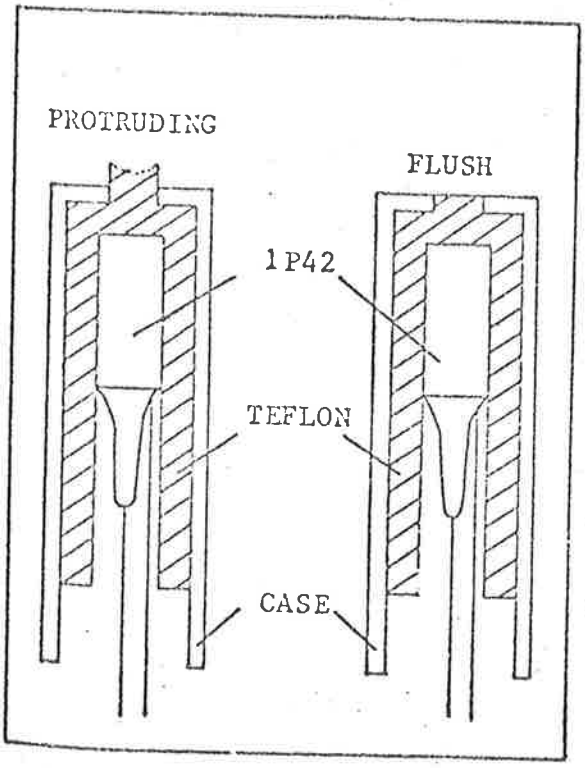

Figure 4.2(a) Cross-sectional diagram of an amplitude radio aspect sensor pair.

Figure 4.2(b) Views of components of aspect sensors (sunslits, amplitude ratio aspect sensors and IR aspect).

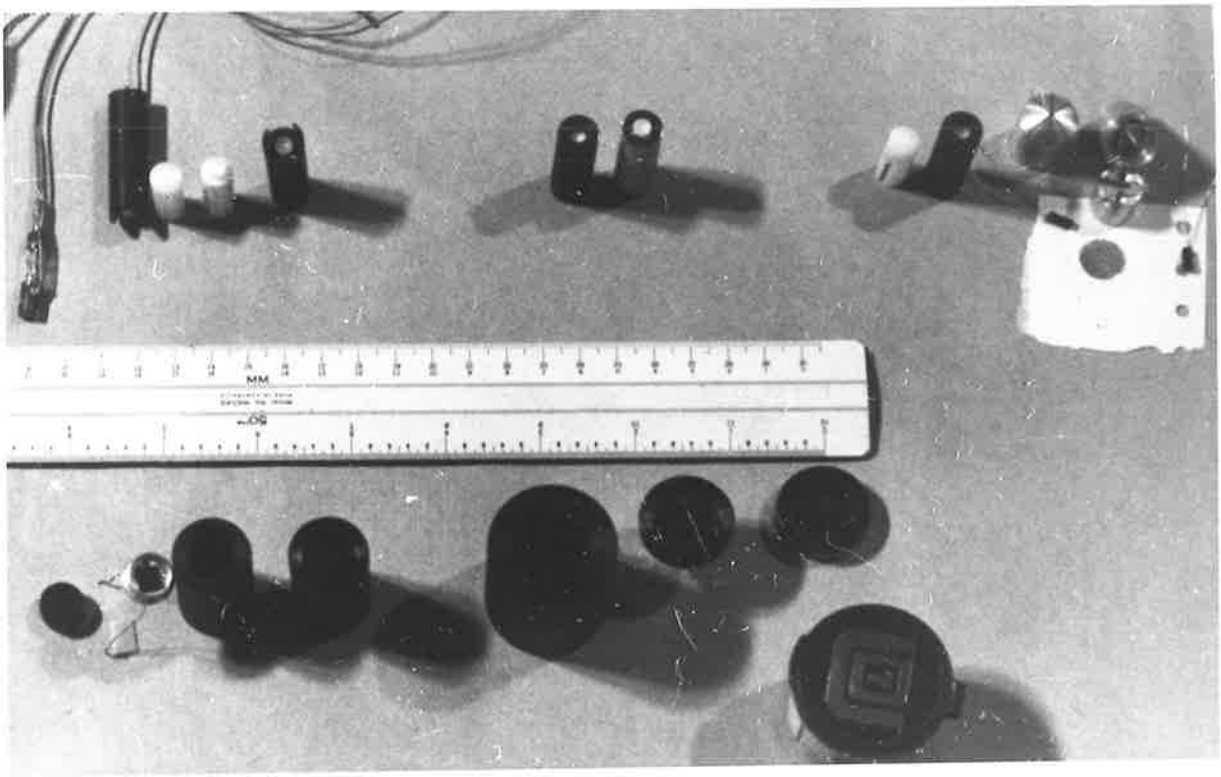
MM

sizes will provide two different angular responses as required. The simplest combination would be to use say one of the teflon (or any other diffuser) inserts as flush with the surface of the aluminium holder and the other protruded past the front face of the holder; the latter resulting in a relatively flatter response. However, extensive laboratory tests were performed to study the effect of the length of the protruded part on the resulting angular response. An optimum length size was determined which gave an almost flat response for ± 40° with slight variations from one piece to another due to machining. After the first of these pairs were flown in flight C1020, it was found that the total field of view of each sensor was too wide and unacceptable since two sensors in opposite sides of the payload (Figure 5.3) shared a single telemetry channel. As a result, zero levels of aspect sensors could not be identified accurately at all times and the useful aspect information could be obtained only at specific times (Section 5.6). Therefore, the field of view of the detectors was reduced. For the flush aspect sensor, it was done by simply withdrawing the teflon diffuser inside the aluminium holder which resulted in a sharper and narrower response. For the protruded sensor, the length of the protruded part was reduced and a cup of suitable radius r and dip h was drilled in the front face (Figure 4.2). This resulted in an angular response of ± 65° which was flat over ± 25°.

Pairs of aspect sensors with narrower field of view developed as discussed above were flown on three successive rockets and provided adequately the necessary aspect information which is discussed in Chapter 5 for individual flights.

For each rocket flight, the angular response of each detector to be flown was measured in the laboratory by rotating it infront of a laboratory lamp with a parallel beam of light. Initially an attempt was made to use a xenon lamp but generally the lamp showed intensity changes during calibration procedure. A special lamp was constructed for this purpose but was

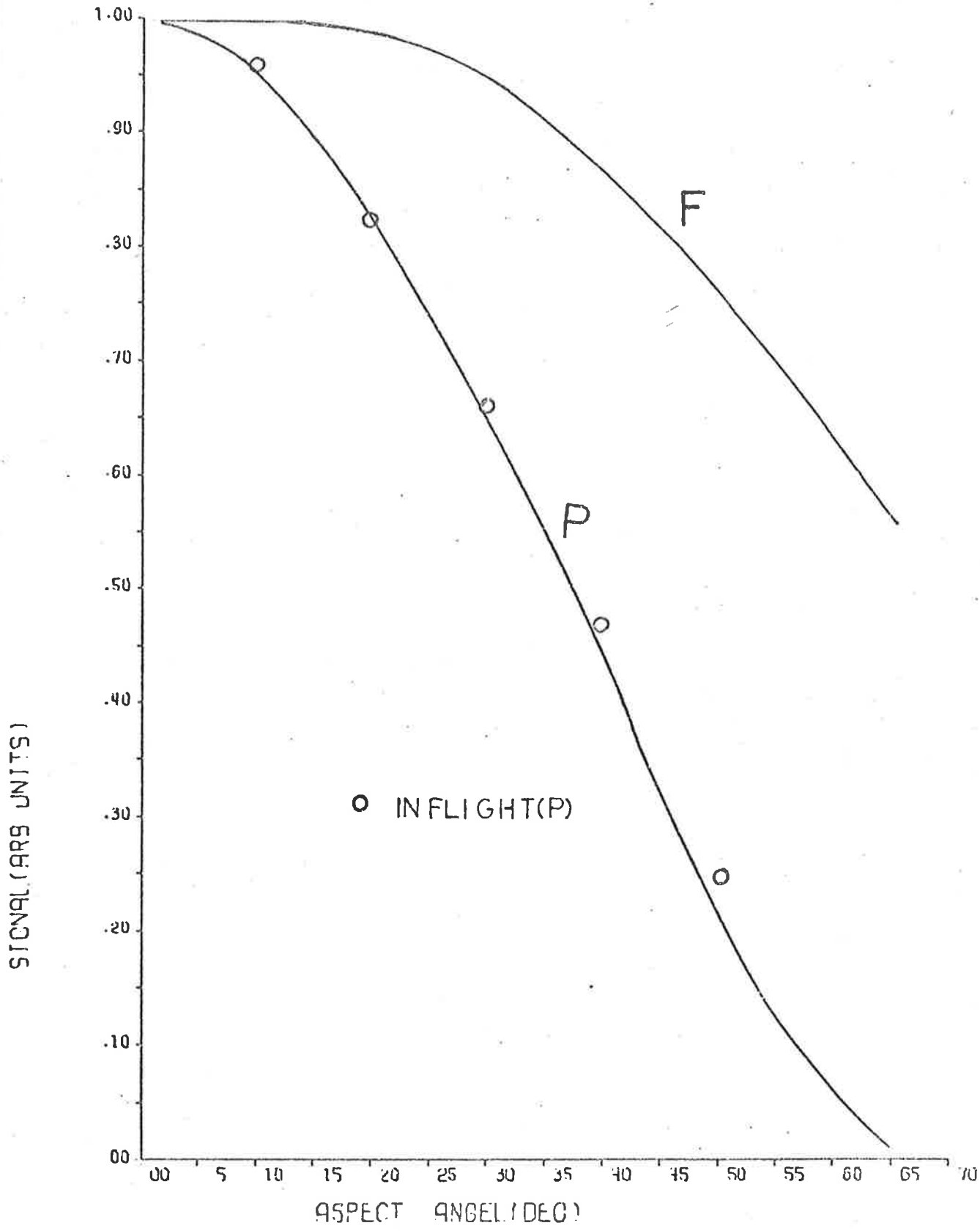

Figure 4.3 Typical angular response curves for an amplitude ratio aspect sensor pair (- Laboratory P: Protruded, F: Flush). (O: In flight).

found unnecessary since the ratio curve would be independent of the spectral distribution of the calibration lamp. A car headlamp was found satisfactory to provide reasonably uniform parrallel beam of light for this purpose. The lamp was placed behind an aperture and the distance between the aperture and the detector was adjusted such that the aperture subtended an angle at the detector equal to the angular diameter of the sun. An especially designed arrangement by O'Brien (1974) was used to mount the entire payload on a turntable for aspect sensor calibrations. The aluminium holders were black anodized to overcome any reflection problems.

The output signal from each detector was obtained by connecting the IP42 and a variable resistor, R, in sensors with a + 45 V supply. The voltage developed across R was then taken to the telemetry switch through an amplifier (Figure 4.4). The absolute level of each detector was adjusted prior to the launch by pointing the aspect sensor directly at the sun and then varying the value of R until the output voltage was about + 2.5 volts. This was to ensure that the telemetry limit of + 5 volts would not be exceeded during the flight due to the unattenuated solar flux. In each flight in which data from this sensor was used, additional information on inflight aspect angles was available from the sunslits. This greatly simplified the reduction of aspect sensor data. With the help of sunslit data, it was possible to obtain an inflight calibration curve for aspect sensors in the aspect range of + 35° to - 35°. This calibration was found to be in good agreement with the laboratory curve (Figure 4.3). Combined results of sunslits and these sensors are presented in Chapter 5.

4.4 QUADRANT RATIO ASPECT SENSOR USED IN THE SPIN-STABILIZED ROCKET VEHICLES

The later series of rocket vehicles used in the present work was of relatively fast-spin. This meant that the coning angle would be rather small and an aspect sensor with an effective aspect coverage of ± 30° could be used to obtain aspect angle information. Although sunslits were

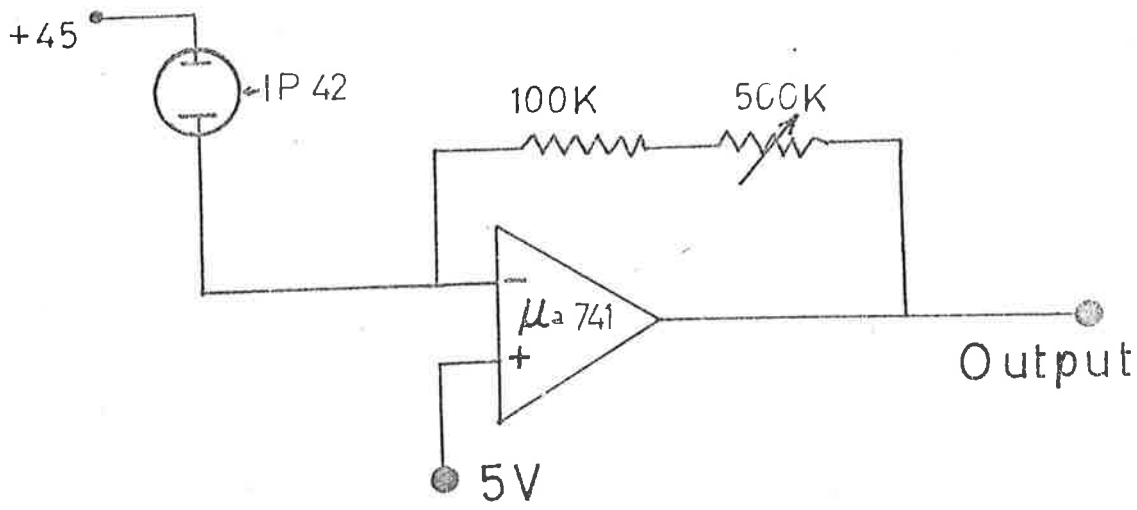

Figure 4.4 Circuit diagram for amplitude ratio aspect sensor amplifier.

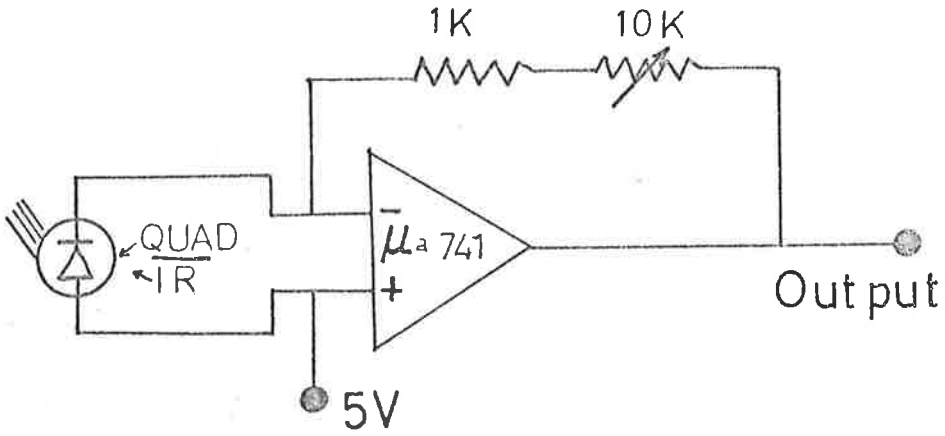

Figure 4.6 Circuit diagram for a quadrant aspect sensor amplifier. (Infrared aspect sensor used an identical amplifier. The amplifier for sunslits employed an identical amplifier with values of 100 K and 100 K for resistors in the series.)

also included in the first two flights of the new series, the spin-rate was too high for them and no useful data could be obtained. A 'quadrant ratio aspect sensor' provided the primary aspect information for all of these payloads.

The principle of operation is based on the ratio amplitude modulation of two responses. It employed a detector of the type UDT SPOT 4D which has 4 quadrants of sensing elements as 4 individual detectors. A rectangular mask in front of sensing elements was deposited by evaporation. This meant that while response of one of the sensing elements varied due to amplitude modulation the other sensor had an additional shadowing effect.

Suppose a beam arrives at the detector at an angle + θ relative to the normal axis of the detector. If we assume the x-y plane containing the sensing elements and the y axis along the rocket axis then the detector normal axis will be along the z axis. The angle + θ would then be termed the aspect angle of the detector.

In general, angle θ is composed of two angles; θx from the z-y plane and θy from the z-x plane in the above reference frame. Obviously, the shadowing effect of the mask in the y-direction would be proportional to the angle θy while in the x-direction would be proportional to the angle θx.

Suppose a length Δy is shadowed by an angle θy, of the sensing elements #1 and #4 (Figure 4.5) and ℓ is the length of the element then

$$\frac{\text{Signal QA1}}{\text{Signal QA2}} = r_{12} \propto (\ell - \Delta y)/\ell$$

If the sensitivity of both the sensors is the same and the distance between mask and sensing surface is h, then

$$r_{12} = \frac{\ell - \Delta y}{\ell} = \frac{\ell - h \tan \theta y}{\ell} \qquad (\text{also } r_{12} = r_{43})$$

or $$\theta y = \tan^{-1} \left[\frac{\ell}{h} (1 - r_{12})\right]$$

similarly $$\theta x = \tan^{-1} \left[\frac{\ell}{h} (1 - r_{14})\right]$$

If the sensitivities are not identical then the ratios need be corrected to represent the ratios for the identical sensitivities before being used in the above expression.

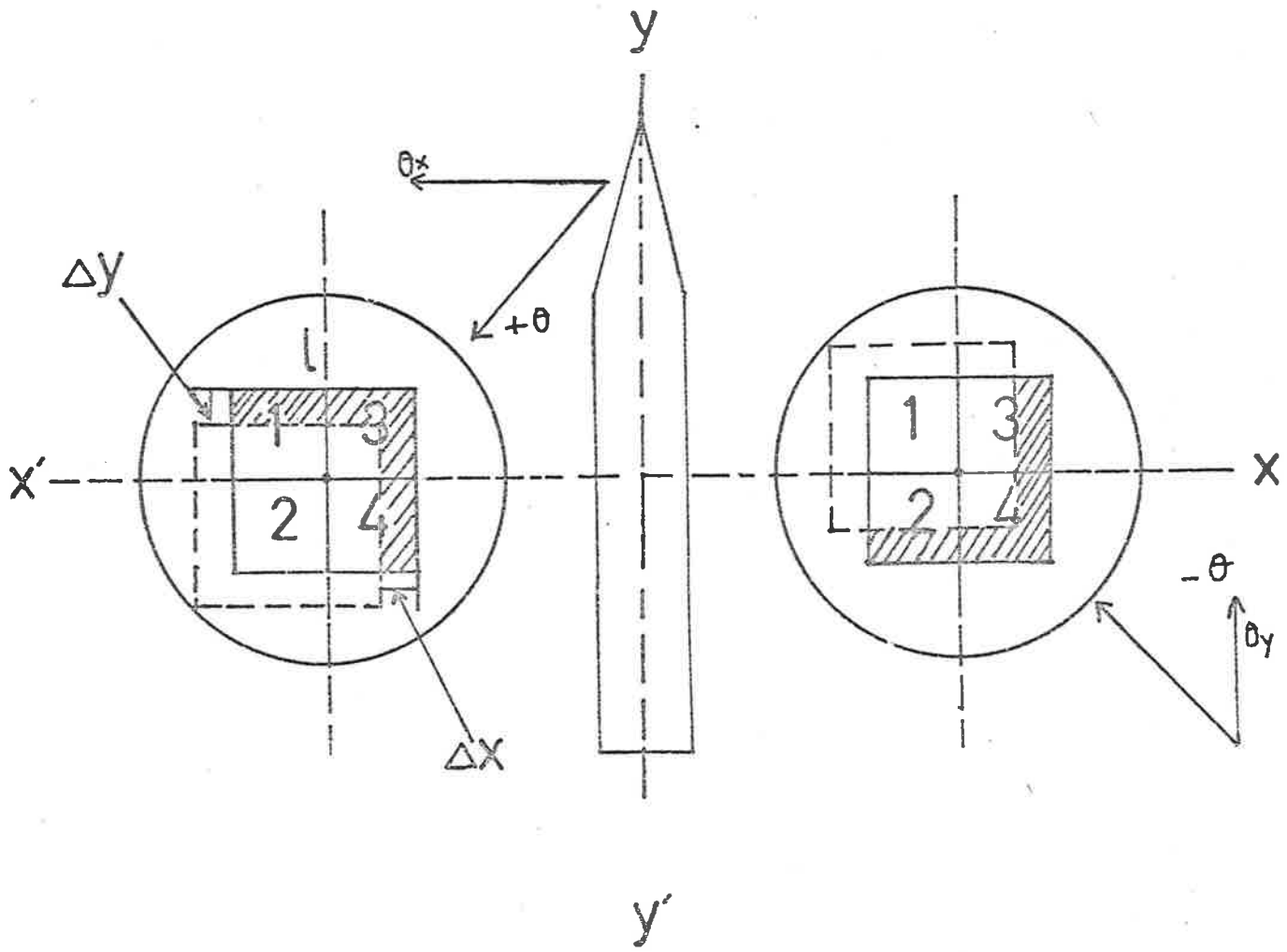

Figure 4.5. Principle of operation of Q-Aspect Sensor

If a rocket vehicle is spinning about its longitudinal axis - in the present reference y-axis - then the minimum aspect angle is the same as θy at the instant when the radiation vector is in the y-z plane.

Since signals from photometers and ionchambers were reduced only for minimum aspect positions (Section 4.1), the aspect determinators were required only for these minimum aspect times. This greatly simplified the aspect data analysis.

Laboratory calibrations of this detector were found to be in agreement with the above theoretical derivation. However, the masking of the aperture is crucial for the theoretical relationship requiring the rectangular masking with its centre at the intersection of sensing elements.

The aspect information (only θy) was obtained for angles less than 29 degrees beyond which one of the two sensing elements was almost completely shadowed for the present masking specifications. Results of aspect angle variations in flights C4007, C4009, C4018 and C4019 are presented in Chapters 5 and 7. In some cases small differences in sensitivity of sensing elements were found which were taken into account in the data reduction. The amplifier connections are shown in Figure (4.6).

4.5 DEVELOPMENT OF AN INFRARED ASPECT SENSOR

4.5.1 Introduction

After first few flights in which 'sunslits' and 'double amplitude modulation sensors' were used as aspect sensors, the need was felt for investigation of a simpler aspect sensor, suitable for small unstable geophysical sounding vehicles.

The simplest technique of obtaining aspect information almost independent of the rocket motion, is that of amplitude modulation but for the atmospheric absorption of the radiation, to which such a detector responds. This problem can be overcome if any optical window in the absorption spectrum of atmospheric gases, mainly, water vapours, oxygen, ozone and carbondioxide can be identified. The near infrared is the potential part

of the spectrum for such a window. This region has the additional advantage that any earth-shine effect (i.e., ratio of reflection from earth to direct sunlight) would be minimum. The absorption bands of the main atmospheric gases indicate the position of such a window around 850 nm (Vasko, 1963). Therefore a detector filter combination responsive to 850 nm can be used. One problem does arise due to any temperature sensitivity of such a detector; when detectors are in rocket payloads particularly near the skin, they encounter considerable temperature changes during the flight due to rocket motion. A detector of UDT type Pin Photodiode (DP series) was found suitable since its response peaks at 850 nm. Laboratory tests showed that the detector signal was virtually independent of temperatures in the range one is likely tc encounter during the rocket flight if the detector is used into a current mode operational amplifier. Since the sensor employed a photovoltaic cell, no collecting voltage was required (Figure 4.6).

The interference filters obtained had a temperature transmission characteristic that showed negligible variation over the temperature range expected viz $20^{\circ}-80^{\circ}$ C.

4.5.2 Flight Tests of Atmospheric Transmission at 850 nm

A filter combination with PIN 5 DP was flown in Cockatoo vehicle C4006. Although due to channel sharing, detailed information was not available, the maximum signal during the flight was close to the level set prior to the flight for direct sunlight. A better interference filter (narrower band width) and a 5 DP detector combination (to be termed as Infra-red or IR detector) was flown in C4009. The primary aspect sensor was a quadrant ratio aspect sensor which provided adequate aspect information between 0° and $\pm 27^{\circ}$ (Section 4.4). The covers came off around 30 seconds after launch, when the rocket was at about 30 km. The IR signal was available from this height onward. Telemetry malfunction at times caused spurious signals which were successfully edited out, as described in Chapter 5. A computer program was used to obtain a polynomial fit

between IR signal and aspect angles near apogee. This angular polynomial curve was then used to correct the IR detector signal for aspect angle variation. These corrections were restricted to angles between -6° and -27° as aspect angles around apogee were not greater than -6°. The aspect corrected signal from the IR detector is shown in Figure (4.7) from which it can be seen that the signal is constant to within ±5% from 30 km onwards. Most of the scatter in the data is a combination of the telemetry interference and large angle corrections retained in the diagram. The latter introduced larger errors for larger angles ($\geqslant 24^{\circ}$) because the field of view of the detector was only about $\pm 35^{\circ}$. Unfortunately not much information was available between ground and 30 km since the rocket became very unstable on the downleg below about 50 km and very large aspect angles were encountered in the height region. The flight signal (corrected to -6° aspect) was found to be about 4% higher than the signal recorded from the detector a few days prior to the flight on the ground for 6° aspect. Since it is within the instrumental error and the day to day solar flux variations, it proved that the spectrum around 850 nm is transmitted to ground almost unattenuated.

4.5.3 Preliminary Results of Aspect Angles

One IR aspect sensor was included in the payload of flight C4018. The sensor was calibrated in the laboratory for its angular response prior to flight. Unfortunately the spin rate of the vehicle was unexpectedly high (~ 12 rps) which meant that in each spin the single telemetry channel was not always picking up the maximum signal corresponding to the minimum aspect from the photometers. This 'beating effect' almost cancelled out in the signal ratios of the quadrant aspect and allowed accurate aspect determinations. However, the effect was found to be very significant in the IR signal.

Still, the laboratory calibrations were used to infer aspect angles from the IR and the results are shown in Figure (4.8) where the aspect angles obtained from the quadrant ratio aspect sensor are also

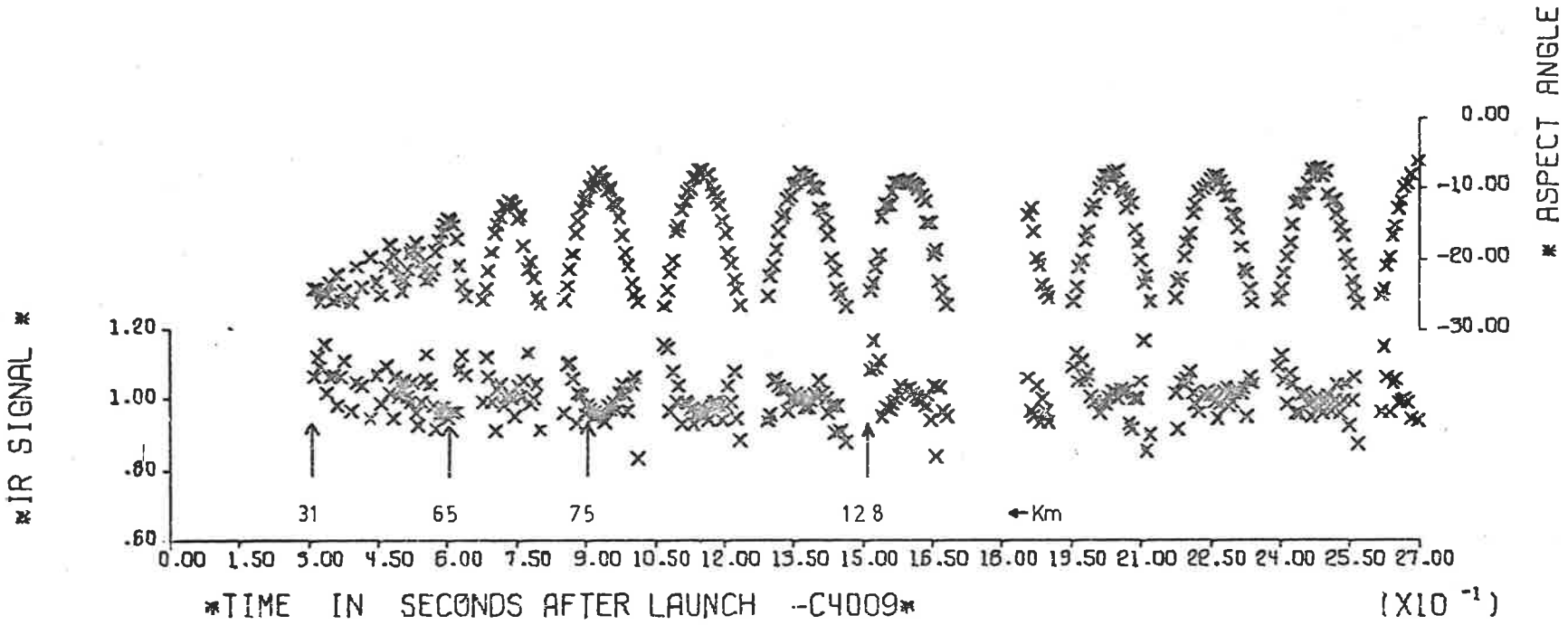
*IR SIGNAL *
1.20
1.00
.80
.60
0.00
-10.00
-20.00
-30.00
* ASPECT ANGLE
31
65
75
128
←Km
0.00 1.50 3.00 4.50 6.00 7.50 9.00 10.50 12.00 13.50 15.00 16.50 18.00 19.50 21.00 22.50 24.00 25.50 27.00
TIME IN SECONDS AFTER LAUNCH -C4009
(X10 -1)

Figure 4.7

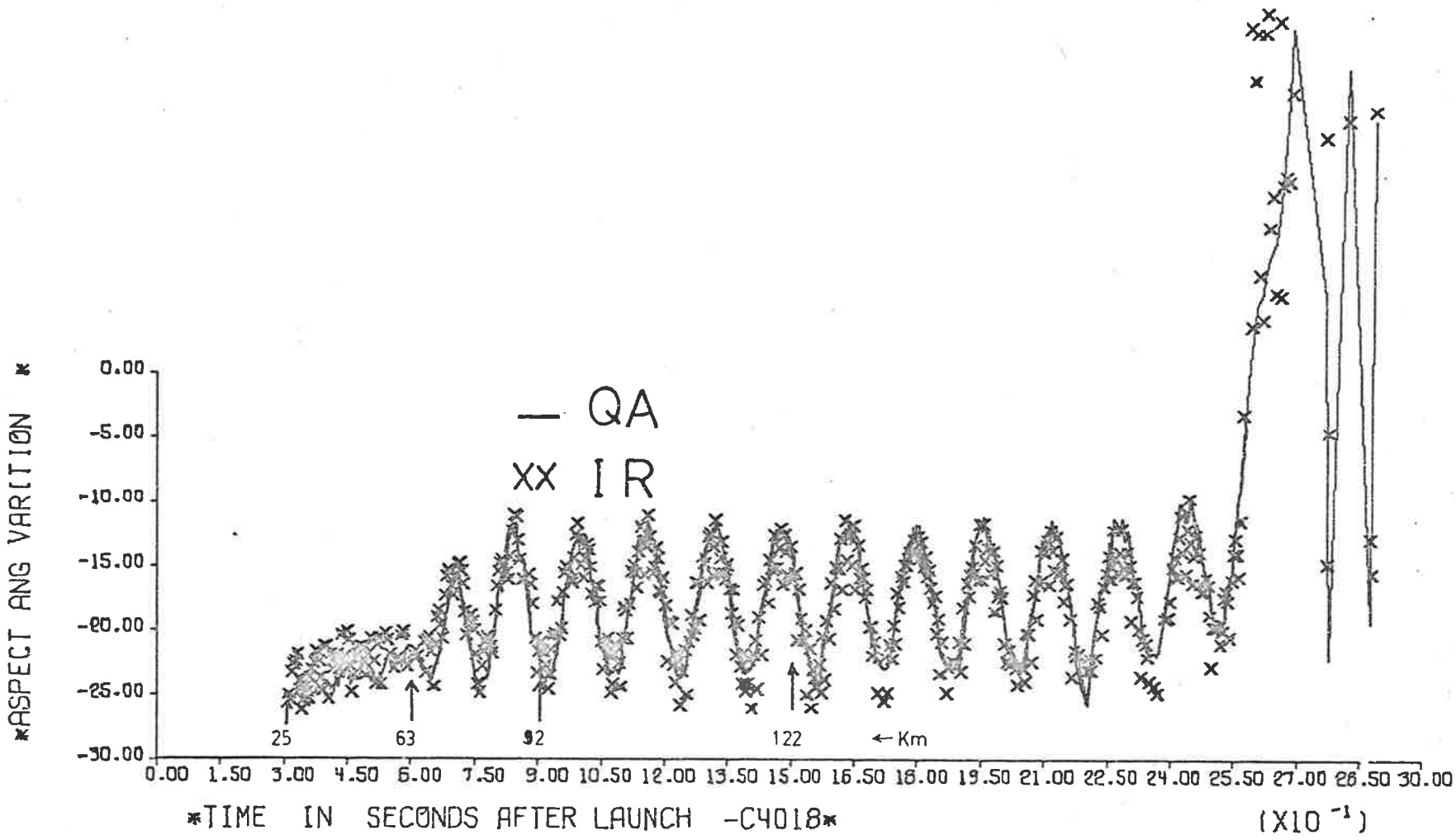
*ASPECT ANG VARITION *
0.00
-5.00
-10.00
-15.00
-20.00
-25.00
-30.00
— QA
xx IR
25
63
92
122
← Km
0.00 1.50 3.00 4.50 6.00 7.50 9.00 10.50 12.00 13.50 15.00 16.50 18.00 19.50 21.00 22.50 24.00 25.50 27.00 28.50 30.00
TIME IN SECONDS AFTER LAUNCH -C4018
(X10 -1)

Figure 4.8

plotted for comparison. It can be seen that the agreement is rather good apart from the scatter in data due to the above mentioned telemetry problem. A polynomial fit was obtained between detector signal and the aspect angles around apogee to obtain an angular response in flight. This was found to be in agreement with the laboratory curve for angles between -11° and -23° - the range of angles around apogee. The scatter in angles is somewhat large and the largest discrepency in aspect angles ($\leqslant 3^{\circ}$) is in the earlier unstable part of the flight (30 sec to 60 sec).

4.6 CONCLUSIONS AND COMMENTS

Several types of aspect sensors have been used which provided the useful aspect information. The 'IR' detector described as Section (4.5) appears to be the simplest inexpensive detector for aspect sensing in small geophysical vehicles. The field of view of such a detector can easily be increased by employing larger radiation sensors available. More than one channel should be allocated for an anticipated high spin rate. The 'quadrant ratio' aspect detector is also simple enough for spinning vehicles.

CHAPTER 5

ROCKET MEASUREMENTS OF MOLECULAR OXYGEN, TEMPERATURE AND SOLAR VUV RADIATION

Rocket experiments to measure the oxygen-density profiles and solar VUV fluxes are described. The details of instrumentation, data acquisition and its analysis are presented along with the results of molecular oxygen densities, mesospheric temperatures and solar UV fluxes. The problem of ionchamber sensitivity change during flight and successful data reduction in such cases is also discussed.

5.1 INTRODUCTION

In the course of this work eleven rocket vehicles were launched, of which nine were instrumented with ionchambers of the types described in Chapter 3. The remaining two vehicles were instrumented with ozone-photometers. These are discussed in Chapter 7. The objectives of the ionchamber experiments were

(a) the measurement of molecular oxygen density profiles by the technique of absorption spectroscopy (Section 2.1) and

(b) the measurement of the intensity of solar radiation at Ly-α and in the wavelength band 155-169 nm. The latter has importance in establishing the value of the solar temperature minimum (Section 1.2).

All of the vehicles were instrumented with LiF-NO and Q-T ionchambers. Also included in the payloads of the last two vehicles were MgF_2-NO ionchambers.

As explained in Section (1.1), in the height range 70 km to 140 km, much more information is required on the variations of molecular oxygen distribution with season, latitude and time of day.

In order to investigate diurnal and seasonal variations of molecular oxygen distribution in the height range 70 km to 140 km, pairs

of morning-afternoon flights were conducted at different times of the year*. Results of oxygen measurements are given in Section (5.7). A discussion of these measurements in comparison to other similar measurements is presented in Chapter 6.

5.2 THE ROCKET EXPERIMENTS

5.2.1 The Rocket Vehicles

The rocket vehicles were of a type designated 'Cockatoo' which was developed by the Australian Department of Supply. It is a two stage vehicle, each stage having solid fuel motors, both burning for approximately 3 seconds with burnout of the second stage occurring approximately 25 seconds after launch at an altitude of about 20 kilometres. The second stage is partially spin stabilized by the action of fins only. The latter four vehicles were relatively fast spun which produced much better stabilization. All but one of the vehicles carried payloads, including ancillary equipment and telemetry systems, to altitudes well in excess of 70 km.

5.2.2 Instrumentation Layout of the Rocket Head

Space for instrumentation is provided in the Cockatoo rocket in the forward section of the second stage which has a diameter of 12.7 cm and a length, including the nosecone, of 101.5 cm. The instrumentation head consists of four main sections viz :(i) Firing and timing (ii) telemetry (iii) Detectors and associated electronics, and (iv) Batteries. The firing and timing section was part of the rocket itself. The batteries to supply all the power necessary for the operation of the electronics associated with the detectors were mounted right in the nosecone.

The telemetry system was an EMI-TM5H. This consisted of a switch motor which was a 24 pin head with a wiper arm. The wiper arm

---

* In fact each of the last two pairs formed part of a programme to study morning-afternoon and night-time ozone concentrations (see Chapter 7).

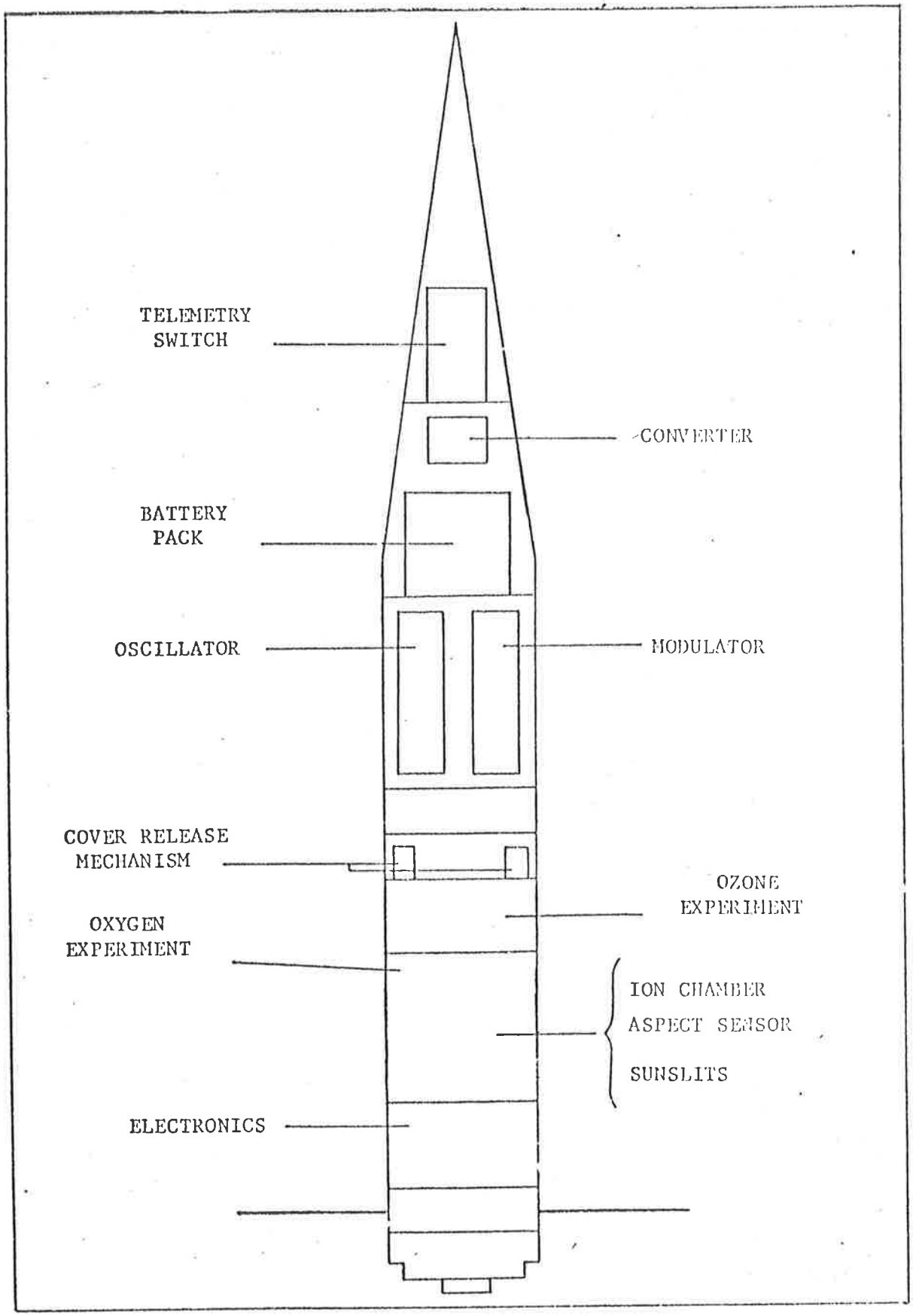

Figure 5.1 Instrumentation layout of the Cockatoo rocket head.

rotated at about 80 rev/sec in case of the first five rockets. This rotation was increased to about 160 rev/sec for the latter fast spinning vehicles. The voltages (0V to 5V) from the different detectors and monitoring circuits which appeared on each of the 24 pins were sampled in turn by the wiper arm and were applied to a voltage controlled oscillator, the frequency modulated output of which was used to amplitude modulate a 465 MHz carrier wave. The telemetry signals were received at the ground and recorded on a magnetic tape. A view of one of the payloads is shown in Figure (5.2) from which it can be seen that the telemetry section was housed immediately above the telemetry aerials and below the detectors section.

The detectors-section was made up of two separate blocks. The upper-part was instrumented with magnetometers, ozone photometers and the associated electronics. The lower part known as the ionchamber block was instrumented with ionchambers, aspect sensors and the associated electronics. Brief description of the design and components of the ionchamber block are given in the following sub-sections.

(a) Design

Two different designs of the ionchamber block were used. In each design, the detectors were arranged in two banks which were mounted on opposite sides of the rocket. In the earlier design (A), used in slow-spin vehicles, each bank consisted of three ionchambers of the same type (i.e., one bank contained Ly-α ionchambers while the other contained Q-T ionchambers) looking at angles of 55°, 90°, and 125° from the rocket axis but in the same plane consisting of all three ionchambers and the rocket axis. This configuration was adopted to ensure adequate data coverage despite very large coning angles. The design was found to be very successful for the earlier four flights in which aspect variations were rather large (Section 5.6). A view of the

Figure 5.2 A view of the various sections of the Cockatoo instrumentation head showing distribution of the payload. The ionchamber block is of design B type. The instrumentation section (in the middle) was later mounted inside the skin shown on the left. The nose-cone was mounted on top of the instrumentation section. A typical complete instrumentation head is shown in Figure 7.3.

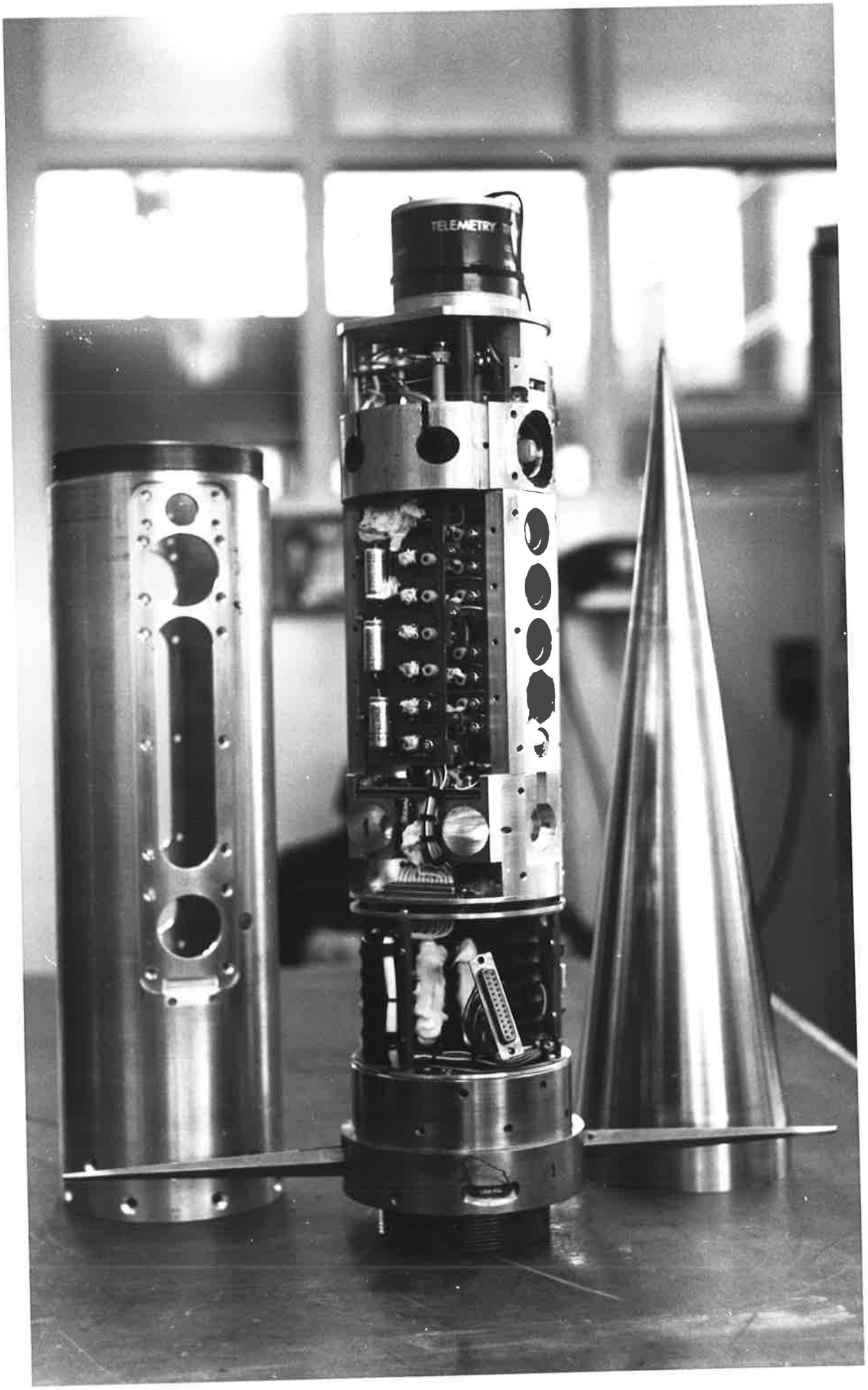
TELEMETRY

ionchamber block in design (A) is shown in Figure (5.3).

Since the spin rate of latter flights was increased signigicantly to provide a better stabilization, the design of these flights (C4007, C4009, C4017 and C4018) was changed to a more conventional system in which all the detectors (ionchambers and aspect sensors) in each bank were mounted parallel to each other and all looking at 90° from the rocket axis. This allowed several other types of the detectors to be instrumented for other experiments. A view of this design (B) can be seen from Figure (5.2).

(b) Ionchambers and Signal Amplification

A set of six ionchambers (3 LiF-NO and 3 Q-T) was installed in the rounds employing design (A), discussed above. In the rest of the flights, 2 Ly-α and at least 1 Q-T (in some cases 2 Q-T) ionchambers were included in the payload. All the ionchambers, manufactured as described in Chapter 3, were operated at unity gas gain. Absolute calibration of the ionchambers was carried out prior to flight as described in Section (3.8).

The signal currents from ionchambers were amplified by F.E.T. input, linear amplifiers operating in the current-feedback mode to give a fast response time. Since expected signals from Q-T chambers are lower by about a factor of 10 than those from Ly-α chambers, two different types of amplifiers were employed to give amplifier gains of the order of 10^{10} V Amp^{-1}. The circuitory was slightly modified in the later part of this work, in which signals were amplified in two stages to give better stability. The gain of the amplifiers could be varied between 1 and 10 to allow for variations in the quantum efficiencies of the ionchambers in order to use the full range of the telemetry. Laboratory tests showed that any zero drifts in the amplifiers during a Cockatoo flight due to temperatures encountered in the payload, would be insignificant and no significant zero drifts were recorded during

Figure 5.3 A view of the ionchamber block (A) as used in the earlier slow spin rocket vehicles (C1020, C1029, C1035 and C4006). The three holes are for ionchambers. The amplitude ratio aspect sensors and sunslits can also be seen.

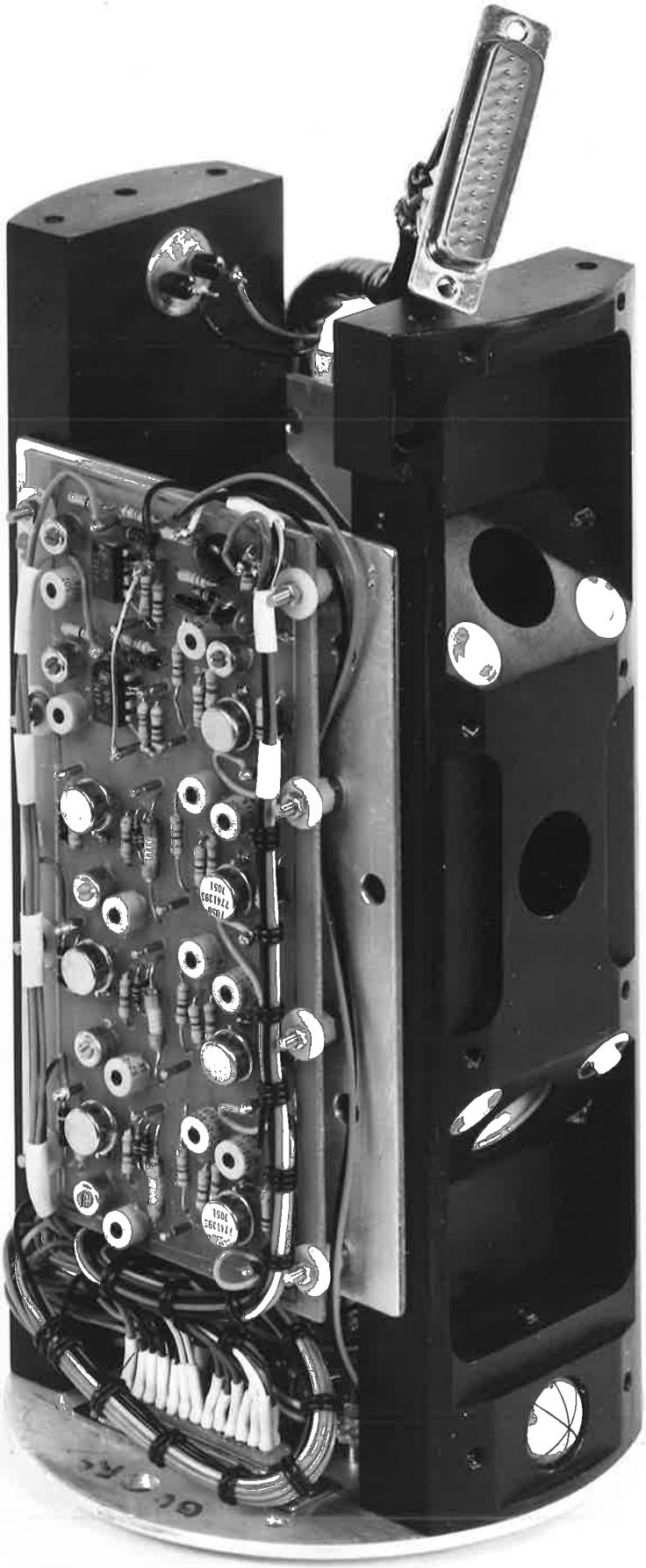

the flights. Circuit diagrams of the ionchamber amplifiers are shown in Figures (5.4) and (5.5).

(c) Optical Aspect Sensors

Ionchamber blocks employing design (A) (i.e. ionchambers looking in different directions) were instrumented with 4 pairs of amplitude modulation aspect sensors (Section 4.3); each pair looking in one of the directions of the outer chambers (Figure 5.3). Also included in each of these payloads were 2 sunslits (Section 4.3) each looking in one of the directions of the two remaining central ionchambers. In each of the last four payloads which employed design (B), a quadrant ratio aspect sensor (Section 4.4) was included instead of the above mentioned amplitude ratio aspect sensors. Sunslits were not included in the last two flights (C4017 and C4018) since they could not be useful for fast spinning vehicles as discussed in Section (4.3.1). Also included in each of the payloads of flights C4009, C4017 and C4018 was an infra-red aspect sensor described in Section (4.5). The performance of these aspect sensors is discussed in Section (5.6) for individual rocket flights.

5.2.3 Preflight Checks of Equipment

The amplifier gains were set as required for each detector before payloads were flown to the Woomera range. At the same time signals were recorded from the absolutely calibrated ionchambers when connected to the payload using a D.C. lamp so that a comparison could be made for efficiencies of the detectors just prior to flight. Also a sensor and telemetry check was carried out using the facilities of the Weapons Research Establishment of the Department of Supply. The complete head was operated and the telemetry received at a remote station to check the operation of sensor channels, monitoring circuits and channel allocations. Further tests of ionchamber efficiency were carried out at the range and any suspected detector was replaced from the spares. Finally, operation

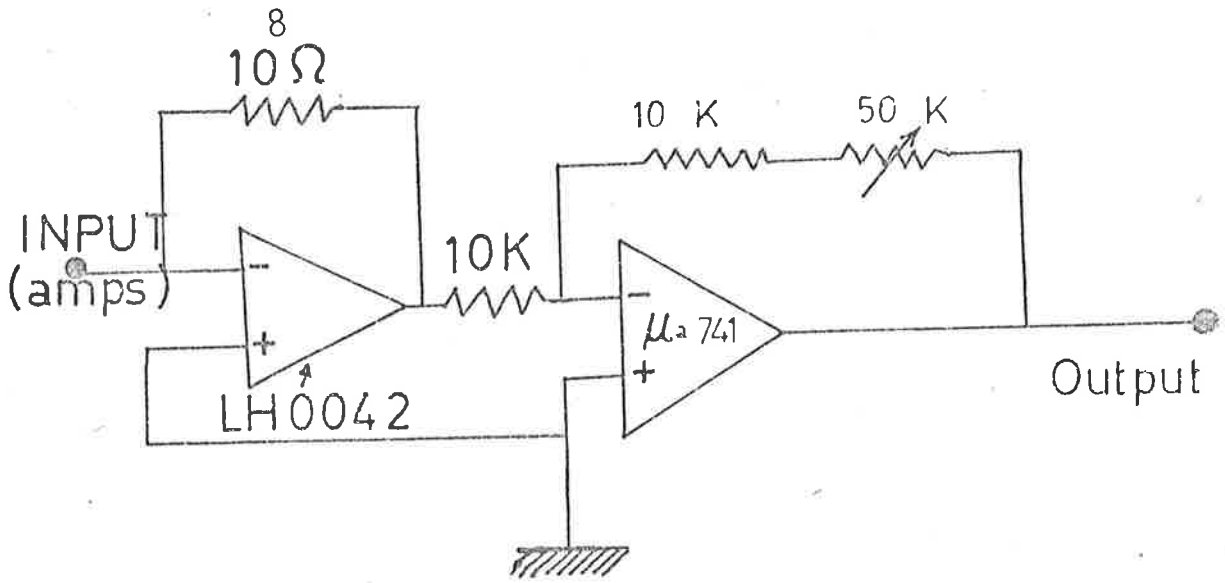

Figure 5.4 Circuit diagram for a Ly-α ionchamber amplifier.

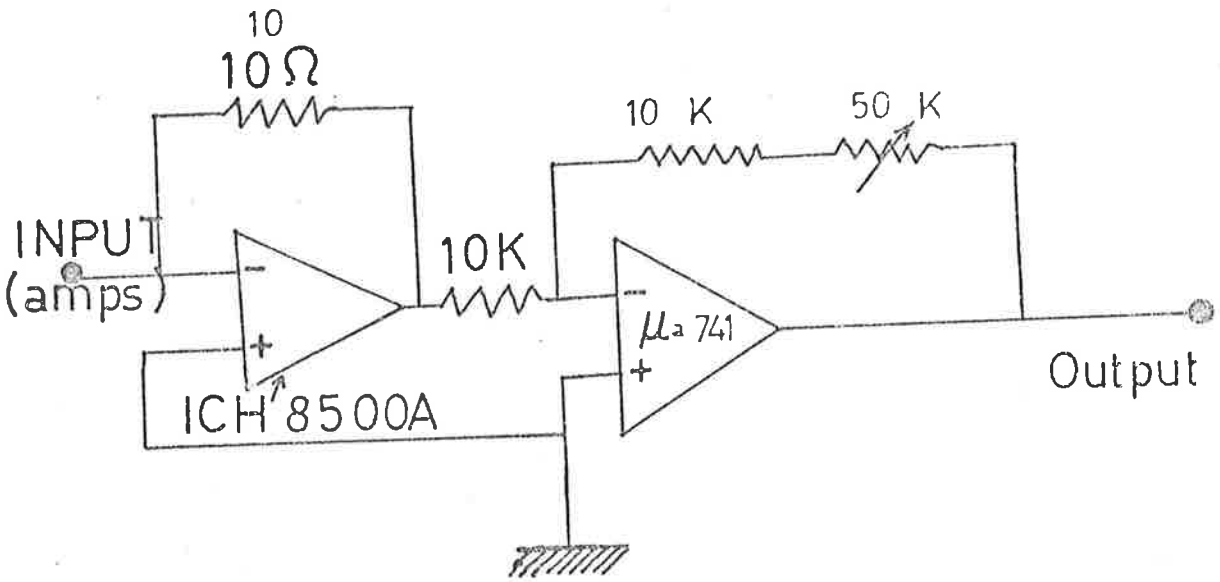

Figure 5.5 Circuit diagram for a Q - T ionchamber amplifier.

of all sensors and channel allocation were checked at the Woomera range and also as part of the immediate prelaunch sequence.

5.3 DETAILS OF THE LAUNCH AND FLIGHT CONDITIONS

All the vehicles used in the present work were launched from the Woomera Rocket Range of the Weapons Research Establishment of the Australian Department of Supply. The range head is situated at 30° 35' south latitude and 136° 31' east longitude.

The first vehicle, C1020, was fired at 1100 CST (Australian Central Standard Time) on 20th July 1972, at which time the sun was at a zenith angle of 56°.

The following two vehicles, C1029 and C1035 - first in a series of morning -afternoon pair of flights - were launched on 23 November 1972 at 0825 CST and 1625 CST respectively. The sun was at zenith angles of 50.3° and 58.7° at these times.

The first vehicle in the next pair of flights, C1046, was fired at 0915 CST on 26th June 1974. Due to a power supply malfunction no signals from ionchambers were received.

Therefore, the afternoon flight, C4006, was postponed till 28th June 1974 on which date, it was launched at 0947 CST. The sun at that time was at 66.9° from zenith.

The third pair of flights, C4009 and C4007, were launched on 2nd October 1974 at 0820 CST and 1725 CST, at which times the sun was at zenith angles of 60.4° and 77.9° respectively.

The last pair of flights, C4018 and C4017, were launched on 29th April 1975 at 0915 CST and 1655 CST respectively. The sun was at zenith angles of 63.6° and 79.6° at the times of these launchings respectively. Due to a malfunction in the second stage motor, the second flight, C4017, was abortive. Details of two additional flights for night-time ozone determinations are given in Chapter 7.

Trajectories for the successful flights are presented in the following section and the results of aspect variations and observed absorption profiles for individual flights are given in Sections (5.6) and (5.7).

5.4 TRAJECTORIES OF THE ROCKET VEHICLES

The range centre line extends to the North-West of the launching site. The flight path of the vehicles was in this direction. The vehicles were skin tracked by on-range FPS16 radar facilities. Magnetic tape records of the radar tracking data were then processed by the Weapons Research Establishment and the resulting output were presented in the form of X, Y, Z, $\dot{X}$, $\dot{Y}$, $\dot{Z}$ and height as a function of time from launch, where X measures the horizontal distance along the range centre line, Y the horizontal distance normal to X, and Z the vertical distance above the launch site. Height was the Z coordinate corrected for height above sea-level and the curvature of the earth. The time interval between listings was 0.5 sec.

Rocket flights C1020, C4006, C4007 and C4018 were well tracked by the radar and trajectory results are represented in Table (5.1). Although radar tracking of flights C1029 and C1035 was somewhat incomplete the missing portions could be computed easily without any significant loss of accuracy, as described below. The tracking of flight C4009 was rather poor as the radar could not lock on the vehicle. However an estimated trajectory could be obtained by comparison with other flights as described below.

In order to interpolate the heights in the missing portions of a trajectory, let us consider the mathematical form of the trajectory. After second stage burnout, the trajectories should be ballistic to a first approximation i.e.

$$h(t) = h(0) - \tfrac{1}{2} g t^2 \qquad (5.1)$$

where t is measured from apogee.

Payload	FLIGHT CONDITIONS			TRAJECTORY	
	Date	Time[1] (CST)	Zenith Angle (Solar)	Apogee Height (km)	Apogee Time (secs)
C1020	20 Jul 1972	1100	56°	128	176
C1029	23 Nov 1972	0825	50.3°	130.5	177
C1035	23 Nov 1972	1625	58.7°	120.2	168.5
C1046*	26 June 1974	0915	-	-	-
C4006	28 June 1974	0947	66°	106.5	157
C4009	2 Oct 1974	0820	60°	132	177.5
C4007	2 Oct 1974	1725	77.9°	137	182.4
C4010*	3 Oct 1974	2050	-	133.5	179.5
C4019	28 Apr 1975	2022	83.5° (lunar)	122.2	171.7
C4018	29 Apr 1975	0915	63.6°	124.8	173
C4017*	29 Apr 1975	1643	-	-	-

[1]: UT = CST-0930

*: No useful data obtained.

The two most important factors that cause the trajectory to deviate from this form are air drag and variations in the acceleration due to gravity (g). The effect of air drag is to make the trajectory unsymmetrical (i.e. $h(-t) < h(t)$) and the effect will decrease as the height increases. Average figures for difference between actual height determined by radar and computed heights from ballistic form (neglecting air drag) for Cockatoo vehicles were found to be 1.5 km at 20 km, 1.0 km at 30 km, 0.5 km at 50 km, 0.1 km at 60 km and negligible above 70 km (O'Brian, 1973). Since for oxygen data, trajectory is only required above about 70 km, air drag effect may be ignored in further discussion.

The value of g varies inversely as the square of the distance from the centre of the earth but over a limited height range of about 70 km, the decrease in g can be approximated by a linear formula and we may write

$$a(t) = - [g_o + K(h(0) - h(t))] \qquad (5.2)$$

where a(t) is the vertical acceleration of the rocket, g_o is the value of g at the maximum height h(0), and K is a small positive constant. If a(t) and g_o are in units of Km sec^{-2} and h(0) and h(t) are in units of Km, then K has the value 3.0866×10^{-6} sec^{-2} (CIRA, 1965).

Equation (5.1) can be written as

$$h(t) - h(0) = - \tfrac{1}{2} \bar{g} t^2 \qquad (5.3)$$

where $\bar{g}$ is the effective value of g during the time interval t experienced by the vehicle.

Since K is small and time is measured from the apogee, we may approximate $\bar{g}$ by g_o for the purpose of substituting equation (5.3) in equation (5.2) i.e.

$$a(t) = - [g_o + \tfrac{1}{2} K g_o t^2] \qquad (5.4)$$

Then, vertical velocity of rocket (V(t)) is given by the expression

$$V(t) = \int_o^t a(t)dt$$

$$= - (g_o t + \frac{1}{6} K g_o t^3) \qquad (5.5)$$

Note that V(t) = 0 when t = 0

Integration of equation (5.5) gives:

$$h(t) = \int_0^h V(t)\, dt$$

$$= h(0) - \tfrac{1}{2} g_o t^2 - \frac{1}{24} K g_o t^4$$

$$h(t) = h(0) - \tfrac{1}{2} g_o t^2 \left[1 + \frac{1}{12} K t^2\right] \qquad (5.6)$$

Equation (5.6) describes quite accurately the trajectory taking into account variation in g. To use this equation two quantities - h(0) or apogee height and apogee time defining t = 0 - have to be determined from the radar data.

The value of g_o for equation (5.6) can be easily evaluated from the exact expression:

$$g(Z) = 979.3244 - 3.0866 \times 10^{-4} Z + 7.259 \times 10^{-11} Z^2 (\text{cm sec}^{-2})$$

where Z is height in meters above the earth's surface (CIRA, 1965).

The radar did not track the vehicle, C1029, between 110 sec and 133 sec from launch as well as most part of the downleg. Fortunately it locked onto the vehicle from 133 sec until 210 sec after launch, which included the apogee (Figure 5.5) before losing it again. Therefore apogee height and corresponding time were directly available from the radar data. However, due to scattering in the height around apogee, observed value of t apogee was varied in intervals of 0.1 sec in the equation (5.6) and computed values of h(t) were compared with the trajectory obtained from radar track below 110 sec until the two curves almost superimposed. The values thus obtained, 177 sec and 130.5 km, were used in equation (5.6) to obtain the composite trajectory.

The second vehicle, C1035, was well tracked until about 223 sec which correspondedto about 106 km on the downleg. Therefore evaluation of t_o and h(0) was relatively easy. However due to a virtual flatness in the trajectory around apogee, t_o was first estimated from symmetry of upleg and downleg. This value was then slightly varied until the computed values of h(t) agreed with the observed trajectory. The apogee time was thus found to be 168.5 sec and an apogee height of 120.17 km.

As mentioned earlier, the tracking of the rocket vehicle, C4009, was poor with the radar never locking onto the vehicle. But the duration of the flight was known from telemetry signals which made it possible to estimate a trajectory. The duration of the flight C4009 (334 ± 1 sec) was found to be comparable with flight durations of C4010 (Chapter 7) and C1029 (339 sec and 341 sec respectively). Since flight C4010 was launched on 3rd October (less than 2 days after C4009) with almost identical payloads, the close proximity of flight durations gave a first approximate trajectory. Further, it was noticed from the trajectory of C1029 and C4010 that the trajectories were identical for about first 100 sec from launch and differences between the two became significant only beyond this time. The trajectory for C4009 was then interpolated between the two and the results are shown in Figure (5.6). The resultant trajectory is estimated to be accurate within ± 2km. The above trajectory was applied to the Ly-α absorption profile corrected for an effective sensitivity change (Section 5.9) and the agreement between upleg and downleg height profiles was found to be excellent. Since the corrections applied were independent of the trajectory, the above result indicates that the accuracy of estimated trajectory is perhaps much better than 2 km in the height region above 70 km.

5.5 FORM AND METHOD OF REDUCTION OF THE TELEMETERED DATA

The telemetered values of the voltages appearing at the outputs of various amplifiers were recorded on magnetic tape. The magnetic tape was then processed by the Weapons Research Establishment and presented in two forms for each successful rocket flights. One form was a film record which gave a plot of voltage against time for each sensor for the duration of the flight. The second form was a digital computer readout of the magnetic tape. Also available were copies of the original magnetic tapes for direct processing. For the slow spinning vehicles (C1020, C1029, C1035,

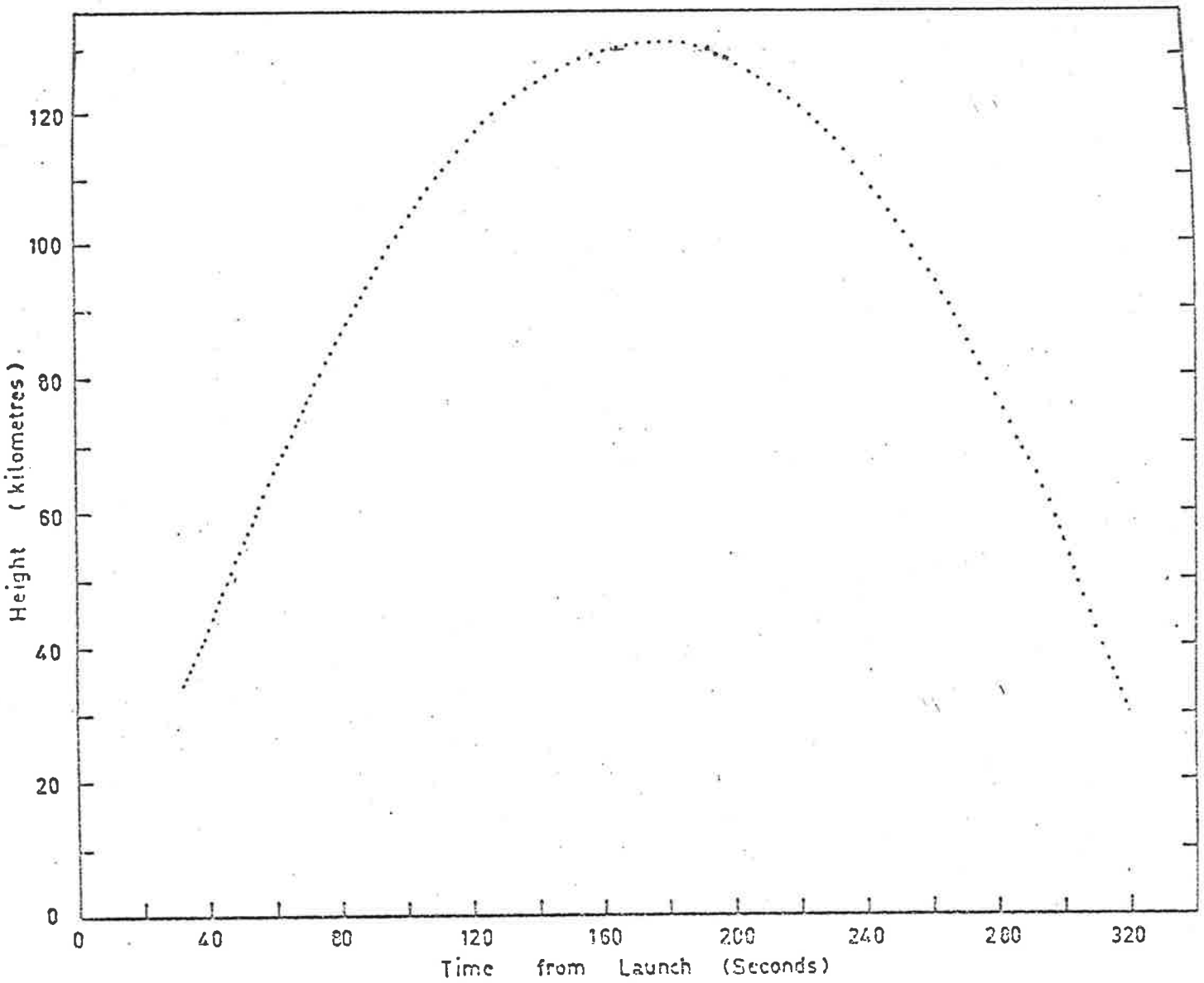

Figure 5.6 Variation of height with time for

C4006) film records were generally found to be very convenient for manual data reduction. A peak was produced in the voltage of each optical sensor as the sensor looked towards the sun once every revolution of the rocket. The peak occurred when the aspect angle of the detector was minimum for that revolution of the rocket (Section 4.1). The peak voltage values for each of the useful sensors (ion chambers and aspect sensors) were recorded from these films once for each spin. Similar values of peaks directly available from the digital records were also used occasionally with appropriate background corrections. The aspect sensor signals were first processed to obtain aspect corrections as a function of time. These corrections were then applied to the ionchamber flux data and thus absorption profiles as a function of time were obtained which were then converted to height vs flux profiles with the help of trajectory data (Section 5.7.1). The height profiles were then used to infer oxygen density profiles as described in Section (5.7.2).

For the fast spinning vehicles (typical spin rate of about 8 rev/sec) it was rather cumbersome to reduce the data as discussed above since the number of useful data points for each sensor was in the range of about 1500. Therefore, a computer program was written which initially could pick up the data points for each sensor at the peak points directly from a copy of the original magnetic tape and store the peak values onto another magnetic tape. Subsequent programs were then used to analyse these data first to obtain aspect angles and then to apply the corrections to the ionchamber data. A time-height function was then used to obtain computer plots of aspect corrected flux profiles as a function of height in addition to the flux profiles as a function of time. The height profiles were then differentiated to obtain density profiles. Data from flights C4007, C4009, C4018 were analysed in this manner. Specific details of absorption profiles and the derived oxygen profiles for each flight are given in Section (5.7).

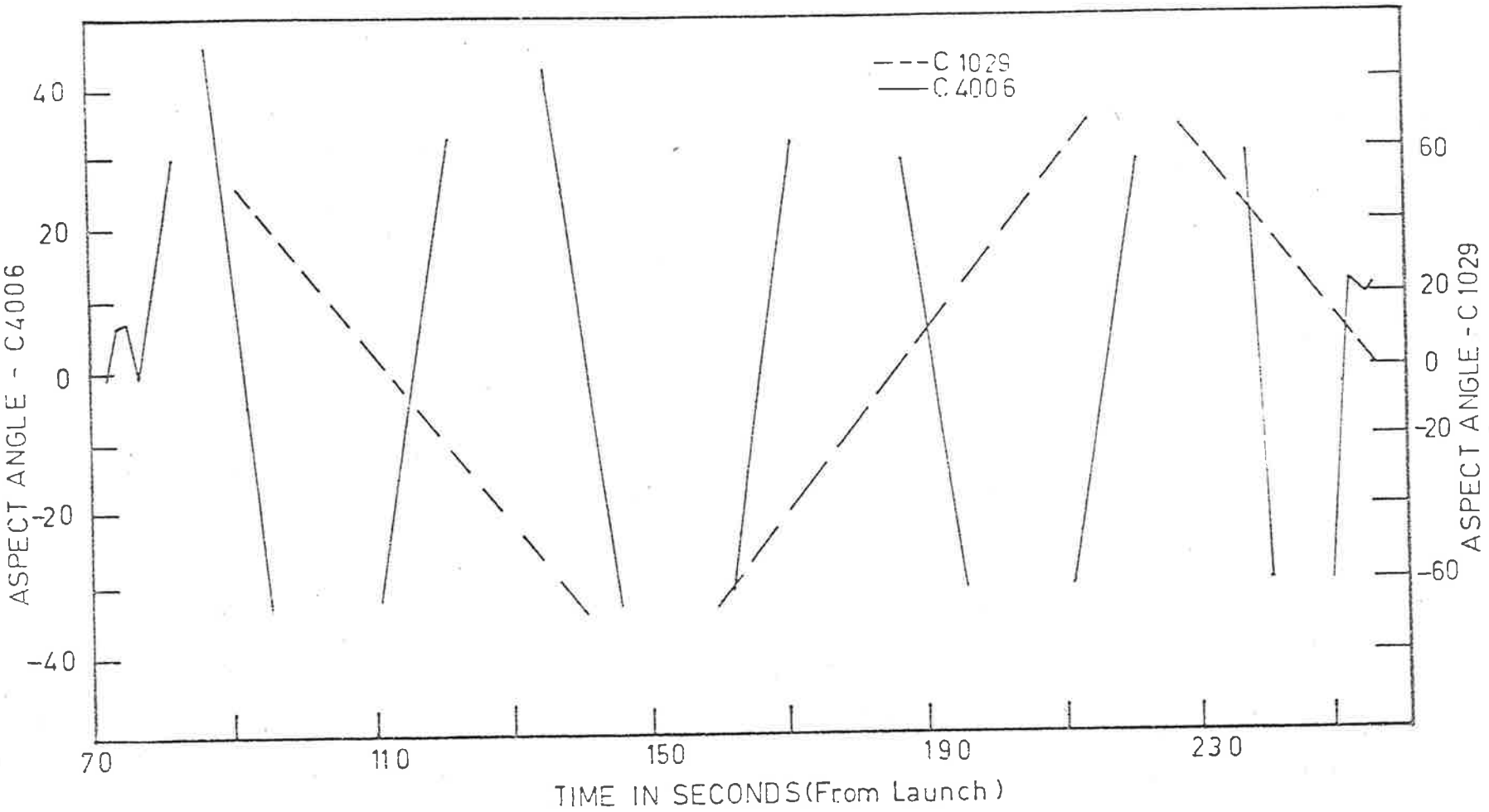

Figure 5.7 Aspect angle variations in flights C1029 and C4006. It can be seen that the precessional angle and time were smaller in the latter case. The stabilisation further improved later fast spin flights, C4007, C4009, and C4018, (Figure 5.8).

5.6 PERFORMANCE OF ASPECT SENSORS AND RESULTS OF ASPECT ANGLE VARIATIONS DURING FLIGHT

Each of the flights C1020, C1029, C1035 and C4006 were instrumented with 2 sunslits and 4 pairs of amplitude ratio aspect sensors (see Section 5.2.2). The description of each of these detectors and the method of data reduction has already been given in Section (4.3).

Although sunslits were also included in the payloads of flights C4007 and C4009, no useful data could be received due to fast vehicle spin for reasons given in Section (4.3.1). The primary aspect sensor on each of the last three flights was a quadrant ratio aspect sensor of the type described in Section (4.4) which provided successful aspect information. Both, sunslits and amplitude ratio aspect sensors provided the useful aspect angle information for flights C1029 and C4006. Sunslits data was useful for angles less than $\pm 35^{\circ}$ whereas the aspect sensors covered a much wider range. In fact data from one of each pair (flush aspect sensor) was found to be sufficient to obtain aspect angles with the aid of preflight laboratory calibrations (see Section 4.2.2 and 4.3). The aspect angles were then weighted in favour of sunslits in the region of mutual coverage although the differences were small. The early cover release in flight C1035 made the vehicle very unstable and only solar fluxes could be determined.

Some problems in aspect determination for the flight C1020 were experienced in aspect sensor data due to uncertainty in zero level signals (Section 4.3.2). The partial aspect information was obtained as follows:

As the normal axes of the amplitude ratio aspect sensors were at $\pm 35^{\circ}$ from the normal to the rocket axis (reference of aspect angle), the signal from one of the two pairs would reach a maximum whenever the aspect angle would be in the vicinity of $\pm 35^{\circ}$ (see Figure 5.3). Also, as the field of view of flush aspect sensors was about $\pm 75^{\circ}$, the other flush aspect would show only a very small signal for this aspect position. Thus, times when aspect angles were in the vicinity of $+ 35^{\circ}$ or $- 35^{\circ}$, could be

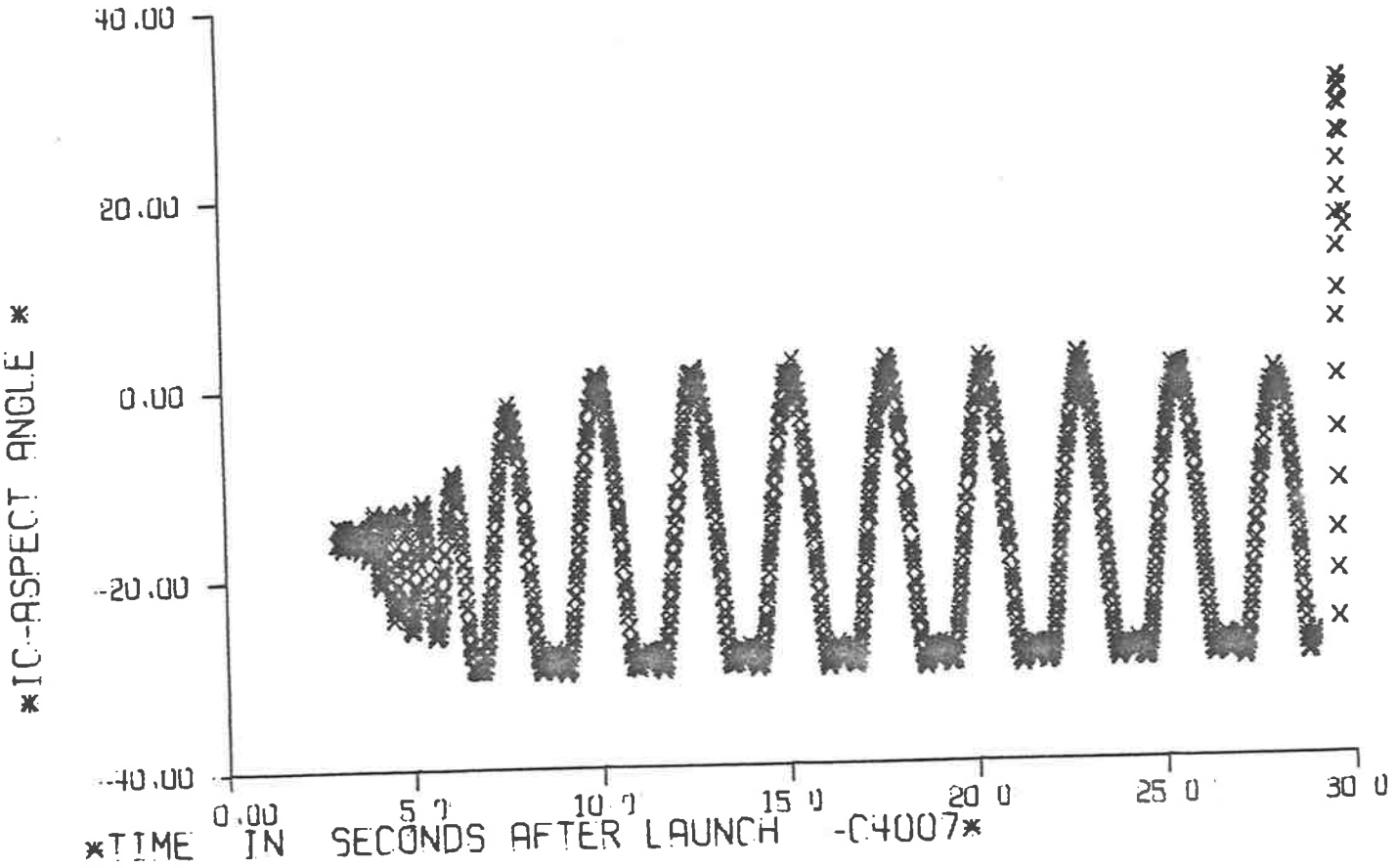

Figure 5.8a Aspect angle variation in flight C4007.

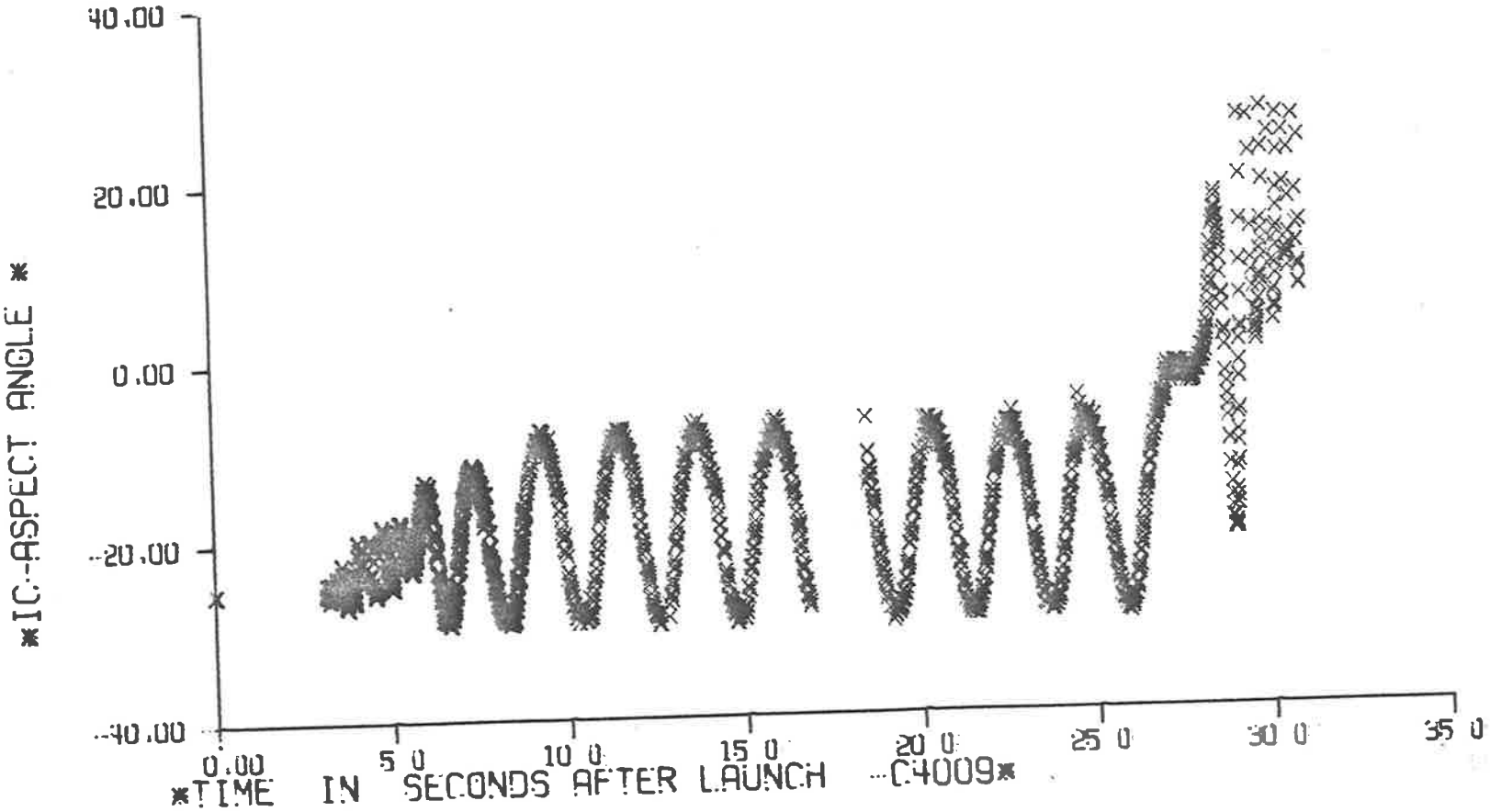

Figure 5.8b Aspect angle variation in fligth C4009.

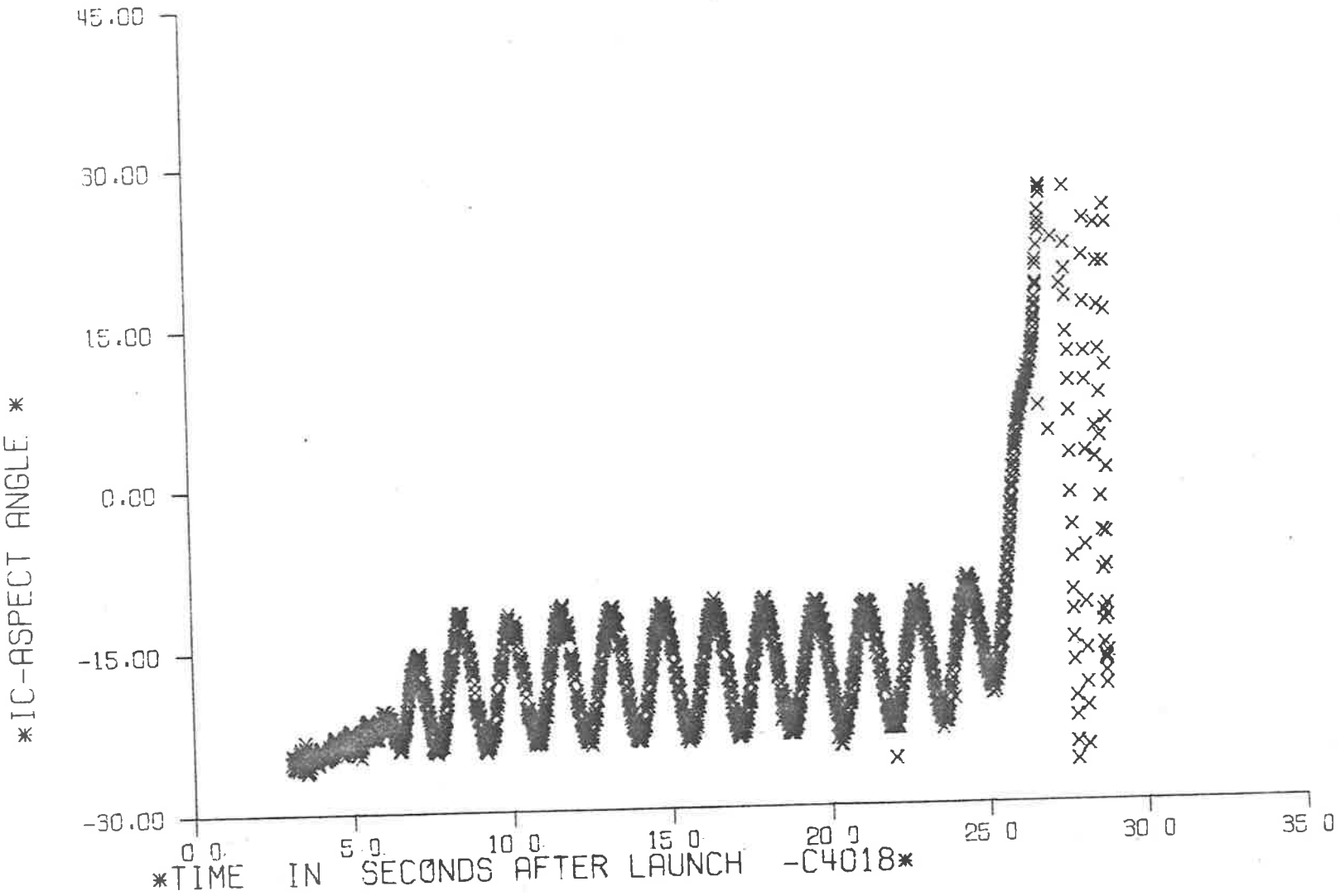

Figure 5.8c Aspect angle variation in flight C4018.

recorded. The signal from LiF-NO chamber in the height range above about 120 km should vary mainly due to aspect variation since no significant absorption takes place in this region. Due to relatively fast spin, the vehicle aspect was found to vary only slowly and therefore a maximum in LiF-NO singal would indicate an aspect in the vicinity of ± 0°. The signals of aspect sensors for these times of about 0° aspect were recorded which were found to be reasonably consistent. Then in the region below 100 km, times were recorded when the signals from flush aspect sensors were close to 0° aspect positions. Thus a set of times for the flight were tabulated corresponding to aspect angles close to ± 0°, + 35° and - 35°. For all these points the signal from one of the magnetometers was used as an additional check. Ionchamber data for only these times were corrected for aspect angle (if angle was not 0°) and then used to derive an absorption profile. It is believed that the errors in the above aspect values would be less than ±5°. Since a position of ± 35° aspect would be 0° aspect for one of the outer ionchambers, an error of ± 5° would introduce no significant error because the angular response of ionchambers is almost flat over ± 5° angle. Most of the data points used were thus for 0° aspect from respective chambers with appropriate normalization.

The aspect angle variations as a function of time are shown in Figures (5.7 and 5.8) for each of the relevant flights. It can be noticed that aspect angle variations for the unstabilized flights were very large (> ± 70°) and the design used for these flights was thus useful. The improvement in stabilization for latter flights due to larger spin rate is also evident from these Figures.

5.7 RESULTS OF MOLECULAR OXYGEN DENSITY AND TEMPERATURE PROFILES

5.7.1 Incident flux absorption profiles

As mentioned in Section (5.5), peak readings of voltage output for each optical sensor (ionchambers and aspect sensors) were recorded as a function of time. Data from aspect sensors was analysed to obtain aspect

angles as a function of time as described in Section (5.6). Ionchamber signals were then corrected to zero aspect angle (Section 3.8.4). Although the angular response of an ionchamber extends to about ± 70°, aspect corrections were restricted to angles less than 35° for the slow spinning vehicles. For the later flights, aspect angle information was limited to less than about 27° due to small field of view of the quadrant aspect sensors (Section 4.4) and thus limiting the aspect corrections to this value. However, in these flights, aspect angles were larger than this value only occasionally (see Figure 5.8).

Since the data acquisition rate for slow spin flights was small (typically 1.5-2.0 km) and partial due to large aspect variations, composite curves of aspect corrected ionchamber signals as a function of height, for all the useful ionchambers of one type included in the payload, were obtained. Due to variation in sensitivity from chamber to chamber, signal levels were normalized arbitrarily if required for each ionchamber of one flight such that all of the same type ionchambers gave the same signal at some heigh altitude level. Due to slow data acquisition rate, upleg and downleg data was plotted together generally to supplement each other and a mean profile was thus obtained for each case.

For the last three fast spun flights, it was adequate to analyse data from each ionchamber and for upleg and downleg separately due to complete data acquisition on each leg with the exception of Ly-α data in C4007. In this case upleg data was normalized upwards such that upleg data was in good agreement with the downleg data in the mutual coverage region. The constant of normalization was found to be 1.4 for the Ly-α ionchamber IC-24. The complete curve from upleg-downleg data was then used to derive the oxygen profile.

Relevant absorption profiles for all the six flights are shown in Figures (5.9) to (5.14). In some cases it was observed that the signal from Ly-α ionchamber kept rising well above the apogee height including the height region of constant unabsorbed incident flux. Fortunately the signal

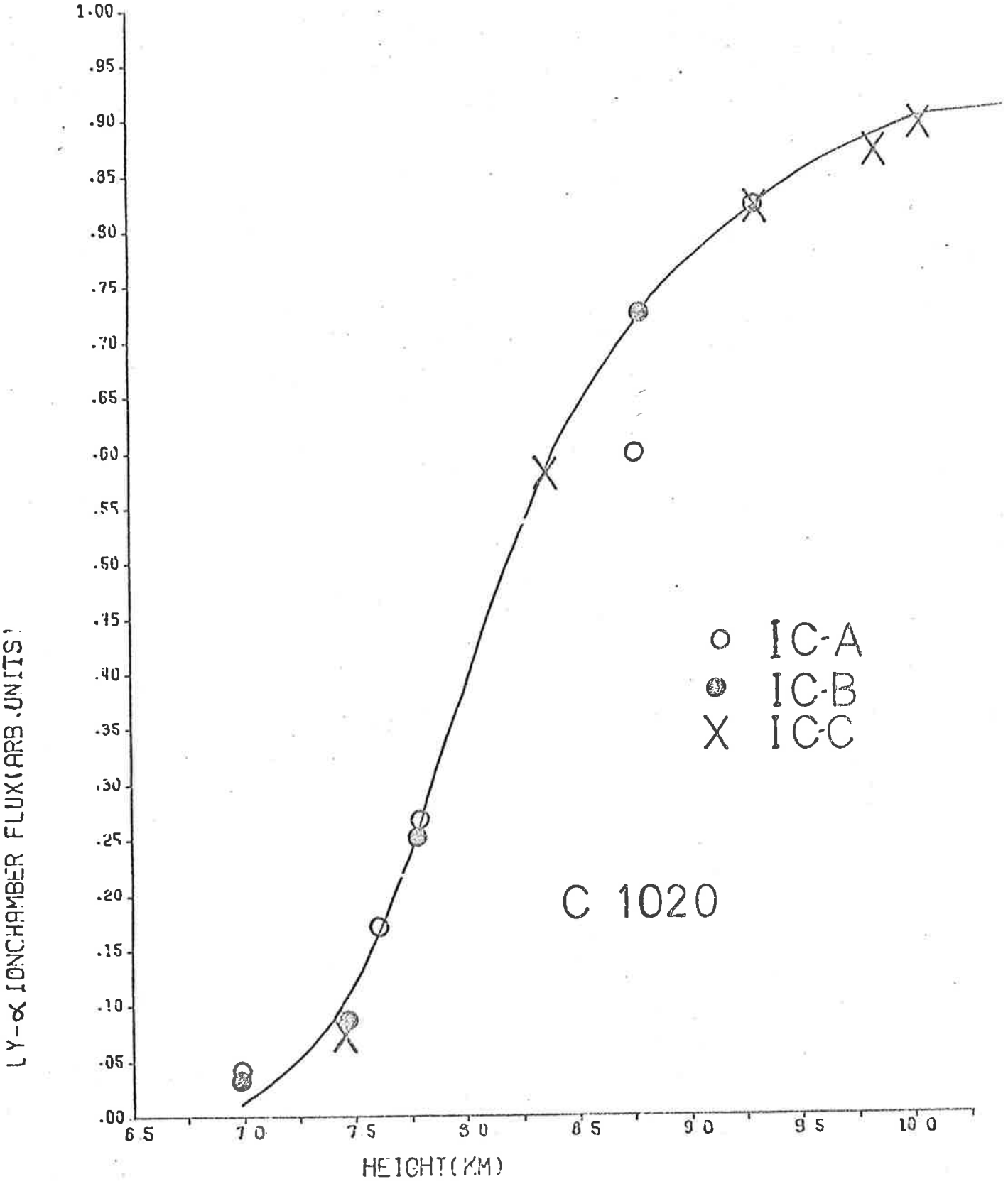

Figure 5.9 Ly-α flux profile (C1020).

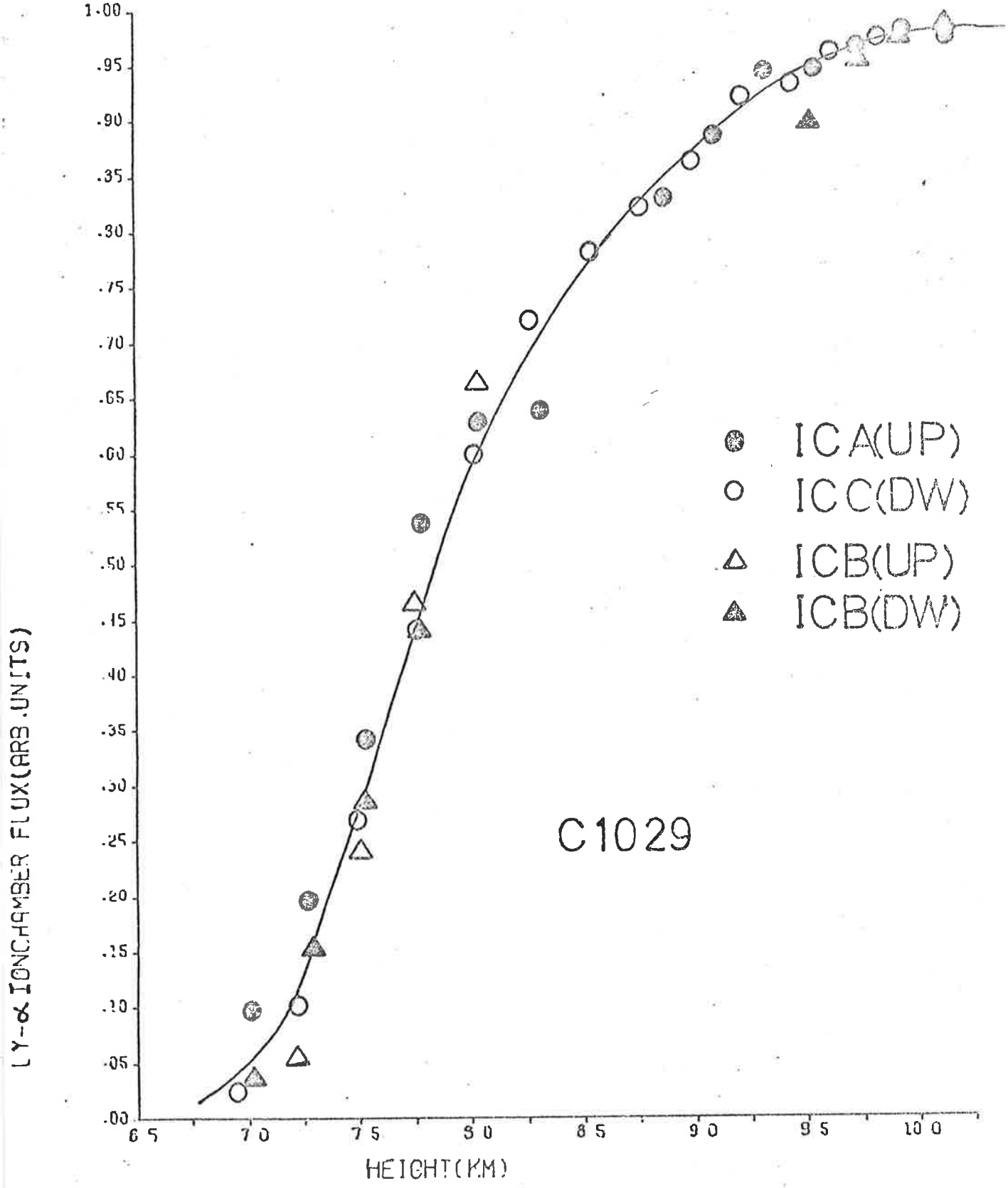

Figure 5.10(a) Ly-α flux profile (C1029).

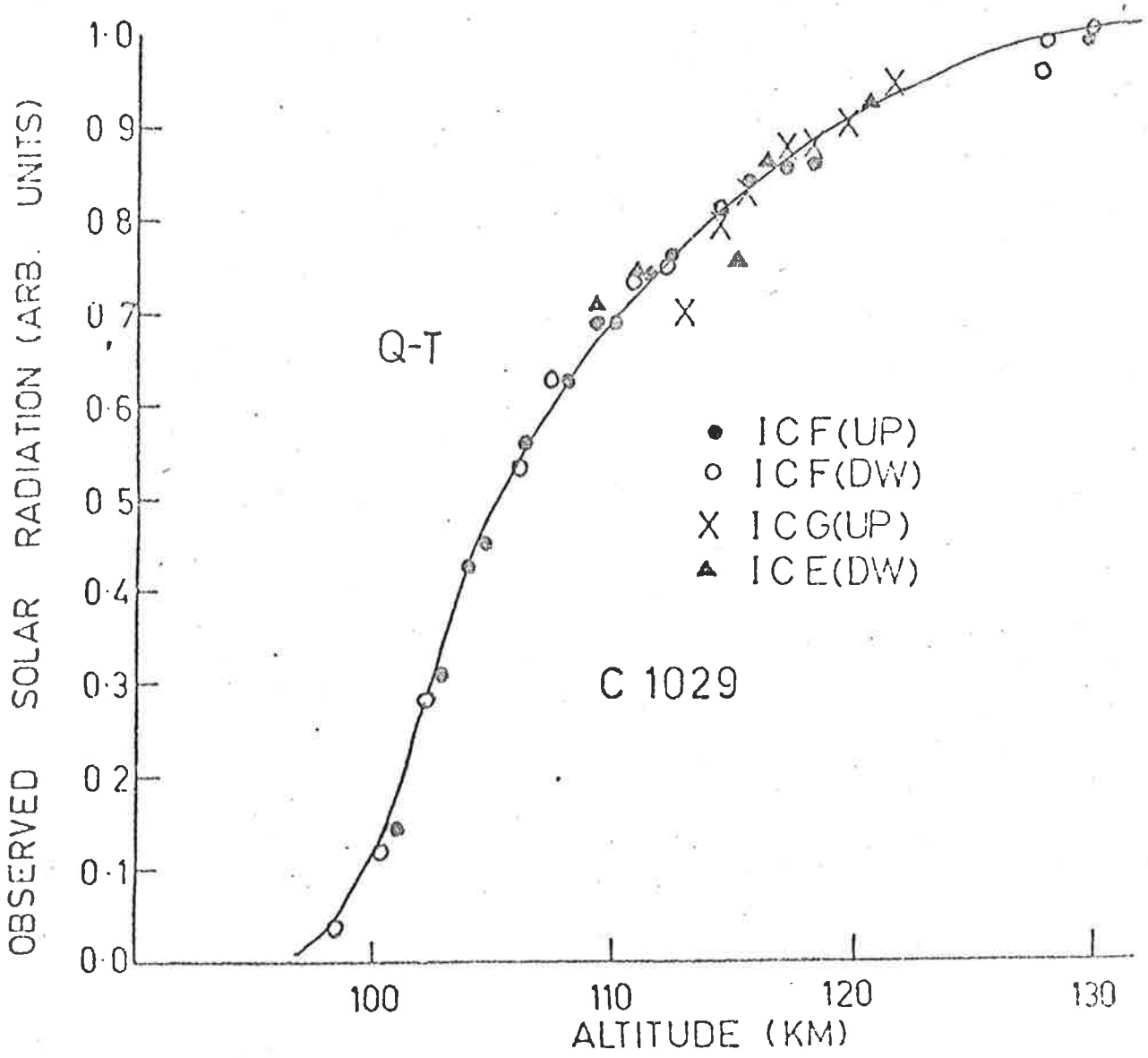

Figure 5.10(b) Flux profile from Q - T ionchambers (C1029).

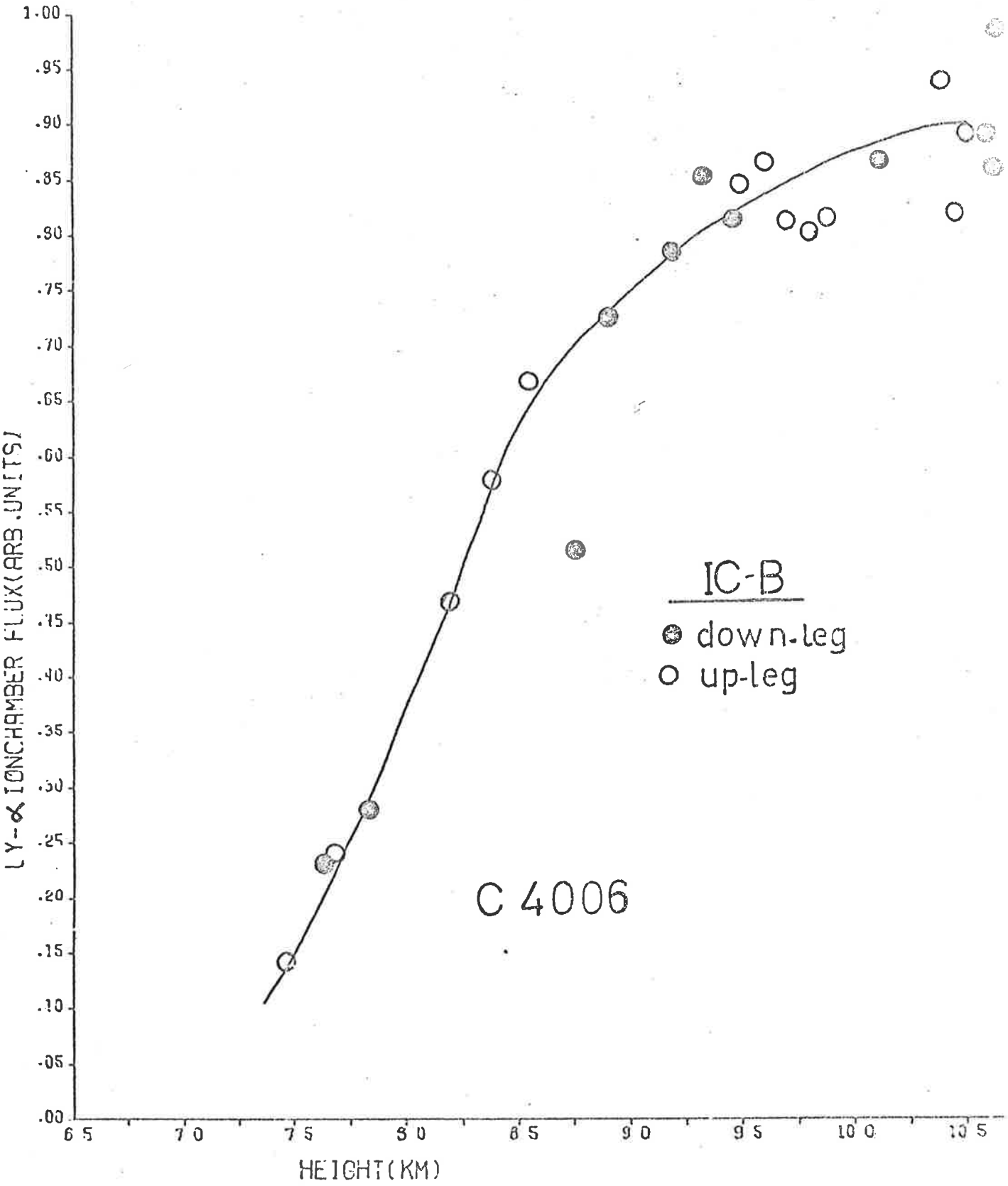

Figure 5.11 Ly-α flux profile (C4006).

became constant on the downleg for each such case well before the rocket entered the absorption region again. The behaviour appears to be due to a sensitivity change during flight until it became stable. A detailed discussion is given separately in Section (5.9) where similar other observations are also discussed. The presence of a constant flux portion in the downleg absorption profiles however ensures the invariability of the detector efficiency on the downleg. Since the density profile is independent of the absolute detector efficiency as long as it remains constant, only the relevant downleg portion is used to derive oxygen densities.

The Q-T ionchambers in later flights registered solar flux at somewhat higher altitudes than expected on the upleg but the signal then rose sharply to a maximum around apogee. Therefore only downleg data could be used. In flights C4007 and C4009, aspect angles were rather large above about 120 km and the flux profiles above these altitudes showed some large aspect modulation. The density profiles from the downleg data of two independent Q-T ionchambers in C4009 were found to overlap at latitudes below 120 km indicating that the downleg data was reliable. The data from below 120 km was found to lie on a straight line when plotted against the overhead oxygen column (Section 5.8) as expected. The scattering in data from flight C4018 has been caused by the unexpectedly high spin rate and a mean profile was used.

5.7.2 Oxygen Density Profiles

As shown in Section (2.2) when the solar zenith angle, Z, in not too large, the number densities can be calculated from the absorption profile by using equation:

$$n_{O_2}(h) = \frac{1}{\sigma_{eff(h,Z)}} \cdot \frac{dI}{I} \cdot \frac{1}{dh} \cdot \frac{1}{Sec Z} \qquad (5.7)$$

The observed absorption height profiles shown in Figures (5.9) to (5.14) were used to obtain $\frac{dI}{I}$ for dh = 1 km. The effective cross-section $\sigma_{eff(hZ)}$ was calculated for each flight as described in Section (2.2.3).

Effective cross-sections for the Ly-α data were calculated using the recent absorption data of Carver et al (1976) at 195° K (Section 2.2.3C).

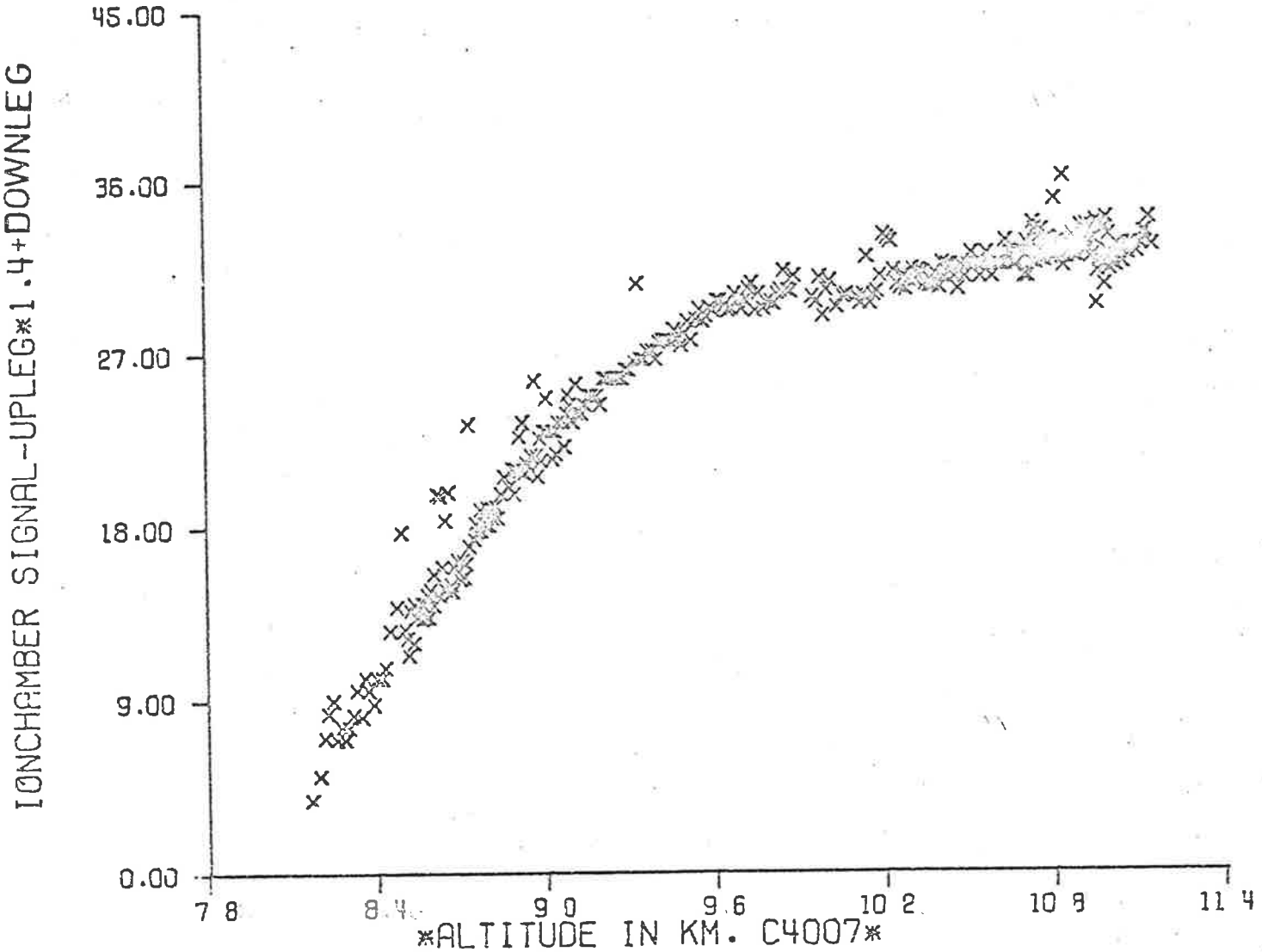

Figure 5.12a Ly-α flux profile - C4007 (up leg and down leg).

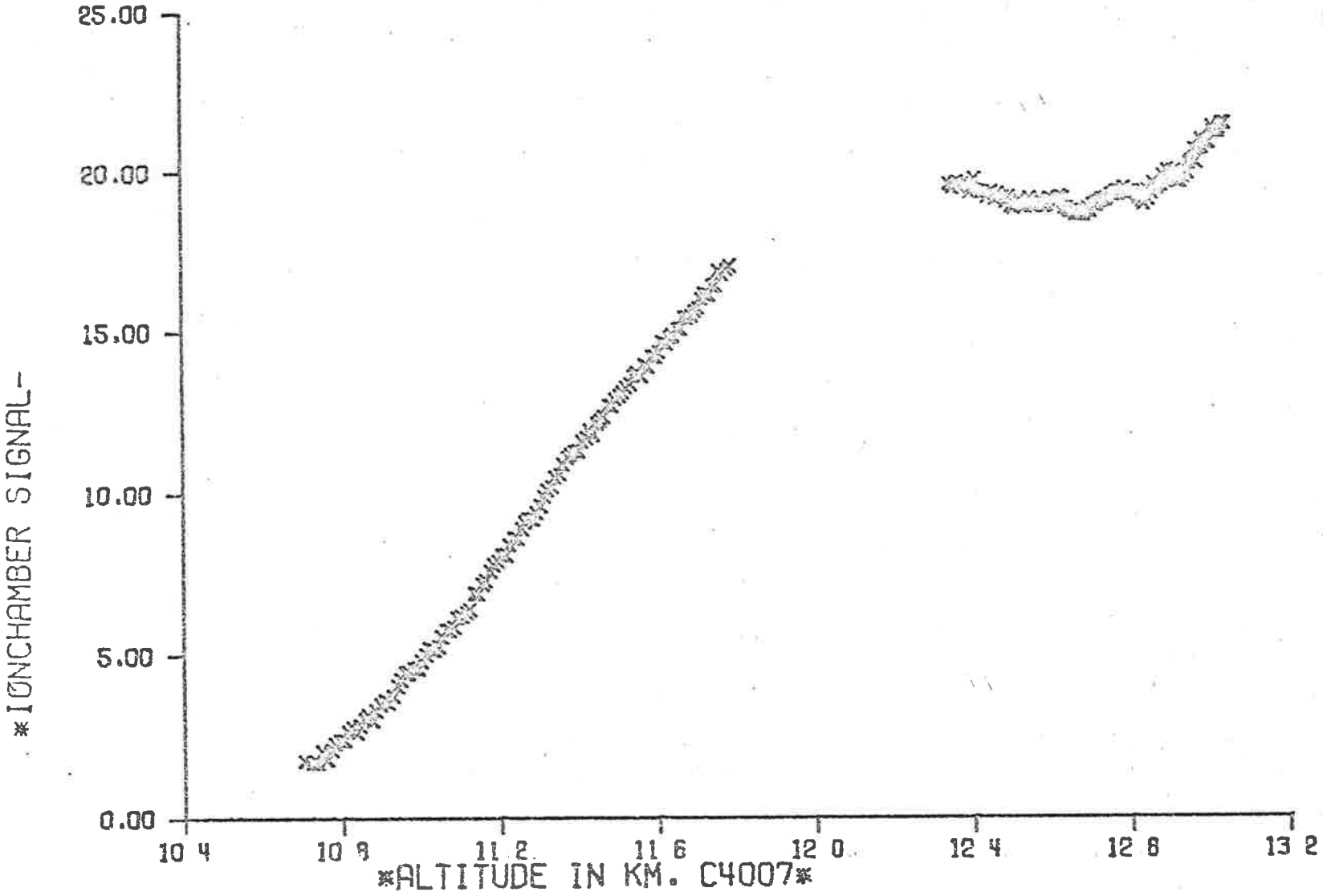

Figure 5.12b Flux profile from Q - T ionchamber - C4007 (down leg).

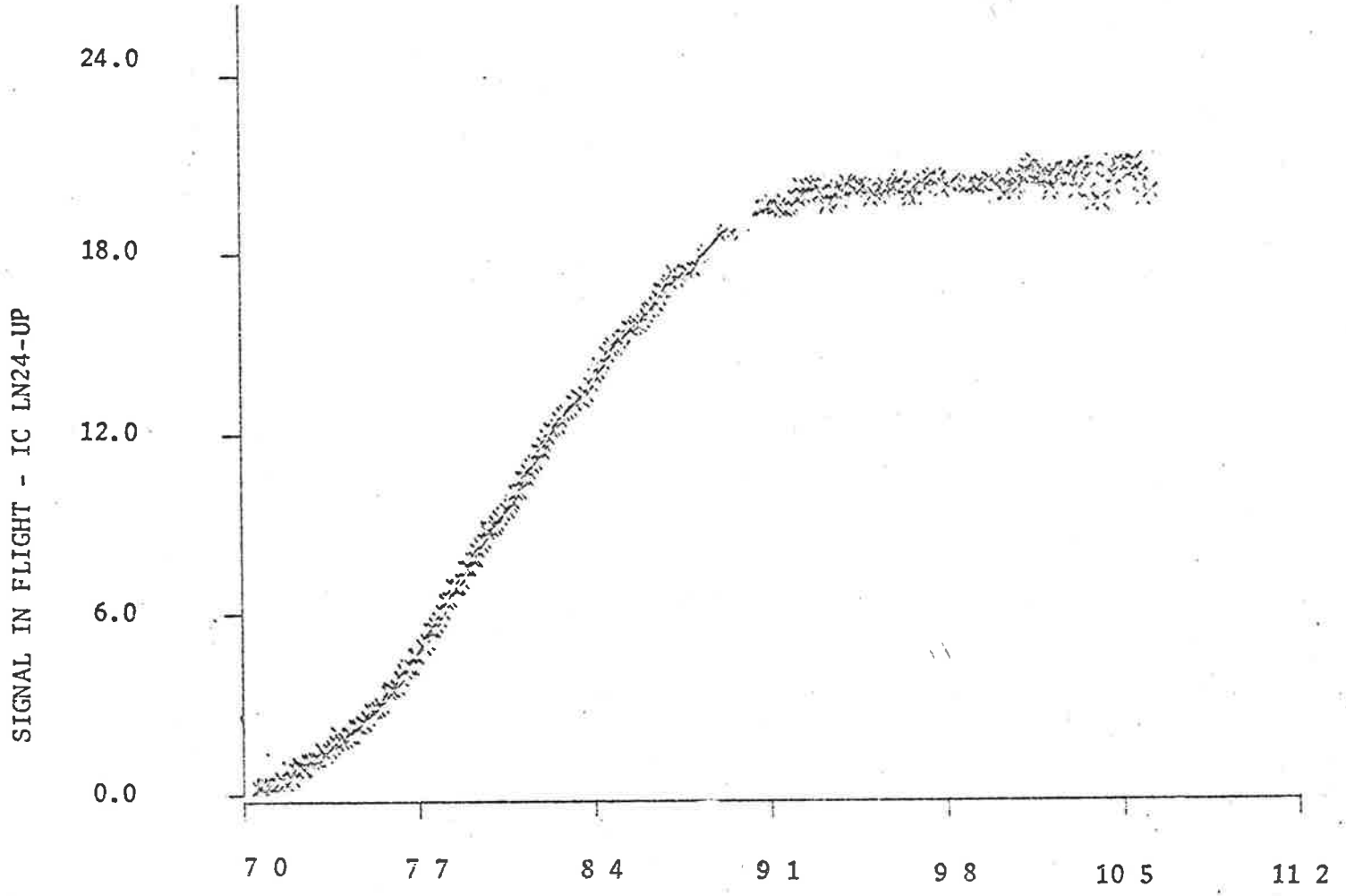

Figure 5.13a Ly-α flux profile - C4009 (down leg).

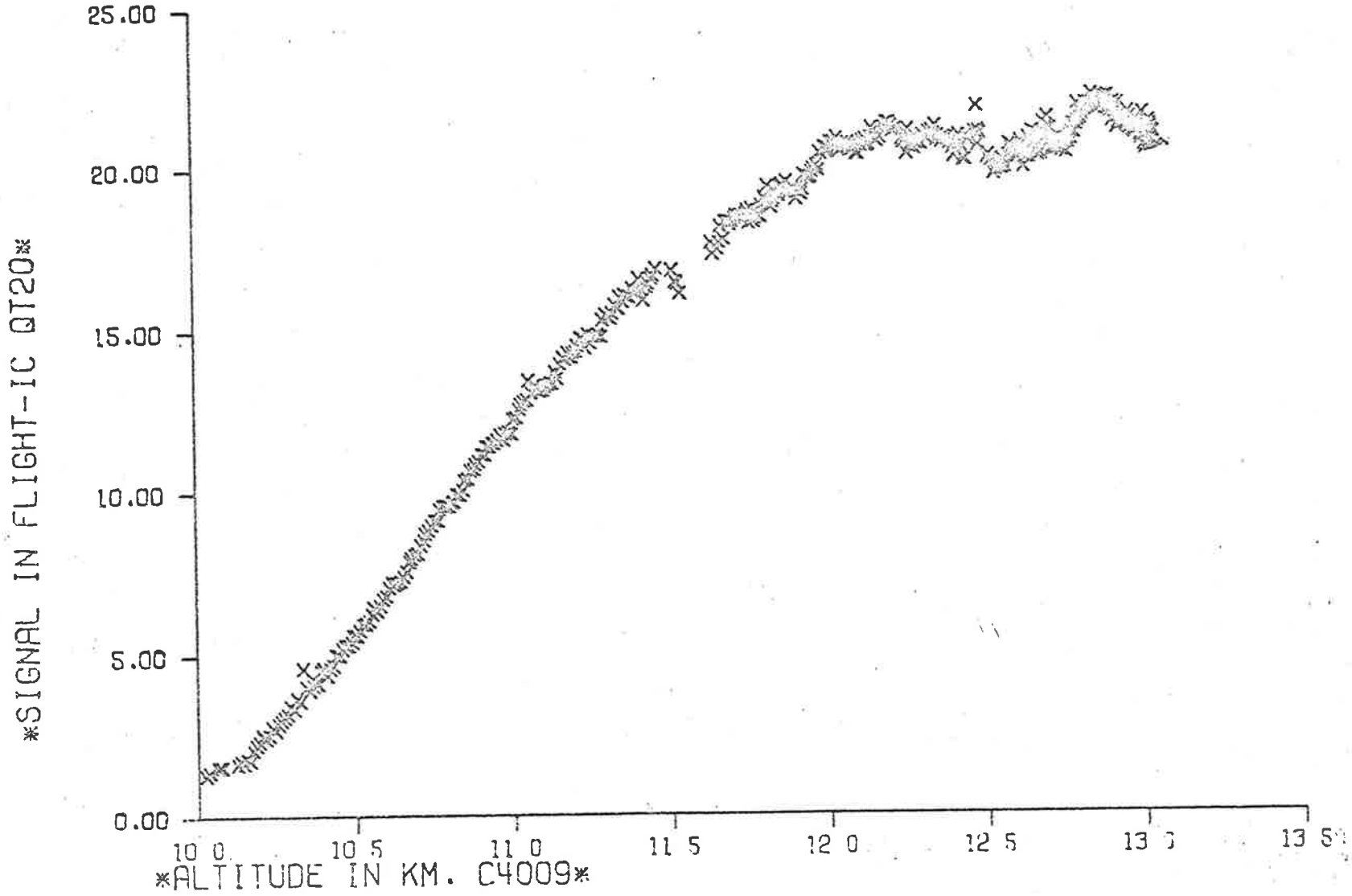

Figure 5.13b Flux profile from Q - T ionchamber - C4009 (down leg).

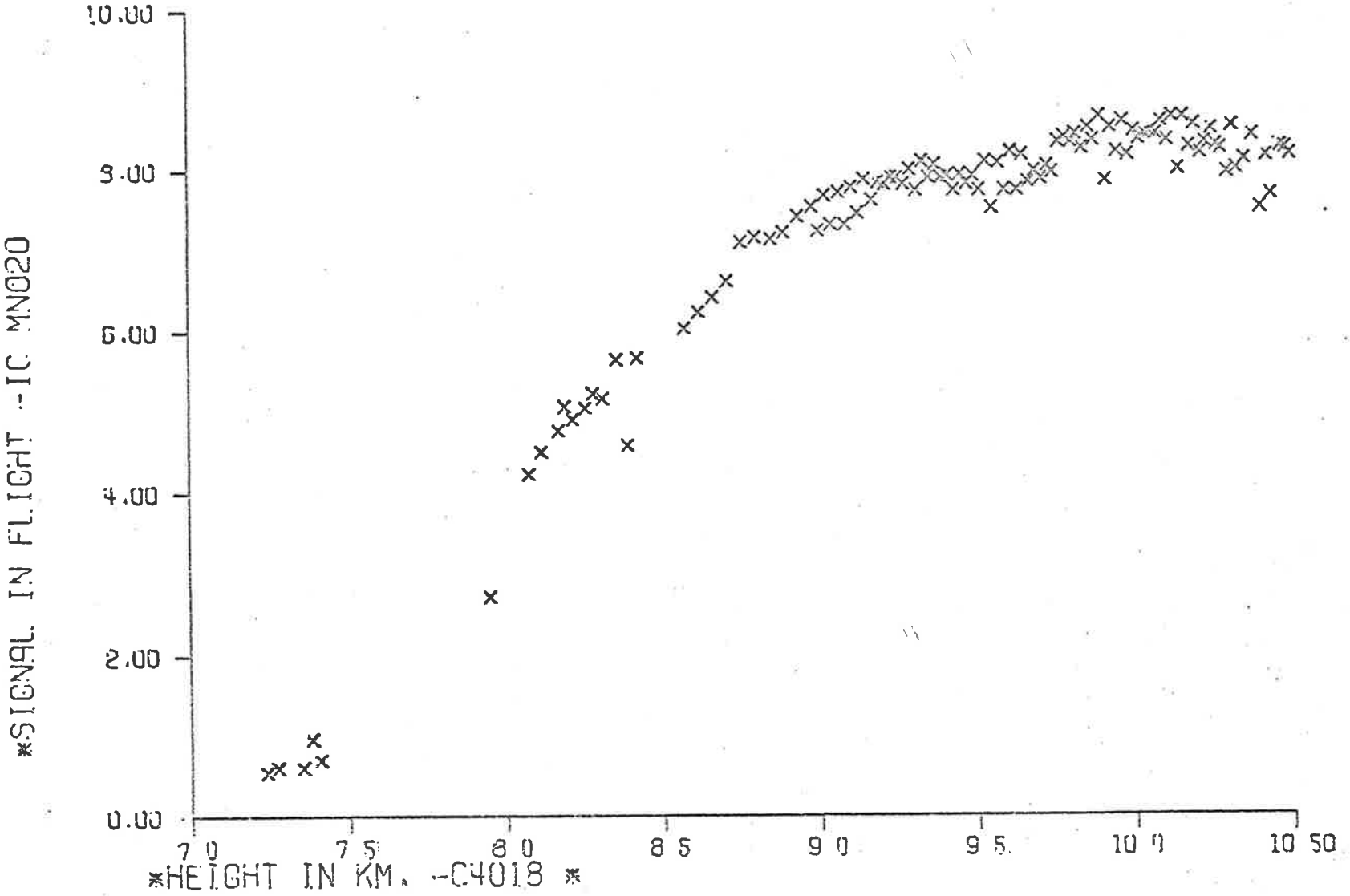

Figure 5.14a Ly-α flux profile - C4018 (down leg).

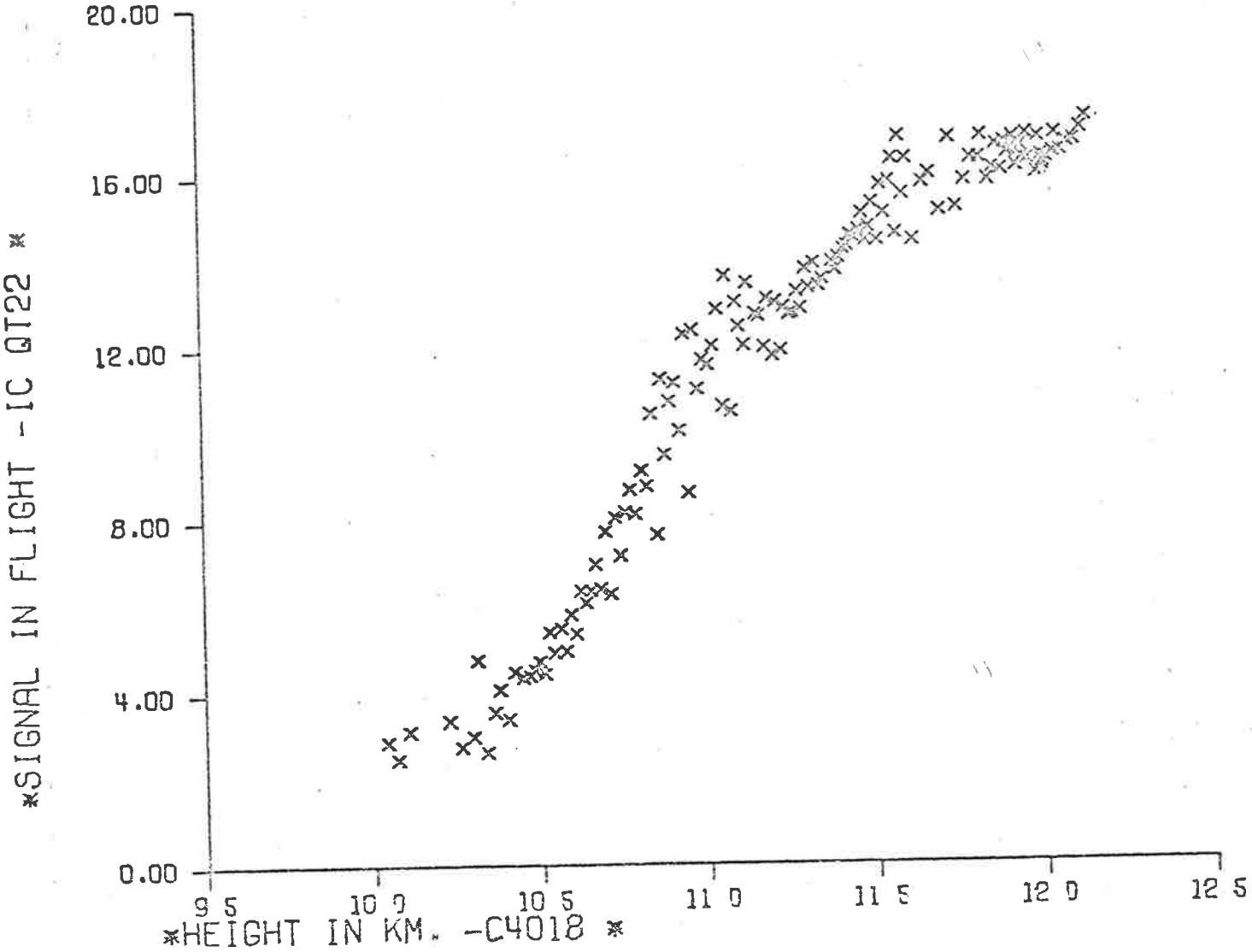

Figure 5.14b Flux profile from Q - T ionchamber - C4018 (down leg).

Results of oxygen densities from both types of ionchambers for each flight are shown in Figures (5.15) and (5.16) and the relevant discussion is presented in Chapter 6.

Random errors in the densities are due to uncertainties arising from the data reduction and noise on the telemetry records. The errors due to telemetry noise are generally less than ±.5% except for the flight C4009. In this case considerable telemetry noise problems in the data were encountered. However, most of the telemetry noise was successfully edited out by not using the data at times where particularly bad noise was present. This can be seen from the discontinuity in the aspect angle data (Figure 5.8). The random errors due to telemetry noise for this flight are believed to be less than ± 5% in the edited data.

The random errors arising from the data reduction would come from two avenues. Firstly, some errors would be introduced while reading the ionchamber signals from flight records. If film records are used then the error is expected to be less than 1% while the digital records would introduce an error of less than 0.2%. Secondly, the errors would be introduced by aspect corrections and would be large in the regions of large aspect angles. Since aspect corrections to individual ionchamber data have been restricted to angles less than 35° (Section 5.7.1), the errors introduced are estimated to be generally less than 2% An additional error is introduced in the mean profiles of the first three flights due to low data acquisition rate necessitating a composite profile from data of all ionchambers. This error is estimated to be about 10% in Ly-α profile of C1020, 5% in Ly-α profile and 2% in Q-T profile in C1029 and about 5% in Ly-α profile of C4006 in the height range where dI/I is a maximum. The error is expected to increase towards each end of the profiles.

This error is expected to be rather small for flights C4007 and C4009 due to high data acquisition rate. The beating effect mentioned in previous section for flight C4018 would result in an additional error of about 10%.

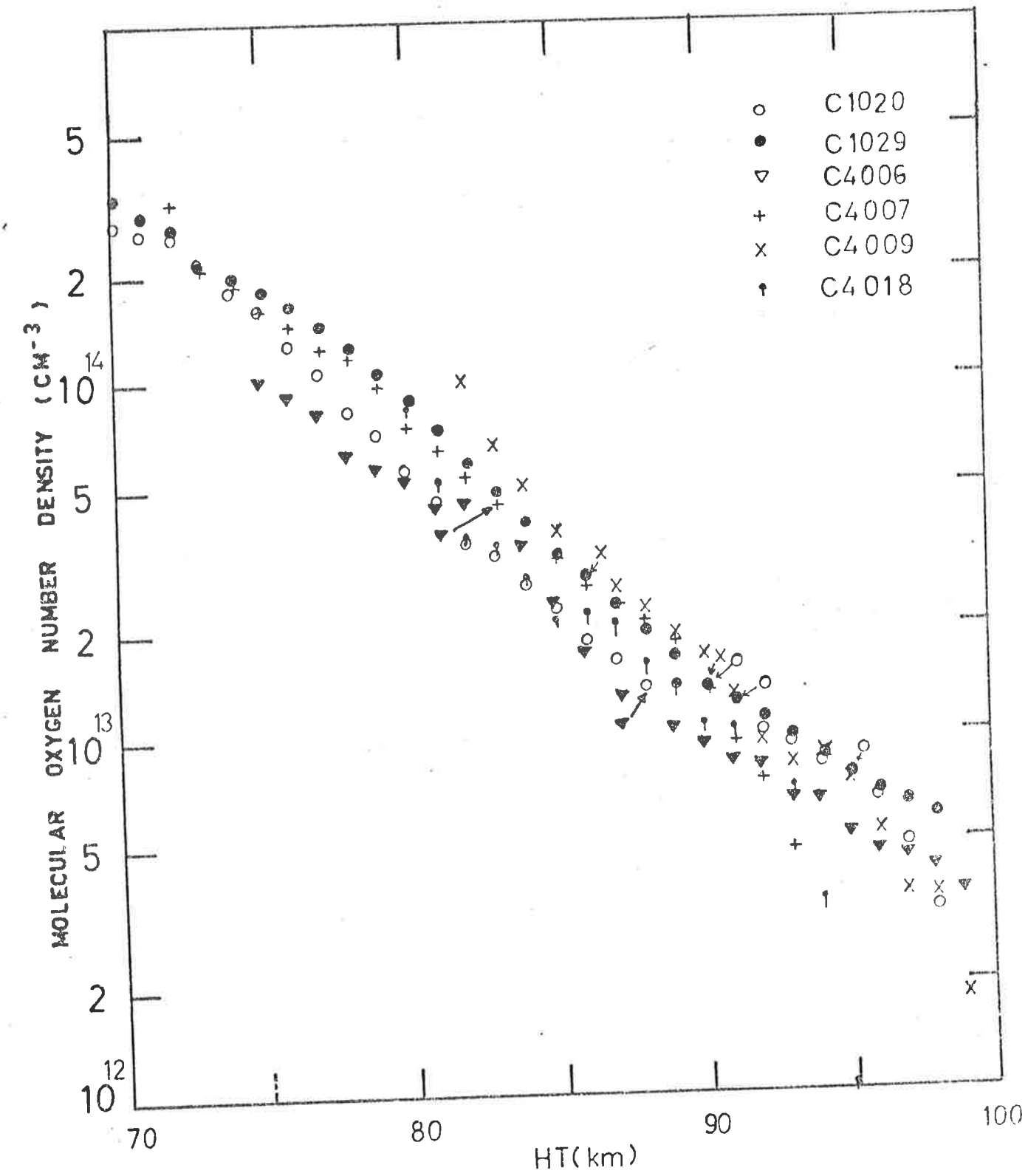

Figure 5.15 Oxygen number densities as obtained from Ly-α ionchambers in this work.

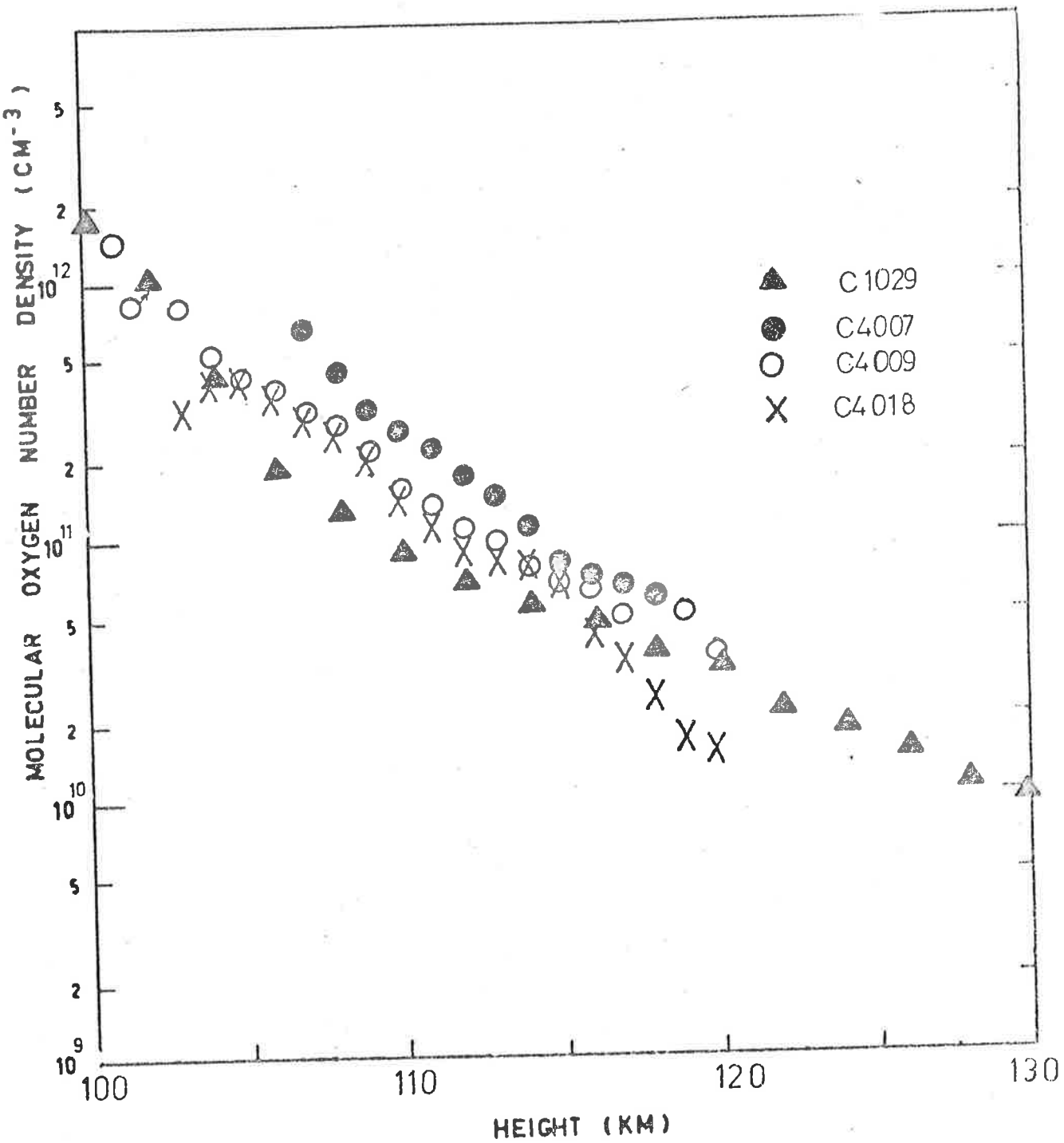

Figure 5.16 Oxygen number densities as obtained from Q - T ionchambers in this work.

The total random errors in the density values are thus expected to be between 3% and 13%. There is a systematic error of ± 2 km in the estimated trajectory of flight C4009 (Section 5.4). The trajectory errors for other flights are less than 100 metres. Additional systematic errors due to effective cross-sections are expected to be about 5% and 10% for Q-T and Ly-α ionchamber data respectively. The latter includes the errors in the Ly-α line profile used for the calculations (Section 1.3).

5.7.3 Temperature Profiles

Oxygen densities derived from Ly-α absorption measurements were used to derive temperature profiles below 95 km where mixing can be assumed (Section 2.5). A computer program was used which enabled computations of temperatures for these and other similar mesospheric oxygen profiles listed in Table (6.1). All the temperature results are presented in Chapter 6.

TABLE 5.2

	DATA ERROR (± %)					TRAJ Error (± KM)
	Tele Noise	Data Reduction		Mean Prof.	Total	
		Recording	Aspect			
C1020	0. 5	1	2	10	13	0.1
C1029	0. 5	1	2	5Ly-$\alpha 2_{QT}$	8(5for) Q-T	0.1
C4006	0.5	1	2	5	8	0.1
C4007	0.5	.2	2	-	3	0.1
C4009	5.	.2	2	-	7	2.0
C4018	0.5	.2	2	10	12	0.1

5.8 RESULTS OF SOLAR VUV FLUX

5.8.1 Introduction

The individual aspect corrected currents from each useful ionchamber can be converted to flux values by using the known effective area of the detector (1.98 cm^2) and its preflight absolute calibration as described in Section (3.8). To obtain the flux above the atmosphere, values of ionchamber currents at heights above which no absorption takes place are required. If this signal is not available directly from the flight data then the observed absorption profile and the resulting oxygen profile together may be used to obtain an extrapolated value of unattenuated signal as shown below.

From the derived oxygen profile an estimation of the scale height, H, is made. Suppose this scale height can be used to describe the distribution above a height h_{min}, i.e.

$$n(h) = n(h_{min}) \exp [-(h-h_{min})/H] \qquad (5.8)$$

for all values of h greater than h_{min}. Then

$$\ell n\, I(h) = \ell n\, Io - \sigma\, N(h)\, F(z,h)$$

$$= \ell n\, Io - \sigma\, N(h_{min}) F(z,h) \exp[-(h-h_{min})/H] \qquad (5.9)$$

where Io is the ionchamber signal above the oxygen absorption and N(h) is the oxygen columnar density above the height h.

Therefore, a plot of the logarithm of the ionchamber current against the slant oxygen mass is made. The latter is given by $N(h)/N(h_{min})^* = \exp [-(h-h_{min})/H]$, where H is the scale height from the observed oxygen profile.

The straight line graph so obtained can be extrapolated to zero slant oxygen mass to obtain the value of Io. The above method of extrapolation may be used to obtain values of Io in general. Recently Hall (1972) has outlined a specific method for obtaining Io for Ly-α ionchambers.

---

* Since the oxygen slant mass = $\exp [-(h-hm)/H] = N(h)/N(hm)$; a model atmosphere such as CIRA72 may be used to obtain N(h)/N(hm) as a function of height directly. The use of expression $\exp [-(h-hm)/H]$ instead does mean the use of the same flux data through H and thus more appropriate value of extrapolated flux Io.

Further discussion is therefore presented separately for Ly-α and Q-T ionchambers.

5.8.2 Flux from Ly-α Ionchamber (121.6 nm)

The problem for the Ly-α ionchambers is of a different nature. The absorption profile at altitudes below about 90 km is purely due to Ly-α. However at higher altitudes, the radiation other than Ly-α in the detector pass-band (105 (114) - 135 nm) also contributes in the detector signal and this contribution increases with altitude. Since the absolute contribution of other radiation may vary from one observation to another (Section 2.4), it becomes necessary to obtain an extrapolated value of Io just for Ly-α from the absorption data below about 90 km. The maximum recorded ionchamber signal above about 110 km can then be used to estimate the other radiation contribution. Sometimes the flatness in the ionchamber signal around 100 km is clearly evident before the signal begins to rise again due to the other radiation. This flatness may give a direct measure of Io and should thus be close to the otherwise extrapolated value.

Hall (1972) has outlined a method for obtaining an estimated value of Io by using the absorption profile and a pressure profile from the model atmosphere appropriate for the time of observation. The method is relatively simpler and perhaps more accurate. He has plotted a curve between $p/K \cos \chi$ and I/Io where p is the pressure, K is a constant, χ is zenith angle at the time of observation and I/Io is the relative ionchamber signal. The plot is shown in Figure (5.17). A value of p at some height h is obtained from a model atmosphere for the time of observation and the quantity $p/K \cos \chi$ is obtained. If the value of I(h) is known then Io can be obtained from the graph (based on the observed value of I at the height h). This method has the advantage that Io can be obtained relative to values of I at more than one height and the internal consistency can thus be checked.

In the present measurements, both methods were used for several flights and the results were found to be generally in good agreement. The

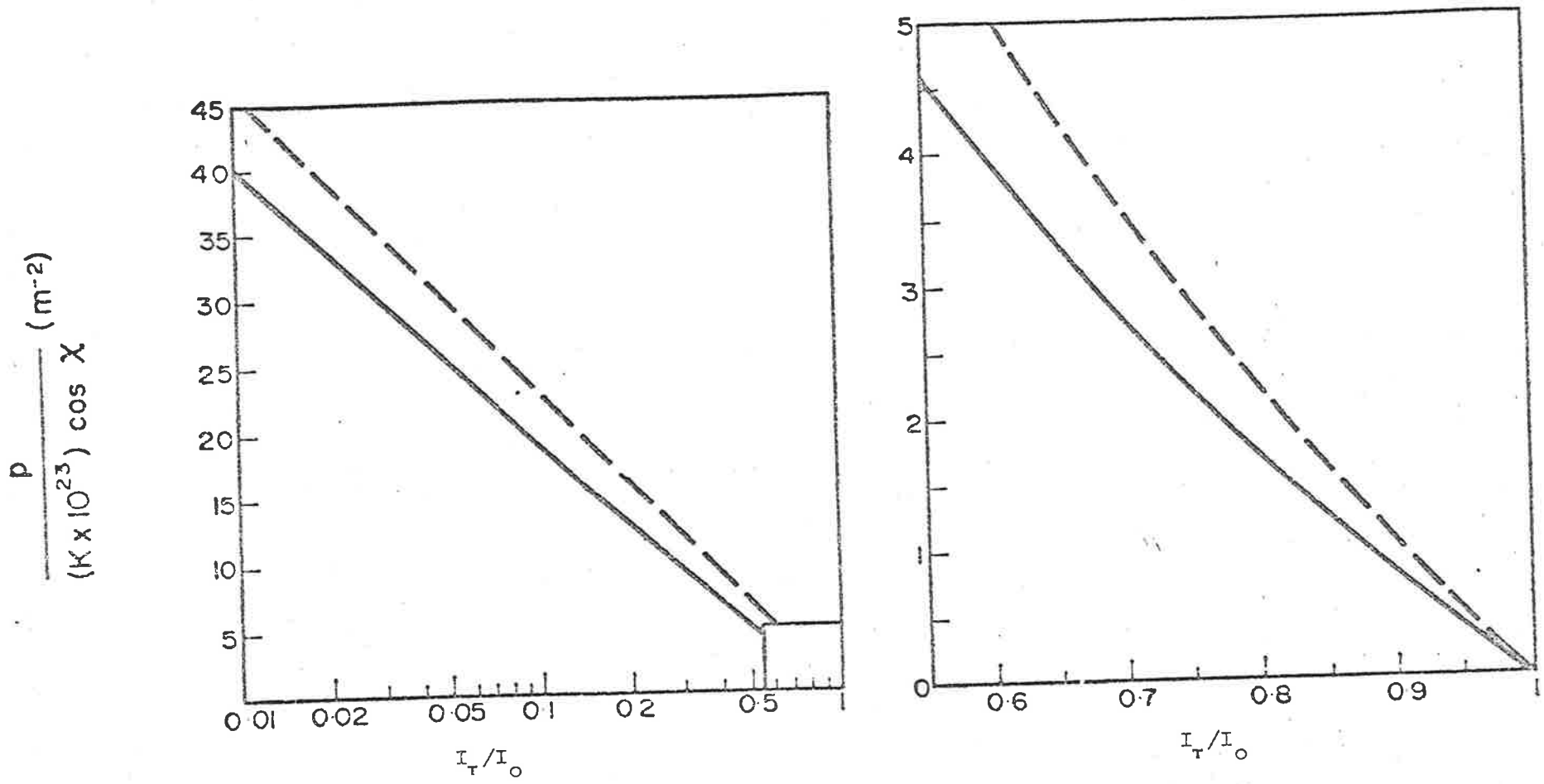

Figure 5.17 The plot of relative Ly-α intensity against pressure for calculations of unabsorbed flux (After Hall, 1972).

results reported here are therefore based on the estimated values of Io by Hall's method.

The conversion of this maximum ionchamber signal Io into absolute Ly-α flux is straight forward and involves only the known absolute quantum efficiency of the detector at Ly-α as measured before the flight. Results of the estimated Ly-α flux for each flight are presented in Table (5.3) and a further discussion is given in Section (6.4).

5.8.3 Flux from Q-T ionchamber (155 - 169 nm)

The values of Io were obtained by extrapolation for all the Q-T ionchambers because in neither case, the absorption profile data was available at altitudes of zero extinction mainly because the rocket apogee height was not high enough (Section 5.7.1).

The Q-T ionchambers respond to radiation in the wavelength band 155 - 169 nm (Figure 3.9). To obtain solar flux values from the Q-T ionchamber current measurement, obtained as described above, it was assumed that the solar continuum spectrum in these wavelength bands could be represented by that of a black body at temperature T. The laboratory calibrations of the efficiency (Section 3.8.3) and spectral response (Section 3.8.2) of the ionchamber was then used to calculate the ionchamber current which would be produced for different values of T. In this way, a brightness temperature was deduced which agreed with the rocket observations. The contributions of emission lines to the ionchamber currents were estimated using the solar spectral data of Detwiler et al (1961 a, and b), a portion of which has been presented in a convenient digitalized form by Brinkman et al (1966). This contribution was 4.5% for the Q-T ionchamber.

In cases where upleg data was spurious (Section 5.7.1), only the downleg data was used for extrapolation of flux to zero extinction and the useful absorption data were found to lie on a straight line when plotted against absorbing column as expected. The results of solar brightness temperatures are presented in Table (5.3) and a comparison with other

similar measurements is made in Section (6.4).

TABLE 5.3

Rocket Payload	Ly-α flux (ergs/cm^2/sec)	156-168 nm solar flux (Equivalent Black Body Temperature).
C1029	2.18 ± 0.40	(4570 ± 30) K
C1035	3.26 ± 0.30	(4580 ± 40) K
C4006	3.12 ± 0.45	
C4007		(4500 ± 50) K
C4009	2.15 ± 0.50	(4440 ± 50) K

5.9 IONCHAMBER SENSITIVITY CHANGE DURING FLIGHT

5.9.1 Introduction

In several ionchamber experiments, an effective change in the detector sensitivity during a rocket flight has been observed. This generally results in a discrepency between upleg and downleg absorption profiles. The detector signal keeps rising in a height region of constant flux where ideally it should not show any change in signal. This continuous increase is equivalent to and may be explained by a continuous change in the effective sensitivity.

The most commonly used detectors with which this problem has been experienced are Ly-α ionchambers. In a rocket experiment, if a detector behaves in this fashion then the data may be used for further analysis only if there is evidence that the detector's effective sensitivity ceased

to change at some time during the flight and the data beyond this time thus remained unaffected. In such a case, while the rocket traverses a constant flux region*, if the detector signal becomes constant at some time before the rocket enters the absorption region again on the downleg, the downleg data may safely be used for obtaining a vertical distribution.

In some of our rocket flights this behaviour of inflight effective sensitivity change was experienced. Fortunately in all such cases the detector sensitivity became stabilized before the rocket entered the absorption region on the downleg thus allowing the use of the downleg data. However an attempt was made to evaluate the coefficient of rate of change and its use for correction of the data to see if in the corrected data, upleg was comparable to the downleg.

5.9.2 The Results of Ionchamber Sensitivity Change and its Correction

Suppose at a time T_o (to be termed as recovery time for reasons given later) the detector signal becomes stabilized where T_o is a time when the rocket is above the absorption region and hence the constant signal region. Therefore the effective sensitivity of the detector may be assumed to remain constant say α_o at all times until impact after T_o. Suppose at some other time t prior to T_o but still in the region of constant flux, the detector efficiency is $\alpha(t)$ such that

$$\alpha(t) = \alpha_o - \beta(T_o - t) \tag{5.10}$$

where β is a constant equal to the rate of change of the efficiency.

Since at times t and T_o, the true intensity is the same, the measured intensities at the two times are related to the true intensities by the relation:

$$I_{mo} = I_o \alpha_o \tag{5.11}$$

and

$$I_{mt} = I_o \alpha(t)$$

or

$$I_{mt} = I_o (\alpha_o - \beta (T_o - t)) \tag{5.12}$$

---

* This varies from one type of ionchamber to another type. The constant flux region for a Ly-α ionchamber may be typically above 100-110 km.

Subtracting equation (5.12) from equation (5.11), we obtain:

$$\beta = \frac{(I_{mo} - I_{mt})}{(T_o - t)} \cdot \frac{1}{I_o} \qquad (5.13)$$

Having calculated β from the data in the constant flux region, we may use it to correct the observed signal at other times including the absorption region for the effective sensitivity change assuming that the rate of change remained constant prior to T_o. The true signal I_T at a time t_1 may thus be obtained through equation (5.12) i.e.

$$I_T(t_1) = I_M(t_1)/1-\beta(T_o-t_1) \qquad (5.14)$$

Generally a Cockatoo vehicle's apogee is above 125 km which means that the above analysis can be successfully applied to the Ly-α ionchambers.

For illustration, time and height absorption profiles for a Ly-α ionchamber from one of the present rocket flights are shown in Figures (5.18 and 5.19). The effect of inflight effective sensitivity change is clearly evident from the height absorption profile.

Values of T_o were obtained from time-absorption profiles similar to Figure (5.18) for all the useful ionchambers which suffered this problem. The values of β_o were then obtained as described above which were used to obtain the curves of effective detector sensitivity $\alpha(t)$ as a function of time prior to T_o. The values of $\alpha(t)$ so obtained were then used to obtain profiles corrected for sensitivity to be equal to α_o. The corrected flux data at several points for one of the ionchambers is shown in Figure (5.19) along with the originally observed data. The upleg is found to almost superimpose on the downleg data thus illustrating the validity and effectiveness of this analysis. Similar results were obtained for other ionchambers. The values of β and T_o were found to be (0.0021/sec, 240 sec), (0.0046/sec, 230 sec), and (0.0081/sec, 240 sec) for LNO-24 (C4007), LNO-24 (C4009) and MNO-20 (C4018) respectively.

In Figure (5.20) are shown the curves of $\alpha(t)$ as a function of flight time for these ionchambers. It is striking to note that the complete recovery time $-T_o$ - is about the same for most of these ionchambers.

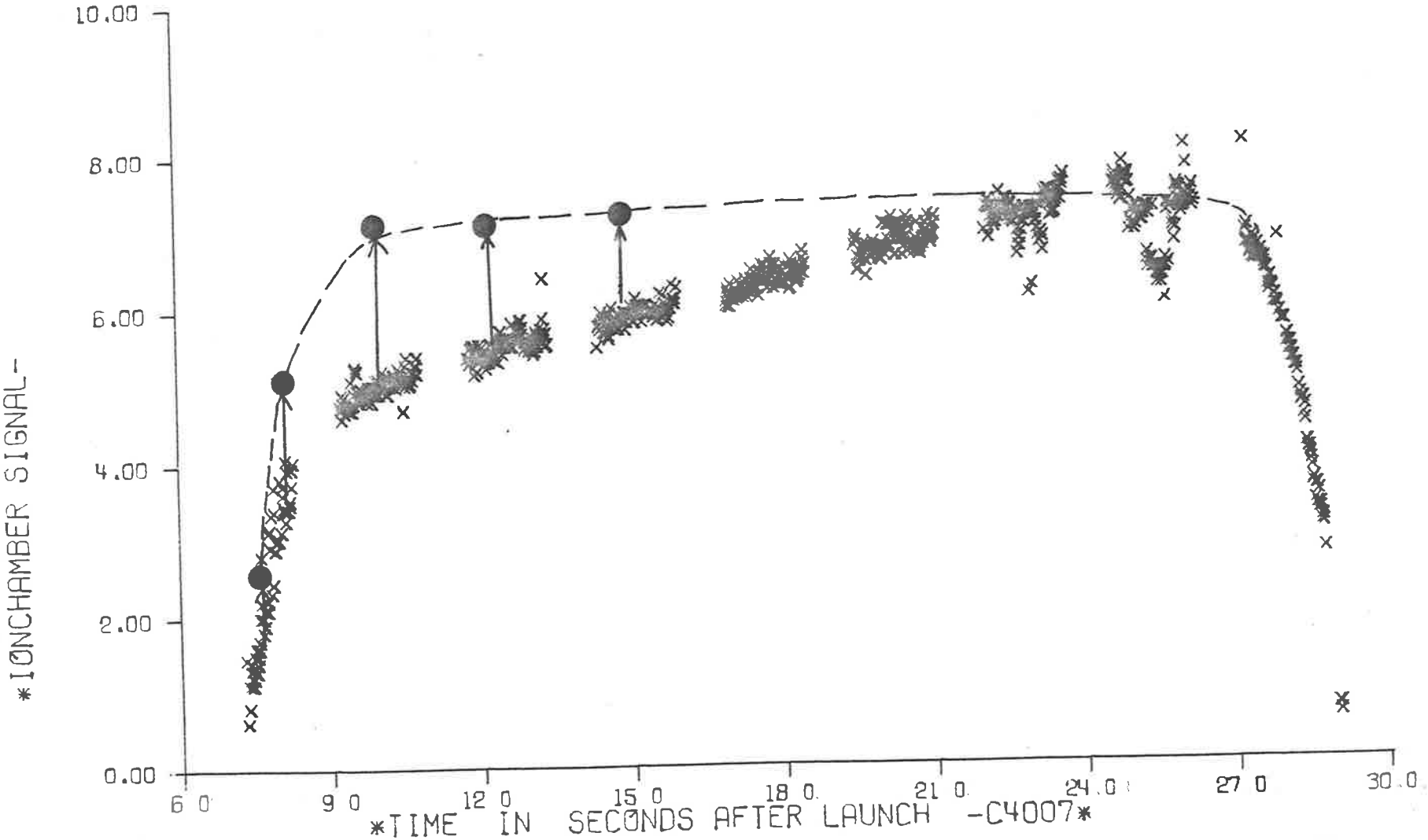

Figure 5.18 Ly-α ionchamber signal during a flight. Also shown are data points after correction for in-flight sensitivity change (●--).

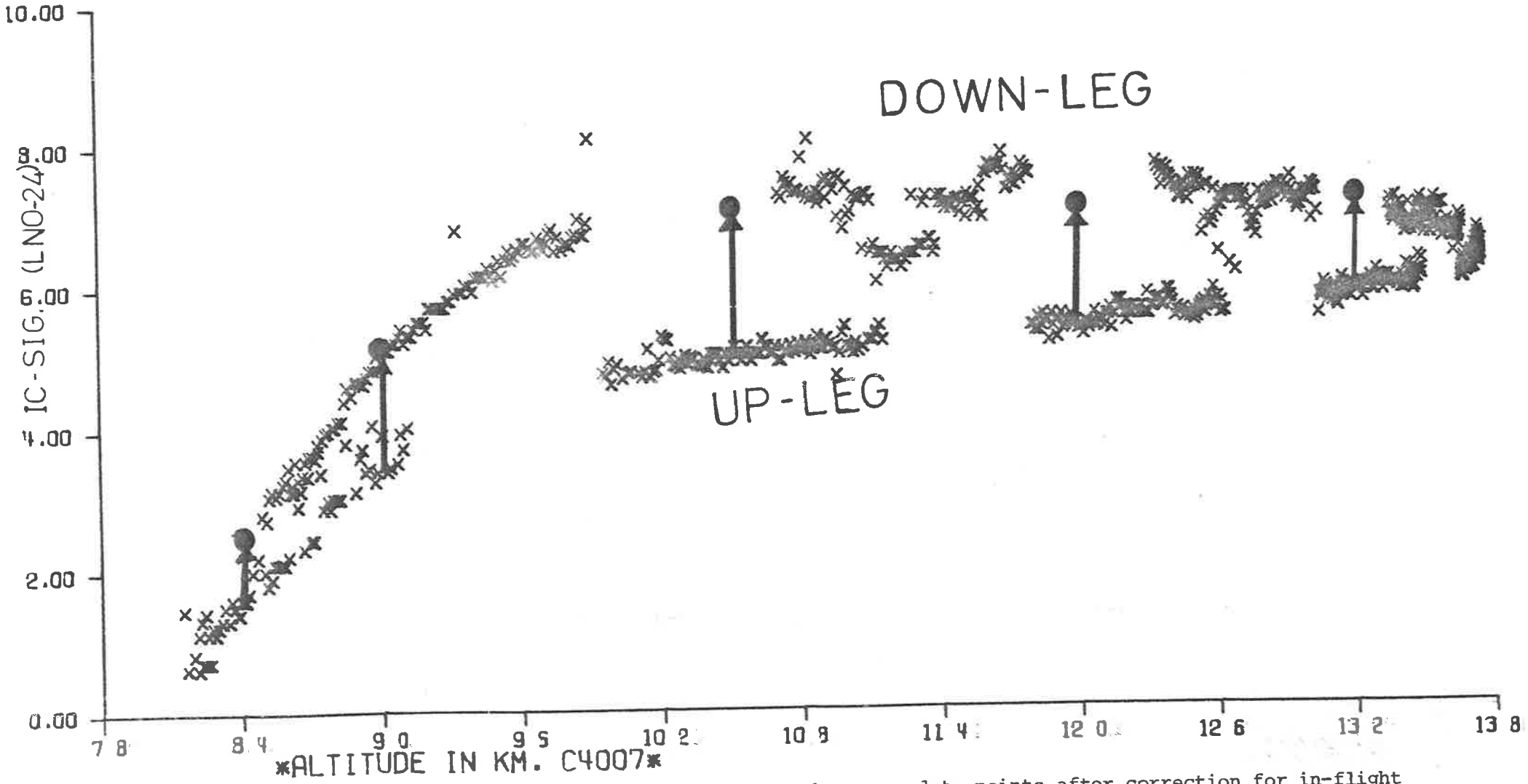

Figure 5.19 Ly-α ionchamber signal during a flight. Also shown are data points after correction for in-flight sensitivity change (●).

It may also be noted from this figure that if the values of $\alpha(t)$ are extrapolated to the time axis then in some cases (perhaps as a result of large contamination) the effective sensitivity may be almost zero and the detector may not show any signal even at heights where it receives significant radiation.

Higashino et al (1966) have reported time absorption profiles for two Ly-α ionchambers which are very much similar to our Figure (5.19). In another rocket flight, Friedman et al (1951) observed a significant upleg-downleg discrepency in the height absorption profile for one of the two Ly-α ionchambers.

More recently, Weeks (1975a) has reported that in his two recent rocket flights, he observed this type of upleg-downleg difference in Ly-α ionchamber data. Similar results of inflight sensitivity change have been reported by Brannon and Hoffman (1971) for Ly-α ionchamber and by Weeks and Smith (1968), Wildman et al (1969) and Weeks (1975b) for S-X ionchamber. It must be pointed out that this inflight sensitivity change behaviour, if present,may become evident only if either both upleg and downleg data are available from a flight or at least the upleg data extend to well above the absorbing region of radiation in the detector band.

Obviously, the upleg-downleg discrepency will result in spurious upleg density profile if the rate of sensitivity change is large. However, if the rate is rather small such that over a limited height region, say 70-95 km, the overall change is small, the upleg densities can be in good agreement with the more reliable downleg densities despite the observed sensitivity change. This was the case with one of the ionchambers in flight C4007. Some of the anomalous results such as those of Subbaraya et al (1974) and Grobecker (1971) may be partly as a result of this effect who apparently used only upleg data of a single Ly-α ionchamber flown in either case.

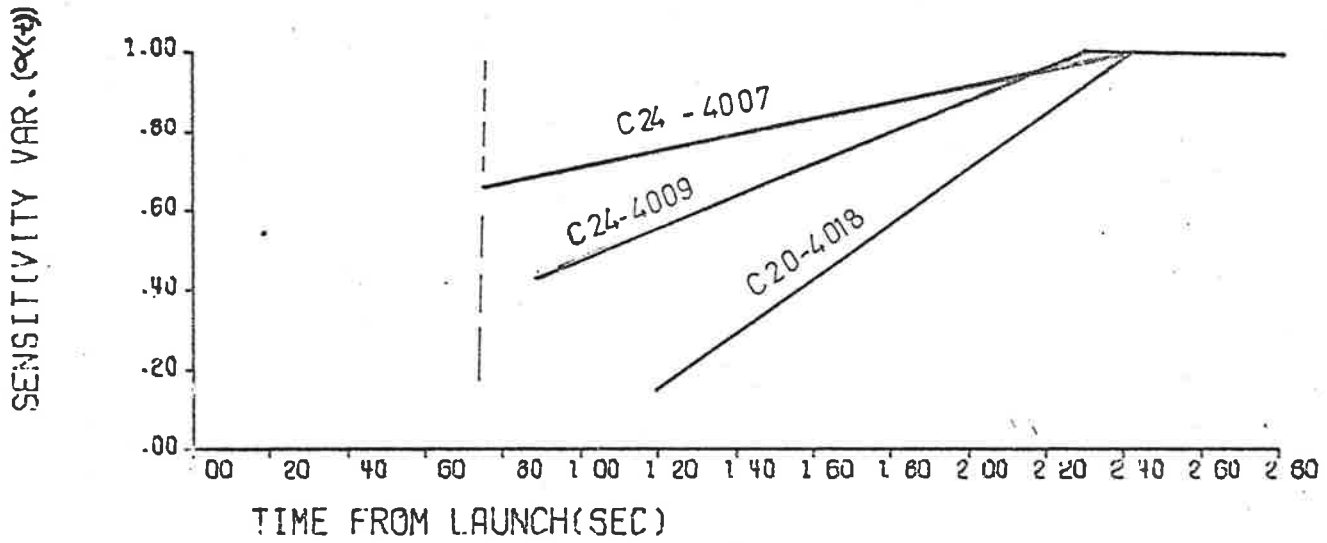

Figure 5.20 In-flight sensitivity variation of several Ly-α ionchambers.

5.9.3 Discussion and Conclusions

A Ly-α chamber may show effective sensitivity variation if some contaminant film particularly water vapour is deposited on the outside of the window prior to flight and thus reducing the effective sensitivity of the ionchamber by absorbing a part of the radiation as explained in Section (3.7.2). However, if during the flight, this contaminant film slowly but continuously evaporates due to the heating near the skin thus decreasing the amount of radiation absorption due to this film, the effective sensitivity will increase continuously as a result until the time T_o when all of it has been evaporated off. It must be pointed out that this contamination of the wondow from outside, generally by water vapour, is different from the water vapour contamination of the ionchamber gas inside the chamber. In the latter case although the effect is to reduce the overall ionchamber sensitivity including at Ly-α, the sensitivity remains constant throughout the flight while in the first case a continuous sensitivity change is the result which renders the data useless.

The behaviour of inflight sensitivity change was exhibited mainly by ionchambers flown in the last three flights. In these flights, ionchambers were installed in the payload about 2 weeks prior to the flight compared to about 2-3 days only in the earlier flights. It appears that in the latter case, despite precautions, the ionchambers got contaminated by water vapour to various degrees during this relatively long period. Another possibility is the outgassing of water vapour from the payload itself until the recovery times T_o. The similar values of T_o for all the three flights lends some weight to this possibility.

We have also considered the deposition of contaminant film from the pump oil during the ionchamber calibrations on the monochromator. Taylor et al (1965) have shown that under an imperfect vacuum, UV radiation can result in the deposition of a contaminant film which deminishes the transmission of an optical window such as LiF and thus reducing the overall sensitivity of the detector. A significant amount of such a film may also

produce results similar to those discussed above by slow evaporation of the film during flight. However it seems most improbable for present detectors since the absolute calibration on the monochromator was done at a few and rather short intervals. The routine sensitivity checks were carried out under atmospheric conditions with a d.c. lamp as described in Section (3.7).

Higashino et al (1965) have attributed this effect to an atmospheric cleaning effect meaning that the window transmission is increased from its laboratory value as the rocket traverses the very low pressure region of the upper atmosphere. Our results of Ly-α fluxes assuming α_o to be the same as the laboratory value are generally lower than the otherwise mean values. A cleaning effect would have meant these flux values to be much higher than the mean values.

We thus conclude that this behaviour is mainly caused by some kind of window contamination perhaps by water vapour. Therefore care should be taken to keep ionchambers under dry atmosphere in the preflight phase and only downleg data should be used for obtaining vertical oxygen distribution if such a behaviour of inflight sensitivity change is observed. In our payloads dry nitrogen was generally used to flush the payloads prior to flight but still these problems were encountered.

5.10 SUMMARY

Six mesospheric and four lower thermospheric oxygen profiles have been successfully obtained from the present series of rocket flights. This mesospheric data have almost doubled the small southern-hemisphere data and represent a significant addition to the overall mesospheric oxygen data. The thermospheric data represent an important contribution to the relatively small amount of oxygen data in the important region of 100 - 115 km which has been yet too low for mass-spectrometric measurements. Unfortunately little success was made in measuring any diurnal variations in O_2 despite four

separate attempts. Nevertheless, the series of flights did provide useful data on seasonal variations at Woomera. Additional useful information on solar VUV fluxes have been obtained.

CHAPTER 6.

DISCUSSION AND COMPARISON OF MOLECULAR OXYGEN DENSITY, TEMPERATURE AND SOLAR VUV FLUX

6.1 INTRODUCTION

As mentioned earlier, the two basic methods for determining the concentration of molecular oxygen in the upper atmosphere are ultraviolet absorption spectroscopy and mass spectrometry. In measurements by absorption spectroscopy, both narrow-band dispersive instruments and broad-band non-dispersive instruments have been used. The most successful non-dispersive detector that has been employed is the ultraviolet ionchamber. Ionchamber of various types were used by Weeks and Smith (Smith and Weeks, 1965; Weeks and Smith, 1968) in a systematic series of rocket flights at solar zenith angles in the range 19° to 95° and covered the height range of 62 to 154 km. Additional O_2 measurements by them were recently reported (Smith and Miller, 1974; Weeks, 1975a,b). All but two of these measurements have been made in the northern hemisphere (Table 6.1). As the density measurements were made at different times of day and in different seasons, they were able to draw some tentative conclusions regarding seasonal and diurnal variations (weeks and Smith, 1968; Weeks 1975 a,b). Several other groups have used Ly-α ionchambers for mesospheric oxygen determinations which are listed in Table (6.1) and discussed in Section (6.3).

In the southern hemisphere, relatively few determinations of molecular oxygen density have been made. In rocket flights from Woomera, Ly-α ion-chambers have been used to determine molecular oxygen densities in the mesosphere (Carver et al, 1964; 1965; 1969 and Lockey, 1972). In one flight, however, molecular oxygen densities were determined from 70 km to 120 km using ionchambers of six different types (Carver et al, 1969). Wildman et al, (1969) used saphire-xylene ionchambers in three flights from Woomera and obtained density distribution over the height range 100 km to 150 km.

Ionchambers have also been used in satellite occulation experiments to determine molecular oxygen densities at satellite sunrise and sunset. Norton and Coworkers have analysed Solrad-8 Lif-NO ionchamber data for satellite passes over a period, which has indicated a seasonal variation in the molecular oxygen number density near 100 km (Norton and Warnock, 1968; Norton, 1970; Roble and Norton, 1972). Stewart and his co-workers (Stewart and Wildman, 1968; 1969 and Parker and Stewart, 1972) have analysed saphire-xylene (S-X) ionchamber data received from the ARIEL-3 satellite and the preliminary results indicate geomagnetic, diurnal and longitudinal variations in the molecular oxygen density at 180 km. More recently, Felske et al (1970; 1972; 1976) and Lockey et al (1969) have reported the determinations of molecular oxygen density using data received from Lif-NO ionchambers in INTERKOSMOS series and WRESAT-I satellites respectively. Although satellite occultation measurements have the advantage of providing data continuously over extended time periods, the accuracy of determinations is rather poor particularly when the sun is used as a source (Roble and Hays, 1972).

Hinteregger and his co-workers (Hall et al, 1965; 1967) have used the photoelectric monochromators to measure the atmospheric absotprion of several solar UV lines which provided the vertical distribution of O_2, N_2 and O above about 120 km.

Nier and others have flown mass-spectrometer in a number of rockets thus using a totally different approach to the determination of atmospheric composition including molecular oxygen. From a day-night pair of flights, with a two days interval, very little diurnal variation in molecular oxygen was found in the altitude range of 120 km to 220 km (Kasperzak et al, 1968). However a true day-night pair on 20th July 1967 (Krankowsky et al, 1968) indicated densities to be substantially higher during the day than the night-time densities thereby inplying that little diurnal variation observed in the first case, was perhaps due to, day to day variations being comparable to the diurnal variations in the altitude range of 120 km to 200 km. This group as well as other workers have reported a number of mass-

spectrometer determinations in the thermosphere (Philbrick et al, 1973; Mauersberger et al, 1968; Pokhunkov, 1972; Hedlin et al, 1964; Nier and Hickman, 1973; Offerman and Grossman, 1973).

The mass spectrometer does not require a pointing control, it can be operated at night and the density determinations are independent of any knowledge of absorption cross-sections and any inherent temperature effect (Section 2.2.4). Its main disadvantage has been that it could only be used above 120 km and it is very difficult to calibrate it absolutely (Nier et al, 1964). As to the first problem some progress has been recently made and one measurement has been reported as low as 90 km (Philbrick et al, 1973). Additional difficulties arise from the dependence of its response on the orientation of the rocket and from its susceptibility to contamination. Although, the photoelectric monochromator provides the most detailed information, it suffers from the fact that its operation is generally limited to altitudes above 120 km, and requires the use of a pointing control. Ionchambers have the advantage of not requiring a pointing control and their ruggedness and small size allow then to be used in small (and relatively inexpensive) unstabilized sounding rockets. Although the information provided by ionchambers is less detailed than that provided by spectrometers, the height resolution is generally better. The ionchamber density determination relies on an accurate knowledge of absorption cross-section (Section 2.2).

It is clear from the above discussion that to date the mesospheric oxygen measurements have been provided exclusively by absorption spectroscopy techniques. All but one (Jursa et al, 1963) of these measurements utilized Ly-α ionchambers. In the lower thermosphere, mass spectrometers have provided most of the data.

In the region of 100 km to 120 km where ionchambers have provided a significant part of the data, the number of measurements is perhaps lowest. Some of these measurements have been made using Ly-α ionchambers at very large solar zenith angles (Weeks and Smith, 1968) and suffer from the data reduction inaccuracies due to finite size of the sun and scale height assumptions (Roble and Norton, 1972; Lockey, 1972 and Felske et al,

1976). The data provided by the present Q - T ionchambers is thus an important addition to the lower thermospheric oxygen data below 120 km. It is compared with some of the data mentioned above in Section (6.2). The mesospheric data provided by the Ly-α ionchambers is used along with other similar measurements to study possible diurnal, seasonal and laitiudinal variations in the mesospheric oxygen and the derived kinetic temperatures in Section (6.3).

6.2 DISCUSSION OF THE DENSITY RESULTS ABOVE 100 Km

The measurements of particular importance for direct comparison with the present measurements are those of Carver et al (1969), Wildman et al (1969), Weeks and Smith (1968), and Philbrick et al (1973).

Measurements in the first two cases have been made at the same geographical location as the present measurements and employed ion-chambers as detectors. Measurements in the last two cases have been made with mass spectrometers and thus provide a comparison between the measurements from two techniques. In Figure (6.1) all the four O_2 density profiles as obtained in the present work are plotted for intercomparison. The results from morning-afternoon pair (C4009 and C4007) are as such somewhat surprising in that the afternoon densities are found to be higher than the morning values at altitudes between 107 and 118 km. Although, there is a possible error of ± 2 km in the trajectory of flight C4009 (Section 5.4), oxygen densities from this flight at altitudes below 95 km are in substantial agreement with densities from flight C4007 and an earlier morning flight in the same season (Figure 6.3) thereby indicating a true diurnal effect. No substantial difference is found in oxygen densities in Spring (C4009) and Autumn (C4018) below about 115 km. A sharp decrease in densities in the latter case above this altitude is apparently due to large errors in the relative intensities (dI/I) because of larger data scattering in the absorption profile (Section 5.8.1). The densities obtained from the flight C1029 are found to be lowest. The results from an earlier flight from Woomera (Wildman et al, 1969) are also shown in the same Figure.

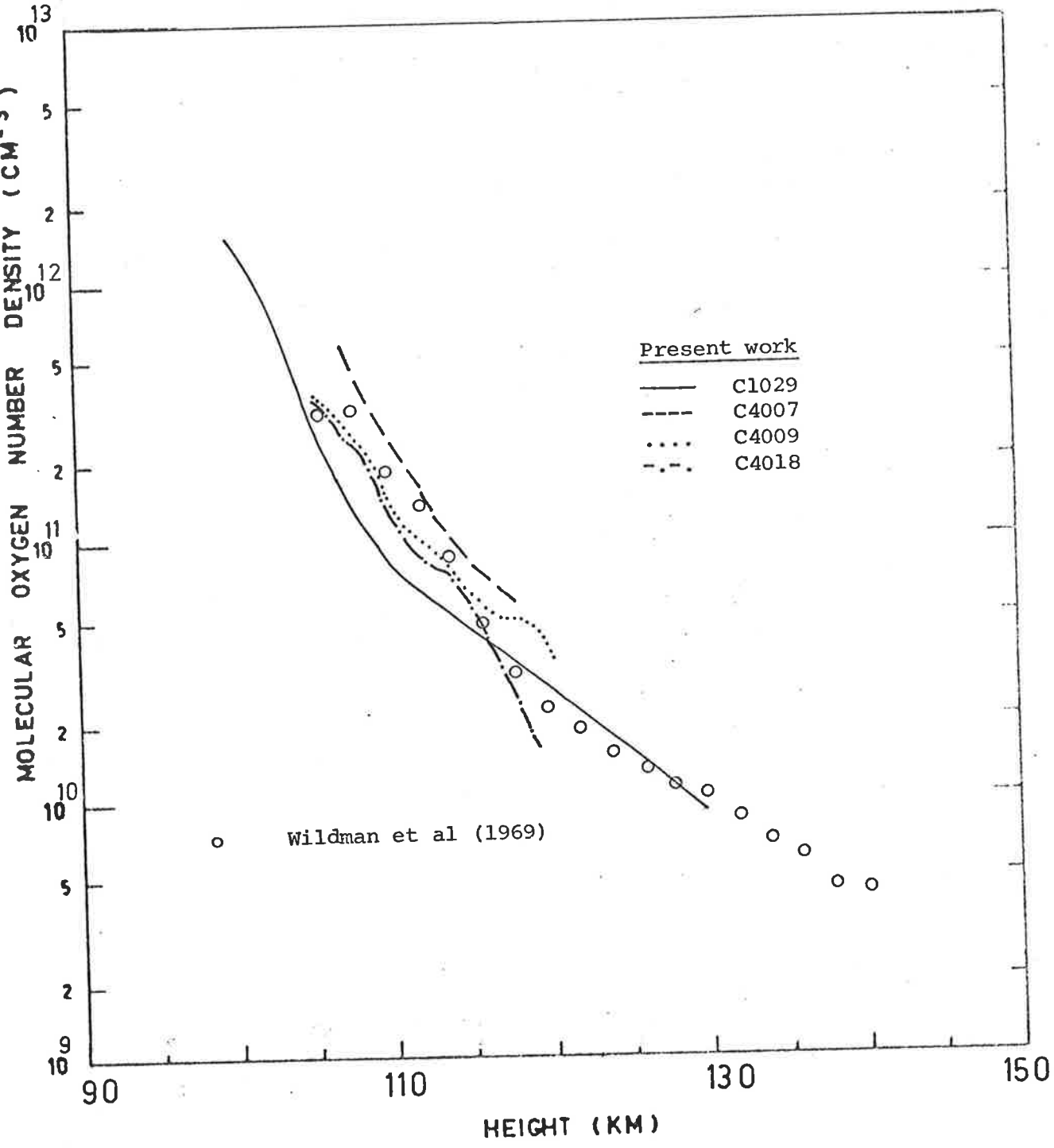

Figure 6.1 O_2 density determinations at Woomera.

This measurement was made on 1st November 1966. This agreement between this and the density profile obtained on 23 November 1972 is very good between 115 and 130 km. Below 115 km, the densities obtained on 1st November are appreciably higher from those obtained on 23 November thus indicating a significant seasonal variation at these altitudes if annual variation is assumed to be negligible. The mean density profile is compared with several other measurements in Figure (6.2) and is found to be in general agreement. Offerman (1974) has recently analysed the oxygen data to study seasonal variation at 120 km and above. The number of measurements in the height range 100-120 km is yet too small for any meaningful statistical analysis of seasonal or diurnal variation. However, below 100 km it has been possible to analyse the oxygen density data statistically and the results are shown in the next section.

6.3 MOLECULAR OXYGEN AND TEMPERATURE VARIATIONS IN THE MESOSPHERE (70-95 km)

6.3.1 Introduction

Data of molecular oxygen measurements above about 120 km have been recently analysed to study seasonal and diurnal variations in molecular oxygen at several thermospheric altitudes (Offerman, 1974; Danilov, 1973). At the mesospheric altitudes, Weeks and Smith (1968) were able to draw some tentative conclusions about seasonal and diurnal variations of molecular oxygen in the northern hemisphere (38° N). The number of oxygen measurements made at Woomera (31° S) over the last several years can now be used to study temporal variations in the southern hemisphere. The number of rocket determinations of molecular oxygen at 80 km is, although still not very large, comparable to those in the lower thermosphere above 120 km and can be used for a preliminary analysis to study global oxygen variations with season and latitude. A collection of rocket-borne mesospheric oxygen data was made for this purpose and the flight conditions are listed in Table (6.1). Most of these measurements were made by Ly-α absorption technique and the data reduction has been

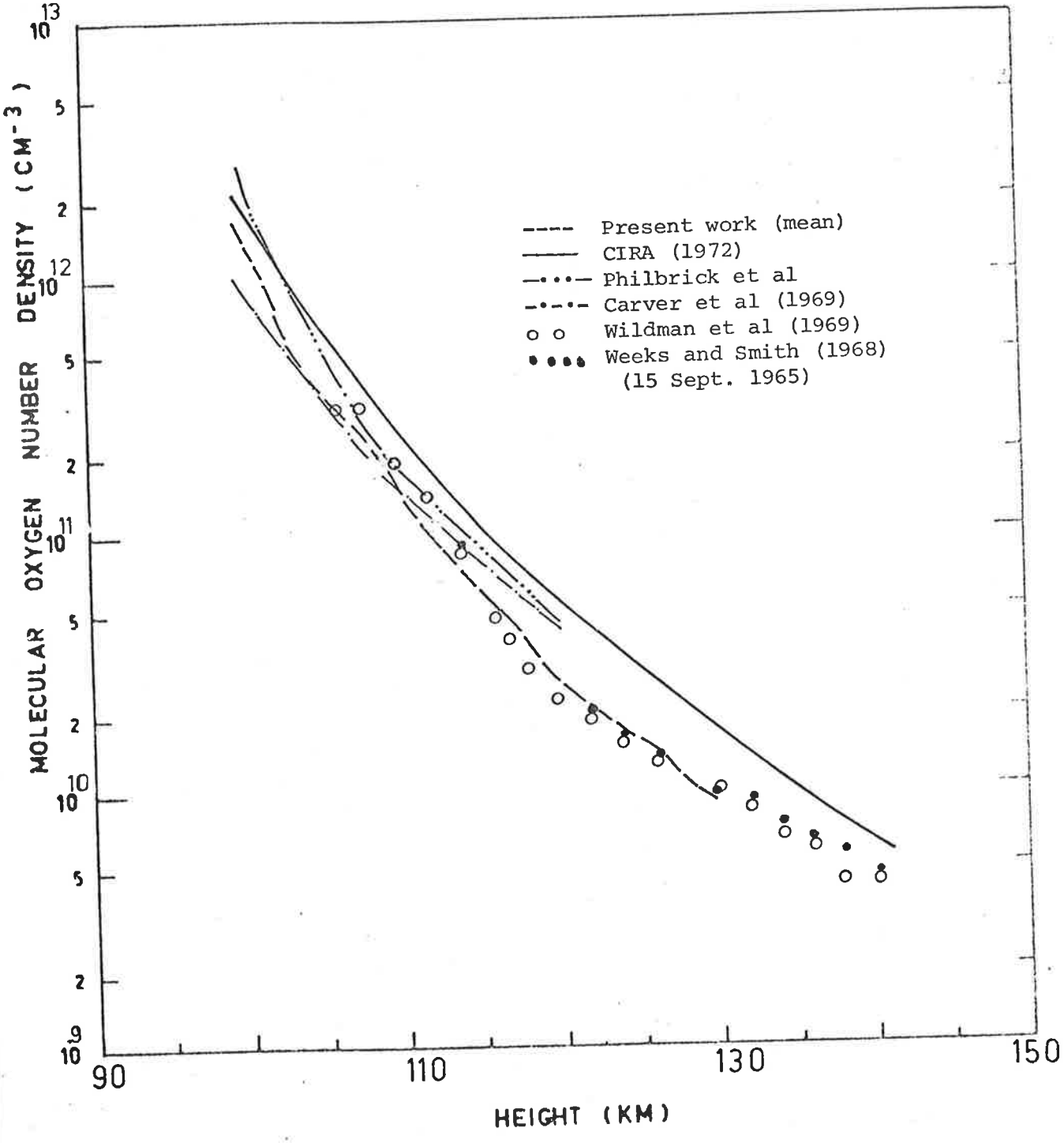

Figure 6.2 Comparison of some O_2 density determinations with CIRA-71 and present measurements.

TABLE 6.1

FLIGHT CONDITIONS FOR THIS ANALYSIS

Date	Payload	Time U.T	Solar Zenith Angle	Location (deg.)	Reference	Activity			Sun Spot No.
						Kp	Ap	$F_{10.7}$	
29 Jul 1957	313F	2200	56°	59N, 93W-FC**	Kupperian et al 1959*	2°	12		142
18 Mar 1958	Aerobee 93	2412	90°	32N, 106W-WS	Jursa et al 1963+	4^-	34		162
23 Mar 1958	319F	1807	60°	59N, 93W-FC	Kupperian et al 1959*	5^-	21		187
27 Feb 1963	N.A. 14.86		56°	38N, 75W-WI	Smith & Weeks 1965	1^-	2		17
20 Jul 1963	N.A. 14.91	2103	48°	59N, 93W-FC	Smith & Weeks 1965	3^+	7		11
20 Jul 1963	N.A. 14.92	2113	49°	59N, 93W-FC	Smith & Weeks 1965	3^+	7		11
20 Jul 1963	N.A. 14.94	2210	56°	59N, 93W-FC	Smith & Weeks 1965	2^-	7		11
6 Dec 1963	HAD301	2342(P)**	37°	31S, 136E-W	Carver et al 1964	4°	28		28
15 Jul 1964	N.A.14.146	1025	84°	38N, 75W-WI	Weeks & Smith 1968	0^+	2		12
4 Feb 1965	HAD304	2255(P)	53°	31S, 136E-W	Carver et al 1965	3°	5	76.4	23
9 Apr 1965	N.A.14.231		59°	44S, 78W-Chile	Weeks & Smith 1968		11	71.9	0
17 Jun 1965	N.A.14.246	2145	61°	38N, 75W-WI	Weeks & Smith 1968	2^-	32	78.7	12
15 Sep 1965	N.A.14.244	2030	60°	38N, 75W-WI	Weeks & Smith 1968	4^-	15	75.7	8
13 Dec 1965	K-9M-16	0620	70°	31N, 131E-Japan	Higashino et al 1966	3^-	6	71.7	14

TABLE 6.1 (continued)

Date	Payload	Time U.T.	Solar Zenith Angle	Location (deg.)	Reference	Activity			Sun Spot No.
						Kp	Ap	$F_{10.7}$	
15 Dec 1965	N.A.14.247	2045	61°	38N, 75W-WI	Weeks & Smith 1968	0°	1	74.4	14
21 Feb 1966	NC 7.180	1958	50°	30N, 87W-FL	Grobecker 1971	0^{+}	4	85.7	42
21 Feb 1966	NC 7.178	2023	73.2°	59N, 93W-FC	Grobecker 1971	0^{+}	4	85.7	42
14 Jul 1966	Dragon-15	1427	32°	31N, 3W-HA	Quessette 1970	1^{-}	4	99.8	42
11 Nov 1966	Longtom 18	2305(P)	48°	31S, 136E-W	Carver et al 1969.	2°	9	121.9	63
31 Jan 1967	N.A.14.275	1950	59°	38N, 75W-WI	Weeks & Smith 1968	0^{+}	2	156.4	108
12 Nov 1967	N.A.14.303		19°	32S, 52W-CB	Weeks & Smith 1968		22	132.7	56
23 May 1968	N. Tomahawk	0445(N)	71°	22N, 160W-BH	Brannon & Hoffman 1971	4^{+}	17	182.6	165
19 Jun 1969	P35H	1503	44°	58N, -SU	Hall 1972	2^{-}	8	147	86
24 Jul 1969	HAD309	0645	78°	31S, 136E-W	Lockey 1972	1^{-}	6	115.7	55
9 Dec 1969	HAD310	2156(P)	59°	31S, 136E-W	Lockey 1972	2°	5	112.1	43
7 Mar 1970	AT-7.895	2323	98°	30N, 87W-FL	Philbrick et al 1973	6^{-}	42	168.4	111
28 Nov 1970	Vertical-1		82°	Mid Lat USSR	Felske et al 1972		8	148.9	89
28 Jan 1971	N.A. 1037	0540	34°	9N, 77E-TI	Subbaraya et al 1974	5^{-}	39	166.2	109

TABLE 6.1 (continued)

Date	Payload	Time U.T.	Solar zenith angle	Location (deg.)	Reference	Activity			Sun Spot
						Kp	Ap	$F_{10.7}$	
8 Aug 1971	F-27	1211	55°	69N, 16E-TR	Thrane & Johannessen 1975			108.6	58
7 Apr 1972	NA 1043	0730	5°	9N, 77E-TI	Subbaraya et al 1974			121.3	71
20 Jul 1972	C1020	0130	56°	31S,136E-W	Ilyas and Horton 1974	$\overline{1}$	5	110.9	56
23 Nov 1974	C1029	2255(P)	51°	31S,136E-W	Carver et al 1974	3^-	13	110.9	69
28 Jun 1974	C4006	0017	66°	31S,136E-W	This work	5^+	29	83.0	18
2 Oct 1974	C4009	2250(P)	60°	31S,136E-W	This work	3^o	28	94.6	53
2 Oct 1974	C4007	0755	77.9°	31S,136E-W	This work	6^o	30	94.6	53
29 Apr 1975	C4018	2345(P)	63.6°	31S,136E-W	This work	1^-	3	73.2	16

TABLE 6.1 (continued)

** Abbreviations

BH Barking Sands, Hawaii

CB Casino, Brazil

FC Fort Churchill, U.S.A.

FL Florida, U.S.A.

HA Hamaguir, Algiers.

SU South Uist, Scotland

TI Thumba, India

TR Tromso, Norway.

W Woomera, Australia

WI Wallops Island, U.S.A.

WS White Sands, U.S.A.

P Previous date

N Next date

* Data multiplied by .82 and then corrected for σ_{eff}

\+ No corrections applied.

for either a constant cross-section of $1.00 \times 10^{-20} cm^2$ or a variable cross-section being larger than $1.0 \times 10^{-20} cm^2$. As discussed in Section (2.2.3), the recent laboratory measurements of oxygen absorption cross-section near solar H-Ly-α line at temperatures comparable to cooler mesospheric temperature conditions result in a height dependent effective cross-section which is significantly lower than the value of $1.00 \times 10^{-20} cm^2$. Therefore, data from each of the profiles listed (including the earlier measurements at Woomera) were first corrected for the new smaller variable cross-section described in Section (2.2.3) and (2.2.4).

The new data was then used for further statistical analysis and the results are presented in Section (6.3.3). The results of seasonal and diurnal variations at Woomera (31° S) are given in the following sub-section (6.3.2).

6.3.2 Seasonal and Diurnal Variations at Woomera (31° S)

All the Ly-α measurements made at Woomera were grouped seasonally. Since the measurements span a period of several years, possible annual variations are likely to bias the results of this study.

Molecular oxygen concentrations obtained during the summer are shown in Figure (6.3). Although each flight was made in a different year, the agreement between the three profiles is very good and the data are well represented by the 6.2 km scale height line.

The Spring profiles shown in Figure (6.4) are also found to be in general agreement. Excellent agreement is found between flights C4009 and LT-18 in the region below 90 km. The data from the third flight, C4007 is in general agreement above 85 km but show larger concentrations at lower altitudes. The profile is limited mainly due to unfavourable aspect on the downleg and somewhat larger solar zenith angle at the time of observation. The larger concentrations may have resulted from possible diurnal effect as this flight was made in the afternoon. Although the morning flight C4009 has a possible trajectory error of ± 2 km, its substantial agreement with two other profiles gives weight to the above conclusion. The data above about 92 km should not in general be

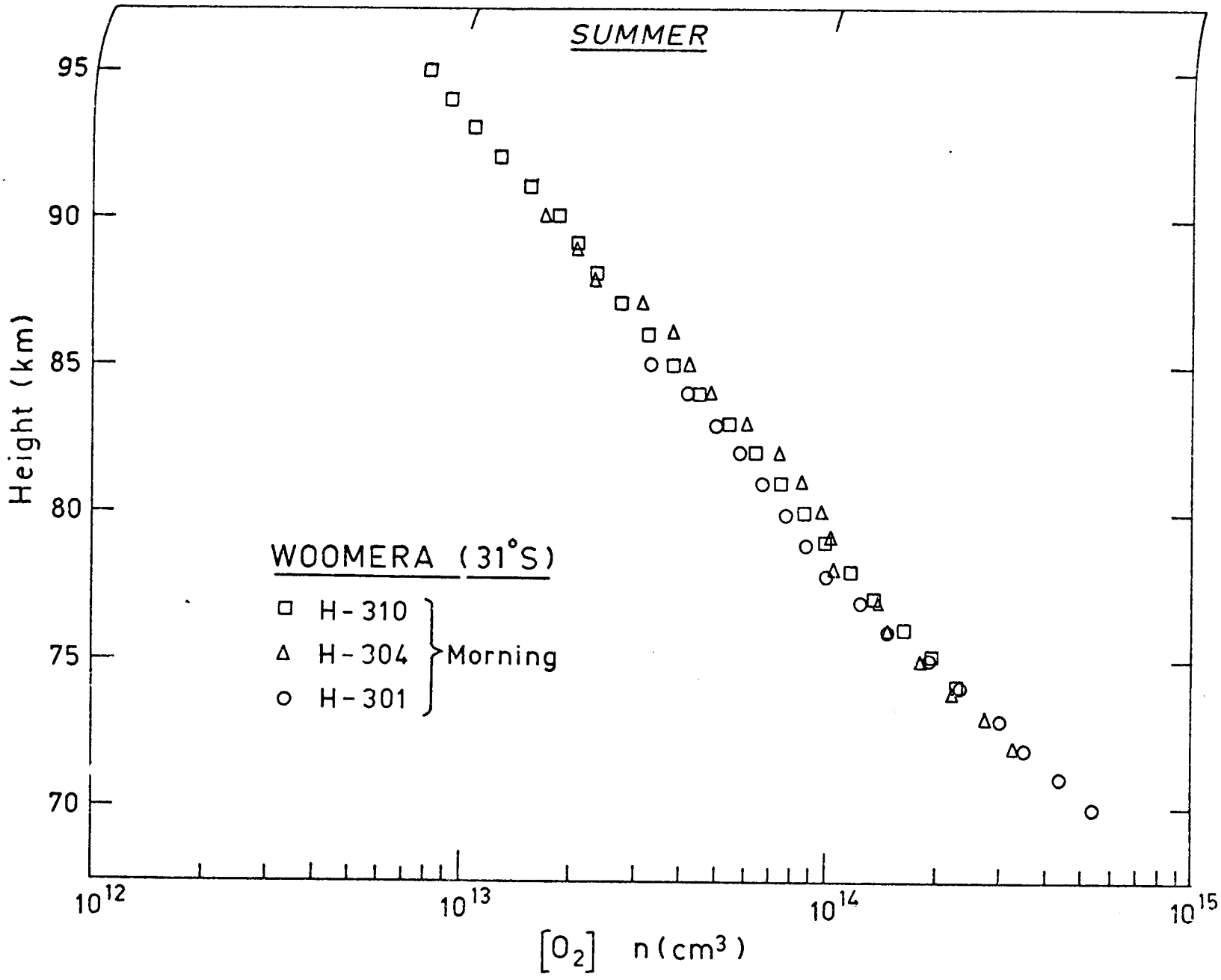

Figure 6.3 Oxygen distribution at Woomera in the summer season.

considered seriously due to other radiation problem (Section 2.4). For comparison data from one of the flights of Weeks and Smith (1968) made in the southern hemisphere at similar latitude and the same season is also shown in the Figure (6.4). The agreement of this data (NA.303) with the data of flights C4009 and LT-18 is good below 85 km. The concentrations from this flight are a little lower above 85 km but the difference is within experimental errors and perhaps indicates negligible longitudinal variation. A mean profile between 72 and 90 km is well represented by 6.2 km scale height line.

Daytime concentrations obtained during the winter season are shown in Figure (6.5). Flights C1020 and H309 took place at about the same time of different years (20 July and 24 July). Data from these two flights is in good agreement above about 82 km and indicate negligible morning to afternoon density variation in winter. However, the concentration from the other morning flight, C4006 are generally lower and indicate a wave-like structure. In the Figure, results from the only night-time oxygen measurements (O'Connor, 1974) made in Winter at Woomera, are also shown.* Although the uncertainty in the data of this measurement is relatively large, it is still useful for comparison and indicates a build up of oxygen concentrations at night time below 90 km. The average scale height for winter data is found to be about 6.8 km.

To eliminate possible variations arising from different times of day, flights at zenith angles near 55° (morning) are considered in Figure (6.6). These profiles show rather small seasonal effect at Woomera in comparison to the results of Weeks and Smith (1968) at Wallops Island (38° N). Since the three profiles originate from different years, any seasonal effect may have been cancelled out by the possible

---

* This measurement is based on airglow intensities of the line centre of the Hydrogen Ly-α and the original data has been multiplied by 1.25 to take into account the temperature effect at the centre of the line as indicated by the results of Carver et al. (1976) - Section (2.2.3).

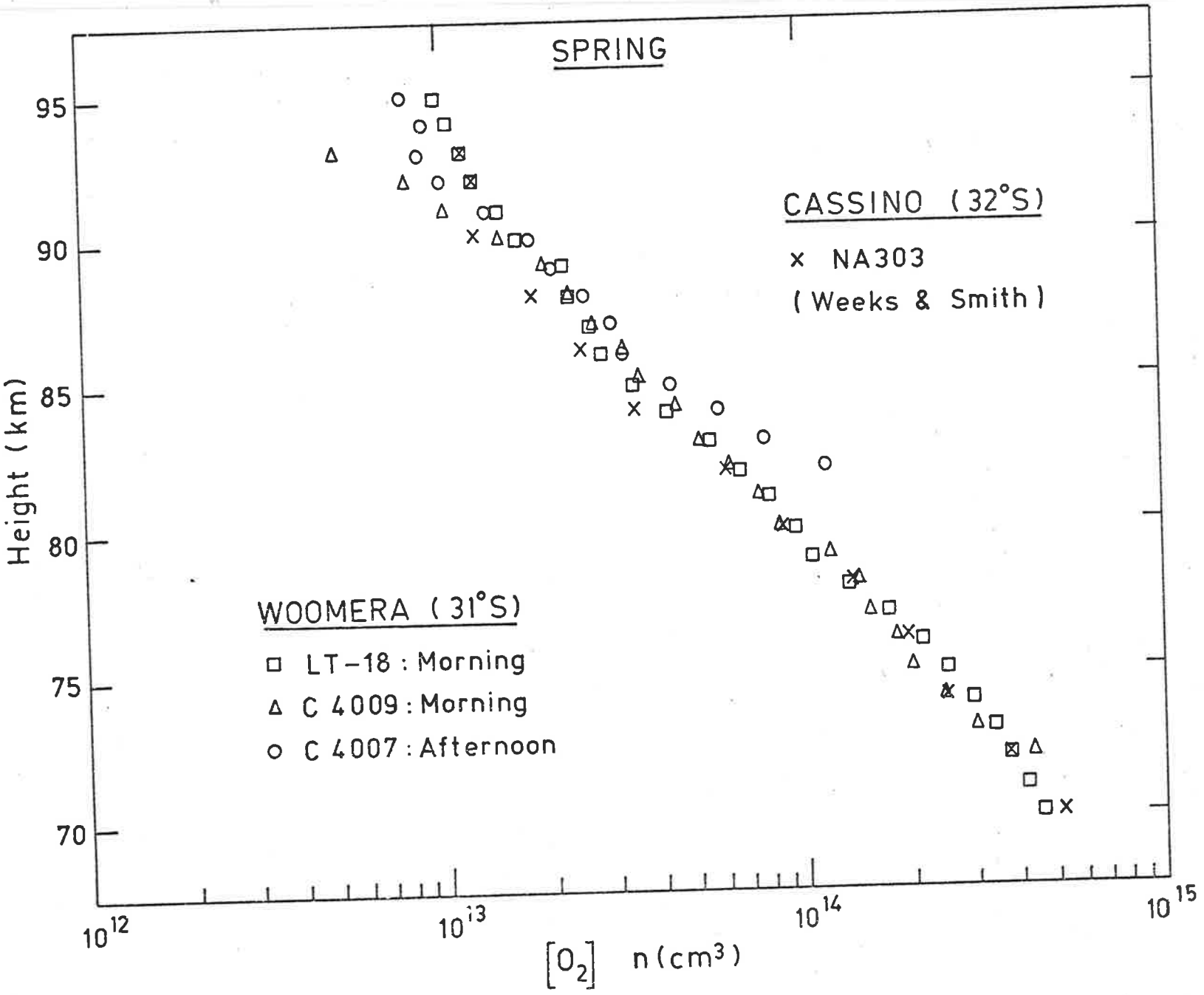

Figure 6.4 Oxygen distribution at Woomera in the spring season.

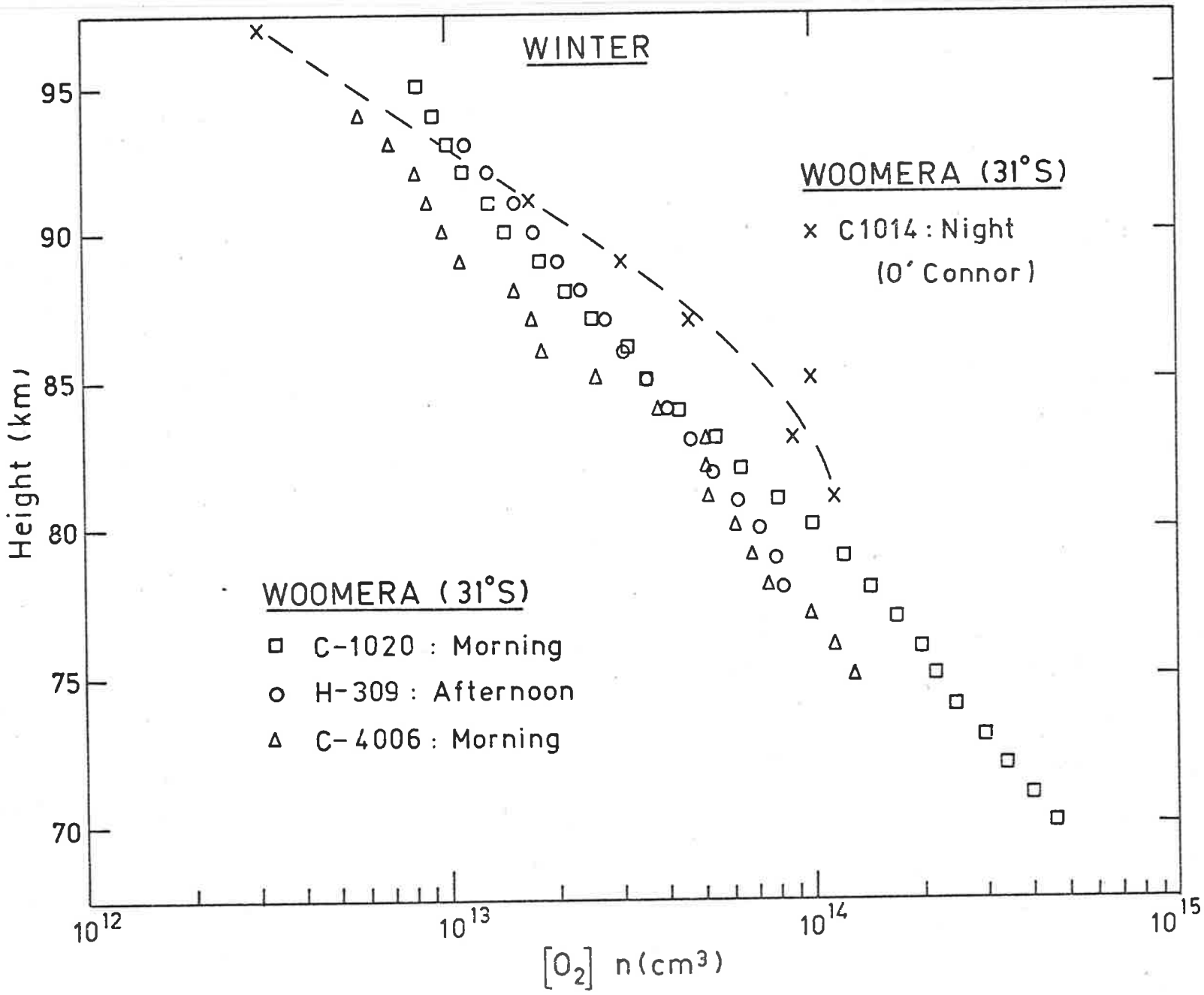

Figure 6.5 Oxygen distribution at Woomera in the winter season.

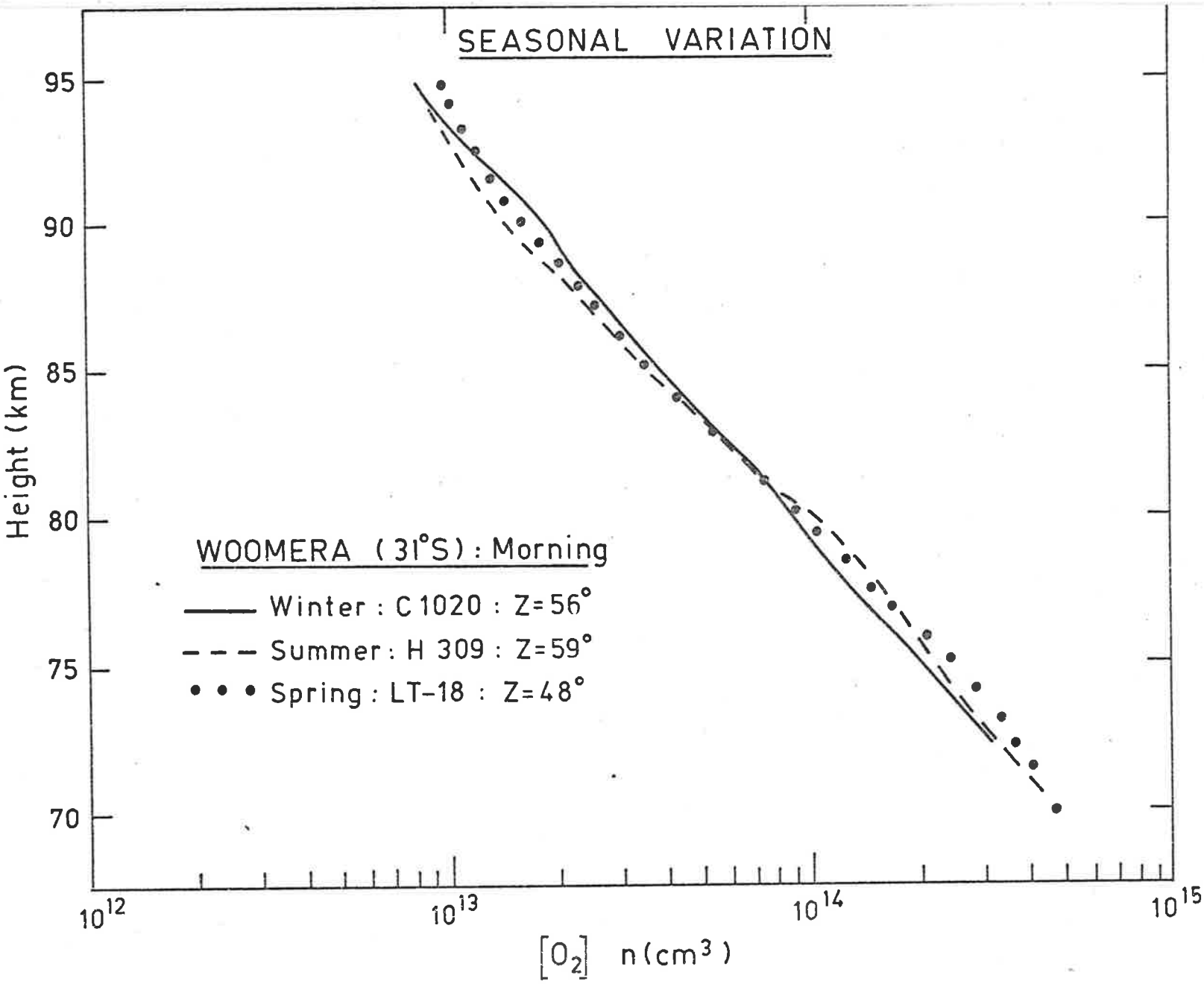

Figure 5.6 Seasonal variations at Woomera

day to day and annual variations even though there appears to be very little annual variation from Figures (6.3, 6.4 and 6.5). Perhaps this small seasonal variation at Woomera is reflected in the scale heights being about the same for the three seasons.

6.3.3 Analysis of Global Oxygen Data to Study Latitudinal and Seasonal Variations

As mentioned in the introduction of this section, a collection of oxygen data below 95 km was made for studying possible variations in molecular oxygen. All the absorption data had to be re-analysed for a variable cross-section based on the new low temperature data of Carver et al, (1976). All the data was converted to a constant cross-section value of $1.0 \times 10^{-20} cm^2$ so that a new variable cross-section correction could be applied. Some of the digital data had to be obtained from the graphical representations which could have resulted in some minor differences from the original data. Where both upleg and downleg data was available, only downleg data was used since upleg-downleg discrepency appears to be due to contamination effects (Section 2.4). Satellite-borne Ly-α ionchamber measurements are generally restricted to altitudes above about 90 km and even here, the accuracy is not as good as the rocket data (Section 6.1). All the data was reduced at 1 km intervals, in some cases by interpolations. A few of the measurements made at very large solar zenith angles have provided data above 85-90 km. Since this analysis is meaningful only between 70 and 90 km; these profiles, only small portions of which could be used, were not included in this analysis.

Effective cross-sections as a function of height and zenith angle were calculated for each flight as described in Section (2.2.3) using the absorption cross-section data of Carver et al, (1976) at 195 K. Oxygen number densities were then recalculated for the new variable cross-section (Section 2.2.4) which were then used for kinetic temperature calculations for each profile by integrating downwards (Section 2.5). The oxygen data was also represented as ratio to mean CIRA (1972) for convenient representation of latitudinal and seasonal variations on a linear scale.

About a third of the data analysed is from Woomera (31° S) while about the same amount belongs to latitudes between 31° N and 38° N which can be treated as 35° N (a significant part of the latter is from Wallops Island - 38° N). The situation is therefore quite favourable in that each group corresponds to predominantly one longitude. Almost all the data near 60° N has come from Fort Churchill. Therefore three means from data of respective latitudes can be formed. These means of ratios with statistical error bars (σ) for each of the three groups are shown in Figure (6.7a).

It can be seen from Figure (6.7a) that mean ratios (hence absolute concentrations) for 31° S are somewhat lower than the corresponding mean ratios for 35° N between 75 km and 85 km. Above about 87 km, the means at 31° S become larger from the means at 35° N. Below 90 km, the statistical error (σ) for the means at 31° S is never more than 6% while it is considerably larger for the 35° N data varying between 8% and 14%. Although the difference between the two means is within the error bars over most of the region; mean total density concentrations at Woomera were found to be lower between 70 and 85 km and higher above this altitude from the 30° N mean model (Pearson, 1974). Therefore, latitudinal difference as observed in the present analysis may be a true hemispherical asymmetry. N-S asymmetry in other constituents has been found to exist at higher altitudes (Keating et al, 1973; Barlier et al, 1974). The means for 60° N are substantially larger than both of the other means for the region 74-92 km and the difference (outside the range of error bars) appears to be real. Since the data for this latitude is predominantly of spring/summer season, the mean is therefore representative of this season rather than an overall mean and as such is in agreement with the model atmosphere (1972).

Mean temperature profiles corresponding to the three latitudes are shown in Figure (6.7b). The results at mid latitudes indicate that possibly southern hemisphere is warmer at mesospheric altitudes. The error-bars are significantly large and may account for the difference as in the case of oxygen concentrations. However, the mean temperature

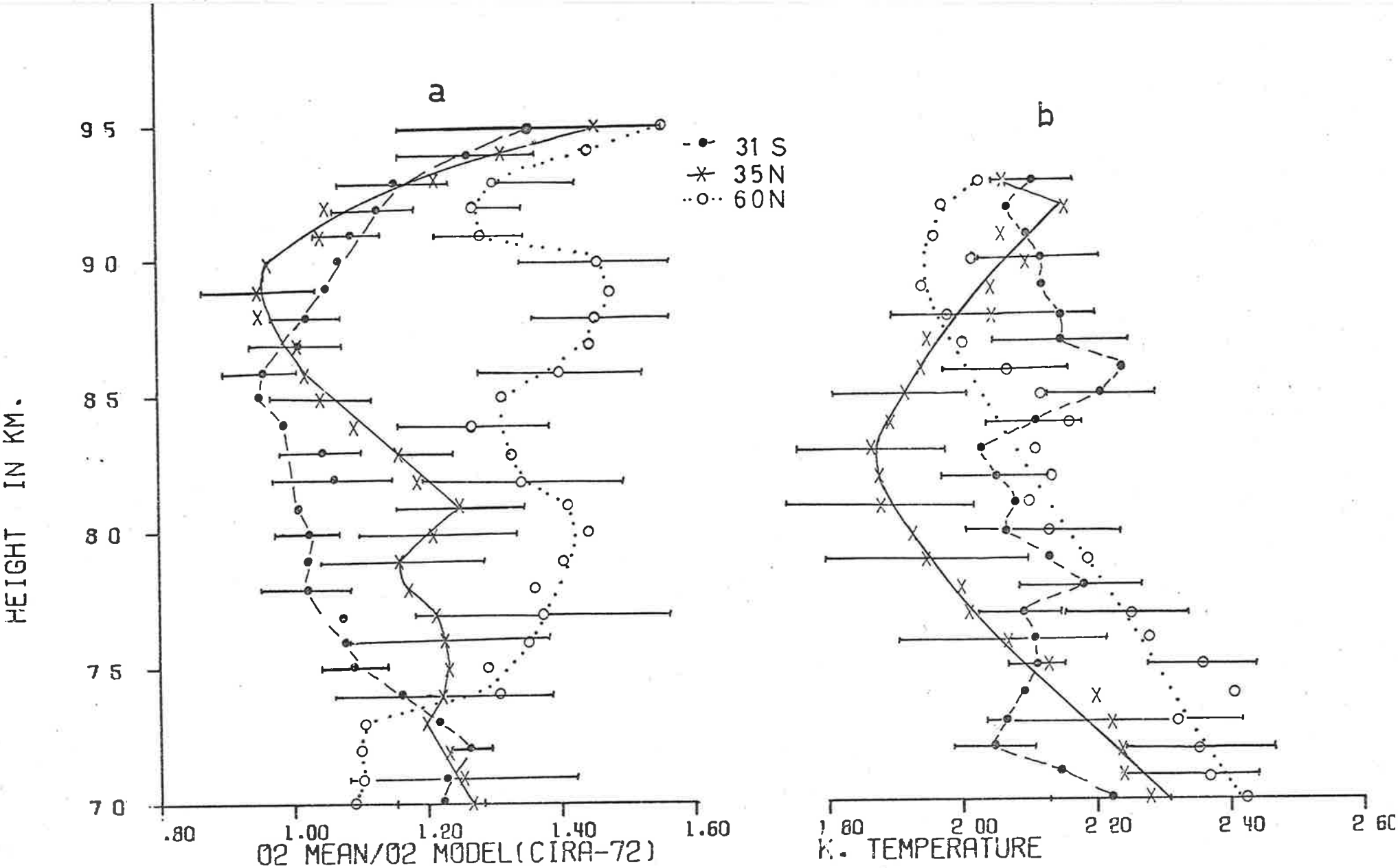

Figure 6.7a Latitudinal distribution of molecular oxygen.

(b) Latitudinal distribution of K temperature.

results of Pearson (1974) also indicate a similar difference. It is interesting to note that the 35° N mean profile is substantially in agreement with the mean model temperatures (CIRA, 1972).

Finally, all the data from different latitudes (Table 6.1) were plotted against the season of the year at five different altitudes. Data from southern latitudes was changed by 6 months. The results are shown in Figure (6.8a).

The oxygen results at 80 km are particularly interesting. These clearly indicate large ratios and therefore larger concentrations in the summer season (southern winter) as deduced from the total density observations (Groves model in CIRA, 1972). The situation at 90 km is not very clear as the data is scattered equally around the mean and the least square fitted curve shows very small seasonal variation. Since 90 km is the intermediate height above which seasonal variation in air density is reversed (Groves' model shows total densities to be minimum in winter at 100 km while maximum in winter at 80 km).

The results at the altitudes 70 km, 75 km and 85 km also indicate a seasonal effect similar to the one at 80 km but the amplitude of variation is smaller. At 70 km, the data are concentrated mainly in the first half of the year.

Similar results of seasonal variations in derived kinetic temperatures are shown in Figure (6.8 b). Unfortunately, the scattering in data at each altitude is relatively larger, the fitted curves do not show as large amplitude of variation as in Figure (6.8 a). The maximum in temperature appears to be near the minimum in oxygen concentrations in early March (≃70 day no.) at 70 km, 75 km and 80 km. This maximum appears to be shifting to early May at 85 km. At 90 km, there appears to be very little seasonal variation.

6.3.4 An Observational Mean Model

It is both desirable and possible to obtain a mean observational model for mesospheric oxygen. A mean profile as obtained for the

Figure 6.8a Seasonal variation of molecular oxygen at several mesospheric altitudes. The dashed line represents observational mean value and the continuous line is a least square polynomial fitted curve of 5th degree. No significant difference was observed for higher degree curves. The goodness of fit is restricted to the range of data points. As the data was concentrated in the earlier part of the year, particularly at lower altitudes, the fitted curve was obtaine over two cycles of the data so as to obtain a continuous fitted curve. In order to check whether the observed O_2 seasonal effect is due to some odd flights, the data were separated for odd years and even years. Seasonal variation curves for each case are shown in Figure 6.8(c) and 6.8 (d) which separately confirm that the seasonal effect observed in this figure (6.8a) is not due to just some odd flight data. Seasonal variations of derived kinetic temperatures are shown in Figure (6.8b).

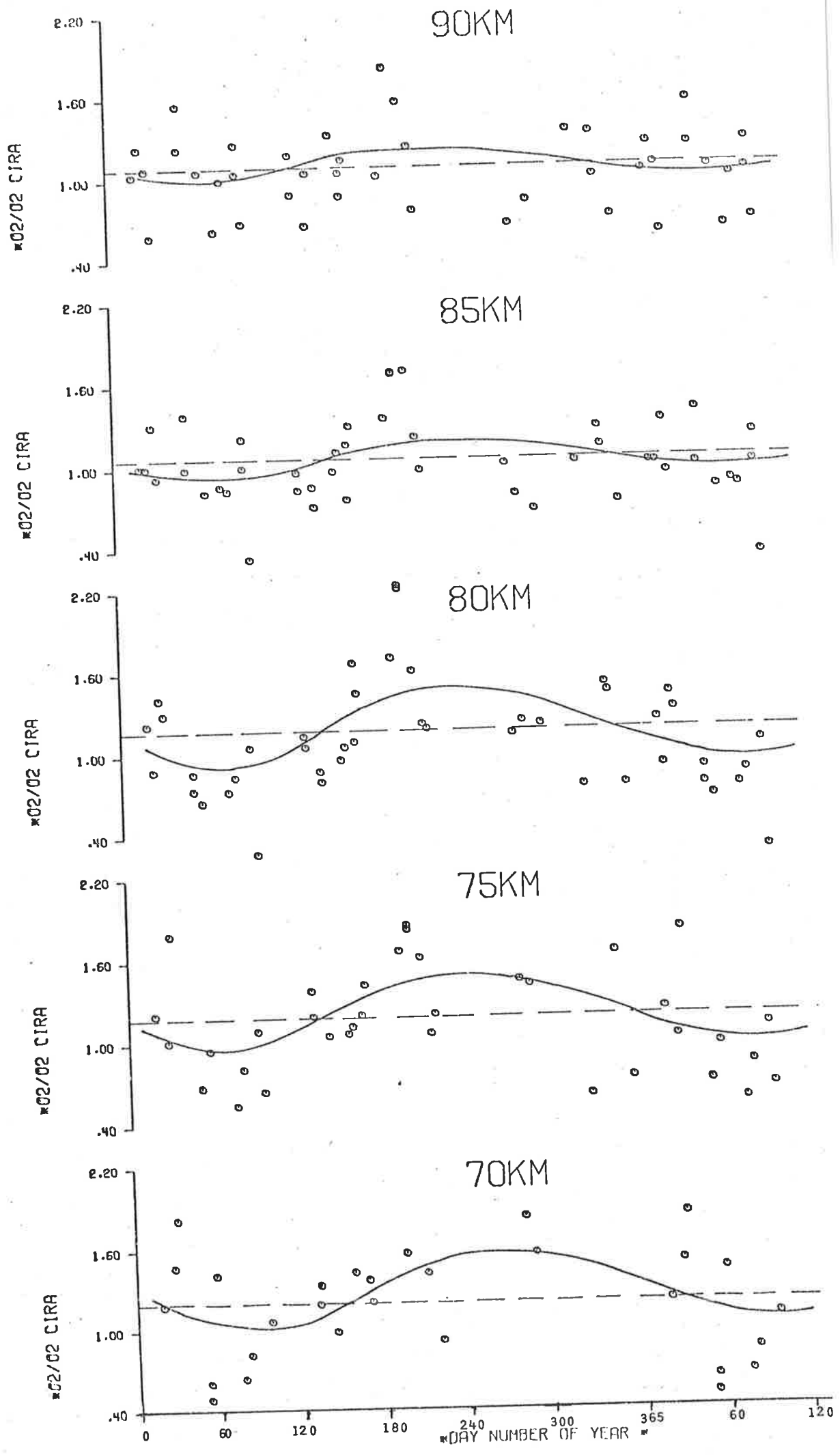
90KM
85KM
80KM
75KM
70KM
2.20
1.60
1.00
.40
*02/02 CIRA
0
60
120
180
240
300
365
60
120
*DAY NUMBER OF YEAR *

Figure 6.8b Seasonal variation of kinetic temperatures.

(For details see figure 6.8a).

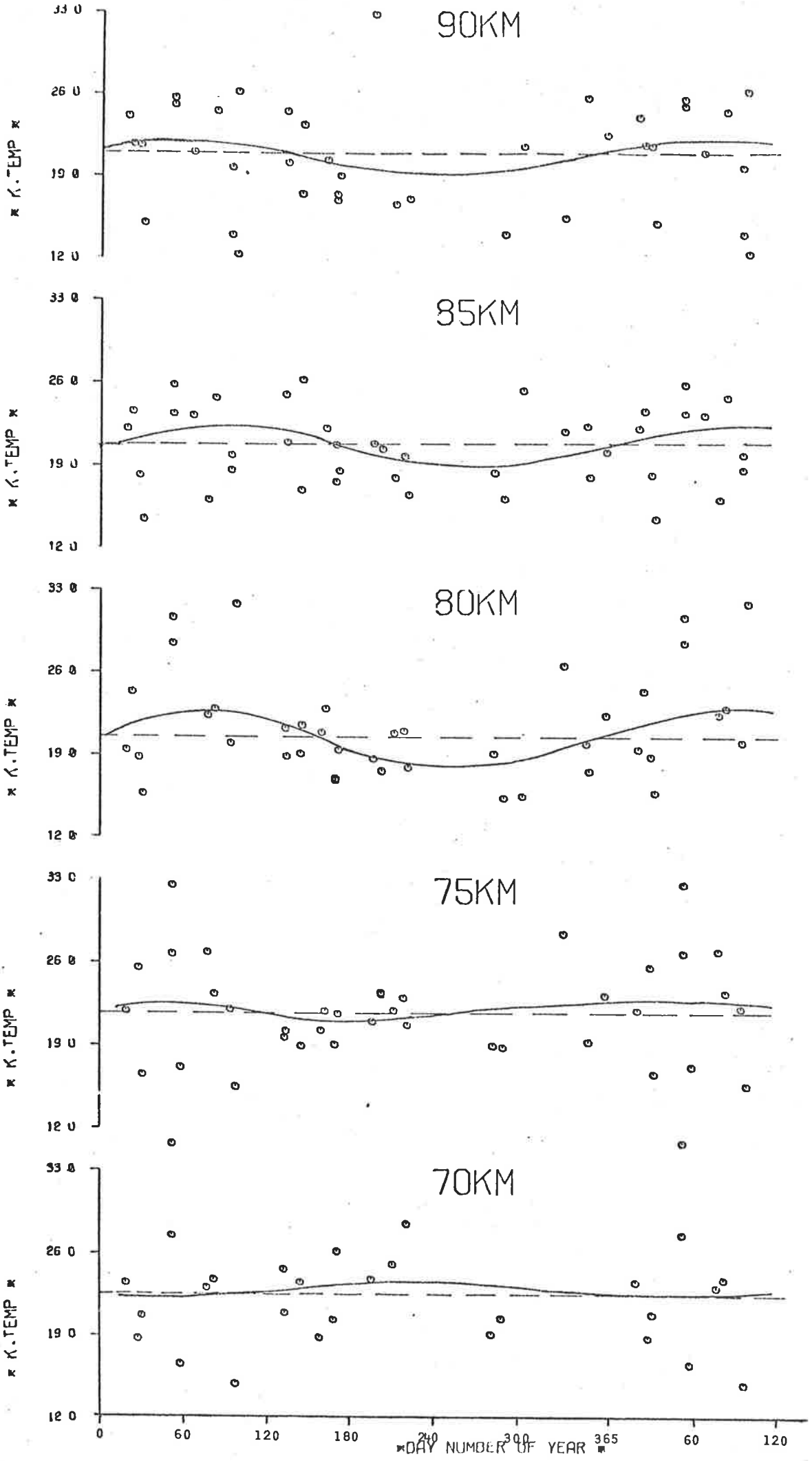
90KM
85KM
80KM
75KM
70KM
K.TEMP
33 0
26 0
19 0
12 0
0
60
120
180
240
300
365
DAY NUMBER OF YEAR

Figure 6.8c Seasonal variations of molecular oxygen using data from odd year flights. Dashed line is observational mean for all flights (odd years + even years).

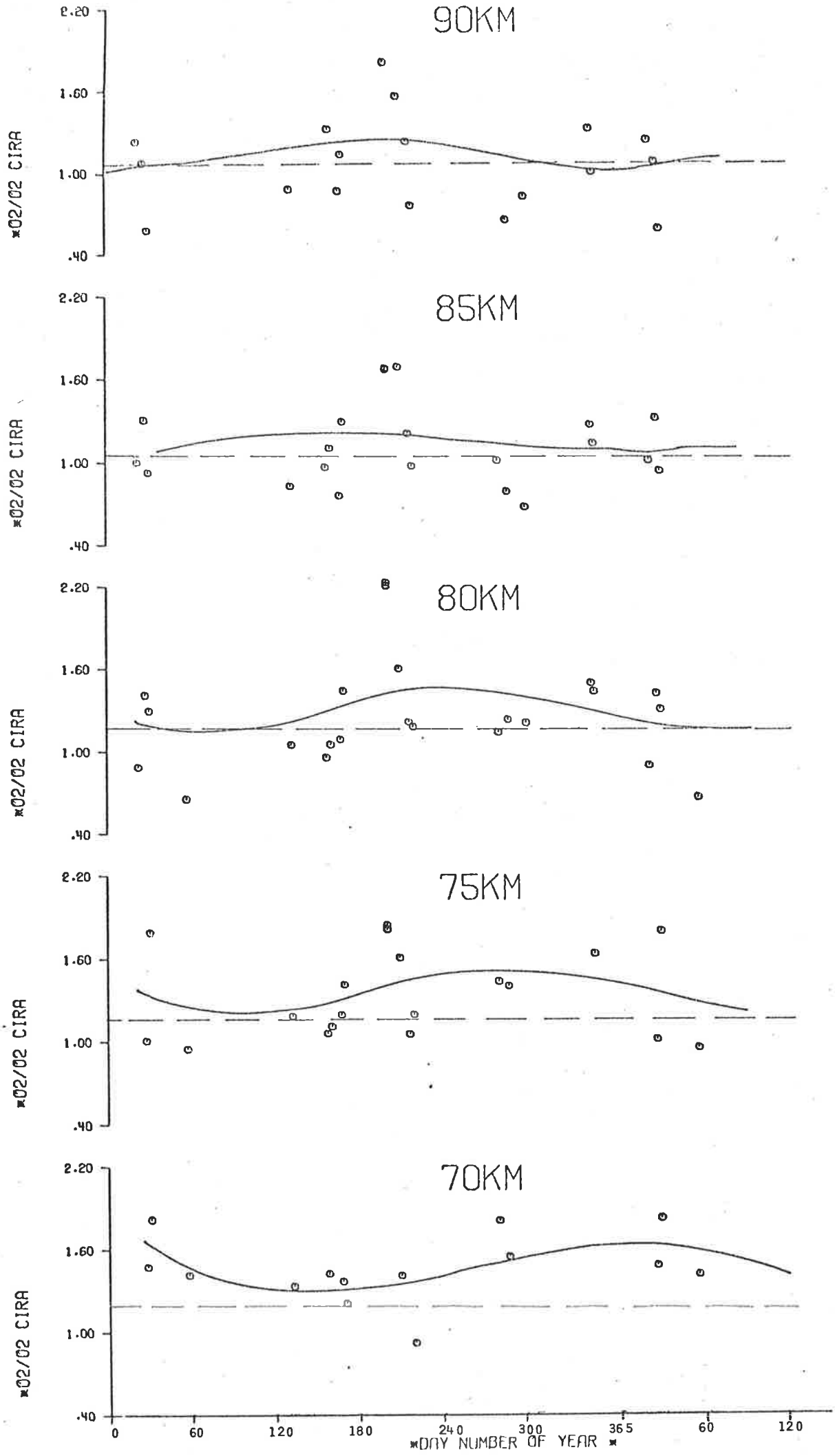
90KM
85KM
80KM
75KM
70KM
*02/02 CIRA
2.20
1.60
1.00
.40
0
60
120
180
240
300
365
60
120
*DAY NUMBER OF YEAR *

Figure 6.8d Seasonal variation of molecular oxygen using data from even year flights. Dashed line is observational mean for all flights (odd years + even years).

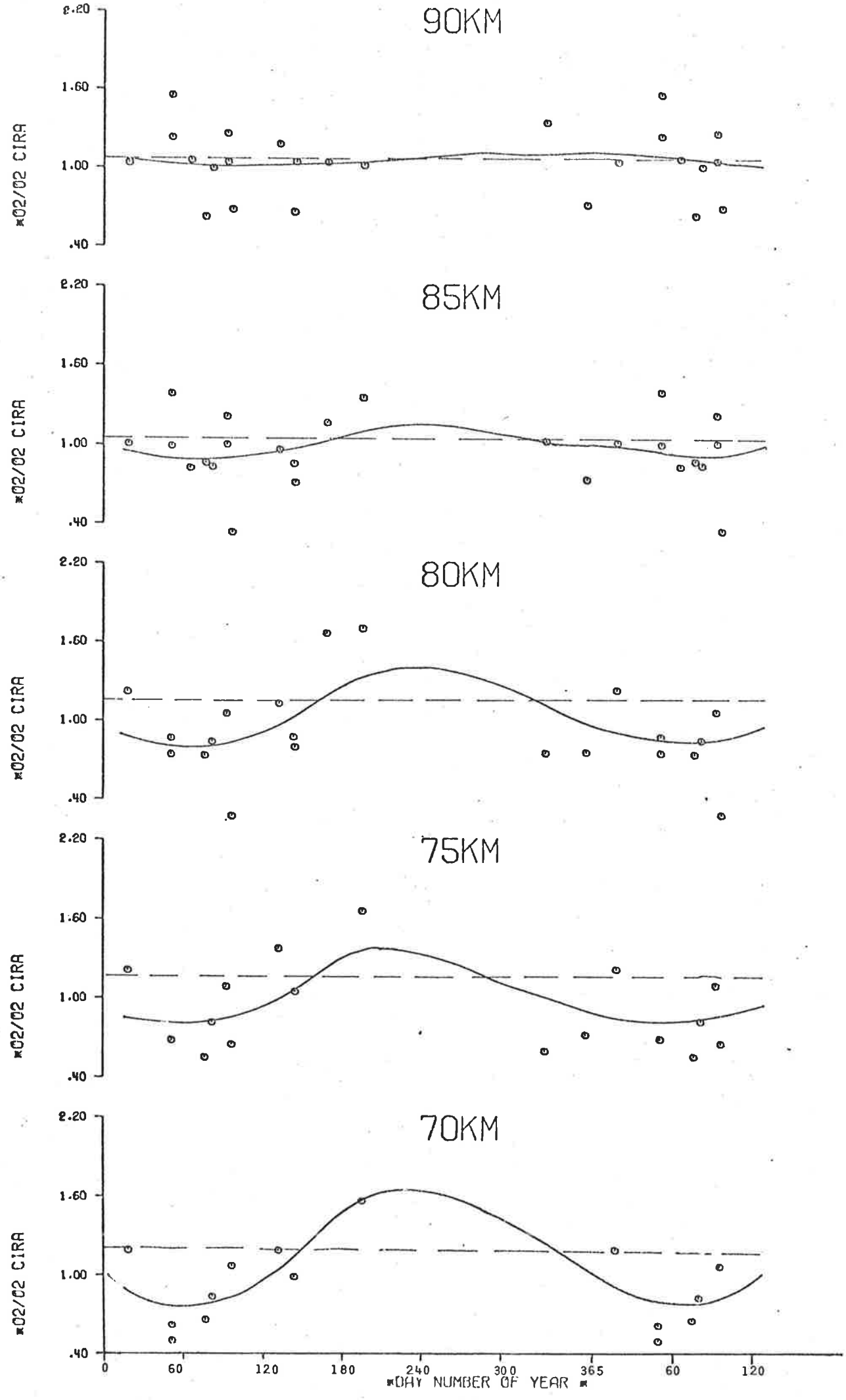
90KM
85KM
80KM
75KM
70KM
*02/02 CIRA
2.20
1.60
1.00
.40
0
60
120
180
240
300
365
60
120
*DAY NUMBER OF YEAR *

re-analysed data of flights listed in Table (6.1) is shown in Figure (6.9). Means of data at altitudes between -31° S to 38° N were also obtained. These values were found to be about 5 percent lower than the means shown for entire data. This indicates that the mean profile represents a reasonable average. The mean O_2 ratios are about 15% - 20% higher at lower altitudes and about 10% higher above about 84 km. The larger ratios at lower altitudes appear to be partly due to the fact that temperatures in this region particularly below 75 km are generally higher than 200 K and a separate cross-section profile at comparable temperature should be used. This is expected to result in larger effective cross-sections and therefore smaller ratios at these altitudes.

There remains an average 10 percent difference between the mean ratios and the mean CIRA (1972) which can be accounted for by the large error bars. The difference may, however, be real since the mean CIRA (1972) is based on total density measurements. The mean O_2 model of Banks and Kockarts (1973) shows O_2 concentrations to be about 10 percent higher than the mean CIRA model and thus gives weight to this point. Nevertheless, two other factors should also be considered. Firstly, the absorption cross-section data have a random uncertainty of about 5 percent. The error in effective cross-section due to uncertainty in Ly-α line profile (which has been found to slowly vary with solar activity, Section 1.3) is estimated to be about 5 percent thus resulting in an estimated quadratic error of about (7) percent in the effective cross-section. The second important factor is that some account should be made for absorption due to other constituents. At present there is a large uncertainty about this factor (Section 2.4). A value of 7.0 ($\pm$2.0)x10^{-22} cm^2 for this factor can account for the above difference (this value of 7.0x$10^{-22}$$cm^2$ is in reasonable agreement with the estimates of Hall (1972) and ours (Section 2.4)). The resultant mean profile will then be in better agreement with the mean model ratios as well as the mean ratios obtained for the theoretical cross-section profile (Section 2.2.3). It

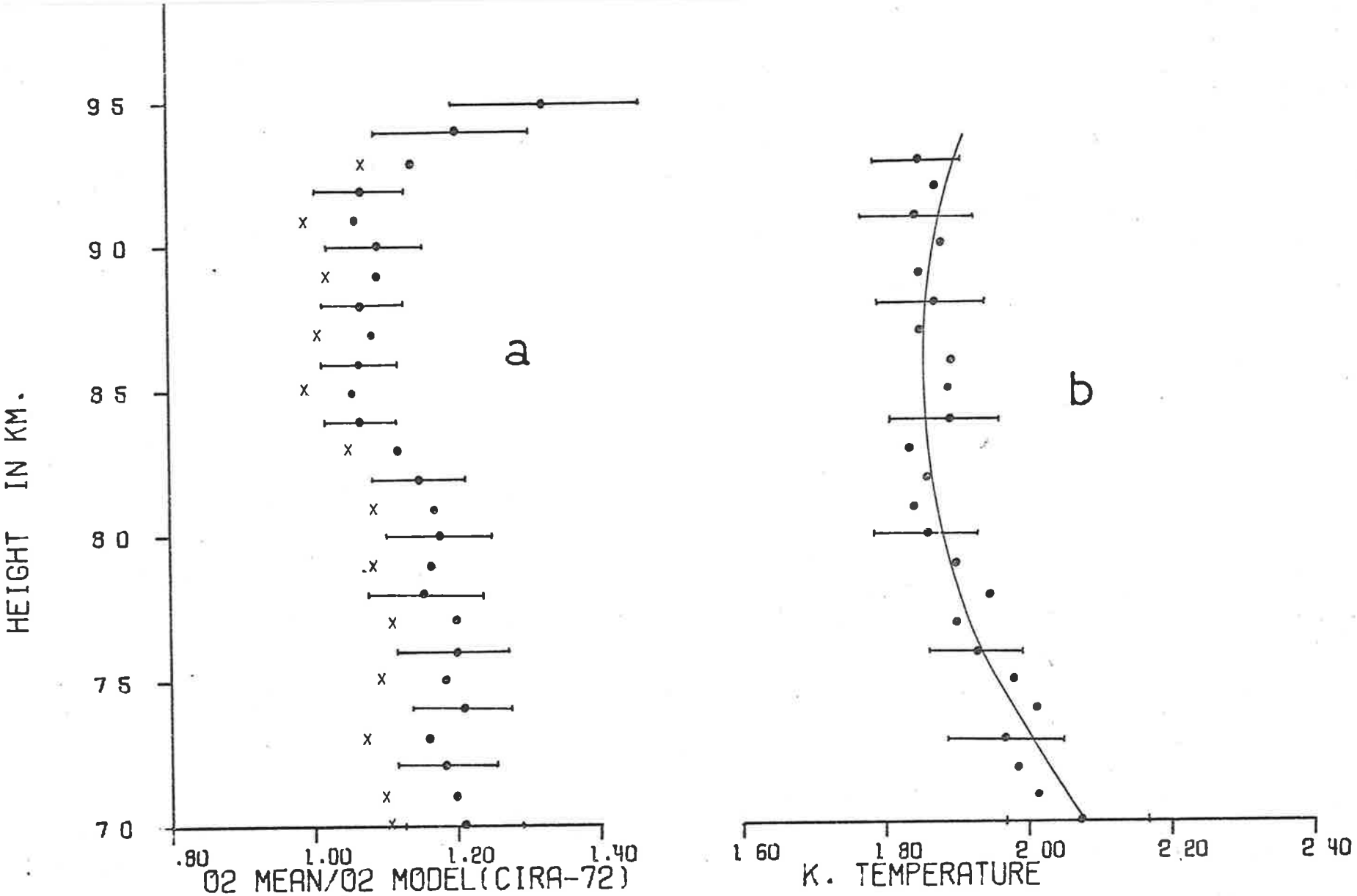

Figure 6.9 (a) Observational mean O_2 (ratios to CIRA-72). . The crosses represent the means if absorption due to other constituents is included as $7.0 \times 10^{-22} cm^2$.

(b) Means of derived kinetic temperatures.

could thus be argued that the theoretical profile represents the total average cross-sections including the effects of absorption due to other constituents as well as the larger temperatures in the lower altitude region as mentioned above.

6.3.5 Conclusions

Mesospheric molecular oxygen data exhibits a clear seasonal variation with concentrations reaching a maximum in the winter season. The data also indicates a possible hemispherical asymmetry in oxygen concentrations and temperatures at the mid latitudes. The seasonal variations in mesospheric molecular oxygen at Woomera (31° S) are found to be rather small in comparison to the variations for the northern latitudes. The observational mean based on the absorption cross-section profile at 195 K is in good agreement with the mean model (1972) and still better if account for absorption due to other constituents is made by adding a constant term $7(\pm 2)\times 10^{-22} cm^2$ to the absorption cross-sections. The mean O_2 ratios with CIRA (1972) over the range 70-90 km may be taken as 1.05 ± 0.10.

6.4 DISCUSSION OF THE SOLAR FLUX RESULTS

The region of the solar temperature minimum (Section 1.2) between the upper photosphere and lower chromosphere is of considerable importance for the theory of the solar atmosphere. The value of the temperature minimum may be inferred from measurements of the brightness temperature of radiation emitted from this region. As explained in Section (1.2), both observation (Tousey, 1964) and theory (Gingerich et al. 1971) suggest that the wavelength range 152.5 nm to 168.2 nm is the part of the spectrum most clearly showing the properties of the solar temperature minimum.

As can be seen from Figure (3.9), the spectral response of a Q - T ionchamber of the type flown in rockets in this work, is particularly well suited to a determination of the solar continuum flux over the above wavelength range. The solar fluxes determined (as described in Section 5.8.3) from Q - T ionchambers in several rocker flights are represented in

Figure (6.10) as black body curves plotted over wavelength range equal to the full width at half maximum (FWHM) response of the ionchamber. Black body curves for various temperatures are also shown in Figure (6.10) for comparison with the observations. The flux values refer to the integrated radiation from the entire solar disk. Combining the results from all four flights and giving less weight to the results from flight C4009 (due to larger errors), a mean value of (4550 ± 50)K is obtained for the minimum solar brightness temperature. These results are consistent with earlier results for similar ionchamber observations (Carver et al. 1969, 1972).

Ionchamber determinations are compared in Figure (6.10) with spectroscopic observations of the solar flux made using dispersing instruments by Parkinson and Reeves (1969), Widing et al. (1970), Bruckner and Moe (1972), Bruckner and Nicholas (1972), Ackerman and Simon (1973) and Nishi (1973, 1975). Widing et al. (1970), using photographic recording techniques, have found that the brightness temperature of the ultraviolet continuum emerging near the centre of the solar disk, passes through a minimum in the region of the silicon ^1D continuum with a value of (4670±100)K. Parkinson and Reeves (1969) have used a photoelectric recording technique to study the spectral region between 140 nm and 188 nm. The observations of Parkinson and Reeves (1969), also made near the centre of the solar disk, suggest a brightness temperature of 4400 K (or lower) and therefore some 300 K lower than the value obtained by Widing et al. (1970). Hinteregger (1970) has reported that the results of a second flight in August 1969 tend to confirm those of the earlier flight of Parkinson and Reeves. Brueckner and Moe (1972) also using photographic recording techniques, have determined the intensity distribution of the continuum radiation emerging from four localized areas on the solar disk at positions 7, 24, 40 and 300 arc sec from the limb. The intensity distribution for the region nearest the centre of the disk is shown in Figure (6.10) and indicates a minimum radiation temperature of 4550 K in the wavelength region from 166 to 174 nm.

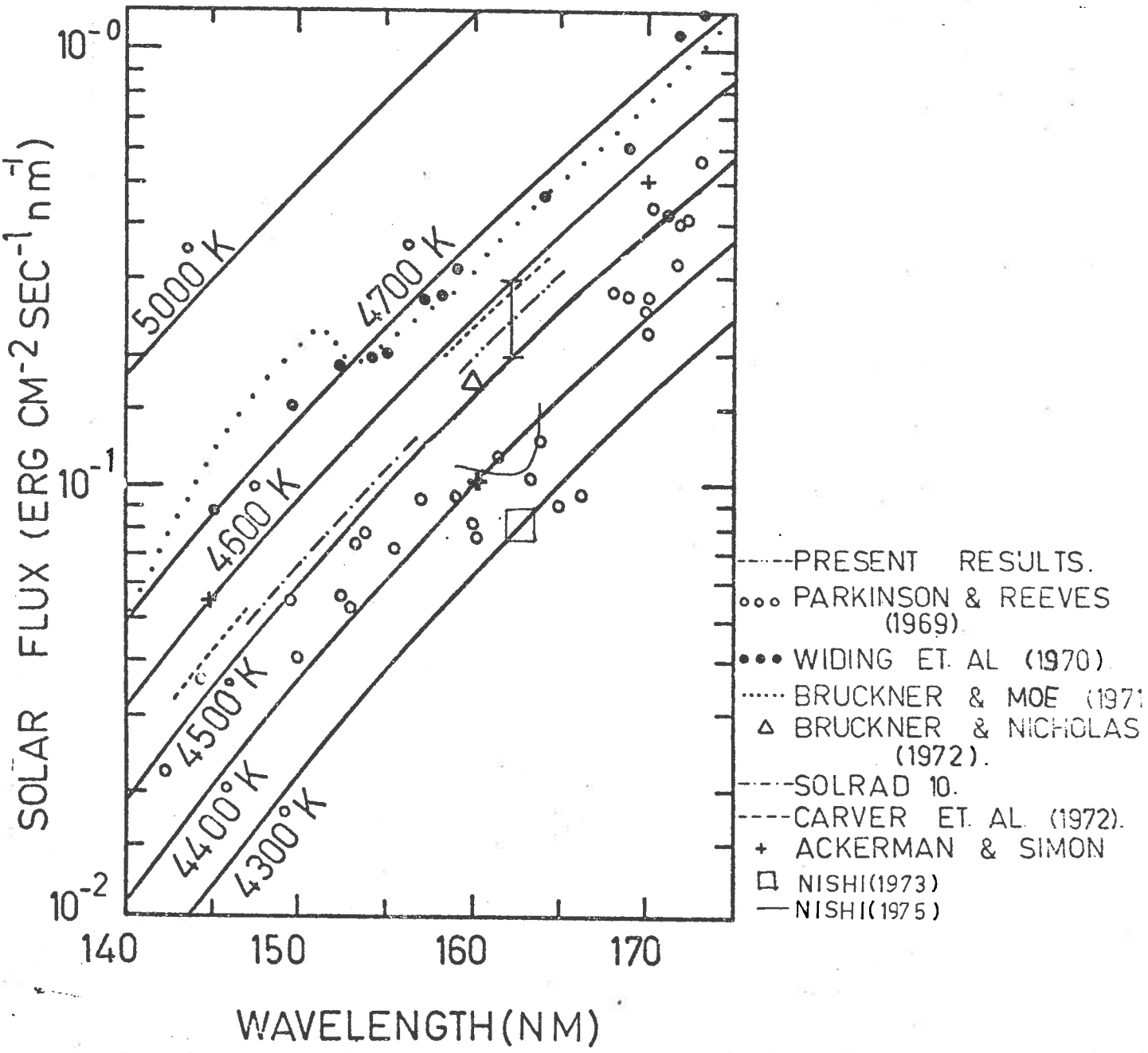

Figure 6.10 Solar ultraviolet flux observations compared with black body curves for a range of solar brightness temperatures.

The results of Nishi (1973, 1975) and Ackerman and Simon (1973) have been obtained using photoelectric techniques. The observations in the two latter cases are for integrated flux from the whole solar disk and can be directly compared with the present ionchamber measurements. All the remaining spectroscopic observations refer to localized areas of the solar disk, and to make the comparison shown in Figure (6.10), the observations have been converted to total disk emissions, assuming that the disk is uniformly bright in the wavelength region concerned (Section 1.2).

The results of Nishi (1975) are consistent with the significantly lower values of Parkinson and Reeves (1969). As explained in Section (1.2), information about the solar temperature minimum region can also be obtained from observations in the infra-red portion of the spectrum. Recent measurements in the infra-red, carried out at wavelengths spanning the region of the solar temperature minimum, yield a mean brightness temperature of (4370±260)K for the spectral range 238 μ to 312 μ (Eddy et al. 1969). This value recorded at aircraft altitude, is in agreement with the ultraviolet measurements of Parkinson and Reeves (1969). However, the nature of the Plank function is such that observations of the ultraviolet continuum intensity should be the most sensitive indicator of the precise value of the minimum temperature.

The difference of approximately 300 K in the value of the brightness temperature determined near 160 nm by the use of photographic and photoelectric recording techniques, represents a difference of a factor of three in the measured solar flux. The ionchamber measurements provide an independent estimate of the solar minimum brightness temperature using simple detectors which are very straight forward to calibrate (Section 3.8). In the important region of the temperature minimum near 160 nm, the present ionchamber observations are inconsistent with the very low flux values reported by Parkinson and Reeves (1969) and Nishi (1975).

Ly-α ionchambers have been used extensively for the purpose of measuring solar Ly-α radiation from both rockets and satellites. A list of most of the rocket measurements up to 1967 has been made by Weeks (1967). Although, the satellite measurements are generally less accurate due to gradual deterioration in detector sensitivity over an extended period and variation in contribution due to other radiation in the detector pass band (Section 2.4), these measurements are very useful in studying long term variations in the Ly-α flux. More recently, satellite measurements have been made using spacecrafts such as Intercosmos-I (Felske et al, 1970), OSO-4 (Timothy and Timothy, 1970), Solrad-8 (Fossi et al, 1970), Wresat-1 (Lockey, 1972) and OSO-5 (Vidal-Majdar, 1975). The results of Vidal-Majdar (1975) are of particular importance since they span a period of four consecutive years in which both total solar Ly-a flux as well as its shape was monitored. This study has enabled the formation of empirical relationship between solar Ly-α flux and solar activity. Some of the more recent rocket measurements of Ly-α flux using both ionchambers and more accurate dispersive instruments are tabulated in Table (6.2). The lower value of the flux from the morning flight C1029, represents a 30% decrease in the flux from its afternoon value and is perhaps due to deterioration in detector sensitivity. Telemetry noise in flight C4009 introduced significantly larger errors. The results are in general agreement with other measurements.

6.5 CONCLUSIONS AND COMMENTS

A detailed analysis of molecular oxygen data in the altitude range 70-95 km has shown substantial seasonal variation in molecular oxygen and derived temperatures. Oxygen concentrations are found to be maximum in the winter season in agreement with the seasonal variability results of neutral atmosphere. However, seasonal variability of molecular oxygen at Woomera (31° S) is found to be relatively small. The results also indicate a hemispherical asymmetry at mid-latitudes in mesospheric oxygen and temperature data. The use of a new low-temperature

TABLE 6.2

Rocket Payload	Date	Ly-α flux (ergs/cm^2/sec)	Reference
S84	28/2/1972	3.43 ± .49	Ackerman and Simon (1973)
S90	28/2/1972	3.43 ± .49	Ackerman and Simon (1973)
C1029	23/11/1972	2.18 ± .40	Present Work
C1035	23/11/1972	3.26 ± .30	
C4006	28/6/1974	3.12 ± .45	
C4009	2/10/1974	2.15 ± .50	
LT-18	11/11/1966	4.2	Carver et al (1969)
H309	24/7/1969	3.9 ± .40	Lockey (1972)
H310	9/12/1969	4.2 ± .40	Lockey (1972)
H301	6/12/1963	5.4 ± .80	Carver et al (1964)
H304	4/2/1965	4.7 ± .80	Carver et al (1965)
NA 14.435	7/3/1970	3.1	Smith (1972)
Vert-1	28/11/1970	3.6	Martini and Shyutte (1973)
Vert-2	20/8/1971	5.3	

cross-section profile in the analysis of Ly-α absorption data has resulted in an observational mean profile which is in agreement (within ±10%) with the mean CIRA (1972) model.

In the altitude range 100-130 km significant seasonal and diurnal variability in molecular oxygen concentrations at Woomera (31° S) are found. The oxygen concentrations at these altitudes are found to be significantly lower from the mean CIRA (1972) model in agreement with other observations.

Recent atmospheric models (Moe, 1970; Jacehia, 1971) have replaced the fixed boundary conditions at 120 km of earlier models (e.g., the 1965 CIRA models) with time varying boundary conditions at 90 km. Therefore the information about seasonal and other variations near 90 km will have specific importance in more realistic modelling in future.

The solar minimum temperature between the photosphere and low chromosphere is an important parameter of theoretical models of the solar atmosphere. The nature of the plank function is such that observations of the ultraviolet continuum intensity should be the most sensitive indicator of the precise value of the solar minimum temperature. However, there is a difference of about 300 K in the values of the brightness temperature determined at wavelengths near 160 nm by the use of dispersive instruments with photographic and photoelectric recording techniques. This temperature difference represents a difference of approximately a factor of three in the absolute flux level. The Q - T ionchamber measurements provide an independent estimate of the solar minimum brightness temperature using simple detectors which are much easier to calibrate than the dispersive instruments. In the important region of the temperature minimum near 160 nm, the present ionchamber determination of (4550)K is inconsistent with that made using photo-electric recording techniques.

CHAPTER 7

ROCKET MEASUREMENTS OF NIGHT-TIME OZONE DENSITIES AND LUNAR MUV FLUXES

7.1 INTRODUCTION

Experiments to measure oxygen (O_2) - one of the major constituents of the terrestrial atmosphere - have been described in detail in the previous chapters. Oxygen (O_2) plays an important role in absorbing almost exclusively ultraviolet radiation in the region of 100 nm to 200 nm. In a similar fashion, ozone (O_3) - the triatomic form of oxygen - is responsible for the atmospheric absorption of ultraviolet radiation between 200 nm and 300 nm (Figure 2.1) and thus shields living things from this destructive radiation. It is through this absorption that ozone plays an important role in the photochemistry of the upper atmosphere. Hence a knowledge of the chemical and photochemical properties of ozone, and its atmospheric abundance as a function of time, are of great importance. The first allows the formulation of atmospheric models while the latter provides the necessary observational data needed, firstly, as an input to the modelling and secondly as a check against the success of the model. The ozone photochemistry has been discussed in detail by Dütsch (1971), Park and London (1974) and Crutzen (1974). Several aeronomic models have been formulated, the most detailed one to date for the region 60-160 km being due to Hunt (1973).

A number of techniques for measuring ozone concentrations have been developed in the past. A detailed description of these is contained in Pittock and Sparrow (1961) and Vassy (1965). Some of the most widely used methods are described below:

(a) The Umkehr Method

This is an indirect optical method and uses the ratio of signals received at ground level from two narrow-band-pass photometers - centred at two wavelengths in the relatively weak Huggins absorption bands of ozone in the region 300 - 350 nm -

as a function of solar zenith angle. The method is used at large zenith angles (50°-90°) and gives an approximate picture of vertical ozone distribution (Craig 1965; Ramanathan and Dave, 1957).

(b) The Electrochemical Method

This chemical method of Brewer and Millford (1960) has been widely used for obtaining the vertical distribution of ozone up to altitudes of about 40 km. It utilizes the oxidation of a chemical (Potassium Iodide has been most commonly used for this purpose) by ozone present in the air samples and the degree of oxidation is measured electrolytically by two electrodes.

(c) The Chemiluminescent Method

This chemical method due to Regener (1960) depends on the chemiluminescent reaction of ozone with certain luminescent materials (e.g. Luminol). The amount of light emitted during the chemiluminescent reaction gives a measure of ozone. Variations of the method have been used by Hodgeson et al (1970) for low altitude measurements and by Randhawa (1966; 1970; 1971; 1974) and Hilsenrath (1971) in rocket-borne dropsonde measurements thus covering a wide range of altitudes.

(d) The Atmospheric Absorption Method

The measurement of vertical distribution of ozone by this method is based on the fact that middle ultraviolet radiation (200 nm - 300 nm) while passing through the atmosphere is strongly absorbed by ozone in the atmosphere. A detector carried in a balloon, rocket or satellite measures the absorption profile with height from which the vertical distribution can be deduced. The geometry and general description of the method has already been given in Section (2.2.1) whereas equation (2.14) gives the basic relation between the observed flux profile and derived vertical distribution of the absorbing species - ozone in the present case.

A number of experimental techniques have been used for these type of measurements. Regener et al (1954) and Johnson et al (1952) have used rocket borne spectrographs to record the absorption profile while Sissons (1974) has used a Paetzold (1961) type ozonesonde in which a quartz sphere is used infront of a filter-photocell combination and the sonde has been flown on balloons and rockets. Several workers (Miller and Stewart, 1965; Reed and Scolnik, 1964; Reed, 1968; Carver et al, 1972b); Hays and Roble, 1973; and Tohamatsu et al, 1974) have used photometers consisting of photomultipliers mounted behind broad-band interference filters. Miller and Stewart have also used a simple prism spectro-photometer for satellite measurements.

Daytime absorption measurements have been made using solar radiation. Carver et al (1972b)used lunar radiation whereas Hays and Roble (1973) used another star for the night-time measurements. Reed and Scolnik have made use of UV night glow as radiation source.

Relative merits and measurement-accuracy for different ozone measuring techniques have been recently reviewed by Vassy (1965) and Dütsch (1971). The absorption technique was employed in the present ozone measurements. These measurements made at night-time employed lunar radiation as the source. A brief description of the instrumentation follows.

7.2 DESIGN AND CALIBRATION OF THE FLIGHT-PHOTOMETER

7.2.1 Introduction

The principles of several widely used techniques of measuring ozone concentrations have been discussed in the previous section. The absorption method is well suited to the ozone determinations although its usefulness is limited for night-time measurements employing the moon as a radiation source. The detectors employed are fairly rugged, compact and light in weight which makes them suitable for satellite and rocket experiments. The technique also has the advantage of not disturbing the part of the atmosphere under test.

The photometers used for the present series of measurements consisted of thin film interference filters mounted infront of photomultiplier tubes. The currents from these were passed through amplifiers and the voltages produced were applied to a telemetry system and transmitted to the recording ground station. Only one (C4019) of the two rocket flights conducted in this series with almost identical instrumentation, was successful. The instrumentation for this flight is given below.

7.2.2 The Photometers

The interference filters used in the rocket flight C4019 were obtained commercially and had nominal peak wavelengths of 212 nm, 248 nm and 268 nm. One difficulty associated with interference filters is the transmission of lower order pass bands at longer wavelengths - particularly in the visible region. Even if the transmission level in this region is much lower than the transmission in the UV region of interest, the integrated signal over the entire visible spectrum may become significantly large as was indicated by the laboratory tests also. To overcome this problem, another filter with a broad band around the main peak was used in series with all the three main filters. The mounting system used for the filters is shown in Figure (7.1). The filters were locked in the instrumentation block by a locking ring from outside.

The photomultipliers were E.M.I. type 9734 QB. The 9734 QB is an end window tube with a Cs S60 cathode and a spectrosil window (having a spectral response which extends from about 170 nm to visible wavelengths).

7.2.3 Electronics

(a) Amplifiers

The amplifiers used were solid-state logarithmic D.C. amplifiers with a dynamic range of six decades. The main reason for using a logarithmic amplifier was to ensure that the output signal due to lunar flux remained within the telemetry range. Some workers have used multiple stage amplifiers and each stage having an output telemetry channel. In principle it is possible

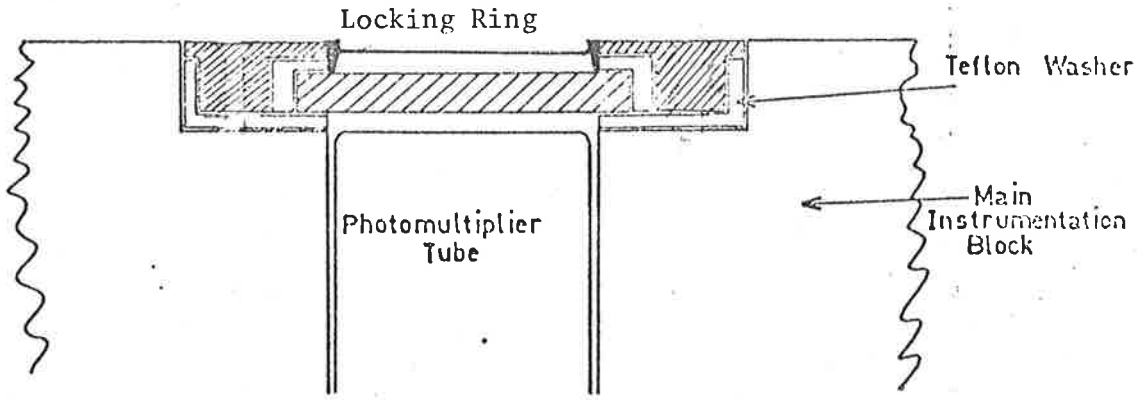

Figure 7.1a Side view of filter mount (not to scale).

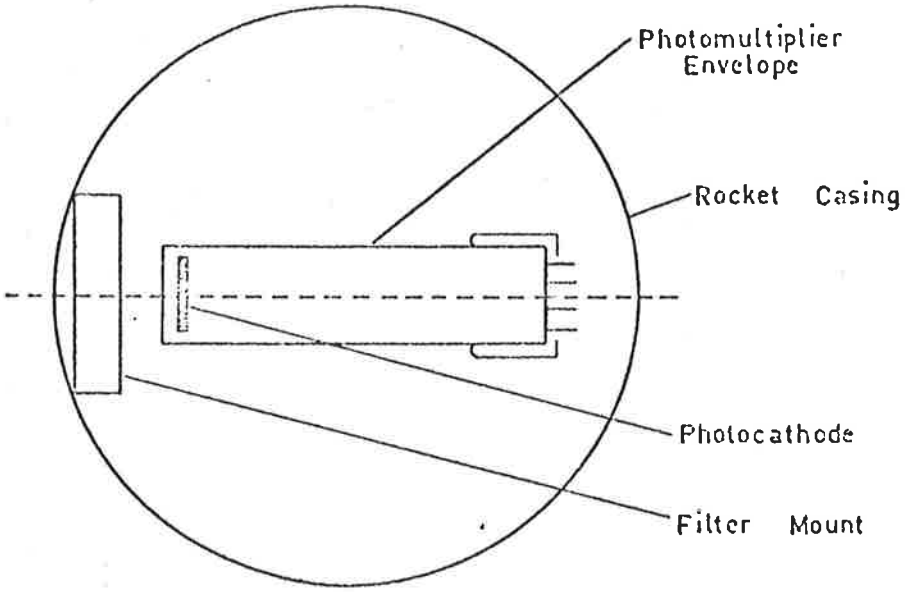

Figure 7.1b Layout for 9734 QB photemultiplier

to calculate the expected maximum signal during a flight as in fact is the case with direct solar UV radiation experiments. However, specific practical problems arise mainly because the absolute lunar flux critically depends on lunar phase angle at the time of observation. The delay of a flight by several days from a planned time may mean a significant change in lunar phase angle. Besides, there is quite a large uncertainty in the absolute flux. Temperature tests carried out by O'Brien (1973) showed that the temperature effect on the gain of the amplifier element would be negligible under temperatures these photometers encounter during a typical Cockatoo flight.

(b) High Tension Supplies and Protection against Dynode Vibration

The high tension voltage for the operation of the photomultipliers was supplied from a D.C. to D.C. converter. The output voltage from the supply was dropped across the resistor chains used to supply the dynode potentials to the photomultiplier tubes. Vibration tests (O'Brian, 1973) had shown that the photomultiplier tubes were susceptible to dynode vibration. To minimize the effects of this vibration a simple timing circuit built-into the electronic package - switched on the high tension unit after the second stage motor had finished burning and the vehicle was almost free of vibration.

7.2.4 Laboratory Calibration of the Flight Photometers

The photometers were calibrated using a 1/3 Meter Higer and Watts type monochromator and a deutierium lamp. The spectral response curves for the three photometers are shown in Figure (7.2). The spectral response curves were measured for several angles of incidence (Figure 7.2) so as to allow determinations of effective cross-sections as a function of aspect angle for each detector by integrating flux over the band passes for different angles of incidence (Section 7.5.1). However, only spectral curves at near normal incidence were used as the aspect angle variations

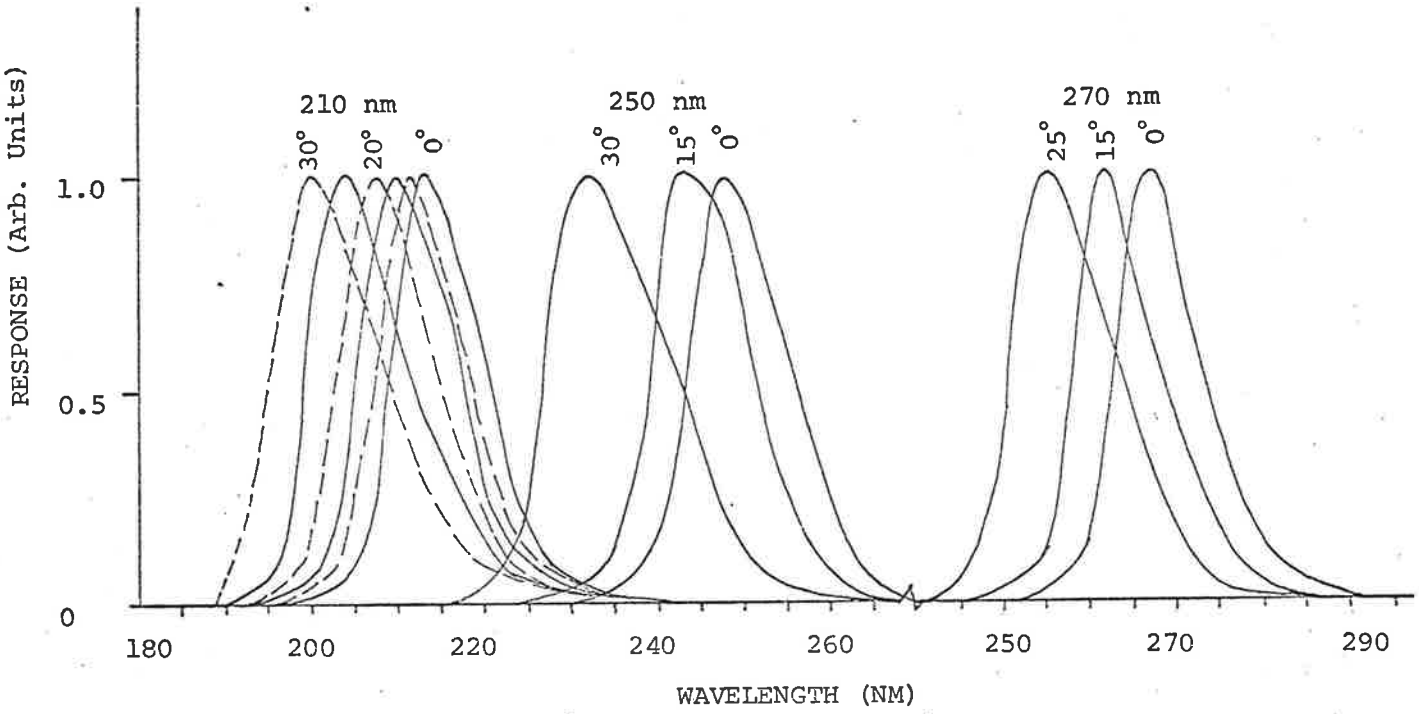

Figure 7.2 Spectral response curves of 210, 250 and 270 nm photometers flown in C4019.

in the earlier useful part of the flight were small (Section 7.3). The absolute calibrations of the spectral response curves were carried out using Standard UV Photodiode described in Section (8.3.2).

7.3 THE COCKATOO OZONE EXPERIMENTS AND FLIGHT PERFORMANCE

7.3.1 Introduction

Two flights were conducted to measure night-time ozone as part of a program to study diurnal and seasonal variations in oxygen and ozone. Each of the two flights was launched in a series of three flights (2 day-time and one night-time) conducted within 24 hours. The day-time flights were instrumented with ozone photometers* and oxygen photometers (Chapter 5) while the night-time flights were instrumented with ozone photometers along with an airglow experiment. Details of the performance of day-time flights has been given in Chapter 5. First of the two night-time flights had a power supply breakdown (immediately after it was switched on around + 30 secs) and no useful data was received. The second flight (C4019) provided useful data, details of which are given in Section (7.3.3).

7.3.2 The Rocket Vehicles, Instrumentation and Preflight Checks

The vehicles used for these flights were of the COCKATOO type and were spin stabilized (Section 5.2.1). The instrumentation layout was similar to the dayrounds (Section 5.2.2) with photometers in place of ionchambers, mounted diametrically in the instrumentation section (Figure 7.1).

All the power necessary for the operation of the electronics associated with the sensors was supplied from batteries, mounted inbetween the telemetry and sensors. All photomultipliers and their associated electronics were potted in Dow Corning Silastic 850RTV Rubber, both for protection against mechanical shock and for electrical insulation. The electronic circuits, after being potted were checked under vacuum. The usual sensor and telemetry checks described in Section (5.2.3) were also carried out for each round. A view of the payload is shown in Figure (7.3).

---

* Flown by another experimenter.

Figure 7.3 Complete Instrumentation head of Cockatoo C4019 showing three ozone photometers and the quadrant aspect sensor.

7.3.3 Location and Times of Rocket Flights

The two vehicles were launched from the Woomera Rocket Range (Section 5.3). As mentioned in the previous section, each of the two flights, formed part of a 'three flights-24 hours' series to study diurnal variation of oxygen and ozone. Since the night-time flights employed the moon as radiation source, selection of times was somewhat critical in order to launch vehicles close to the full moon. Another aim of these experiments was to extend ozone measurements to higher altitudes by conducting the experiments at times of large lunar zenith angles. Plotts of lunar and solar zenith angles were obtained well in advnace close to the full moon for a number of days. This enabled the selection of times fulfilling the requirements of large lunar zenith angles but small aspect angles in the vicinity of the full moon.

Cockatoo C4019 was fired at 2022 hours CST on 28 April 1975. At the time, the moon was at a zenith angle of 83° and a phase angle of 32°. The vehicle reached a maximum altitude of 122.3 km in 171.8 secs from launch and provided useful data for night-time ozone determinations and lunar fluxes. A discussion of these is presented in the following sub-section.

7.3.4 Reduction of Data and Results of Absorption Profiles - C4019

The vehicle was well tracked by on-range radar facilities and the tracking records were available in a convenient form as described in Section (5.4). The telemetered data from the optical sensors was available in the form of magnetic tape records as well as digital records as described in Section (5.5). The magnetic-tape records were directly processed on a CDC 6400 computer as in case of earlier fast spin vehicles (See Section 5.5) to obtain peak voltage outputs of optical sensors for each spin. The voltage outputs of ozone sensors were converted to linear form since the amplifiers used were logarithmic.

A quadrant ratio aspect sensor (Section 4.4) provided the useful aspect information. The results of aspect angle variations are shown in

Figure (7.4) from which it can be seen that the aspect angle variations were rather small until about 70 km on the upleg. The vehicle then went into a stead precession. On the downleg the vehicle became very unstable from about 70 km downward and no useful absorption data could be obtained. However, the constancy of aspect angles ($6^{\circ} \pm 2^{\circ}$) up to about 70 km greatly simplified the data reduction from ozone sensors since aspect corrections could be neglected. The absorption profiles as obtained from the two sensors are shown in Figure (7.5). These profiles were used to derive ozone density profiles which are presented in the next Section. The quality of absorption profile obtained from the third sensor (212 nm) was not very good and no further use of this data was made.

7.4 RESULTS FROM C4019 FLIGHT AND DISCUSSION

7.4.1 Vertical Ozone Distribution

The absorption profiles shown in Figure (7.5) can be used through equation (2.14) to obtain vertical ozone distribution i.e.

$$n_{O_3}(h) = \frac{dI}{I} \cdot \frac{1}{dh} \cdot \frac{1}{F(h,Z)} \cdot \frac{1}{\sigma_{eff(h,Z)}}$$

where $\frac{dI}{I}$ is relative change in photometer signal over a height range dh, $F(h,Z)$ is optical depth factor and $\sigma_{eff(h,Z)}$ is the effective absorption cross-section of ozone for the photometer pass band. The general procedure for evaluation of effective cross-section bas been described in detail in Section (2.2). The variation of absorption cross-section of ozone over the wavelength range 200-300 nm is shown in Figure (7.6) from which it can be seen that the absorption cross-section in the vicinity of 250 nm is virtually constant and the variation in cross section over the spectral band pass of present 248 nm photometer can be neglected thereby simplifying the evaluation of effective cross-section. The constant effective cross-section was used as $10 \times 10^{-18} cm^2$ for the 248 nm data. The variation in absorption cross-section over the present 268 nm band pass is significant. Strictly speaking, height dependent effective cross-section calculations, similar to those described in Section (2.2.3), should

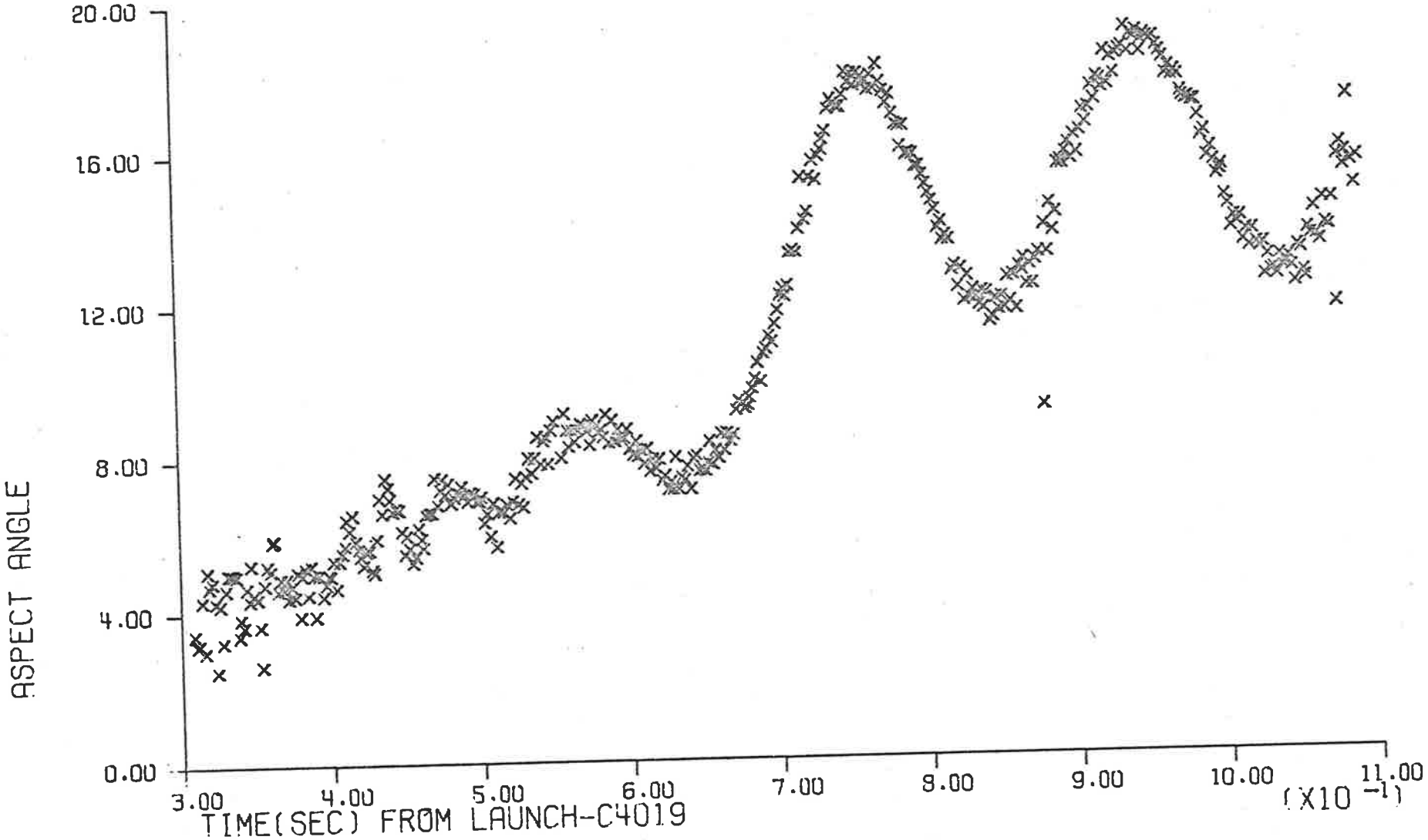

Figure 7.4a Aspect angle variation as a function of time - Flight C4019.

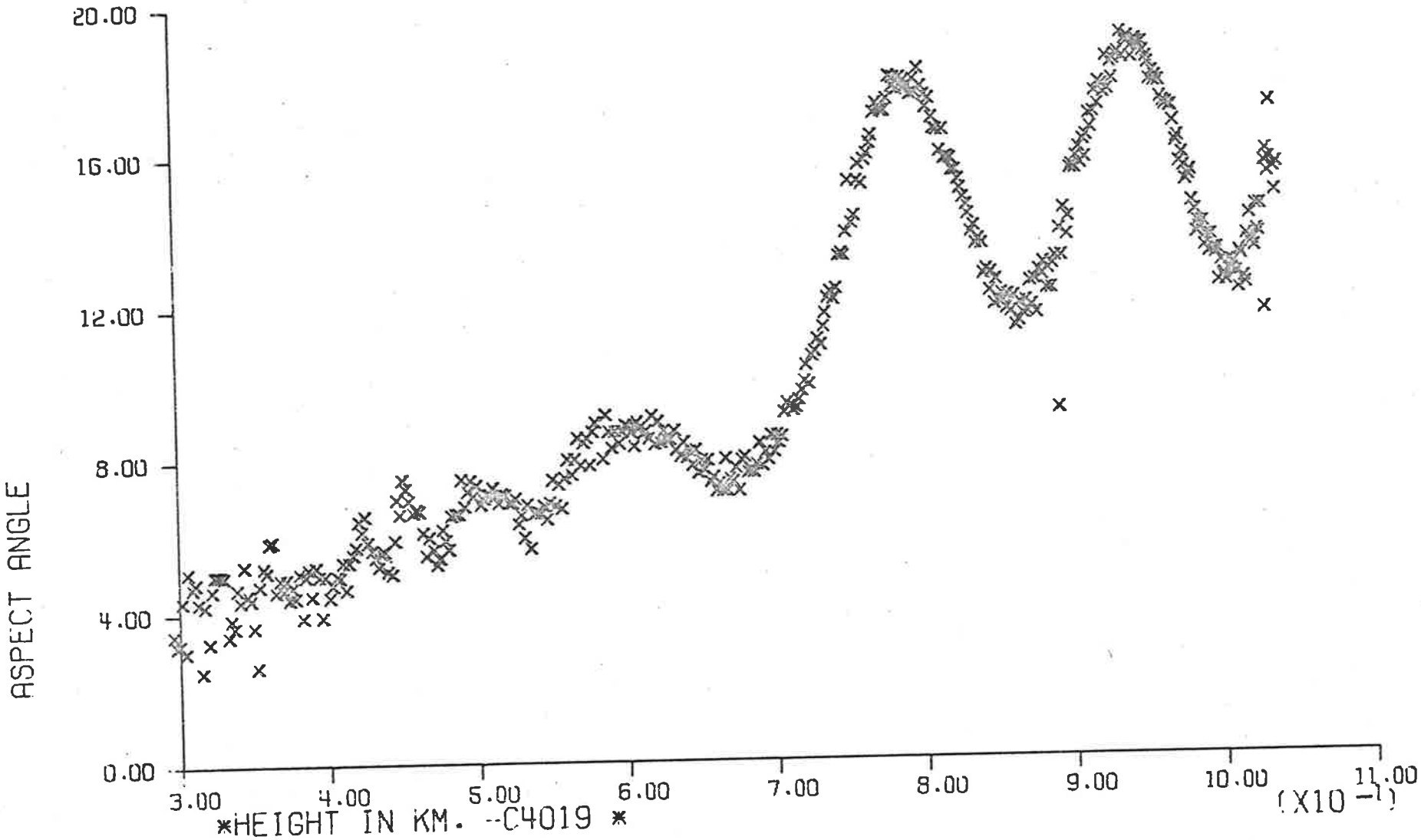

Figure 7.4b Aspect angle variation as a function of height - Flight C4019.

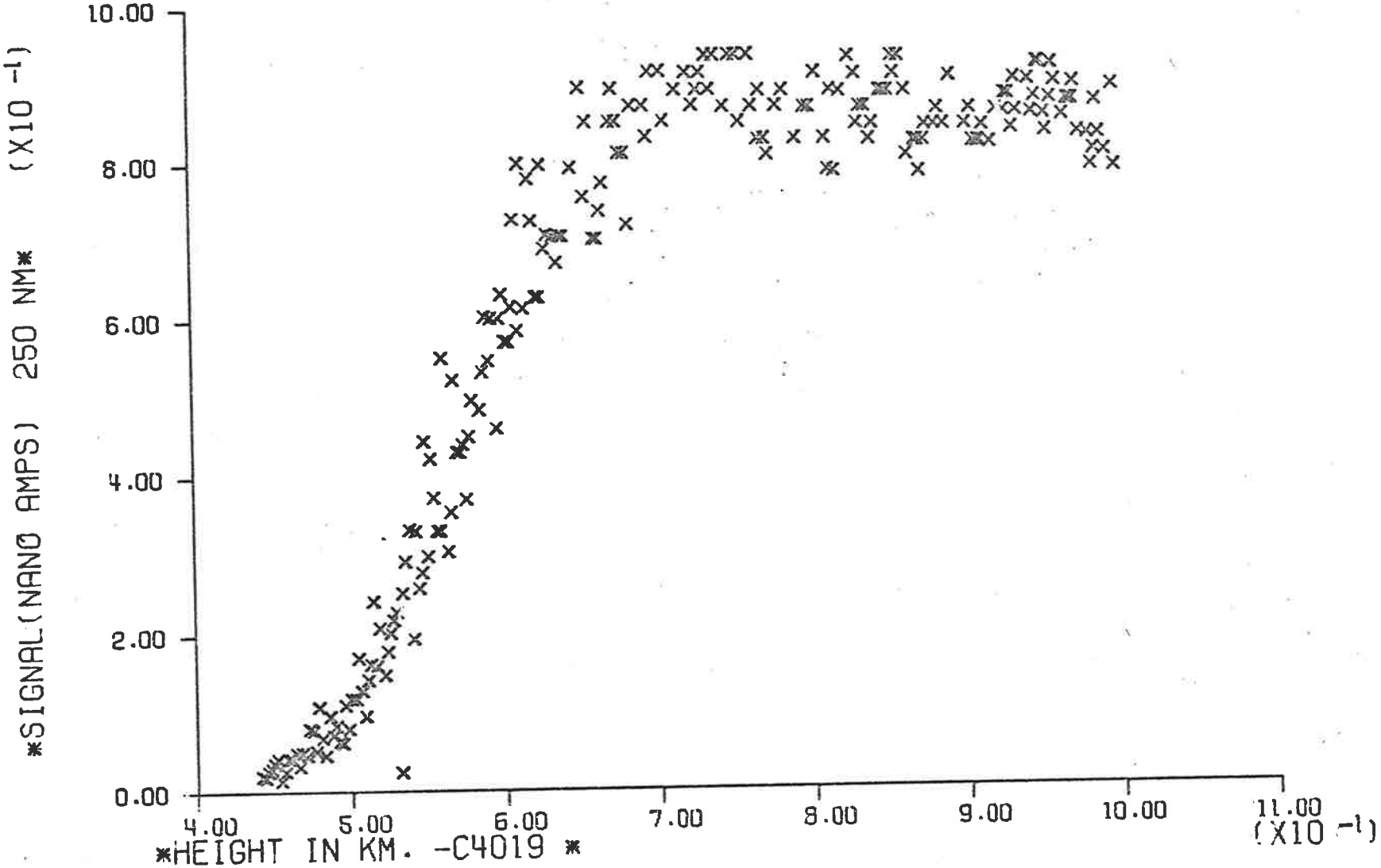

Figure 7.5a Absorption profile 250 nm data (C4019).

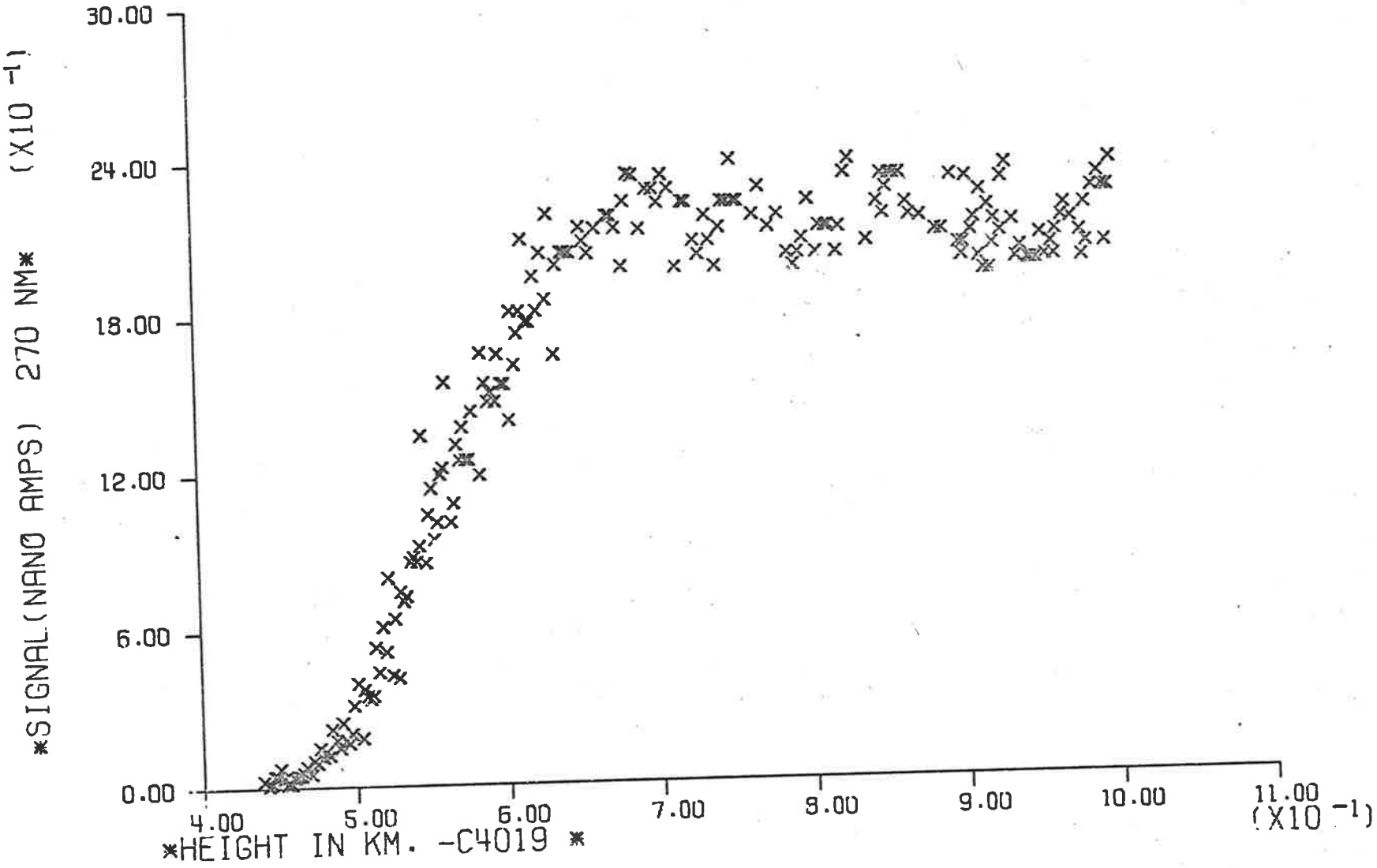

Figure 7.5b Absorption profile 270 nm data (C4019).

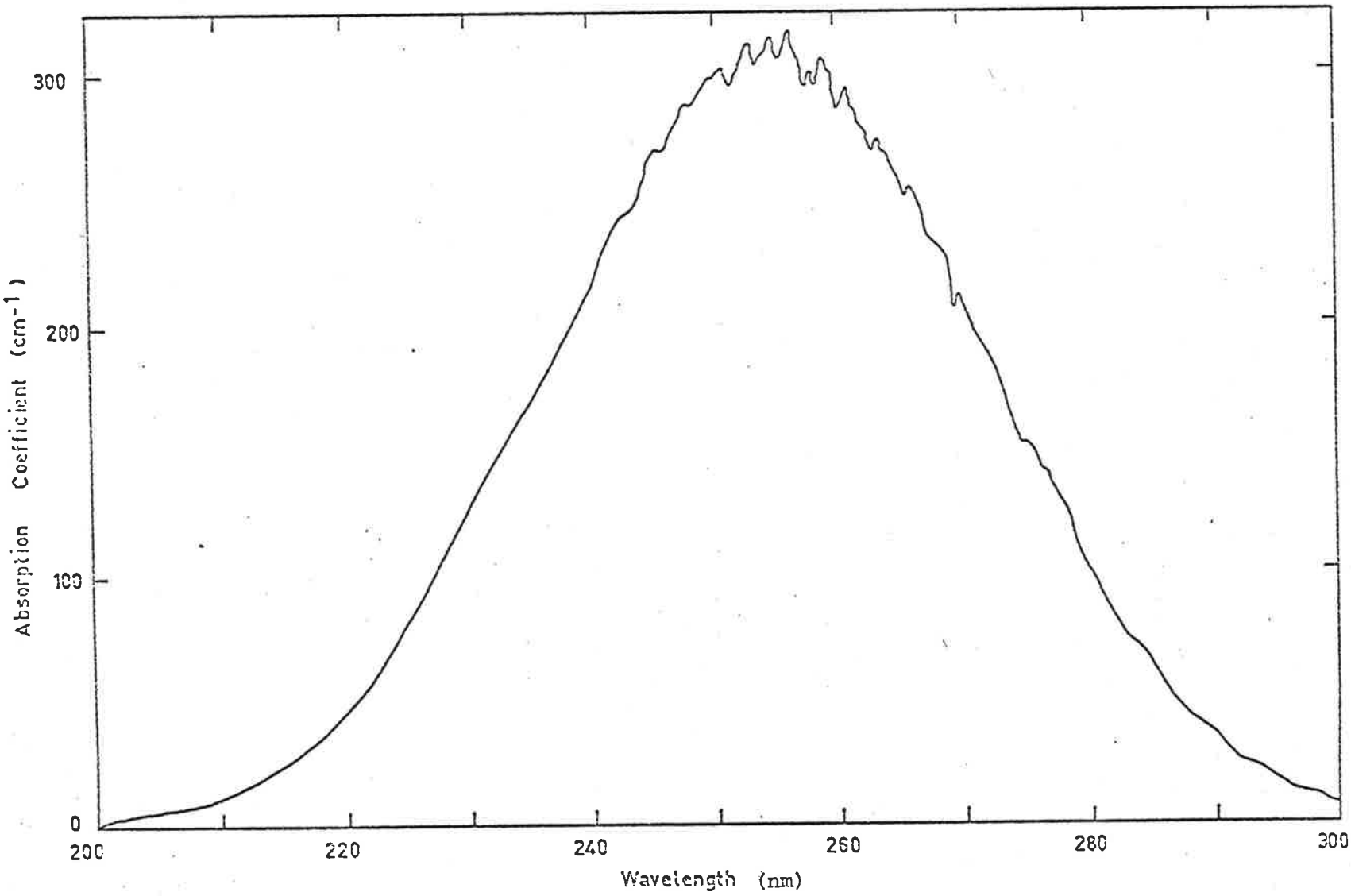

Figure 7.6 Absorption coefficient of O_3 (after Inn and Tanaka, (1959)).

be made. However, the spectral distribution of lunar ultraviolet flux, is not very accurately known. The effective cross-section calculations of O'Brien (1973) for a similar photometer showed this effect to be rather small at altitudes above about 50 km. Therefore effective cross-section at the top of the absorbing atmosphere was calculated using equation (2.12) which was used at all heights. The relative spectral distribution of lunar flux was taken to be the same as that for solar flux (Donnelly and Pope, 1973) assuming that the lunar albedo was constant at least within the spectral band of the photometer. The absorption cross-sections were taken from Inn and Tanaka (1959). The effective cross-section was used as $4.32 \times 10^{-18} cm^2$ for the 268 nm data. The resultant ozone profiles are shown in Figure (7.7a). These results are in general agreement with other ozone determinations(Figure 7.7b). This measurement was made to study diurnal ozone variation at Woomera. The data analysis from the successful daytime flight (C4018) has not yet been completed* and a useful comparison will be presented elsewhere. Considerable amount of mesospheric ozone data has now been accumulated and a detailed statistical analysis of this data (similar to that of mesospheric oxygen (Section 6.3)) would be of significant importance.

7.4.2 Lunar UV Fluxes and Lunar Albedo

The rocket apogee of 122.3 km meant that the values of the detector signal due to incident flux with negligible absorption were directly available from the absorption profiles at upper altitudes. Since each detector's response curves was absolutely calibrated, the incident photon flux could be determined assuming the constant photon flux over the Full Width Half Maximum (FWHM) of the detector pass band for each case. Two corrections were then applied, viz:

(i) A correction for the phase angle of the moon - this was needed to bring the value of flux up to the full moon value.

(ii) A correction for the earth-moon distance - this was needed because the earth-moon distance varies with time and the flux

---

* Another investigator

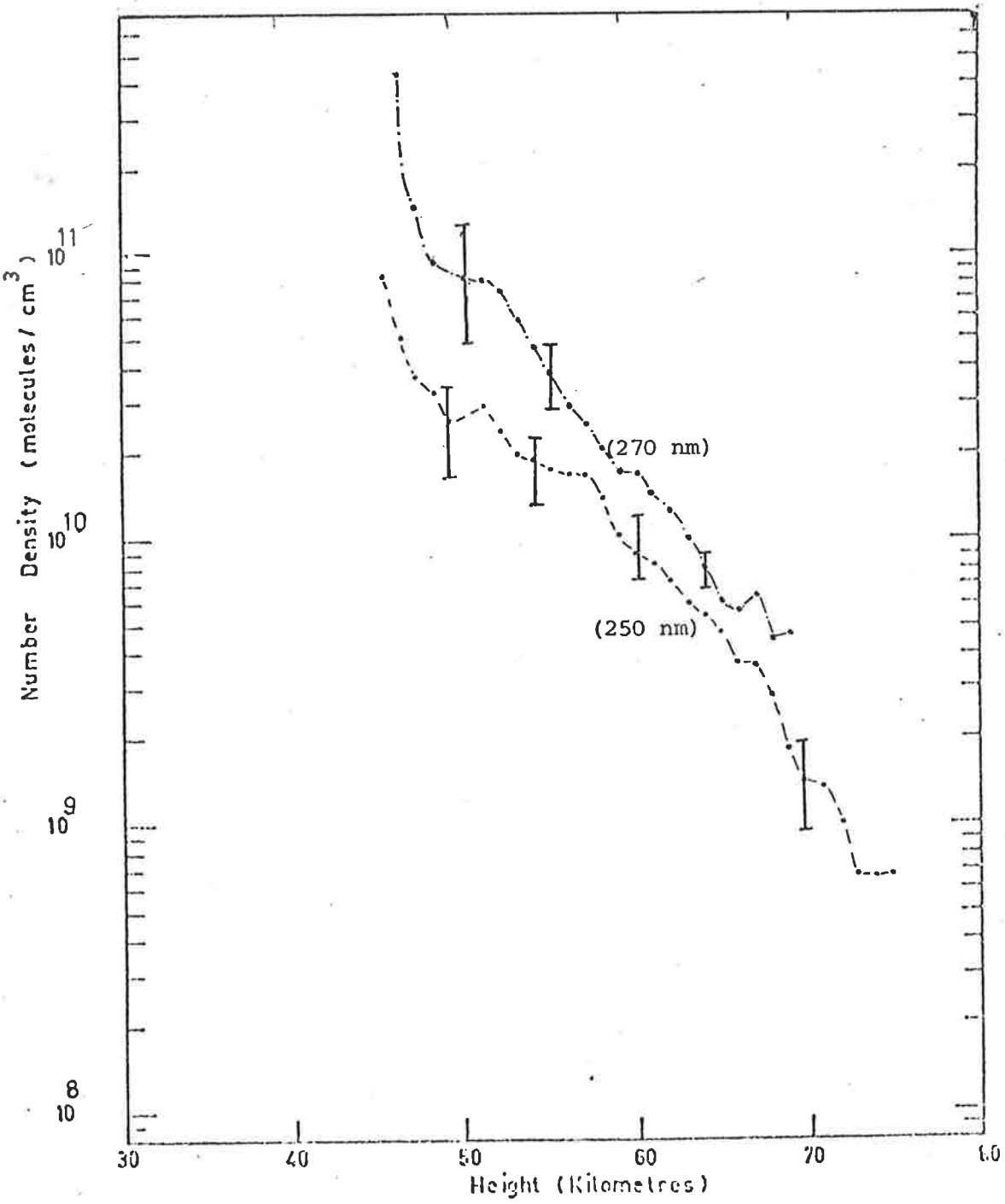

Figure 7.7a Nocturnal ozone density determinations at Woomera (C4019).

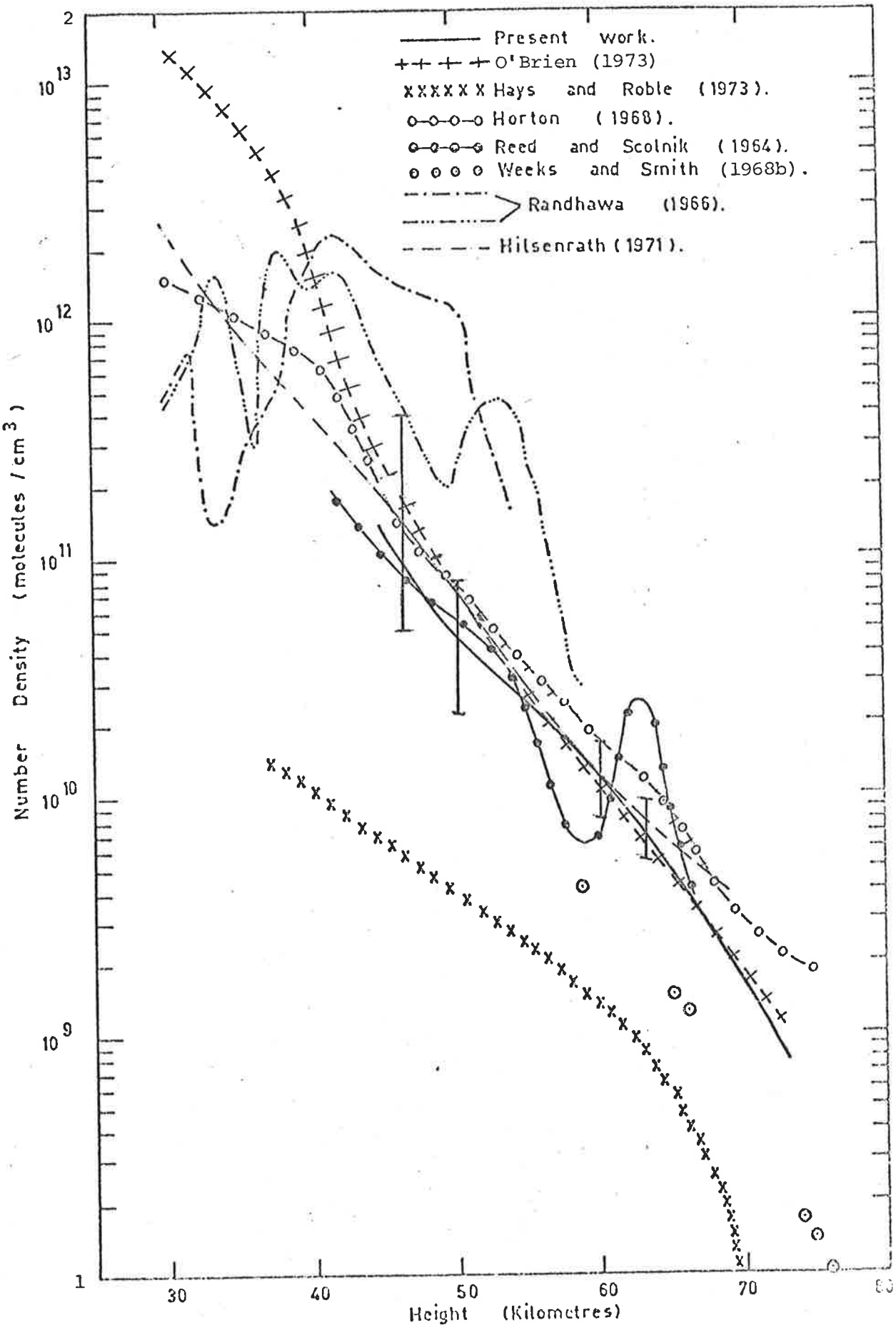

Figure 7.7b Comparison of nocturnal ozone measurements. (The bars indicate spread in data from the photometers).

values cannot be meaningfully compared unless referred to some mean distance.

The phase correction was applied by assuming that the phase law in the untraviolet was the same as in the visible. The lunar brightness relative to full moon was calculated from Rougier's Phase Law (Figure 7.8).

To correct for the earth-moon distance, the semi-diameter of the moon at the time of launch was obtained from the Ephemeris tables. To obtain the correction factor, the value of the semi-diameter was divided into the mean value of the semi-diameter (taken to be 15'32.58" of arc) and the resulting ratio squared. This factor was then multiplied by the value of full-moon flux to give the value of flux at the mean earth-moon distance. The time of nearest full-moon for flight C4019 was 2008 CST on 1st October 1974. The results of lunar flux are shown in Table (7.1).

TABLE 7.1

Effective Wavelength* (nm)	Lunar Flux $erg/cm^2/s/nm$	Phase Corr	Full Moon Flux $erg/cm^2/sec/nm$	Solar Flux $erg/cm^2/sec/nm$	Albedo percent
211	9.35×10^{-6}	2.14	2.0×10^{-5}	36	1.6±.5
245	1.64×10^{-5}	2.14	3.5×10^{-5}	66	1.5±.3
264	4.67×10^{-5}	2.14	1.0×10^{-4}	190	1.5±.2

* The lunar aspect angle in the unabsorbed flux region was 12.5° and the pass band at this aspect value was centred at these wavelengths which are different from the nominal peaks at o° aspect (see Figure 7.2).

The flux near the earth from the full moon can then be used to calculate the lunar spherical albedo A defined by (Kopal, 1969):

$$A = 0.585 \frac{LM}{LS} \left(\frac{r}{a}\right)^2$$

where r is the mean earth-moon distance (3.84×10^5 km), a is the radius of the moon, and LM (measured) and LS (calculated) are the lunar and solar fluxes. The factor 0.585 comes from a numerical integration of Rougier's phase law (Figure 7.8b), assuming that the visible phase law can be applied at ultraviolet wavelengths. The flux LS was calculated for each detector

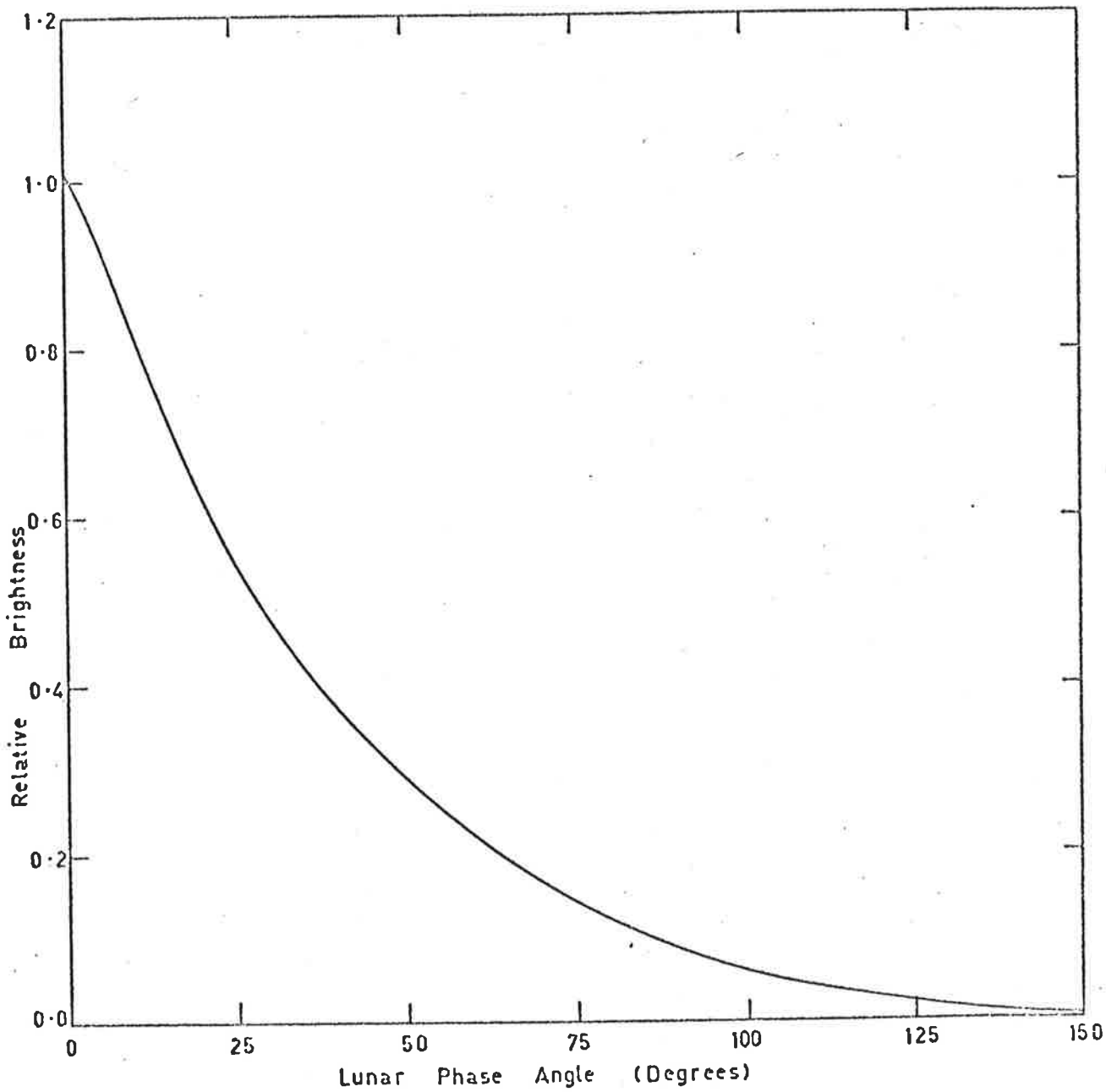

Figure 7.8a Variation of lunar brightness with phase angle (Allen, 1962)

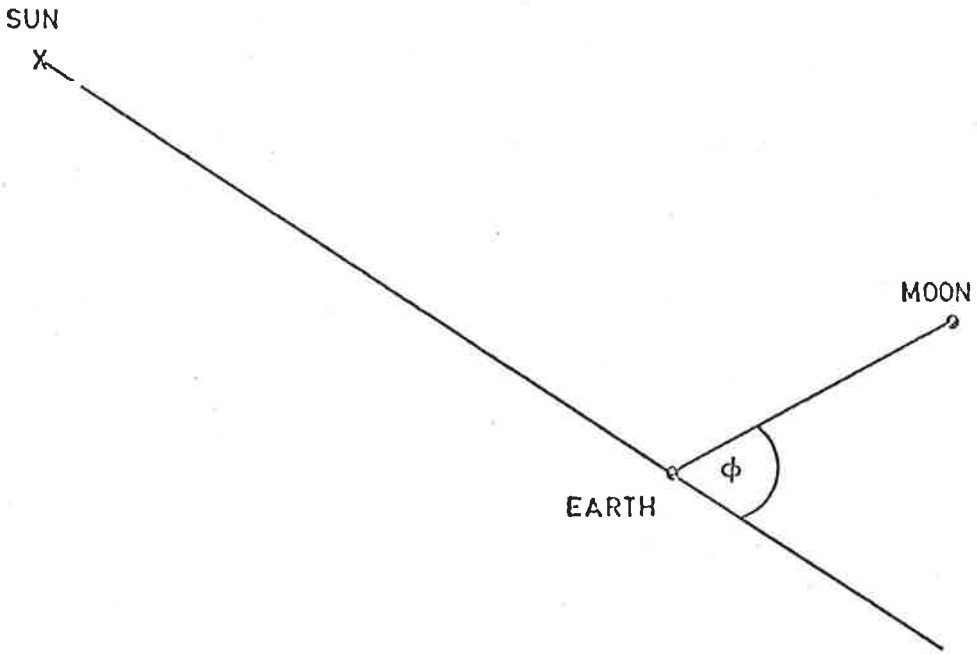

Figure 7.8b Showing how the lunar phase angle ϕ is defined with respect to the earth - sun line and the earth - moon line. ϕ is taken as positive after full moon, negative before full moon.

using the solar ultraviolet fluxes from Donnelly and Pope (1973). The results of spherical Albedo are shown in Table (7.1).

The lunar Albedo results have been recently compared by Bentley et al (1974) and Carver et al (1974b). The present results of lunar albedo are higher from the results of Carver et al (1974b). The photometers used in flights H305 and H312 (Carver et al, 1974b)were absolutely calibrated using sodium salicylate as a wavelength converter from Ly-α (121.6 nm) to MUV range (Horton, 1968). The transfer factor was taken to be 1.31. The present measurements (Sections 8.5 and 8.6) indicate this factor to be about 1.0 for wavelengths in the range 240-300 nm. Therefore Albedo results from these two flights should be increased by about 30 percent and agreement between these and present results will then be better.

CHAPTER 8

LABORATORY MEASUREMENTS OF THE QUANTUM EFFICIENCY OF SODIUM SALICYLATE AND ITS VARIATION WITH TIME BETWEEN 100 nm AND 300 nm

A brief review is made of the previous measurements of rel.q.e of sodium salicylate and its variation with the age of the film. New measurements of rel.q.e between 110 nm and 270 nm and the aging effect over a period of about 52 weeks are presented and discussed.

8.1 INTRODUCTION

Sodium salicylate has been used extensively as a wavelength converter in the near and vacuum ultraviolet (VUV) spectral region. When excited by radiant energy of wavelengths shorter than about 350 nm, salicylate fluoresces in a band covering the range 350 nm - 550 nm (Thurnau, 1956; Hamman, 1958; Kristianpoller and Knapp, 1964). It has been found that the quantum efficiency* of sodium salicylate is relatively constant over an extremely large range which makes it a very useful phospor. Generally it is the constancy of the efficiency as a function of wavelength which is important rather than the absolute value of the efficiency.

For absolute flux measurements, photometers need to be calibrated absolutely. The accuracy of calibration employing sodium salicylate as a wavelength converter would depend directly upon the accuracy of the relative quantum efficiency curve in the region of interest. In the present work, one of the ionchambers (Q - T) was being used to infer absolute solar fluxes and the solar minimum brightness temperature (Section 5.8.3). In view of the conflicting results in the region between 100 nm and 160 nm (Section 8.2), it was decided to carry out our own measurements to check the nature of the quantum efficiency curve in this region.

Except for the two earlier measurements of Johnson et al (1951) and

---

* The quantum efficiency is defined here as the number of fluorescent photons produced per exciting photon incident on the salicylate.

Watanabe and Inn (1953), none of the rather detailed measurements have been made over the entire spectral region from 100 nm to 300 nm. The necessity of such a measurement becomes evident when a photometer operative in the MUV (above 200 nm) is calibrated against another photometer operative in the VUV region (for instance a Ly-α ionchamber) using sodium salicylate as a wavelength converter (Horton, 1968). Therefore, it was decided to extend our measurements over the entire range of 110 nm to 270 nm. In order to study the aging effect over an extended time (about 52 weeks) four important wavelengths (144, 160.8, 200 and 253.7 nm) were selected at which variations of quantum efficiency relative to Ly-α (121.6 nm) were studied as a function of time. Details of the experimental procedure and method of analysis are presented in Sections (8.3 and 8.4). Section (8.2) contains a brief review of previous measurements of salicylate quantum efficiency.

8.2 PREVIOUS MEASUREMENTS OF THE QUANTUM EFFICIENCY OF SODIUM SALICYLATE - A BRIEF REVIEW:

Many groups have investigated the relative quantum efficiency of sodium salicylate in various spectral regions from 350 nm down to 10 nm, one of the first studies being due to Déjardin and Schwégler* (1934) who reported a constant efficiency between 220 nm and 340 nm. The constancy of quantum efficiency above about 200 nm has since been reported by several other workers (Hamman, 1958; Slavin et al, 1961; Kristianpoller and Knapp, 1964). The earliest extension of these measurements to wavelengths shorter than 200 nm was made by Johnson et al (1951) who covered the range from 85 nm to 230 nm. They reported the efficiency to be almost constant (within ± 20%) between 85 nm and 200 nm. Later, Watanabe and Inn (1953) repeated the measurements over the wavelength range 85 nm to 280 nm (plus one point at 58.4 nm) and confirmed the almost constant efficiency between 85 nm and 200 nm. The efficiency at 58.4 nm was found to decrease by about 15 percent. The results of Vassuer and Cantin (1963) show a substantial

---

* Just prior to the construction of the first photomultiplier (Zworykin et al, 1936).

increase in the rel.q.e. with wavelength from 50 nm to 300 nm. More detailed measurements in the wavelength range of 100 nm to 200 nm have since been reported by Knapp and Smith (1964), Samson (1964), Allison et al (1964, a,b) and Bruner (1969). Samson (1964, 1967) subsequently extended these measurements to 20 nm and a verification of Samson's (1967) results was made by Harrison et al (1969). Most recently Samson and Haddad (1974) have been able to extend the measurements further down to 11.6 nm which together with earlier measurements of Samson (1964) show that the quantum efficiency of sodium salicylate remains almost constant over the entire range 11.6 nm to 100 nm.

The results of Knapp and Smith (1964) and Samson (1964) showed a marked increase in the quantum efficiency from about 120 nm to 160 nm which was found to increase further with the age of the salicylate layer in both cases. Recent results of Allison et al (1964, a,b) show almost the same q.e. at wavelength 121.6, 160.8, and 253.7 nm and no aging effect at either 121.6 nm or 160.8 nm thus in direct support of the results of Johnson et al (1951) and Watanabe and Inn (1953). Knapp and Smith (1964) have attributed the non-constancy behaviour observed in their measurements for a fresh layer possibly to contaminats in the monochromator environment.

Relatively few measurements have been made of the absolute quantum efficiency of sodium salicylate partly because the absolute value has been found to vary with (a) layer thickness (Seya and Masuda, 1963; Kristianpoller and Knapp, 1964), (b) temperature (Kristianpoller and Knapp, 1964) and (c) age of the film (Section 8.6). There is a wide discrepency among the reported absolute values due to some of the above reasons. A summary of these results has been given by Samson (1967).

8.3 DESIGN OF THE EXPERIMENT TO MEASURE THE QUANTUM EFFICIENCY OF THE SODIUM SALICYLATE FILMS

8.3.1 Introduction

The most common procedure used for measuring quantum efficiency of a phosphor film has been to view a beam from the exit slit of a

monochromator by a thermopile and measure its energy. Then the beam is made to fall on a phosphor film and a photomultiplier views the secondary photons from the phosphor. Usually the film is prepared on a glan substrate and placed inbetween the beam and the photomultiplier. Johnson et al (1951) and Watanabe and Inn (1953) deposited their films directly onto the photomultiplier envelope rather than on a separate glass substrate. The signals from the photomultiplier and thermopile are recorded alternately rather than simultaneously and a comparison between the two signals gives the relative quantum efficiency (Knapp and Smith 1964). The system has the disadvantage that if the source is not a stable one, it would be troublesome to relate the two signals. Slavin et al (1961) overcame the problem by using a beam splitter which partially reflected and partially refracted the incident light. This type of splitter has a limitation that it requires a material which has an almost constant reflectance and transmittance properties over the entire wavelength range of desired measurements. A novel beam splitter particularly suitable for such measurements and used for the present measurements is described in Section (8.3.2). Furthermore, we employed a photon detector (photodiode) rather than an energy detector (thermocouple) to monitor the beam strength thus giving a direct comparison between primary photons and secondary photons. A description of the photodiode is given in the following subsection and a complete experimental procedure is outlined in Section(8.3.3).

8.3.2 Instrumentation

The basic instrumentation consisted of a ½M monochromator of the Seya Type, the source of radiation being a d.c. discharge through hydrogen as described in Section (3.8.2). The beam from the exit slit of the monochromator entered into a beam splitting chamber which was so arranged that a portion of the beam passed through while the remainder was absorbed by the phosphor coating deposited on the splitter.

The fluorescence photons resulting from the absorbed flux were

viewed by a side photomultiplier mounted on the external end of a light pipe. The other part of the signal was viewed by a photodiode and the currents were recorded from Kiethly microelectrometers (Section 3.8.2). The splitting chamber also had two accessary arms to which filtering windows could be attached. One or both of the windows could be moved in or out of the beam from outside without disturbing the inside vacuum. The first arm was located infront of the beam splitter and thus allowing filtering of the beam from the exit slit, the second arm was located after the beam splitter and allowed the filtering of only the transmitted portion of the beam from the splitter. Details of the beam splitter and photodiode are given in the following subsections. An exploded view of the splitting chamber is shown in Figure (8.1).

(a) Beam Splitter: Extensive use has been made of a beam splitter in our laboratory over the years. The standard design consists of a wire mesh soldered at 45° inside a cylindrical shell. A phosphor coating is then deposited upon the wire mesh by spraying a concentrated solution of the phosphor (Section 8.3.3). For the present study, relatively large number of coatings were planned to be prepared and studied over an extended period, particularly to study the aging effect. Deposition of these coatings on a mesh type splitter would have meant the manufacturing of a rather large number of entire splitter assemblies. To avoid this, a modified beam splitter was used with two wide supporting legs between the outer circular rings. A groove in each of the legs was cut at 45° such that a glass slide could be passed through the grooves. Two small arms were attached on each of the legs so that the distance of the lower end of the slide from the longitudinal axis of the cylindrical splitter could be varied thus varying the position of the beam passing underneath the coated slide. Views of the splitter can be seen from Figure (8.1).

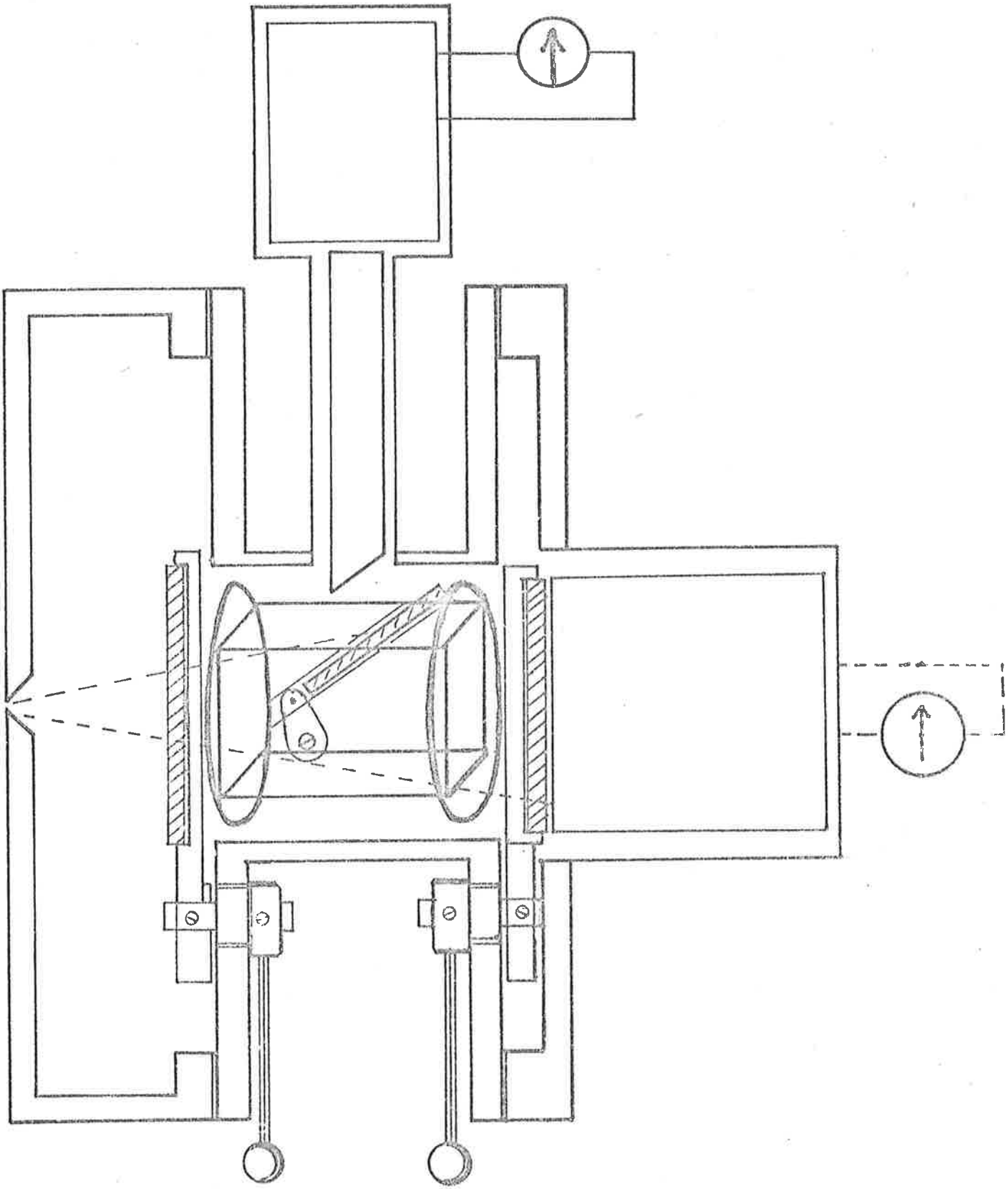

Figure 8.1a An exploded view of the splitting chamber and beam splitter used for relative quantum efficiency studies of sodium salicylate.

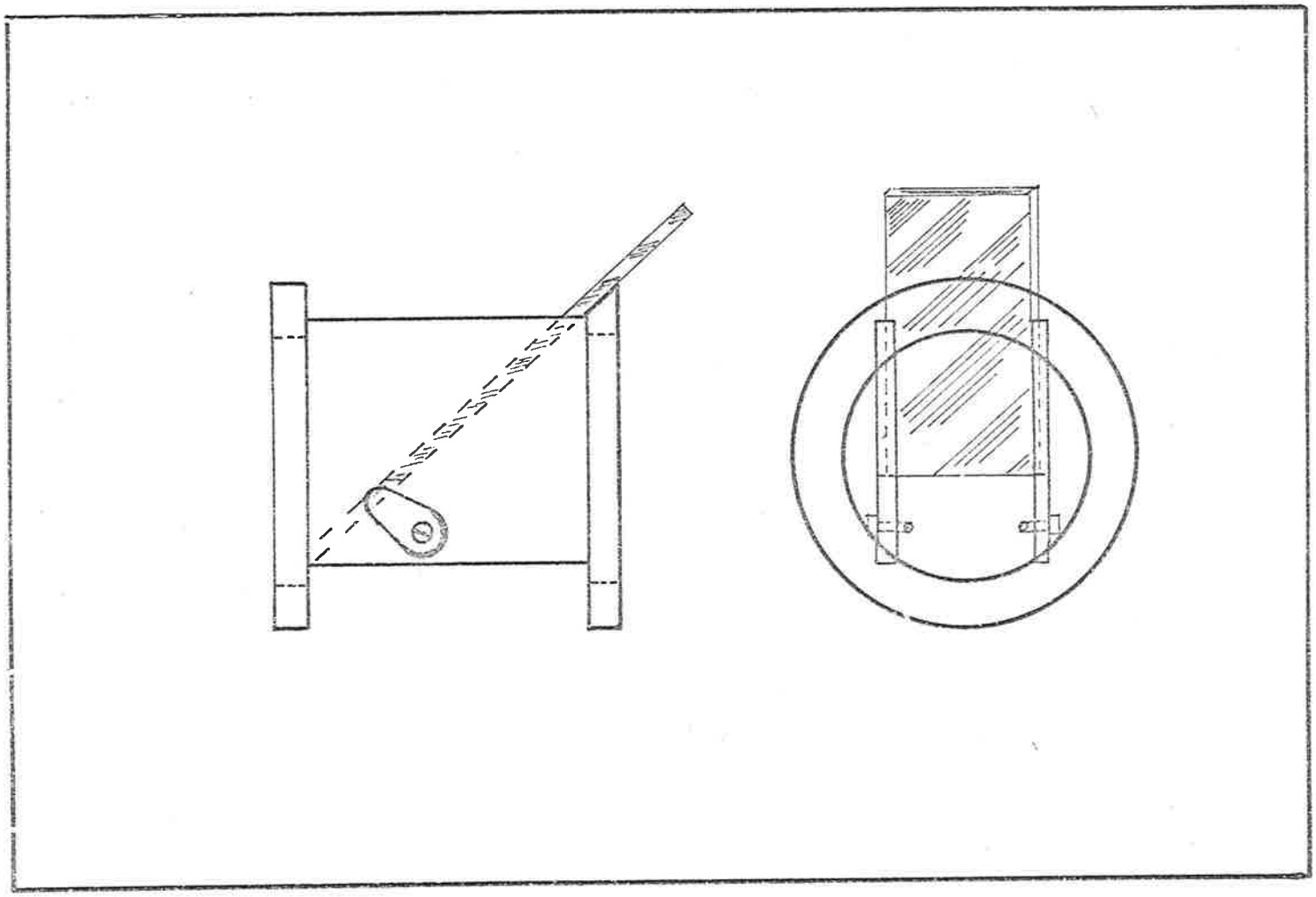

Figure 8.1b Views of the beam splitter.

(b) Photon Detector: The photon detector used in these measurements for monitoring the beam strength was a Far ultraviolet photo-diode, EMR model 543P-09-00. It is a solar-blind, end-on, magnesium-fluoride window tube with a 2.8 Cm diameter and semi-transparent rubidium telluride photocathode with a spectral sensitivity from 115 nm to about 320 nm.

The detector was calibrated absolutely at the National Bureau of Standards, Washington, for a number of lines between 115 nm and 254 nm. A typical cathode sensitivity curve was also available to allow extrapolation of absolute efficiency curve beyond 254 nm. The absolute calibration of the detector efficiency is shown in Figure (8.2). Data points beyond 253.7 nm are extrapolated values obtained with the help of typical cathode efficiency curve.

8.3.3 Preparation and Storage of Sodium Salicylate Samples

Sodium salicylate was disolved in methyl alcohol to form a saturated solution and was then sprayed onto a glass slide with an atomizer. The atomizer sprayed the solution parallel to the glass slide while a heat gun blew hot air continually, directly onto the glass slide. This meant that only smaller drops from the atomizer passing between the slide and the heat gun were blown onto the slide resulting in a rather uniform layer. The heat gun also helped the evaporation of the alcohol. The spraying continued until almost all the glass surface was covered. However no attempt was made to maintain a constant layer thickness to introduce some randomness in the layer thickness among various samples. The thickness of individual sample was later recorded by weighing the sample .

The samples so prepared were stored under dust free atmospheric conditions by placing them in the 'petri dishes' at all times except when they were placed in the splitting chamber for the purpose of actual observations. This duration was typically less than 10 minutes for the observations related to 'the aging effect study'.

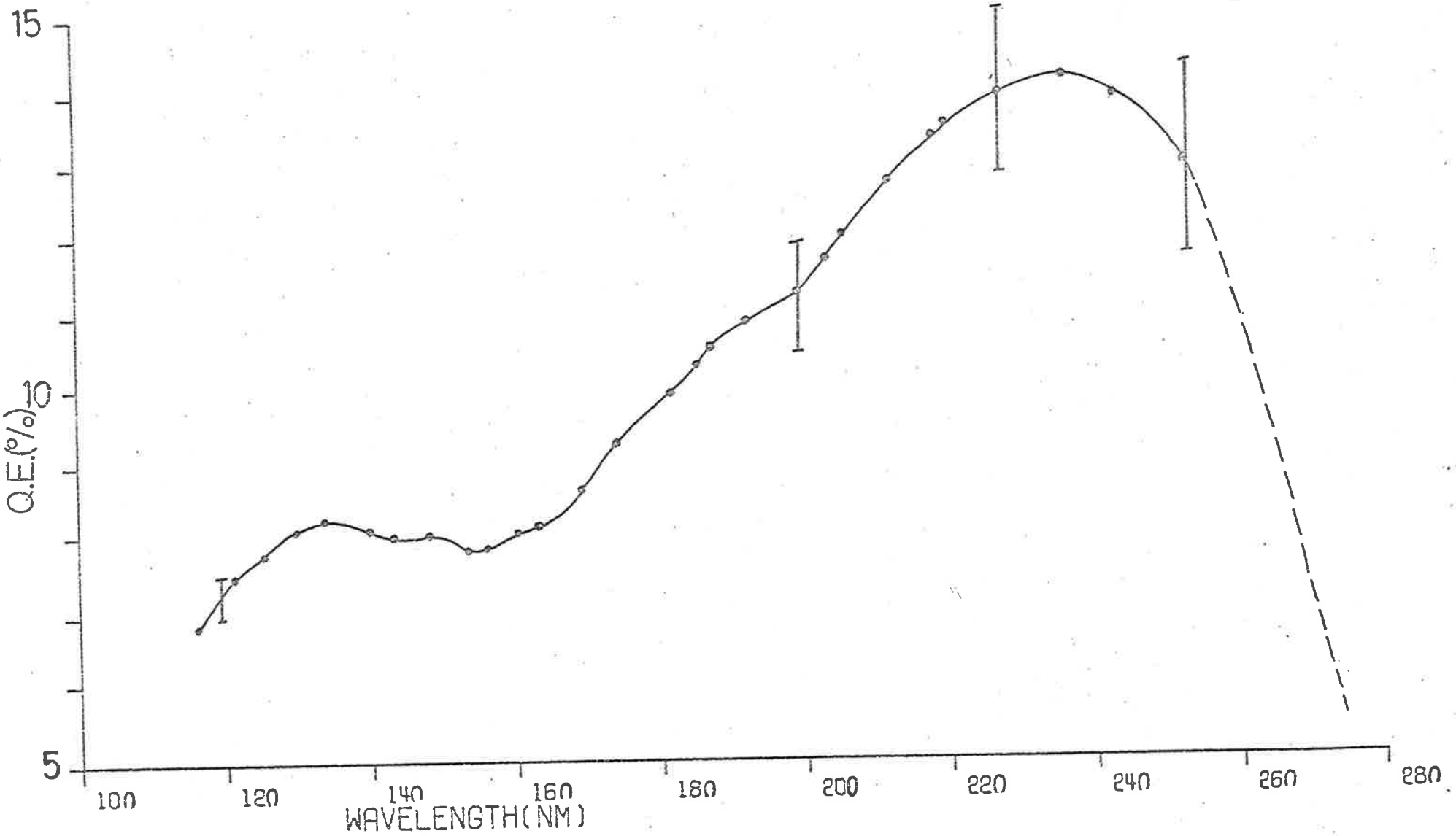

Figure 8.2 Absolute quantum efficiency calibration of the standard photo-diode.

8.3.4 Experimental Procedure

The experimental procedure consisted of two parts; firstly to prepare sodium salicylate sample layers and their subsequent storage and secondly to carry out actual measurements of quantum efficiency by recording the partial beam intensivity and fluorescent intensity. For the purpose of studying the aging effect a large number of samples with different ages were used. A set of three numbered samples was prepared and stored each week for nine weeks. This provided 9 sets whose ages varied between 0 and 9 weeks. The first observation was made in the middle of the 6th week and repeated, initially with a time interval of one week. Then the observations were repeated with a time interval of 2 weeks followed by three observations with time intervals of 3 weeks, 7 weeks and 23 weeks respectively. The longer durations towards the end were mainly to minimize any possible radiation fatigue effects (Knapp and Smith, 1964). Initially only two of the three samples of each set (numbers 1 to 9 and 11 to 19) were used and the third one of each set (numbers 21 to 29) was stored unexposed until the last observation. These 9 samples were then used hitherto unirradiated to make similar measurements of the aging effect. A comparison between the data of this and the other two groups provided a check if the observed aging effect for later observations has been caused by the radiation fatigue due to exposures of the samples to UV radiation during previous observations (Section 8.5.1).

For observations of the relative quantum efficiency between 115 nm to 260 nm, freshly prepared samples were used. One of the samples was kept in position undisturbed and observations repeated to obtain relative efficiency variations over a period of about 90 hours. The experimental set-up was similar in either case and differed only in the method of data analysis.

8.4 ANALYSIS OF EXPERIMENTAL DATA

In order to analyse the recorded signals from the photomultiplier and photodiode, it is needed to investigate the relationship between these

signals and the respective detector efficiencies.

The beam from the exit slit of the monochromator is divided into two parts by the beam splitter (Fig 8.3). A fraction of the beam directly reaches the photodiode whereas the remainder is absorbed by the sodium salicylate layer deposited on the glass slide resulting in the fluorescence emission in the visible. If the total photon flux at a wavelength λ, emerging out of the exit slit is represented by $Fo_{(\lambda)}$ and the fraction $S_{(\lambda)}$ directly reaches the photodiode then signals out of the photodiode and the photomultiplier may be represented as:

$$i_{(\lambda)} = [Fo_{(\lambda)} \cdot S_{(\lambda)}] \cdot \eta_{(D,\lambda)} \tag{8.1}$$

and

$$I_{(\lambda)} = (1-S_{(\lambda)})\ Fo_{(\lambda)} \cdot C_{(p,\lambda)} C_{(S)} \cdot \eta_{(S,\lambda)} \tag{8.2}$$

where

$i_{(\lambda)}$ = Signal out of the photodiode in Amps.

$I_{(\lambda)}$ = Signal out of the photomultiplier in Amps.

$Fo_{(\lambda)}$ = flux of the beam from the exit slit in photons.

$S_{(\lambda)}$ = Splitting factor of the beam splitter.

$C_{(p,\lambda)}$ = Efficiency of the photomultiplier

$C_{(S)}$ = fraction of the solid angle subtended at the photomultiplier from phosphor layer.

$\eta_{(D,\lambda)}$ = Quantum efficiency of the photodiode (photons to electrons)

$\eta_{(S,\lambda)}$ = Quantum efficiency of the phosphor (photons to photons)

λ is the wavelength of observation.

Dividing equation (8.2) by equation (8.1) and rearranging the terms (cancelling out $Fo_{(\lambda)}$) we can write:

$$\eta_{(S,\lambda)} = \left(\frac{I(\lambda)}{i(\lambda)}\right) \cdot \frac{S(\lambda)}{1-S(\lambda)} \cdot \frac{1}{C_{(p,\lambda)}} \cdot \frac{1}{C_{(S)}} \cdot \eta_{(D,\lambda)} \tag{8.3}$$

For a given position of the beam splitter, $S_{(\lambda)}$ would be

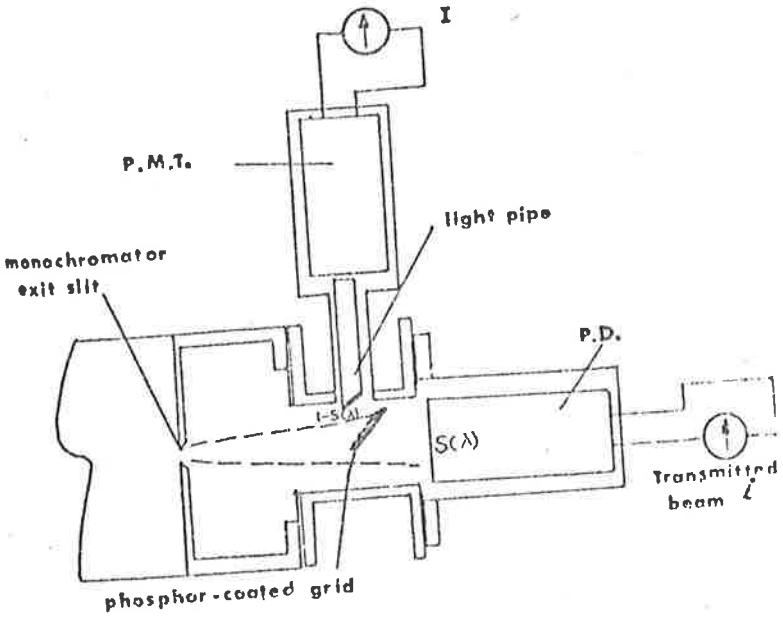

Figure 8.3 Schematic arrangement for quantum efficiency measurements of sodium salicylate.

independent of wavelength. Since the photomultiplier is always viewing the fluorescence radiation from the phosphor film and since the emission spectrum of sodium salicylate is independent of the incident UV radiation wavelength (Section 8.1), the photomultiplier detection efficiency $C_{(p,\lambda)}$ would be a constant for present observations. The quantity $C_{(S)}$ obviously is independent of wavelength and depends only on the relative geometry of the photomultiplier and phosphor layer. Therefore we can write

$$\eta_{(S,\lambda)} = \frac{I(\lambda)}{i(\lambda)} \cdot C \cdot \eta_{(D,\lambda)} \tag{8.4}$$

where all the constant terms are amalgamated in a single constant C. The quantity C would be independent of wavelength for a given orientation of the beam splitter but would vary if the orientation is varied.

Equation (8.4) is thus the basic equation relating the observer quantities $i(\lambda)$ and $I(\lambda)$ to obtain quantum efficiency of the phosphor layer if C and detector efficiency are known. In order to study the aging effect on the quantum efficiency spectrum, the sample should be left in place undisturbed and measurements of $i(\lambda)$ and $I(\lambda)$ repeated at intervals over the spectrum of observations. This poses two problems: (a) if a long term aging effect is planned, it requires the occupation of the monochromator for the duration of the observations and (b) it allows the use of only one sample at a time. Often it is the quantum efficiency of the phosphor at some wavelength relative to some other wavelength (very often relative to Ly-α) which is required. Therefore in such a calibration, the aging effect in relative efficiency and corresponding corrections would be of main interest.

If we write $I(\lambda)/i(\lambda) = I'(\lambda)$; equation (8.4) can be rewritten for two wavelengths λ_1, λ_2 as

$$\eta(S,\lambda_1) = I'(\lambda_1) \cdot C \cdot \eta(D,\lambda_1) \tag{8.5}$$

$$\eta(S,\lambda_2) = I'(\lambda_2) \cdot C \cdot \eta(D,\lambda_2) \tag{8.6}$$

or we can write

$$\eta(S,\lambda_2)/\eta(S,\lambda_1) = \frac{I'(\lambda_2)}{I'(\lambda_1)} \cdot \frac{\eta(D,\lambda_2)}{\eta(D,\lambda_1)} \tag{8.7}$$

or $$\eta S_{2,1} = I'_{2,1} \cdot \eta D_{2,1} \qquad (8.8)$$

where $$\eta S_{2,1} = \eta(S,\lambda_2)/\eta(S,\lambda_1)$$

$$I'_{2,1} = I'(\lambda_2)/I'(\lambda_1)$$

$$\eta D_{2,1} = \eta(D,\lambda_2)/\eta(D,\lambda_1)$$

Equation (8.8) gives the relative quantum efficiency at wavelength λ_2 relative to wavelength λ_1 without involving the geometry factor if relative efficiency of the detector $\eta D_{(2,1)}$ is known.

Suppose a series of measurements are made for a given layer at different time-intervals then rel.q.e. for m^{th} and n^{th} observations can be written with the help of equation (8.8) :

$$\eta S_{2,1}(m) = I'_{2,1}(m)\ \eta D_{2,1} \qquad (8.9)$$

$$\eta S_{2,1}(n) = I'_{2,1}(n)\ \eta D_{2,1} \qquad (8.10)$$

Dividing equation 8.10 by 8.9 we obtain

$$\frac{\eta S_{2,1}(n)}{\eta S_{2,1}(m)} = \frac{I'_{2,1}(n)}{I'_{2,1}(m)} \qquad (8.11)$$

Equation 8.11 thus enables one to study the aging effect in rel.q.e for a given layer and does not require any calibration of the detector. (m) can be taken as the first observation of the layer and (n) runs for the later observations. However in the present case first relative quantum efficiency $\eta S_{2,1}(n)$ were obtained for each observation by using equation (8.8). About 30 different sample layers were used for this purpose and the entire set of observations was arbitrarily normalized. These measurements were carried out at four wavelengths -144.1 nm, 160.8 nm, 200 nm and 253.7 nm - relative to 121.6 nm (Ly-α) which often serves as a transfer wavelength in the VUV region.

8.5 RESULTS OF THE QUANTUM EFFICIENCY OF SODIUM SALICYLATE

8.5.1 Variation of rel.q.e with time at 144.1 nm, 160.8 nm, 200 nm and 253.7 nm

Absolute rel.q.e values were determined using equation (8.8) over

an extended period of about 52 weeks, for about 30 different samples and at four selected wavelengths (relative to Ly-α (121.6 nm)). Entire data for each wavelength was arbitrarily normalized for simplified representation. The normalized data is plotted in Figure (8.4). By plotting the data for 20 samples at one particular wavelength, the variation in rel.q.e due to sample variation is evident although relatively small (generally within ± 10% except at 253.7 nm where smaller radiation intensity would also cause some spread). The overall trend seems to be similar for all the layers at each of the wavelengths. The average effect appears to be almost negligible for about first ten weeks at all the four wavelengths. The rel.q.e increases almost linearly after about 15 weeks at 160.8 nm and 253.7 nm. At wavelengths 144.1 nm and 200 nm rel.q.e first increases (very small increase at 144.1 nm) but appears to be settling down back to the initial values from the last set of data (after an interval of 23 weeks). Relative quantum efficiency data for the third set (see Section 8.4.3) was obtained only for the latest time sequence. A comparison thus provides a check whether the linear increase at 160.8 nm and 253.7 nm is due to possible UV irradiation effect. The data from this set was found to be comparable to the other data, thus indicating that the observed increase is possibly due to the aging effect. Since absolute calibration of the detector is immaterial for these measurements the main source of error would come from low lamp intensity particularly at 253.7 nm. The apparent large variation in the rel.q.e at 253.7 nm between samples is perhaps partly due to this fact. Comparison of these measurements with other similar measurements and the relevant discussion is given in Section (8.6).

8.5.2 Relative Quantum Efficiency from 110 nm to 270 nm

A number of fresh sodium salicylate samples were prepared and their relative quantum efficiency curves obtained with the help of equation (8.8). A magnesium fluoride window was attached to the arm in the splitting chamber which could swing the window in or out of the beam immediately after the monochromator beam (Section 8.3.1) to provide adequate filtering of the

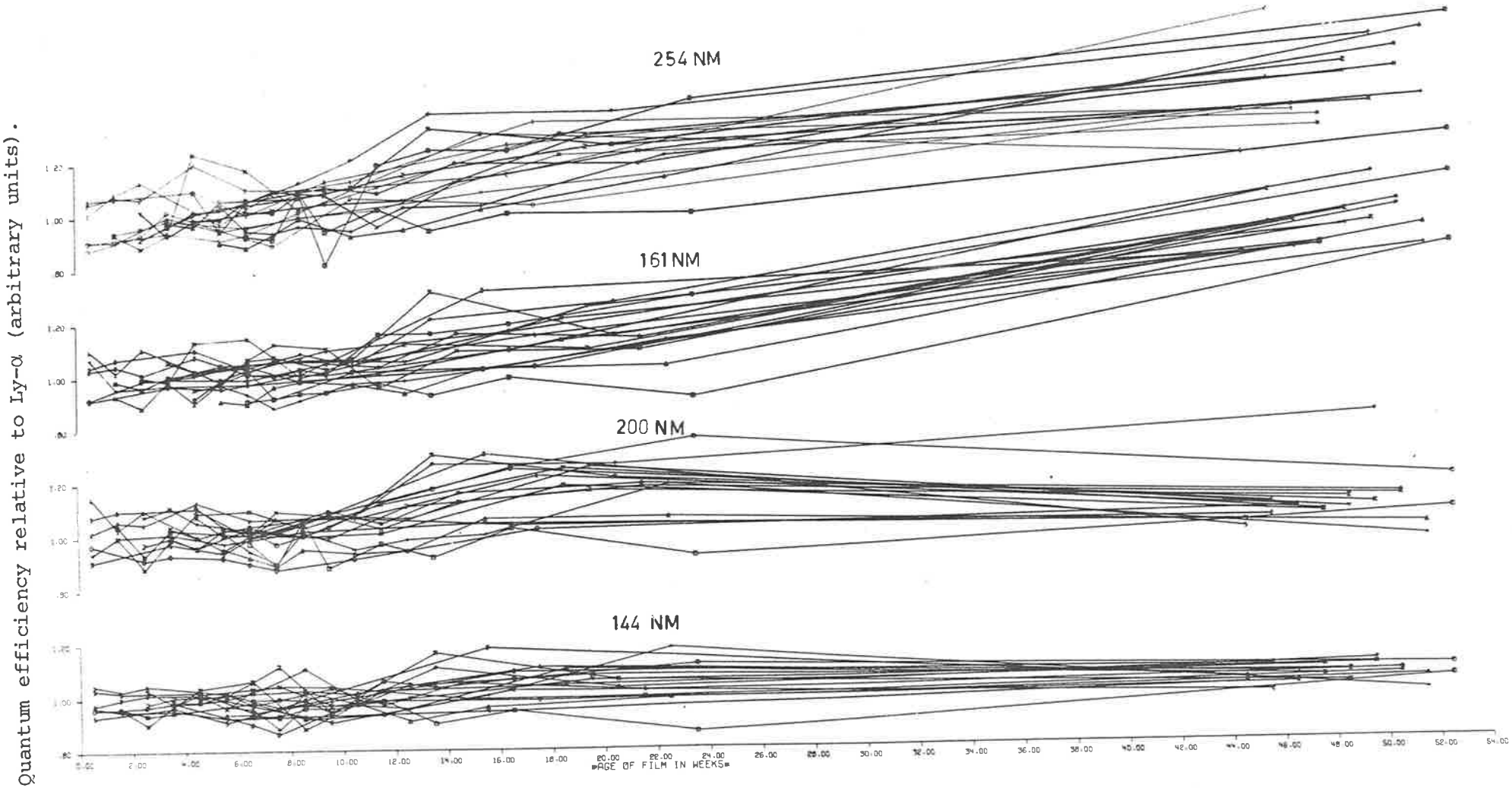

Figure 8.4 Variation of rel.q.e. at 144 nm, 161 nm, 200 nm, and 254 nm relative to Ly-α (121.7 nm) with age of the film.

TABLE 8.1

THICKNESS OF SODIUM SALICYLATE FILM USED FOR THE AGING EFFECT STUDY

S.N.	Identification	Layer Thickness ($mg\ cm^{-2}$)	Symbols used in Figure 8.4
1	#01	1.3453	⊡
2	#11	1.1558	⊙
3	#02	1.6725	△
4	#12	2.5974	+
5	#03	2.0131	×
6	#13	1.5612	◇
7	#04	1.3351	↑
8	#14	1.2579	⧖
9	#05	0.9987	Z
10	#15	0.9295	Y
11	#06	1.5633	⌘
12	#16	1.4230	*
13	#07	1.5688	⧖
14	#17	1.3180	1
15	#09	1.4426	2
16	#19	1.2598	3
17	#30	2.1243	4
18	#20	1.6883	5

beam from higher order(s) radiation. The use of a MgF_2 window as a filter (cut off 114 nm) ensured that the radiation between 114 to 230 nm would be free of higher orders. Similarly use of a quartz window (cut off 155 nm) would ensure this freedom between 150 nm and 330 nm. In the present measurements this higher order effect was found to be significant in the region between 160 nm and 230 nm but insignificant above 230 nm. This can be seen from Figure (8.5) where measured quantum efficiency curves without any filtering are shown for three fresh samples. The peak behaviour around 170 nm is primarily due to the presence of higher order (mainly second order) radiation.

For the above reasons, use of a MgF_2 window as a filter was necessary and sufficient for these measurements of rel.q.e over the wavelength range 110 nm to 270 nm.

The rel.q.e curves for several fresh samples are shown in Figure (8.6). It can be seen that the variations in the rel.q.e due to sample variation are rather small. One of the samples was kept in position to study the aging effect on q.e. curve for about a period of 90 hours. The results are shown in Figure (8.7). The q.e. is found to increase slowly at all wavelengths in agreement with the most recent results of Samson and Haddad (1974) but contrary to those of Samson (1964) and Knapp and Smith (1964). A discussion of the shape of the curve is given in Section (8.6).

8.5.3 Higher Order Radiation Effect

As mentioned in the previous subsection it was found necessary to employ proper filtering of higher order radiation. The procedure of evaluation and the results of the higher order radiation effect in the absense of a proper filtering is discussed below.

In an experiment of the rel.q.e measurement, if the intensity detector is an energy detector rather than a photon detector (as in the present case) it will be shown that the effect of higher order radiation

would be significantly different and may in fact explain some of the past discrepencies.

(a) Higher Order Radiation in the Present Case

It may be pointed out again that the detector employed in the present measurements of the rel.q.e was a photon detector with a lower cut off at about 114 nm. This meant that at any wavelength λ > 114 nm, the detector would not record any photons of wavelengths lower than 114 nm, present in the second (photons of $\lambda/2$ wavelength) and higher orders. However the salicylate would emit fluorescent photons in proportion to the photons of wavelength λ in the first order as well as to the photons of the second (wavelength $\lambda/2$) and higher orders. The result being that photomultiplier signal would be in proportion to all photons irrespective of their orders and would be higher than the signal if only photons of wavelength λ in the first order were present. The resulting ratio of I_{PM} (at λ)/i(D,λ) α η(S, at λ) would be greater than $I_{PM}(\lambda)/i(D,\lambda)$ α $\eta(S,\lambda)$. The ratio of the true value $\eta(S,\lambda)$ and η(S, at λ) would depend primarily on the higher order contribution since the quantum efficiency of sodium salicylate does not vary too much over the range 60 nm to 200 nm. Initially, the rel.q.e for a sample was obtained with MgF_2 window in and window out and the ratio of the two thus directly gives the error in the rel.q.e due to this higher order radiation effect. As a check, two other windows (MgF_2 and LiF) were used with similar results. A more direct method is to find the window transmission using the photodiode as detector and then using the sodium salicylate sensitized photomultiplier as the detector. The true transmission would be given by the photodiode which would not record any higher order radiation (mainly second order) of wavelengths lower than 114 nm when the filter is out. However, this higher order radiation present when the filter is out would

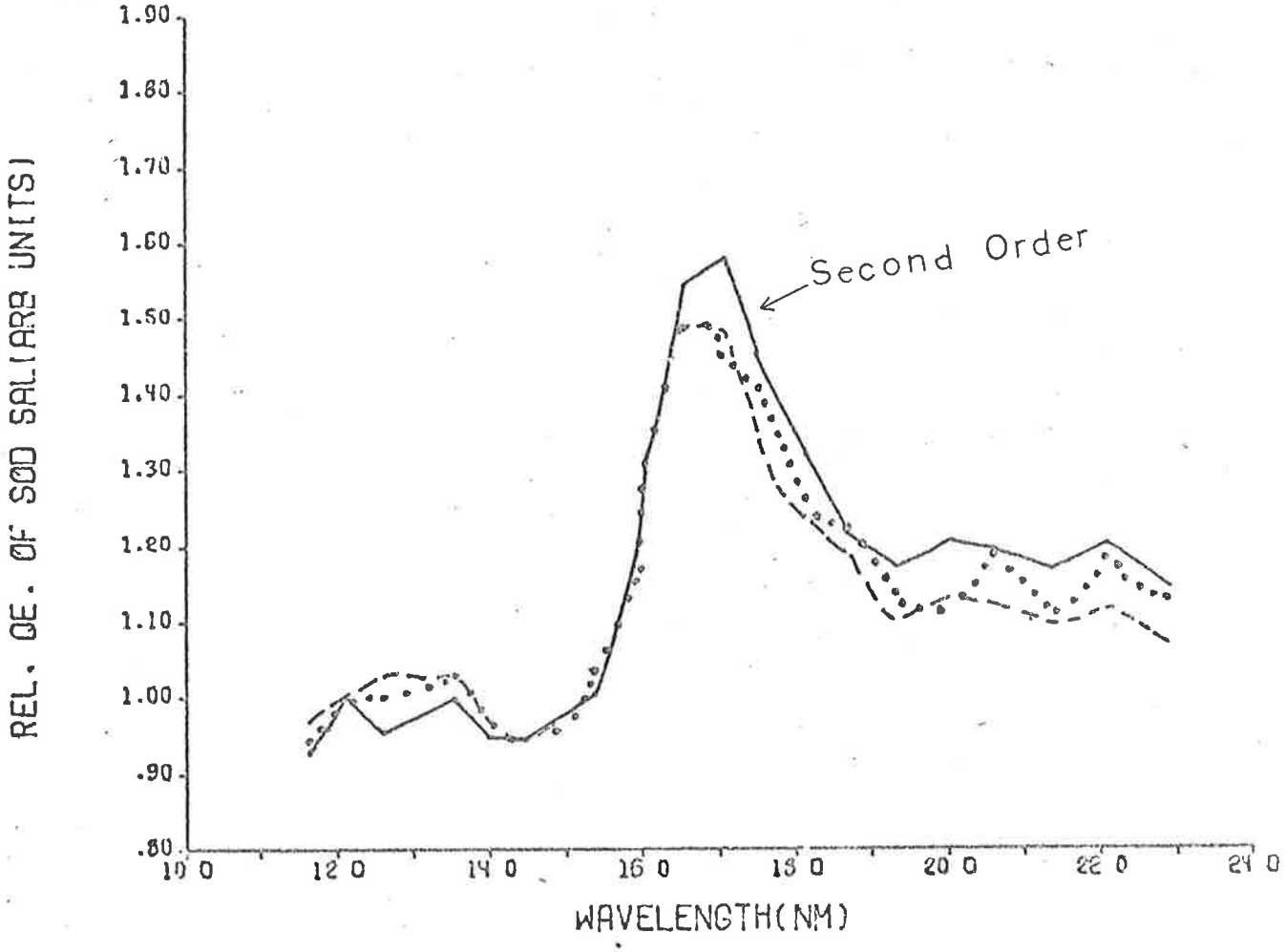

Figure 8.5 Relative quantum efficiency of three sodium salicylate films measured without any filtering.

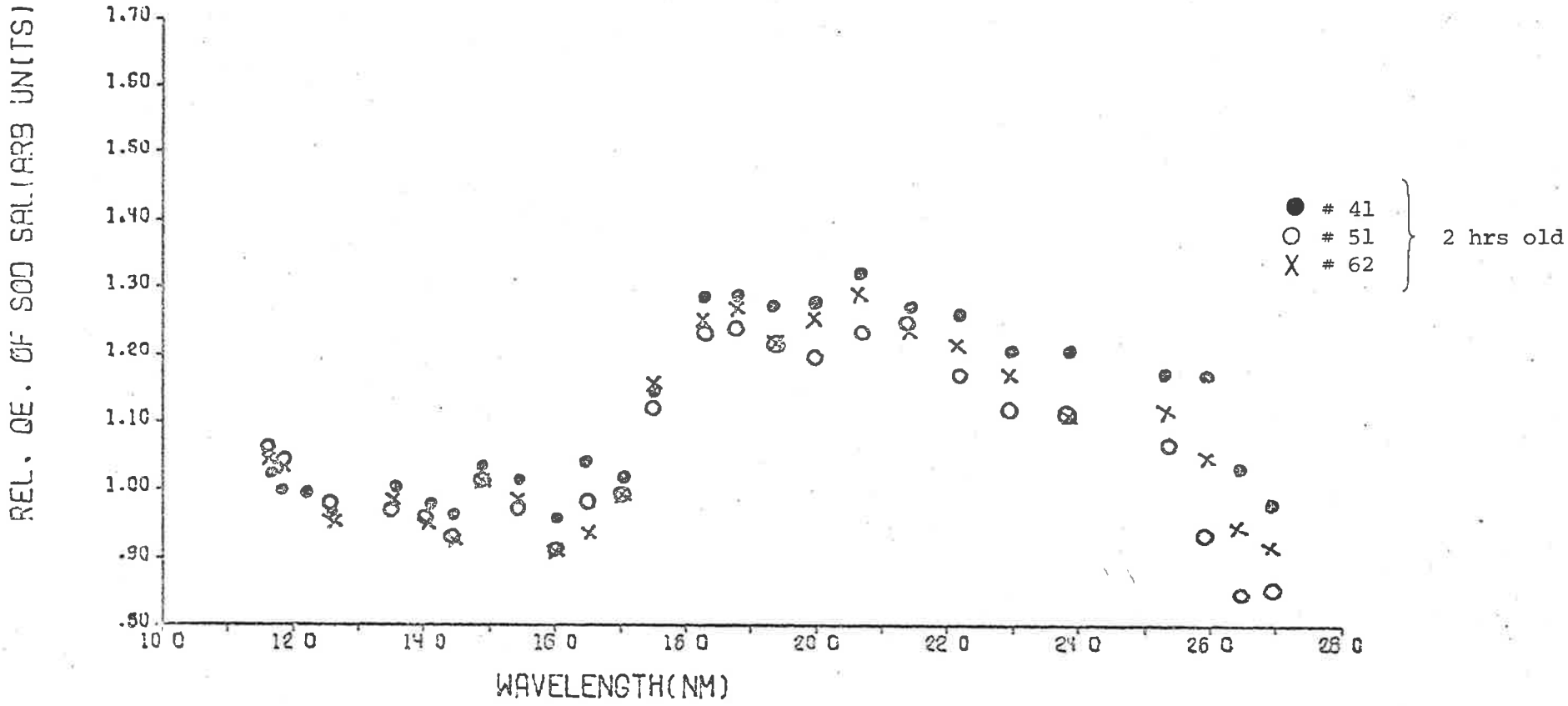

Figure 8.6 Quantum efficiency of sodium salicylate samples measured with proper filtering.

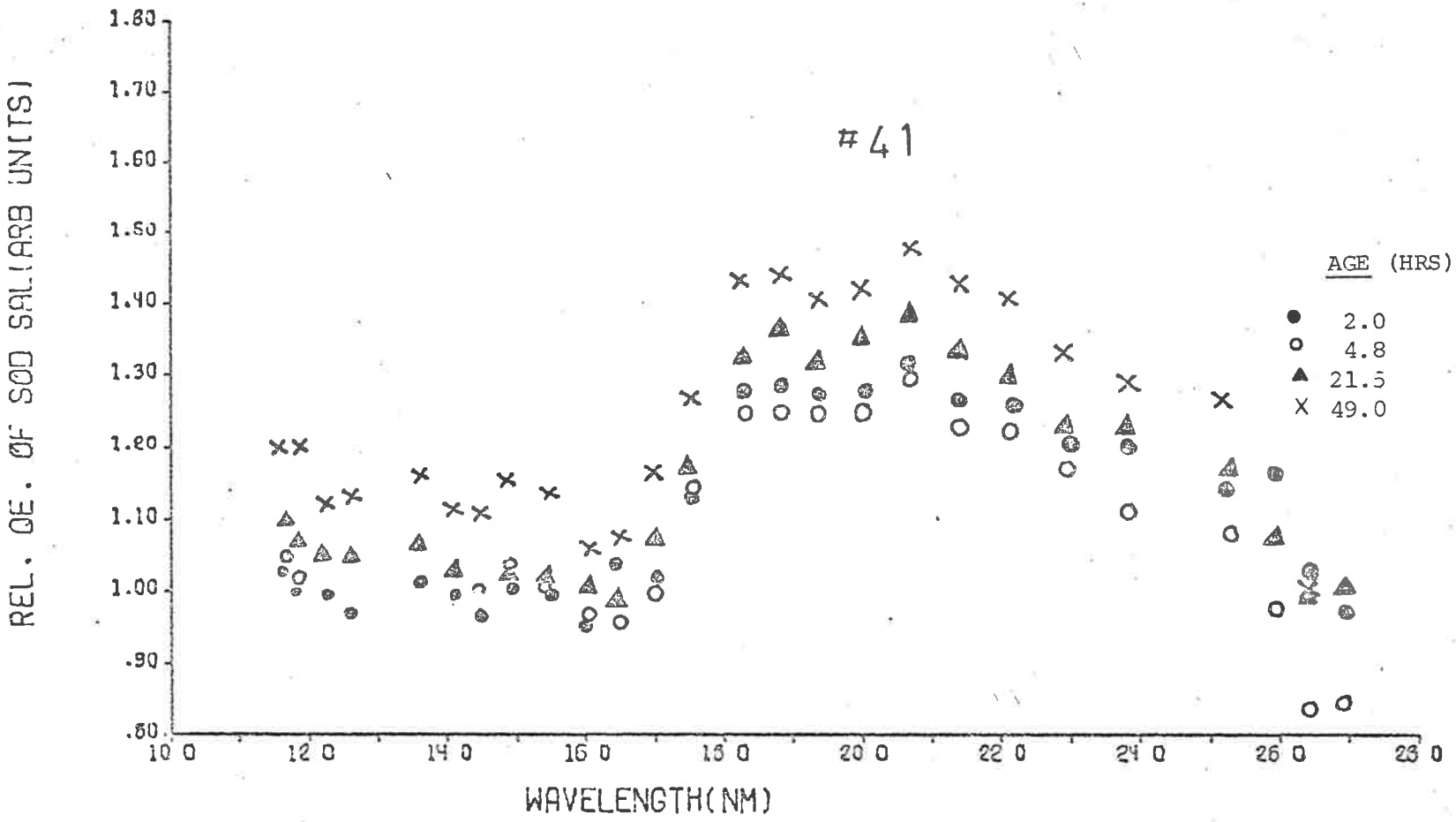

Figure 8.7 Variation of relative quantum efficiency of one of the sodium salicylate samples as a function of age of the film.

result in additional fluorescent photons from the phosphor and thus the resulting transmission as measured by the photomultiplier would be lower than the true value and the difference would be larger where this contribution is larger. This was done with the split beam used in the present measurements as well as with the beam splitter out and each detector mounted directly at the rear of the splitting chamber. The resulting transmission curves are shown in Figure (8.8) and the effect of this radiation is clearly evident between 160 nm and 230 nm. It was found that the additional higher order radiation effect in the present experimental set-up was less than 3% if a quartz window was used as a filter instead of a MgE_2 window.

(b) Higher Order Radiation effect if an Energy Detector is Employed:

Almost in all the previous measurement of the rel.q.e of sodium salicylate, thermopiles or thermocouples have been used for monitoring the beam intensity. In order to investigate the effect of higher order radiation on the experimentally determined rel.q.e. we may proceed as follows:

Since a thermopile or a thermocouple is an energy detector, a photon of wavelength $\lambda/2$ produces a signal equivalent to two photons of wavelength λ.

Suppose at an experimental wavelength λ, there are m_1 photons of first order (wavelength λ), m_2 photons of (wavelength $\lambda/2$) and so on. Suppose the relative quantum efficiency of the phosphor is $\eta S(\lambda), \eta_2, \eta_3$ at wavelengths λ, $\lambda/2$, $\lambda/3$.

The energy reaching the energy detector would be

$$\frac{m_1 hC}{\lambda} + \frac{m_2 hC}{\lambda/2} + \frac{m_3 hC}{\lambda/3} + \ldots$$

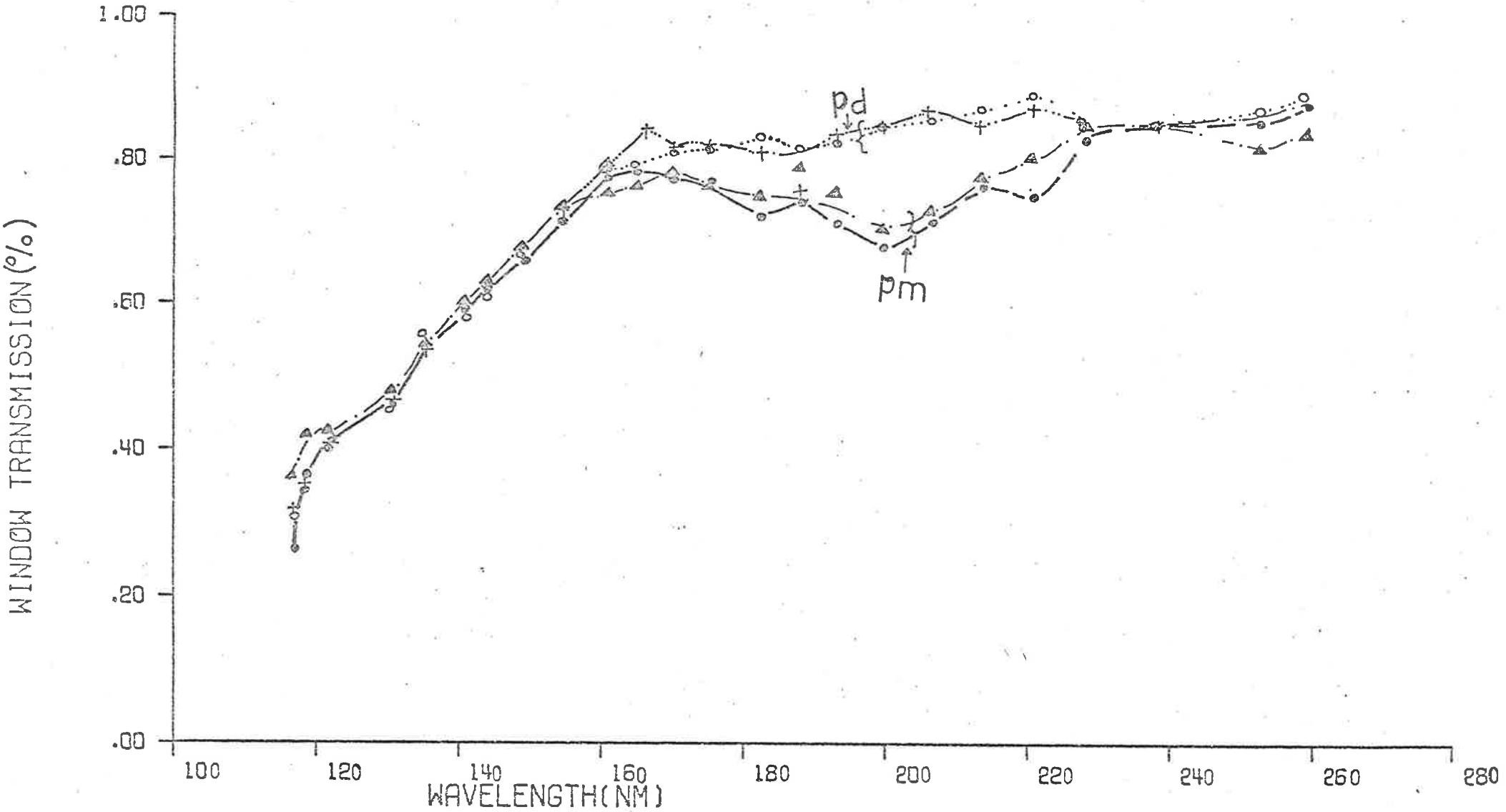

Figure 8.8 Transmission of a LiF window as measured using photomultiplier and photodiode as detectors. The lower transmission values obtained using photomultiplier are due to higher order impurities (O, ▲, Beam splitter in; +, ● Beam splitter out).

or $$E\ (\text{at } \lambda) = (m_1+2m_2+3m_3+....)\ \frac{hC}{\lambda} \qquad (8.12)$$

The signal from the photomultiplier as a result of fluorescent photons can be written as:

$$I_{PM}\ (\text{at } \lambda) = (m_1+m_2\ \frac{\eta_2}{\eta S} + m_3\ \frac{\eta_3}{\eta S} +...)\eta S(\lambda)\cdot K \qquad (8.13)$$

(K is a geometry constant)

Therefore, observed ηS is given by

$$\eta S\ (\text{at } \lambda) = \frac{I_{PM}}{E_o \lambda} = \frac{(m_1+m_2\cdot\eta_2/\eta S(\lambda)+m_3\eta_3/\eta S(\lambda)+...)}{(m_1+2m_2+m_3....)} \cdot (\frac{K}{hc})\cdot\eta S(\lambda) \qquad (8.14)$$

Let us assume for simplicity that the intensity of the third and higher orders is negligibly small so that we can write:

$$R = \eta S\ (\text{at } \lambda)/\eta S(\lambda) = (m_1+m_2 \cdot \eta_2/\eta S)/(m_1+2m_2) \cdot (K/hc) \qquad (8.15)$$

On the basis of up to date measurements, it can be safely assumed that for the region 110 nm to 240 nm, $\frac{\eta_2}{\eta S} \leqslant 1$.

For the region where $\frac{\eta_2}{\eta S} \sim 1$ we can write

$$R' \sim \frac{m_1+m_2}{m_1+2m_2} \propto \eta(\text{observed})/\eta(\text{true})$$

A graph of $\frac{m_1}{m_2}$ (rel. contribution) VS $R' \sim \frac{m_1+m_2}{m_1+2m_2}$ is shown in Figure (8.9) which shows that the presence of higher order radiation in this case is that the observed rel.q.e. is lower than the true value.

8.6 COMPARISON OF THE QUANTUM EFFICIENCY RESULTS AND DISCUSSION

8.6.1 The Aging Effect

Measurements of particular importance for comparison are those of Knapp and Smith (1964), Samson (1964), Hamman (1958) and Allison et al (1964). The measurements of both Knapp and Smith (1964) and Samson (1964) were made with samples kept in the atmosphere of monochromator under vacuum whereas in the present case the samples were kept under atmospheric conditions. The rel.q.e. curves of Knapp and Smith have been used to obtain values of q.e. at 144.1 nm and 160.8 nm relative to 121.6 nm as a function

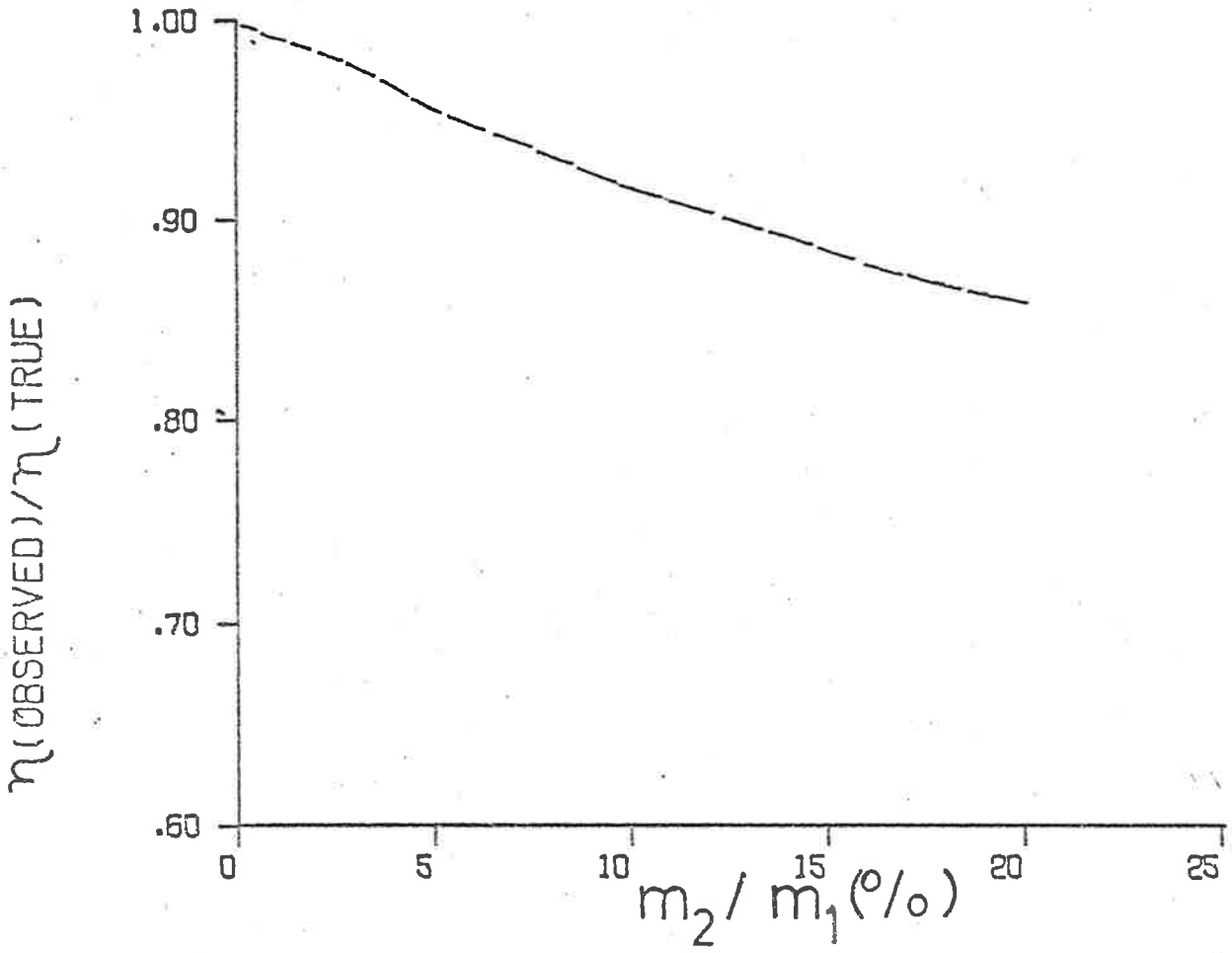

Figure 8.9 Effect of second order radiation on measured quantum efficiency of a phosphor using energy detector. (Calculations).

of the age of the film. The resulting data thus can be directly compared with the present measurements. This is plotted in Figure (8.10) along with our mean curves. It can be seen that the increase in q.e. relative to 121.6 nm both at 144.1 nm and 160.8 nm are large compared to the present observations. Over the period of about 6 weeks we find virtually no change in the rel.q.e. Allison et al (1964b) have reported that they observed no change in quantum efficiency at either 121.6 nm or 160.8 nm over a period of about 30 weeks. Therefore, the resultant rel.q.e. would remain constant. Hamman's (1958) measurements did not indicate any change in q.e. above 230 nm including at 253.7 nm over a period of more than a year. If this data is coupled with the results of Allison et al (1964) at 121.6 nm, it indicates that the q.e. at 253.7 nm relative to 121.6 nm would remain constant. Therefore, the slow increase in rel.q.e. observed in the present measurements at 160.8 nm and 253.7 nm after about 13 weeks may be due to excessive radiation effect although the third set of samples did not indicate so. Our results of the rel.q.e. (Figure 8.6) indicate an increase in q.e. at all wavelengths with the age in agreement with the recent observations of Samson and Haddad (1974) at shorter wavelengths but contrary to the results of Knapp and Smith (1964) and Samson (1964) who reported a decrease at all wavelengths with time between 100 nm and 160 nm. There is no other 'aging effect' measurement available at 200 nm. On the basis of the results of Allison et al (1964) that the q.e. at 121.6 nm remains constant, we may conclude that the q.e. at 144.1 nm and 200 nm also remain unchanged over long periods but perhaps a slow increase takes place at 160.8 nm and 253.7 nm after a period of about 10 weeks.

8.6.2 Relative Quantum Efficiency

The relative quantum efficiency results of Johnson et al (1951), Watanabe and Inn (1953) and Vassuer and Cantin (1963) are of particular importance as these measurements have been made in the range 100 nm to 230 nm, 85 nm to 280 nm and 50 nm to 300 nm respectively. The remaining measurements

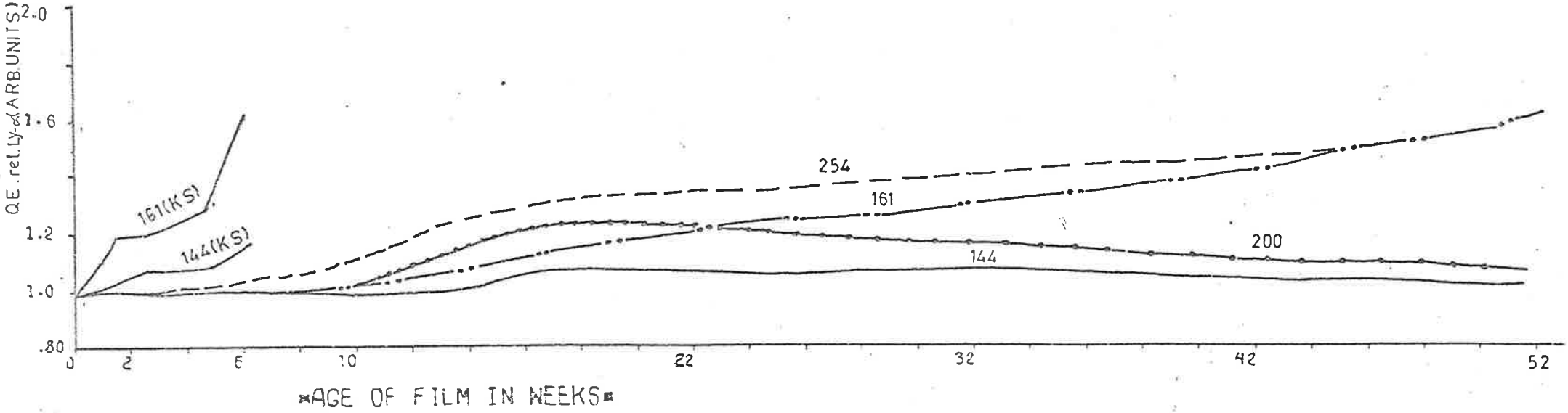

Figure 8.10 Mean curves of quantum efficiency relative to 121.6 nm at 144 nm, 161 nm, 200 nm and 254 nm. Also shown are the results of Knapp and Smith (1964) for two wavelengths.

are divided into two groups - those of Knapp and Smith (1964) and Samson (1964) extending to below 165 nm; those of Dejardin and Schwegler (1934), Hamman (1958) and Slavin et al (1961) extending from about 220 nm onward and those of Kristianpoller and Knapp (1964) extending from about 180 nm onward. Each of these groups thus provides a comparison in the respective wavelength intervals.

Our results indicate a constant q.e. between about 115 nm and 170 nm. The rel.q.e. is found to rise between 170 nm and 185 nm with an increase of about 30% around 180 nm. The rel.q.e. appears to be almost constant from 185 nm to about 260 nm. Our results of flatness of the rel.q.e. below about 170 nm are in good agreement with those of Watanabe and Inn (1953) and Johnson et al (1951) but in disagreement with those of Knapp and Smith (1964) and Samson (1964). Neither Johnson et al (1951) nor Watanabe and Inn (1953) observed any step increase in the rel.q.e. between 170 nm and 185 nm as observed in the present case. Since the lamp intensity decreased sharply at longer wavelengths and the errors in absolute calibration of the photodiode also increase (10% at 253.7 nm), the slow downward trend above 220 nm may be due to experimental errors. However this decrease is less than 10% up to about 260 nm beyond which the photodiode calibration has been based only on typical cathode curve and the errors involved due to lamp intensity and calibration are expected to be rather large. Thus our results are substantially in agreement with those of Johnson et al (1951), Watanabe and Inn (1953), Dějardin and Schwégler (1934), Hamman (1958) and Slavin et al (1961). Kristianpoller and Knapp (1964) observed a drop between 200 nm and 220 nm amounting to about 25%. We do not find any such drop except the step rise around 170 nm as discussed earlier.

The results of Vassuer and Cantin (1963) indicate a continuous increase in the rel.q.e. from 50 nm to 300 nm. It appears that the results have been obtained in two regions i.e. below 180 nm and above 230 nm separately. Also these results do not show wavelengths at which actual data have been obtained. The increase from 100 nm to 270 nm in this case

amounts to about 100% which is too large in comparison to the present results. Apparently neither Johnson et al (1951) nor Watanabe and Inn (1953) used any filtering during the rel.q.e. measurements although some corrections were made for stray light in the earlier case. Higher order radiation present at wavelengths above 170 nm would tend to reduce the rel.q.e. for the two cases in discussion as shown in Section (8.5.3). It would be therefore desirable to carry out similar measurements in this region of discrepency around 170 nm preferably by two independent types of detectors (thermopile and photodiode) with proper filtering.

8.7 CONCLUSIONS AND COMMENTS

From the results and discussion presented in the previous section it can be concluded that the rel.q.e. of sodium salicylate is almost constant from 115 nm to 165 nm and from 185 nm to 260 nm separately. The step rise of about 30% takes place around 170 nm. The effect of aging on the sodium salicylate films is slowly to increase the q.e. at all wavelengths such that the rel.q.e. remains substantially the same. The rel.q.e. relative to Ly-α (121.6 nm) remains virtually constant (within 10%) at each of the wavelengths 144.1 nm, 160.8 nm, 200 nm and 153.7 nm for a period of about 10 weeks. A slow increase particularly at 160.8 nm and 253.7 nm amounting to about 50% over a period of one year is found in the rel.q.e.

APPENDIX A

PUBLICATIONS

1. Carver, J.H., Horton, B.H. and Ilyas, M.: 1974,"Rocket Measurements of High Altitude Molecular Oxygen", Report of Proceedings First Special Assembly (Melbourne) IAMAP publication number 51a, p. 63 (Abstract) and Report ADP122, University of Adelaide (May, 1974).

2. Ilyas, M. and Horton, B.H.: 1974, Paper presented at the first AIP National Congress, Adelaide, (May 1974) and published as ADP Report 121, University of Adelaide (May 1974).

3. Ilyas, M.: 1976, "Rocket measurements of mesospheric oxygen from Lyman-α absorption spectroscopy", Paper LA5, Presented at the 2nd National Congress (Sydney), August 1976 (To be submitted shortly for publication).

4. Molecular Oxygen densities in the lower thermosphere (To be submitted shortly for publication).

5. UV Ionchamber measurements of Solar Ultraviolet fluxes and Solar minimum brightness temperatures. (To be submitted).

6. Fluorescent efficiency of Sodium Salicylate and the aging effect between 110 and 270 nm. (To be submitted in App. Optics).

BIBLIOGRAPHY

ACKERMAN, M. and SIMON, P.: 1973, Solar Phys., 30, 345.

ALLEN, C.W.: 1962, Astrophysical Quantities, (Athlone Press), p. 146.

ALLISON, R., BURNS, J. and TUZZOLINO, A.J.: 1964a, J. Opt. Soc. Am. 54, 747.

ALLISON, R., BURNS, J. and TUZZOLINO, A.J.: 1964b, J. Opt. Soc. Am. 54, 1381.

BANKS, P.M. and KOCKARTS, G.: 1973, Aeronomy, (Academic Press)

BARLIER, F., BAUER, P., JAECK, C., THUILLIER, G. and KOCKARTS, G.: 1974, J. Geophys. Res., 79, 5273.

BARTH, C.S.: 1966, Ann. Geophys., 22, 198.

BATES, D.R. and WITHERSPOON, A.E.: 1952, Mon. Not. R. Astr. Soc., 112 101.

BENTLEY, A.N., De JONCKHEERE, C.G. and MILLER, D.E.: 1974, Astron. J., 79, 401.

BLAKE, A.J., CARVER, J.H. and HADDAD, G.N.: 1966, J. Quant. Spectrosc. Radiat. Transfer, 6, 451.

BOLAND, B.C., JONES, B.B., WILSON, R., ENGSTRON, S.F.T. and NOCI, G.: 1971, Phil. Trans. Roy. Soc. A., 270, 29.

BRANNON, P.J. and HOFFMAN, J.M.: 1971, J. Geophys. Res., 76, 4630.

BREWER, A.W., and MILLFORD, J.R.: 1960, Proc. Roy. Soc. A., 256, 470.

BRINKMAN, R.T., GREEN, A.E.S. and BARTH, C.A.: 1966, NASA Tech. Report No. 32-951.

BRUECKNER, G.E. and MOE, K. : 1972, Space Research, 11, 1595.

BRUECKNER, G.E. and NICOLAS, K.: 1972, reported in Carver et al (1972).

BRUNER, Jr., E.C.: 1969, J. Opt. Soc. Am., 59, 204.

BRUNER, E.C. and PARKER, R.W.: 1969, J. Geophys. Res., 74, 107.

BRUNER, E.C. and RENSE, W.A.: 1969, Astrophys. J., 157, 417.

CARVER, J.H. and MITCHELL, P.: 1964, J. Scient. Instrum., 41, 555.

CARVER, J.H. and MITCHELL, P.: 1967, J. Opt. Soc. Am., 57, 738.

CARVER, J.H., HORTON, B.H. and ILYAS, M.: 1974, Report of Proceedings, First Special Assembly (Melbourne), IAMAP, Publication No.15a, p.16 (Abstract) and Report ADP 122, University of Adelaide (May, 1974).

CARVER, J.H., MITCHELL, P., MURRAY, E.L. and HUNT, B.G.: 1964, J. Geophys. Res., 69, 3755.

CARVER, J.H., MITCHELL, P., MURRAY, E.L. and ROFE, B.: 1965, Space Research, 6, 373.

CARVER, J.H , HORTON, B.H., LOCKEY, G.W.A. and ROFE, B.: 1972, Solar Phys., 27, 347.

CARVER, J.H., HORTON, B.H., O'BRIEN, R.S., and ROFE, B.: 1972b, Planet. Space Sci., 20, 217.

CARVER, J.H., HORTON, B.H., O'BRIEN, R.S. and O'CONNOR, G.G.: 1974b, The Moon, 9, 295.

CARVER, J.H., GIES, P., HOBBS, T.I., LEWIS, B.R. and McCOY, D.G.: 1976, To be Published.

CARVER, J.H., EDWARDS, P.J., GOUGH, P.L., GREGORY, A.G., ROFE, B. and JOHNSON, S.G.: 1969, J. Atmos. Terr. Phys., 31, 563.

CHAMPION, K.W.S. and SCHWEINFURTH, R.A.:, 1972, in Reference Atmosphere, 'CIRA-1972'.

CHAPMAN, S. and KENDALL, P.C.: 1965, Quart. J. Roy. Meteorol. Soc., 91, 115.

CHUBB, T.A. and FRIEDMAN, H.: 1955, Rev. Sci. Instrum., 26, 493.

CIRA. (Cospar International Reference Atmosphere): 1965, North-Holland Publ. Co.: Amsterdam.

CIRA, (Cospar International Reference Atmosphere): 1972, Academic Verlag, Berlin.

COOK, G.R. and CHING, B.K.: 1965, Rep. No. TDR-469 (9260-01)-4 (Aerospace Corp.).

CRAIG, R.A.: 1965, "The Upper Atmosphere - Meterology and Physics", (Academic Press), p. 184.

CRUTZEN, P.: 1974, Can. J. CHem., 52, 1569.

CUNY, Y.: 1971, Solar Phys., 16, 293.

DANILOV, A.D.: 1972, Space Research, 12, 891.

DÉJARDIN, G. and SCHWEGLER, R.: 1934, Reveu D' Optique, 13, 313.

DETWILER, C.R., PURCELL, J.D. and TOUSEY, R.: 1961a, Mem. Soc. Roy. Sci. Liege, ser. 5, 4, 253.
DETWILER, C.R., GARRETT, D.L., PURCELL, J.D. and TOUSEY, R.: 1961b, Annls. Geophys., 17, 9.
DITCHBURN, R.W., BRADLEY, J.E.S., CANNON, G.G. and MUNDAY, G.: 1954, Rocket Exploration of the Upper Atmosphere, Ed. R.L.F. Boyd and M.J. Seaton (London: Pergamon Press), p. 327.
DONNELLY, R.F. and POPE, J.H.: 1973, NOAA Technical Report ERL 276-SEL 25.
DUNKELMAN, L. HENNES, J.P. and FOWLER, W.B.: 1962, Applied Optics, 1, 695.
DUNKELMAN, L., HENNER, J.P. and FOWLER, W.B.: 1963, Space Research, 3, 1174.
DÜTSCH, H.V.: 1971, Advances in Geophysics, 15, 219.
EDDY, J.A., LÉNA, P.J. and MacQUEEN, R.M.: 1969, Solar Physics, 10, 330.
FELSKE, D. and SONNERMANN, G.: 1976, Space Research, 16 (in press).
FELSKE, D., MARTINI, L. STARK, B. and TAUBENHEIM, J.: 1970, Nature, 228, 1298.
FELSKE, D., MARTINI, L. STARK, B. and TAUBENHEIM, J.: 1972, Space Research, 12, 651.
FOSSI, B.C., POLETTO, G. and TAGIAGERRI, G.L.: 1970, Space Research, 10, 903.
FRIEDMAN, H., LICHMAN, S.W. and BYRAM, E.T.: 1951, Physical Review, 83, 1025.
FRIEDMAN, H., CHUBB, T.A. and SIOMKEJLO, J.M.: 1964, Sounding Rocket Research Techniques, Instruction Manual No. 9 IQSY (Secretariat, London), pp. 88-104.
GAILY, T.D.: 1969, J. Opt. Soc. Am., 59, 536.
GINGERICH, O., NOYES, R.W., KALKOFEN, W. and CUNY, Y.: 1971, Solar Phys., 18, 347.
GOLDBERG, L.: 1967, Ann. Rev. Astron. Ap., 5, 279.
GROBECKER, A.J.: 1967, Ph.D. Thesis, University of California, U.S.A.
GROBECKER, A.J.: 1971, Solar Flus and "Total" Particle and O_2 Denisty in Upper Atmosphere, I.D.A. Science and Technology Division, Paper P-695.
GROSS, M.J. and HEDDLE, D.W.O.: 1964, Proc, Roy. Soc. A, 279, 523.
GROVES, G.L.:1972, in CIRA-1972.
HALL, J.E.: 1972, J. Atmos. Terr. Phys., 34, 1337.
HALL, L.A., SCHWEIZER, W. and HINTEREGGER, H.E.: 1965, J. Geophys. Res., 70, 105.
HALL, L.A., CHAGNON, C.W. and HINTEREGGER, H.E.: 1967, J. Geophys. Res., 72, 3425.
HAMMAN, J.: 1958, Z. Angew. Phys., 10, 107.
HARRISON, H., SCHOEN, R.I., CAIRNS, R.B. and SCHUBERT, K.E.: 1969, J. Chem. Phys., 50, 3930
HAYS, P.B. and ROBLE, R.G.: 1973, Planet. Space Sci., 21, 273.
HEDIN, A.E., AVERY, C.P. and TSCHETTER, C.D.: 1964, J. Geophys. Res., 69, 4637.
HERZBERG, L.: 1965, Physics of the Earth's Upper Atmosphere; Ed. C.O. Hines, I. Paghis, T.R. Hartz and J.A. Fejer; Prentice-Hall, N.J., p. 40.
HIGASHINO, I., MASUOKA, T., HISAKA, H., SASANUMA, M., and OSHIO, T.: 1966 Memoirs, Faculty of Engineering, Osaka City University, Japan, 8, 213.
HILSENRATH, E.: 1971, J. Atmos. Sci., 28, 295.
HINTEREGGER, H.E.: 1962, J. Atmos. Sci., 19, 351.
HINTEREGGER, H.E.: 1965, Space Sci. Rev., 4, 461.
HINTEREGGER, H.E.: 1970, Annals. Geophys. 26, 547.
HODGESON, J.A., FROST, K.J., O'KEEFE, A.E. and STEVENS, R.K.: 1970, Analytical Chemistry, 42, 1795.
HORTON, B.H.: 1968, Ph.D. Thesis, University of Adelaide (Australia).
HUDSON, R.D., CARTER, V.L. and STEIN, J.A.: 1966, J. Geophys. Res., 71, 2295.
HUNT, B.G.: 1973, J. Atmos. Terr. Phys., 35, 1755.
ILYAS, M. and HORTON, B.H.: 1974, Paper Presented at the Ist AIP National Congress, Adelaide (May 1974) and Published as ADP Report 121 (May 1974) University of Adelaide (Australia).
INN, E.C.Y. and TANAKA, Y.: 1959, Advances in Chemistry, 21, 263.
INN, E.C.Y., WATANABE, K. SELIKOFF, M.: 1953, J. Chem. Phys., 21, 1648.
JACCHIA, L.G.: 1971, Ape. Rep. Smithson, Astrophys. Obs., No. 332 (also in CIRA-1972).

JOHNSON, F.S.: 1973, Reviews Geophys. Space Phys., 2, 741.
JOHNSON, F.S., PURCELL, J.D., TOUSEY, R. and WATANABE.K: 1952, J. Geophys. Res., 57, 157.
JOHNSON, F.S., WATANABE, K. and TOUSEY, R.: 1951, J. Opt. Soc. Am., 41, 701.
JURSA, A.S., NAKAMURA, M. and TANAKA, Y.: 1963, J. Geophys. Res., 68, 6145.
JURSA, A.S., NAKAMURA, M. and TANAKA, Y.: 1965, J. Geophys. Res., 70, 2699.
KALLMAN-BIJL, H.K. and SIBLEY, W.L.: 1963, Planet. Space Sci., 11, 1379.
KASPRZAK, W.T., KRANKOWSKY, D. and NIER, A.D.: 1968, J. Geophys. Res., 73, 6765.
KEATING, G.M., McDOUGAL, D.S., PRIOR, E.J. and LEVINE, J.S.: 1973, Space Research, 13, 327.
KNAPP, R.A. and SMITH, A.M.: 1964, Appl. Opt., 3, 637.
KOPAL, Z.: 1969, The Moon (Reidal Pub. Co.) Holland.
KRISTIONPOLLER, N. and KNAPP, R.A.: 1964, Appl. Opt., 3, 915.
KRANSKY, D., KASPRZAK, W.T. and NIER, A.O.: 1968, J. Geophys. Res., 73, 7291.
KUPPERIAN, J.E., Jr., BYRAM, E.G. and FRIEDMAN, H.: 1959, J. Atmos. Terr. Phys., 16, 174.
KUPPERIAN, J.E., Jr., and KREPLIN, R.W.: 1957, Rev. Sci. Inst., 28, 14.
LEE, P.: 1955, J. Opt. Soc. Am., 45, 703.
LOCKEY, G.W.A.: 1972, Ph.S. Thesis, University of Adelaide, (Australia).
LOCKEY, G.W.A., HORTON, B.H. and ROFE, B.: 1969, Nature, 223, 387.
MARMO, F.F.: 1953, J. Opt. Soc. Am., 43, 1186.
MARTINI, L. and SHYUTTE, N.M.: 1973, Cosmic Research, 11, 643.
MASUOKO, T. and OSHIO, T.: 1974, Rev. Sci. Inst. 45, 1012.
MAUSERSBERGER, K., MULLER, D. OFFERMAN, D. and VON ZAHN, U,: 1968, J. Geophys. Res., 73, 1071.
McKINNON, P.J. and SMITH, L.G.: 1964, G.C.A. Technical Report, 64-12-N.
MILLER, D.E., and STEWART, K.H.: 1965, Proc. Roy. Soc. A., 288, 540.
MILLER, D.E. and RYDER, P.: 1973. Planet. Space Sci., 21, 963.
METZGER, P.H. and COOK, G.R.: 1964, J. Quant. Spectrosc. Radiat. Transfer, 4, 107.
MEIRA, L.G. Jr.: 1971, J. Geophys. Res., 76, 202.
MITCHELL, D.: 1966, Ph.D. Thesis, University of Adelaide, (Australia).
MOE, K.: 1971, Orbital Atmospheric Model Development, NASA Tech. Report MDC-Go574.
NAKATA, R.S., WATANABE, K. and MATSUNAGA, F.M.: 1965, Sci. Light Tokyo, 14, 54.
NEWELL, H.E. Jr.: 1953, High altitude Rocket Research (Academic Press Inc. New York), pp. 95-105.
NIER, A.O. and HICKMAN, D.R.: 1973, Space Research, 13, 235.
NIER, A.O., HOFFMAN, J.H., JOHNSON, C.Y. and HOLMES, J.C.: 1964, J. Geophys. Res. 69, 979.
NISHI, K.: 1973, Solar Phys., 33, 23.
NISHI, K.: 1975, Solar Phys., 42, 37.
NORTON, R.B.: 1970, (cf. Lockey, 1972).
NORTON, R.B. and WARNOCK, J.M.: 1968, J. Geophys. Res., 73, 5798.
NOYES, R.W.: 1971, Ann. Rev. Astron. Ap., 9, 209.
O'BRIEN, R.S.: 1973, Ph.D. Thesis, University of Adelaide, (Australia).
O'CONNOR, G.G.: 1973, Ph.D. Thesis, University of Adelaide, (Australia).
O'CONNOR, G.G.: 1974, WRE Technical Note 1316 (RW&D).
OFFERMAN, D.: 1974, J. Geophys. Res., 79, 4281.
OFFERMAN, D. and GROSSMAN, K.U.: 1973, J. Geophys. Res., 78, 8296.
OGAWA, M.: 1968, J. Geophys. Res.: 73, 6759.
PAETZOLD, H.K. and PISCALAR, F.: 1961, Naturwissenschaften, 48, 474.
PARK, J.H. and LONDON, J.: 1974, J. Atmos. Sci., 31, 1898.
PARKER, A.E. and STEWART, K.H.: 1972, J. Atmos. Terr. Phys., 34, 1223.
PARKINSON, W.H. and REEVES, E.M.: 1969, Solar Phys., 10, 342.

PEARCE, J.B.: 1969, J. Geophys. Res., 74, 853.
PEARSON, P.H.O.: 1974, Space Research, 14, 67.
PHILBRICK, C.R., FAUCHER, G.A. and TRZCINSKI, E.: 1973, Space Research, 13, 255.
PITTOCK, A.B. and SPARROW, J.G.: 1961, Aust. Met. Mag., 9, No.33, 37.
POCHUNKOV, A.A.: 1972, Space Research, 12, 657.
PRESTON, W.M.: 1940, Phys. Rev., 57, 887.
PRINZ, D.K.: 1974, Astrophys. J., 187, 369.
PURCELL, J.D. and TOUSEY, R.: 1960, J. Geophys. Res., 65, 370.
PURCELL, J.D. and TOUSEY, R.: 1961, Mem. Soc. Roy. Sci. Liege, Ser.5, 4, 234, 283.
QUESSETTE, J.A.: 1970, J. Geophys. Res., 75, 839.
RAMANATHAN, K.R. and DAVE, J.V.: 1957, Annals of the I.G.Y., 5, 23.
RANDHAWA, J.S.: 1966, U.S. Army Electronics Command Reports - ECOM-5039 (March) and ECOM-5064 (July).
RANDHAWA, J.S.: 1970, J. Geophys. Res., 75, 1693.
RANDHAWA, J.S.: 1971, J. Geophys. Res., 76, 8139.
RAMDHAWA, J.S.: 1974, Ind. J. Rad. Space Phys., 3, 62.
RAWCLIFFE, R.D., MELOY, G.E., FRIEDMAN, R.M. and ROGERS, E.H.: 1963, J. Geophys. Res., 68, 6425.
REED, E.T.: 1968, J. Geophys. Res., 73, 2951.
REED, E.T. and SCOLNIK, R.: 1964, NASA Report X-613-64-267.
REGENER, V.H.: 1960, J. Geophys. Res., 65, 3975.
REGENER, E., PAETZOLD, H.K. and EHMERT, A.: 1954, in Rocket Exploration of the Upper Atmosphere, Ed. R.L.F. Boyd (Pergamon Press) p. 202.
ROBLE, R.G. and HAYS, P.B.: 1972, Planet. Space Sci., 20, 1727.
ROBLE, R.G. and NORTON, R.B.: 1972, J. Geophys. Res., 77, 3524.
SAMSON, J.A.R.: 1964, J. Opt. Soc. Am., 54, 6.
SAMSON, J.A.R.: 1967, Techniques of Vacuum Ultraviolet Spectroscopy, (John Willey & Sons, Inc.) p. 215.
SAMSON, J.A.R. and HADDAD, G.N.: 1974, J. Opt. Soc. Am., 64, 1346.
SCHILLING, G.F.: 1968, Meteorological Monographs Vol. 8, No. 31, 82.
SEYA, M. and MASUDA, F.: 1963, Sci. Light, 12, 9.
SHARDANAND: 1967, NASA TN D-4225.
SISSONS, N.V.: 1974, Proceedings of UAPRC Conference held at Melbourne (Australia) 14-25 January, 1974, Vol I, p. 373.
SLAVIN, W., MOONEY, R.W. and PALUMBO, D.T.: 1961, J. Opt. Soc. Am., 51, 93.
SMITH, E.V.P. and GOTTLIEB, D.M.: 1974, Space Sci. Rev., 16, 771.
SMITH, L.G.: 1972, J. Atmos. Terr. Phys., 34, 601.
SMITH, L.G. and MILLER, K.L.: 1974, J. Geophys. Res., 79, 1965
SMITH, L.G. and WEEKS, L.: 1965, G.C.A. Tech. Report No. 65-10-N.
STEWART, K.H. and WILDMAN, P.J.L.: 1968, Nature, 219, 714.
STEWART, K.H. and WILDMAN, P.J.L.: 1969, Proc. Roy. Soc.A., 311, 591.
STOBER, A.K., SCOLNIK, R. and HENNESS, J.P.: 1963, Appl. Opt., 2, 735.
SUBBARAYA, B.H., PARKASH, S. KUMAR, V. and PAREEK, P.N.: 1974, Space Research, 14, 173.
SWIDER, J.Jr.: 1964, Planet. Space Sci., 12, 761.
TANAKA, Y.: 1974, Reported by Weeks (1975a).
TANAKA, Y., OGAWA, M. and JURSA, A.S.; 1964, J. Chem. Phys., 40, 3690.
TAYLOR, R.G., CHUBB, T.A. and KREPLIN, R.W.: 1965, J. Opt. Soc. Am. 55, 1078.
TCHEN, C.M.: 1971, Space Research, 11, 899.
THOMAS, R.M. and DAVISON, P.J.N.: 1972, Planet. Space Sci., 20, 331.
THRANE, E.V. and JOHANNESSEN, A.: 1975, J. Atmos. Terr. Phys., 37, 655.
THURNAU, D.H.: 1956, J. Opt. Soc. Am., 46, 346.
TIMOTHY, A.F. and TIMOTHY, J.G.: 1970, J. Geophys. Res., 75, 6950.
TISONE, G.C.: 1973, J. Geophys. Res., 78, 746.
TOHMATSU, T., OGAWA, T. and WATANABE, T.: 1974, Space Research, 14, 177.
TOUSEY, R.: 1963, Space Sci. Rev., 2, 3.
TOUSEY, R.: 1964, Quart. J. Roy. Astron. Soc., 5, 123.
VAN ALLEN, J.A.: 1952, The Angular Motion of High Altitude Rockets; in "Physics and Medicine of the Upper Atmosphere" (University of New Mexico Press, Alberquerque).

VASKO, A.: 1963, "Infrared Radiation".
VASSEUR, J. and CANTIN, M.: 1963, Proceedings, XI Colloque Int'l de Spectroscopie, Belgrade, p. 491.
VASSY, A.: 1965, Adv. Geophys., 11, 115.
VIDAL-MADJAR, A.: 1975, Solar Phys., 40, 69.
WATANABE, K.: 1957, J. Chem. Phys. 26, 542.
WATANABE, K.: 1958, Adv. Geophys., 2, 153.
WATANABE, K. and INN, E.C.Y.: 1953, J. Opt. Soc. Am., 43, 32.
WATANABE, K. and ZELIKOFF, M.: 1953, J. Opt. Soc. Am., 43, 753.
WATANABE, K., INN, E.C.Y. and ZELIKOFF, M.: 1953a, J. Chem. Phys., 21, 1026.
WATANABE, K., MARMO, F.F. and INN, E.C.Y.: 1953b, Phys. Rev., 90, 155.
WATANABE, K., NAKAYAMA, T. and MOTTL, J.: 1962, J. Quant. Spectrosc. Radiat. Transfer, 2, 361.
WATANABE, K., MATSUNAGA, F.M. and SAKAI, H.: 1967, Appl. Opt., 6, 391.
WEEKS, L.H.: 1967, Astrophys. J., 147, 1203.
WEEKS, L.H.: 1974, AFCRL-TR-74-0109.
WEEKS, L.H.: 1975a, J. Geophys. Res., 80, 3655.
WEEKS, L.H.: 1975b, J. Geophys. Res., 80, 3661.
WEEKS, L.H. and SMITH, L.G.: 1968, J. Geophys. Res., 73, 4835.
WEEKS, L.H. and SMITH, L.G.: 1968b, Planet. Space Sci., 16, 1189.
WIDING, K.G., PURCELL, J.D. and SANDLIN, G.D.: 1970, Solar Phys., 12, 52.
WILDMAN, P.J.L., KERLEY, M.J. and SHAW, M.S.: 1969, J. Atmos. Terr. Phys., 31, 951.
WILLMORE, P.: 1961, Mem. Soc. Roy. Sci.Liege, ser.5, 4, 103.
ZWORYKIN, V.K., MORTON, G.A. and MALTER, L.: 1936, Prod. I.R.E.24, 351.